A SECOND-ORDER DIFFRACTION THEORY FOR WAVE RUNUP AND WAVE FORCES ON A VERTICAL CIRCULAR CYLINDER

By

DAVID LANE KRIEBEL

A DISSERTATION PRESENTED TO THE GRADUATE SCHOOL
OF THE UNIVERSITY OF FLORIDA IN
PARTIAL FULFILLMENT OF THE REQUIREMENTS
FOR THE DEGREE OF DOCTOR OF PHILOSOPHY

UNIVERSITY OF FLORIDA

1987

TABLE OF CONTENTS

ACKNOWLEDGEMENTS v

LIST OF TABLES vi

LIST OF FIGURES vii

LIST OF SYMBOLS xiii

ABSTRACT xviii

CHAPTERS

1 INTRODUCTION 1

1.1 Problem Statement 1

1.2 Problem Formulation 3

1.3 First-Order Solution 8

1.4 Second-Order Problem Formulation 12

2 REVIEW OF THE LITERATURE 14

2.1 Introduction 14

2.2 Solutions Prior to 1979 14

2.3 Asymptotic Solutions 17

2.4 Green's Function Solutions 18

2.5 Fourier-Bessel Integral Solutions 20

2.6 Other Recent Solutions 21

2.7 Irregularity of Second-Order Solution 22

2.8 Discussion of Literature 24

3 SOLUTION FOR SECOND-ORDER VELOCITY POTENTIAL 27

3.1 Introduction 27

3.2 General Solution Procedure 27
3.3 Far-Field Boundary Condition 30
3.4 Second-Order Solution 35
3.4.1 Solution for Scattered Potential ϕ_2^H 35
3.4.2 Solution for Incident Potential ϕ_{2P}^{ii} 37
3.4.3 Solutions for ϕ_{2P}^{is} and ϕ_{2P}^{ss} 38
3.4.4 Summary of Forced Wave Motion 47
3.5 Complete Solution Satisfying the No-Flow Condition 47
3.6 Discussion of Solution for Φ_2 49
3.7 Numerical Computation of Φ_2 52
4 FREE SURFACE ELEVATIONS AND WAVE RUNUP 57
4.1 Introduction 57
4.2 First-Order Water Surface 58
4.3 Quadratic Components of the Second-Order Water Surface 63
4.3.1 Mean Water Levels 64
4.3.2 Oscillatory Quadratic Free Surface 67
4.4 Free Surface from Second-Order Velocity Potential 69
4.5 Free Surface Complete to Second-Order 73
4.6 Summary of Nonlinear free surface 79
5 WAVE FORCES 89
5.1 Introduction 89
5.2 First-Order Wave Forces 91
5.3 Quadratic Components of Second-Order Force 94
5.3.1 Mean Drift Forces 95
5.3.2 Oscillatory Quadratic Forces 97
5.4 Forces from Second-Order Velocity Potential 99
5.5 Wave Forces Complete to Second-Order 102

5.6 Summary of Nonlinear Forces 104

6 EXPERIMENTAL VERIFICATION OF SECOND-ORDER THEORY 111

6.1 Description of Laboratory Experiments 111

6.2 Literature Review of Previous Experiments 117

6.3 Results of Wave Runup/Rundown Experiments 122

6.4 Results for Photopole Experiments 129

6.5 Results of Wave Force Experiments 131

7 SUMMARY AND CONCLUSIONS 140

APPENDICES

A DERIVATION OF QUADRATIC TERMS 154

A.1 Notation 154

A.2 Quadratic Forcing in Combined Free Surface Boundary Condition 155

A.3 Representation of Quadratic Terms by Fourier Series 158

A.4 Exact Form of f^{ii} Quadratic Forcing Terms 159

A.5 Asymptotic Form of the Free Surface Forcing Terms 160

A.6 Quadratic Terms For Evaluation of Second-Order Free Surface 161

A.7 Quadratic Terms For Evaluation of Second-Order Wave Forces 163

B DERIVATION OF COEFFICIENTS FOR SCATTERED WAVE SOLUTION . 169

C USEFUL INTEGRALS 171

D RESULTS OF WAVE RUNUP EXPERIMENTS 173

E RESULTS OF PHOTOPOLE EXPERIMENTS 196

F RESULTS FOR WAVE FORCE EXPERIMENTS 209

BIBLIOGRAPHY 232

BIOGRAPHICAL SKETCH 236

ACKNOWLEDGEMENTS

I am most appreciative of the advice and friendship of Dr. Robert G. Dean and I thank him for his guidance not only during this study but during the six years that I have worked with him. I am grateful to Dr. James Kirby, Dr. Robert Dalrymple, and Marc Perlin for numerous useful discussions, to Claudio Neves for customizing the word processing software, and to my committe members, Drs. Thomas Bowman, Joseph Hammack, Lawrence Malvern, Michel Ochi, and Hsiang Wang for their input. I also thank Dr. Wang and the Coastal and Oceanographic Engineering Department for financial support, as well as the staff of the Coastal Engineering Laboratory for help in the experimental and numerical phases of the study.

Numerous friends and fellow students provided daily encouragement and made this a great experience, especially Mike Barnett, Kevin Bodge, Danny Brown, Bill Dally, Claudio Neves, Marc and Terri Perlin, and Harley Winer.

Most of all, however, I would like to express my gratitude to my best friend, my wife Debbie. She has endured more than her share of lonely nights and weekends but her faith, her optimism, her patience, and her love, have enabled us both to realize this goal.

LIST OF TABLES

6.1 Wave Conditions for Laboratory Experiments 113

6.2 Nondimensional Parameters From Laboratory Experiments 113

6.3 Normalized Fourier Amplitudes for Wave and Force Data 132

LIST OF FIGURES

1.1 Definition sketch 4

3.1 Amplitude of f^{ss} quadratic forcing applied to free surface, (a) side view, (b) front view 33

3.2 Amplitude of f^{is} quadratic forcing applied to free surface, (a) side view, (b) front view 34

3.3 Definition sketch for point-source of applied surface pressure 39

3.4 Amplitude of $\tilde{f}_1^{is}$ forcing with Gibb's phenomenon after one iteration . 55

3.5 Amplitude of $\tilde{f}_1^{is}$ forcing with reduced Gibb's phenomenon after 50 iterations 55

4.1 Runup profiles from linear theory for various values of ka. 60

4.2 Maximum wave runup as a function of diffraction parameter, ka. . . . 60

4.3 Envelope of first-order free surface along axis of wave propagation, $ka = 1.0$ 61

4.4 Contours of first-order wave crest envelope, $ka = 1.0$ 62

4.5 Second-order mean water levels along x axis for reference case, $ka = 1.0$, $kd = 1.57$, and $kH = 0.5$ 65

4.6 Contours of second-order mean water level for reference case, $ka = 1.0$, $kd = 1.57$, and $kH = 0.5$ 66

4.7 Envelope of second-order oscillatory quadratic components, $ka = 1.0$, $kd = 1.57$, and $kH = 0.5$ 68

4.8 Envelope from second-order velocity potential and effect of second-order potential on free surface, $ka = 1.0$, $kd = 1.57$, and $kH = 0.5$ 72

4.9 Total wave envelope to second-order for reference case $ka = 1.0$, $kd = 1.57$, and $kH = 0.5$ 74

4.10 Contours of total wave crest amplitude to second-order for reference case $ka = 1.0$, $kd = 1.57$, and $kH = 0.5$ 77

4.11 Oblique view of wave field near cylinder to second- order, phase of maximum runup$-\pi/2$, for reference case $ka = 1.0$, $kd = 1.57$, and $kH = 0.57$ 78

4.12 Oblique view of wave field near cylinder to second- order, phase of maximum runup, for reference case $ka = 1.0$, $kd = 1.57$, and $kH = 0.5$ . . . 79

4.13 Example of second-order wave envelope for large cylinder, $ka = 1.57$, $kd = 1.57$, $kH = 0.5$ 81

4.14 Example of second-order wave envelope for small cylinder, $ka = 0.2$, $kd = 1.57$, $kH = 0.5$ 82

4.15 Example of second-order wave envelope for deep water, $ka = 1.0$, $kd = 3.14$, $kH = 0.5$ 83

4.16 Example of second-order wave envelope for near-shallow water, $ka = 1.0$, $kd = 0.628$, $kH = 0.1$ 84

4.17 Comparison of first and second-order wave runup at $\theta = \pi$ as a function of the diffraction parameter and wave steepness 86

4.18 Percent difference between second and first order maximum runup . . . 87

5.1 Maximum linear wave force as a function of the diffraction parameter ka 93

5.2 Oscillatory quadratic force compared to linear force for reference conditions 99

5.3 Second-order forces from the second-order velocity potential for reference condition 102

5.4 Total second-order wave forces for reference conditions 103

5.5 Example of second-order force for large cylinder, $ka = 1.57$, $kd = 1.57$, and $kH = 0.5$ 104

5.6 Example of second-order force for small cylinder, $ka = 0.2$, $kd = 1.57$, and $kH = 0.5$ 105

5.7 Example of second-order force for deep water, $ka = 1.0$, $kd = 3.14$, and $kH = 0.5$ 106

5.8 Example of second-order force for near-shallow water, $ka = 1.0$, $kd = 0.628$, and $kH = 0.1$ 107

5.9 Comparison of first and second-order maximum forces as a function of the diffraction parameter and wave steepness 109

5.10 Percent difference between second and first-order maximum force . . . 110

6.1 Model basin and experimental setup 112

6.2 Test conditions compared to approximate limits of validity for Stokes theories 114

6.3 Instrumented cylinder for measuring total wave forces 116

6.4 Side view of cylinder with photopole array 117

6.5 Comparison of linear theory to available force data in the diffraction regime 120

6.6 Comparison of measured runup to linear and second-order theories . . 126

6.7 Percentage difference between measured maximum runup and linear theory 127

6.8 Percentage difference between measured maximum runup and second-order theory 128

6.9 Comparison of measured maximum forces to linear and second-order theories 135

6.10 Percentage difference between measured maximum forces and linear theory 137

6.11 Percentage difference between measured maximum forces and second-order theory 138

6.12 Comparison of measured drift forces to second-order theory 139

D.1 Runup/rundown envelope for $ka = 0.271$, $kd = 0.750$, and $kH = 0.132$ 174

D.2 Runup/rundown envelope for $ka = 0.271$, $kd = 0.750$, and $kH = 0.178$ 175

D.3 Runup/rundown envelope for $ka = 0.271$, $kd = 0.750$, and $kH = 0.215$ 176

D.4 Runup/rundown envelope for $ka = 0.308$, $kd = 0.853$, and $kH = 0.085$ 177

D.5 Runup/rundown envelope for $ka = 0.308$, $kd = 0.853$, and $kH = 0.137$ 178

D.6 Runup/rundown envelope for $ka = 0.308$, $kd = 0.853$, and $kH = 0.182$ 179

D.7 Runup/rundown envelope for $ka = 0.308$, $kd = 0.853$, and $kH = 0.250$ 180

D.8 Runup/rundown envelope for $ka = 0.308$, $kd = 0.853$, and $kH = 0.296$ 181

D.9 Runup/rundown envelope for $ka = 0.374$, $kd = 1.036$, and $kH = 0.122$ 182

D.10 Runup/rundown envelope for $ka = 0.374$, $kd = 1.036$, and $kH = 0.205$ 183

D.11 Runup/rundown envelope for $ka = 0.374$, $kd = 1.036$, and $kH = 0.286$ 184

D.12 Runup/rundown envelope for $ka = 0.374$, $kd = 1.036$, and $kH = 0.385$ 185

D.13 Runup/rundown envelope for $ka = 0.374$, $kd = 1.036$, and $kH = 0.402$ 186

D.14 Runup/rundown envelope for $ka = 0.481$, $kd = 1.332$, and $kH = 0.186$ 187

D.15 Runup/rundown envelope for $ka = 0.481$, $kd = 1.332$, and $kH = 0.317$ 188

D.16 Runup/rundown envelope for $ka = 0.481$, $kd = 1.332$, and $kH = 0.438$ 189

D.17 Runup/rundown envelope for $ka = 0.481$, $kd = 1.332$, and $kH = 0.530$ 190

D.18 Runup/rundown envelope for $ka = 0.631$, $kd = 1.745$, and $kH = 0.683$ 191

D.19 Runup/rundown envelope for $ka = 0.684$, $kd = 1.894$, and $kH = 0.391$ 192

D.20 Runup/rundown envelope for $ka = 0.684$, $kd = 1.894$, and $kH = 0.572$ 193

D.21 Runup/rundown envelope for $ka = 0.917$, $kd = 2.536$, and $kH = 0.631$ 194

D.22 Runup/rundown envelope for $ka = 0.917$, $kd = 2.536$, and $kH = 0.806$ 195

E.1 Photopole data compared to theoretical wave envelope along x-axis for $ka = 0.308$, $kd = 0.853$, and $kH = 0.085$ 197

E.2 Photopole data compared to theoretical wave envelope along x-axis for $ka = 0.308$, $kd = 0.853$, and $kH = 0.137$ 198

E.3 Photopole data compared to theoretical wave envelope along x-axis for $ka = 0.308$, $kd = 0.853$, and $kH = 0.182$ 199

E.4 Photopole data compared to theoretical wave envelope along x-axis for $ka = 0.374$, $kd = 1.036$, and $kH = 0.122$ 200

E.5 Photopole data compared to theoretical wave envelope along x-axis for $ka = 0.374$, $kd = 1.036$, and $kH = 0.205$ 201

E.6 Photopole data compared to theoretical wave envelope along x-axis for $ka = 0.374$, $kd = 1.036$, and $kH = 0.286$ 202

E.7 Photopole data compared to theoretical wave envelope along x-axis for $ka = 0.481$, $kd = 1.332$, and $kH = 0.186$ 203

E.8 Photopole data compared to theoretical wave envelope along x-axis for $ka = 0.481$, $kd = 1.332$, and $kH = 0.317$ 204

E.9 Photopole data compared to theoretical wave envelope along x-axis for $ka = 0.481$, $kd = 1.332$, and $kH = 0.438$ 205

E.10 Photopole data compared to theoretical wave envelope along x-axis for $ka = 0.684$, $kd = 1.894$, and $kH = 0.391$ 206

E.11 Photopole data compared to theoretical wave envelope along x-axis for $ka = 0.684$, $kd = 1.894$, and $kH = 0.572$ 207

E.12 Photopole data compared to theoretical wave envelope along x-axis for $ka = 0.917$, $kd = 2.536$, and $kH = 0.631$ 208

F.1 Theoretical and experimental results for (1) wave profile at $r = 10a$ and $\theta = \pi/2$ and (2) depth-integrated force, for $ka = 0.271$, $kd = 0.750$, and $kH = 0.132$ 210

F.2 Theoretical and experimental results for (1) wave profile at $r = 10a$ and $\theta = \pi/2$ and (2) depth-integrated force, for $ka = 0.271$, $kd = 0.750$, and $kH = 0.178$ 211

F.3 Theoretical and experimental results for (1) wave profile at $r = 10a$ and $\theta = \pi/2$ and (2) depth-integrated force, for $ka = 0.271$, $kd = 0.750$, and $kH = 0.215$ 212

F.4 Theoretical and experimental results for (1) wave profile at $r = 10a$ and $\theta = \pi/2$ and (2) depth-integrated force, for $ka = 0.308$, $kd = 0.853$, and $kH = 0.085$ 213

F.5 Theoretical and experimental results for (1) wave profile at $r = 10a$ and $\theta = \pi/2$ and (2) depth-integrated force, for $ka = 0.308$, $kd = 0.853$, and $kH = 0.137$ 214

F.6 Theoretical and experimental results for (1) wave profile at $r = 10a$ and $\theta = \pi/2$ and (2) depth-integrated force, for $ka = 0.308$, $kd = 0.853$, and $kH = 0.182$ 215

F.7 Theoretical and experimental results for (1) wave profile at $r = 10a$ and $\theta = \pi/2$ and (2) depth-integrated force, for $ka = 0.308$, $kd = 0.853$, and $kH = 0.250$ 216

F.8 Theoretical and experimental results for (1) wave profile at $r = 10a$ and $\theta = \pi/2$ and (2) depth-integrated force, for $ka = 0.308$, $kd = 0.853$, and $kH = 0.296$ 217

F.9 Theoretical and experimental results for (1) wave profile at $r = 10a$ and $\theta = \pi/2$ and (2) depth-integrated force, for $ka = 0.374$, $kd = 1.036$, and $kH = 0.122$ 218

F.10 Theoretical and experimental results for (1) wave profile at $r = 10a$ and $\theta = \pi/2$ and (2) depth-integrated force, for $ka = 0.374$, $kd = 1.036$, and $kH = 0.205$ 219

F.11 Theoretical and experimental results for (1) wave profile at $r = 10a$ and $\theta = \pi/2$ and (2) depth-integrated force, for $ka = 0.374$, $kd = 1.036$, and $kH = 0.286$ 220

F.12 Theoretical and experimental results for (1) wave profile at $r = 10a$ and $\theta = \pi/2$ and (2) depth-integrated force, for $ka = 0.374$, $kd = 1.036$, and $kH = 0.385$ 221

F.13 Theoretical and experimental results for (1) wave profile at $r = 10a$ and $\theta = \pi/2$ and (2) depth-integrated force, for $ka = 0.374$, $kd = 1.036$, and $kH = 0.402$ 222

F.14 Theoretical and experimental results for (1) wave profile at $r = 10a$ and $\theta = \pi/2$ and (2) depth-integrated force, for $ka = 0.481$, $kd = 1.332$, and $kH = 0.186$ 223

F.15 Theoretical and experimental results for (1) wave profile at $r = 10a$ and $\theta = \pi/2$ and (2) depth-integrated force, for $ka = 0.481$, $kd = 1.332$, and $kH = 0.317$ 224

F.16 Theoretical and experimental results for (1) wave profile at $r = 10a$ and $\theta = \pi/2$ and (2) depth-integrated force, for $ka = 0.481$, $kd = 1.332$, and $kH = 0.438$ 225

F.17 Theoretical and experimental results for (1) wave profile at $r = 10a$ and $\theta = \pi/2$ and (2) depth-integrated force, for $ka = 0.481$, $kd = 1.332$, and $kH = 0.530$ 226

F.18 Theoretical and experimental results for (1) wave profile at $r = 10a$ and $\theta = \pi/2$ and (2) depth-integrated force, for $ka = 0.631$, $kd = 1.745$, and $kH = 0.683$ 227

F.19 Theoretical and experimental results for (1) wave profile at $r = 10a$ and $\theta = \pi/2$ and (2) depth-integrated force, for $ka = 0.684$, $kd = 1.894$, and $kH = 0.391$ 228

F.20 Theoretical and experimental results for (1) wave profile at $r = 10a$ and $\theta = \pi/2$ and (2) depth-integrated force, for $ka = 0.684$, $kd = 1.894$, and $kH = 0.572$ 229

F.21 Theoretical and experimental results for (1) wave profile at $r = 10a$ and $\theta = \pi/2$ and (2) depth-integrated force, for $ka = 0.917$, $kd = 2.536$, and $kH = 0.631$ 230

F.22 Theoretical and experimental results for (1) wave profile at $r = 10a$ and $\theta = \pi/2$ and (2) depth-integrated force, for $ka = 0.917$, $kd = 2.536$, and $kH = 0.806$ 231

LIST OF SYMBOLS

a	cylinder radius
a_n	coefficient in scattered wave solutions
a_{nm}	coefficient in scattered wave solutions
A_n	radial function for the first order velocity potential
$c.c.$	complex conjugate quantity
C	general constant coefficient
CFSBC	combined free surface boundary condition
$C(t)$	Bernoulli function
d	water depth
DFSBC	dynamic free surface boundary condition
D_n	wavenumber spectrum
f	quadratic forcing terms in second-order CFSBC
f^{ii}	forcing due to self-interaction of first-order incident wave
f^{is}	forcing due to cross-interaction of first-order incident and scattered waves
f^{ss}	forcing due to self-interaction of first-order scattered wave
f_n	quadratic forcing in series form of second-order CFSBC; function of r only
f_n^{ii}	forcing due to self-interaction of first-order incident wave; function of r only
f_n^{is}	forcing due to cross-interaction of first-order incident and scattered waves; function of r only
f_n^{ss}	forcing due to self-interaction of first-order scattered wave; function of r only
F	total depth-integrated force on cylinder in x direction
F_1	force to first-order
F_2	force to second-order

F_{21}	quadratic second-order force, total
F_{21f}	quadratic second-order force, from first-order free surface
F_{21v}	quadratic second-order force, from velocity-squared terms
F_{21}^{o}	oscillatory quadratic second-order force
F_{21}^{s}	steady quadratic second-order force or drift force
F_{21f}^{s}	steady quadratic second-order force, from first-order free surface
F_{21f}^{o}	oscillatory quadratic second-order force, from first-order free surface
F_{21v}^{o}	oscillatory quadratic second-order force, from velocity-squared terms
F_{21v}^{s}	steady quadratic second-order force, from velocity-squared terms
F_{22}	second-order force from second-order velocity potential
g	gravitational acceleration constant
$g_{m,n}$	nondimensional function of r in series expansions in Appendix A
$g(\theta)$	general complex function of θ
G	Green's function
G_n^o	radial function for oscillatory quadratic free surface; defined in Appendix A.6
G_n^s	radial function for steady quadratic free surface; defined in Appendix A.6
$h_{m,n}$	nondimensional function of r in series expansions in Appendix A
$h(\theta)$	general function of θ
H	wave height
H_n	Hankel function of the first kind of order n
H_n'	radial derivative of Hankel function with respect to argument
J_n	Bessel function of the first kind of order n
J_n'	radial derivative of Bessel function with respect to argument
k	first-order free wavenumber from $\sigma^2 = gk \tanh kd$
ka	relative cylinder radius
kd	relative depth
kH	wave steepness

k_2	second-order free wavenumber from $4\sigma^2 = gk_2 \tanh k_2 d$
KBBC	kinematic bottom boundary condition
KFSBC	kinematic free surface boundary condition
KSBC	kinematic structural boundary condition
K_n	modified Bessel function of second kind of order n
K_n'	radial derivative of modified Bessel function with respect to argument
P	pressure, either on free surface or in fluid
PV	Cauchy principal value integral
r	radial distance, center of cylinder to field point
r'	radial distance, center of cylinder to source point
R	radial distance, source point to field point
t	time
T	wave period
u	radial water particle velocity
v	tangential water particle velocity
w	vertical water particle velocity
x	cartesian coordinate in direction of wave propagation
y	cartesian coordinate transverse to direction of wave propagation
Y_n	Bessel function of the second kind of order n
Y_n'	radial derivative of Bessel function with respect to argument
z	cartesian coordinate in vertical direction
α	horizontal angle from x axis in local coordinate system relative to point source
β_n	complex coefficient defined as $(2 - \delta_{n0})i^n$
γ	y coordinate of source point
δ	Dirac delta function
δ_{n0}	Kronecker delta function, nonzero when $n = 0$
ϵ	perturbation parameter equal to wave steepness

ς	z coordinate of source point
η	free surface elevation
η_1	first-order free surface elevation
η_2	second-order free surface elevation
η_{21}	second-order quadratic free surface components derived from first-order velocity potential
η_{21}^o	oscillatory second-order quadratic free surface components
η_{21}^s	steady second-order quadratic free surface components
η_{22}	second-order free surface component derived from second-order velocity potential
θ	horizontal angle to field point in global coordinate system
θ'	horizontal angle to source point in global coordinate system
κ	general wavenumber
κ_j	first-order wavenumber for evanescent modes; from $\sigma^2 = -g\kappa_j \tan \kappa_j d$
κ_{2j}	second-order wavenumber for evanescent modes; from $4\sigma^2 = -g\kappa_{2j} \tan \kappa_{2j} d$
μ	x component of wavenumber vector
ν	y component of wavenumber vector
ξ	x coordinate of source point
ρ	density of water
σ	wave frequency equal to $2\pi/T$
ϕ	velocity potential with time dependence removed; same definition applies with any subscript or superscript
ϕ^F	velocity potential for forced wave due to point source of pressure
ϕ^R	velocity potential for radiated wave due to point source of pressure
Φ	velocity potential, including time dependence
Φ_1	first-order velocity potential
Φ_2	second-order velocity potential
Φ_1^i	first-order incident velocity potential
Φ_1^s	first-order scattered velocity potential

Φ_2^i	second-order incident velocity potential
Φ_2^s	second-order scattered velocity potential
Φ_2^H	second-order velocity potential for homogeneous solutions
Φ_2^P	second-order velocity potential for particular solutions
Φ_{2H}^{ii}	second-order homogeneous solution for scattering of forced wave due to f^{ii} forcing
Φ_{2H}^{is}	second-order homogeneous solution for scattering of forced wave due to f^{is} forcing
Φ_{2H}^{ss}	second-order homogeneous solution for scattering of forced wave due to f^{ss} forcing
Φ_{2P}^{ii}	second-order particular solution for forced wave due to f^{ii} forcing
Φ_{2P}^{is}	second-order particular solution for forced wave due to f^{is} forcing
Φ_{2P}^{ss}	second-order particular solution for forced wave due to f^{ss} forcing
ψ_n	phase angle defined as $\tan^{-1}(Y_n'(ka)/J_n'(ka))$
∇	gradient operator
$\Re$	real part of complex quantity
$\tilde{}$	used over another symbol to denote nondimensional quantity
$\hat{}$	used over another symbol to denote complex conjugate quantity

Abstract of Dissertation Presented to the Graduate School
of the University of Florida in Partial Fulfillment of the
Requirements for the Degree of Doctor of Philosophy

A SECOND-ORDER DIFFRACTION THEORY FOR WAVE RUNUP AND WAVE FORCES ON A VERTICAL CIRCULAR CYLINDER

By

DAVID LANE KRIEBEL

August 1987

Chairman: Robert G. Dean
Major Department: Engineering Sciences

A solution is developed for the interaction of a second-order Stokes wave with a large vertical circular cylinder. At first-order, the solution is the usual linear diffraction theory, consisting of an incident plane wave and an outwardly radiating scattered wave. At second-order, quadratic forcing terms, due to nonlinear interactions of the first-order incident and scattered waves, appear in the free surface boundary condition and behave like an applied surface pressure to generate additional waves at twice the frequency of the linear waves.

The second-order solution consists of (1) particular solutions representing forced wave motions due to the quadratic forcing and (2) complementary or homogeneous solutions representing scattered wave motions due to the interaction of the forced waves with the cylinder. One forced wave component is the usual Stokes second-order plane wave. Other forced wave motions are found in closed integral form by applying a source distribution method in which the source strengths and phases are given by the quadratic forcing on the free surface. The scattered wave solutions consist of outwardly radiating second-order free waves plus local evanescent modes which satisfy the homogeneous form of the second-order boundary value problem.

Theoretical results are compared to 22 laboratory experiments in which measurements were obtained for (1) wave runup and rundown around the circumference of the cylinder, (2)

wave crest and trough envelopes in front and behind the cylinder, and (3) total wave forces. The second-order theory explains a significant portion of the measured wave runup and scattered/diffracted wave envelope. Measured maximum runup exceeds linear theory by 44 percent on average but exceeds the nonlinear theory by only 11 percent; in some cases both measured runup and the second-order theory exceed the linear prediction by more than 50 percent. The second-order forces also agree with measured data and exceed linear forces by as much as 20 percent for certain conditions. The nonlinear diffraction theory is found to be valid for the same relative depth and wave steepness conditions applicable to Stokes plane wave theory.

CHAPTER 1
INTRODUCTION

1.1 Problem Statement

At present, there is no consensus on a complete and consistent second-order theory for the scattering and diffraction of water waves about a large surface-piercing vertical circular cylinder. For small piles, second and higher-order estimates of wave loadings are obtained through the semi-empirical Morison equation, e.g. Morison et al. (1950), with wave kinematics described by one of the higher-order wave theories, based on the assumption that the incident wave is not distorted by the cylinder . For large piles, this assumption is no longer reasonable. Higher-order solutions for wave flow past a large cylinder must include (1) wave-structure interactions, such as scattering of the incident plane wave, and (2) wave-wave interactions between the incident and scattered waves. In theory, inertial terms are dominant in the equations of motion for flow around a large cylinder and the resulting boundary value problem is "simplified" to the potential flow limit. In practice, however, the resulting problem has proved difficult to solve when extended to second-order due to the combination of imposed boundary conditions, which include quadratic forcing in the free surface boundary condition, the kinematic requirement for no-flow through the cylinder boundary, and a poorly specified form of the radiation condition far from the cylinder.

The boundary value problem for the first perturbation order, corresponding to linear diffraction theory, was solved by Havelock (1940) for the deep water case and by MacCamy and Fuchs (1954) for finite water depth. Since the mid-1970s, several solutions for the second-order diffraction theory have been proposed, yet none has achieved acceptance as a "correct" solution. The earlier solutions, i.e. before 1979, either failed to satisfy the nonhomogeneous free surface boundary condition imposed at second-order, or failed to

recognize that both free and forced wave motion must exist at second order. Forced waves must exist due to the applied quadratic forcing in the second-order free surface boundary condition while dispersive free waves must exist due to the scattering of the forced waves from the cylinder. Since 1979, proposed solutions have seemingly satisfied the required free surface boundary conditions and have included free and forced wave components. However, due to the mathematical form of these solutions, and due to continued lack of agreement on a proper far-field radiation condition, it is not clear that any of these proposed solutions are complete such that all physical second-order wave motions are represented.

The ultimate goal of all proposed second-order solutions has been to determine second-order wave forces for the design of large offshore structures. Given the lack of agreement on a complete solution for the second-order velocity potential, there is similarly no agreement on a proper formulation for second-order forces. The importance of second-order effects on wave loadings is not known with certainty and no conclusive design criteria are available. Based on a comparison of laboratory wave force data to linear diffraction theory, it has been speculated that second-order effects may account for as much as a 20 percent increase in wave forces. However, the comparison of theoretical second-order force solutions to laboratory data has been incomplete and none of the proposed solutions is well verified.

Surprisingly, no effort has been made in any previous solution to consider the behavior of the wave field around the cylinder or to compare the resulting scattering or diffraction effects with phenomena observed in other wave-structure interaction problems. Only two of the proposed second-order solutions consider the resulting second-order wave runup around the cylinder, and neither of these have developed general design guidelines for wave runup on cylindrical members. In general, little physical interpretation of the second-order free and forced wave motions is offered in any of the proposed methods; this has made it especially difficult to evaluate the completeness of the proposed solutions.

The basic objective of this study is to obtain a complete solution, consistent to the second perturbation order, for the interaction of regular Stoke's waves with a large surface

piercing vertical circular cylinder. Second-order effects are investigated, both through development of a unified second-order theory and through comparison of the theory to laboratory data. Specific goals, addressed in subsequent chapters, are to

1. Review the previously proposed solutions for the second-order velocity potential in order to assess the completeness and validity of each method.

2. Develop a complete solution for the second-order velocity potential which rigorously accounts for all free and forced wave motions.

3. Determine the second-order free surface displacements around the pile, including wave runup, scattering and diffraction effects, and second-order mean water levels.

4. Determine the second-order wave forces on the cylinder, including the mean drift forces and the time-dependent dynamic forces.

5. Compare the theoretical potential flow solution for the dynamic forces, mean drift forces, and wave runup to laboratory data.

6. Assess the relative importance of second-order effects over the range of relevant nondimensional parameters to determine the range of validity of the second-order solution.

1.2 Problem Formulation

A fixed, vertical, surface-piercing cylinder, of radius, a, in water of uniform depth, d, is subjected to regular periodic waves of height, H, propagating in the positive x direction as shown in Figure 1.1. It is assumed that the fluid is irrotational and incompressible such that the velocity vector may be represented by the positive gradient of a scalar velocity potential. In cylindrical coordinates, the velocity potential is given as $\Phi(r, \theta, z, t)$ such that the physical fluid velocity components are

$$u = \frac{\partial \Phi}{\partial r} = \Phi_r \tag{1.1}$$

$$v = \frac{1}{r}\frac{\partial \Phi}{\partial \theta} = \frac{1}{r}\Phi_\theta \tag{1.2}$$

$$w = \frac{\partial \Phi}{\partial z} = \Phi_z \tag{1.3}$$

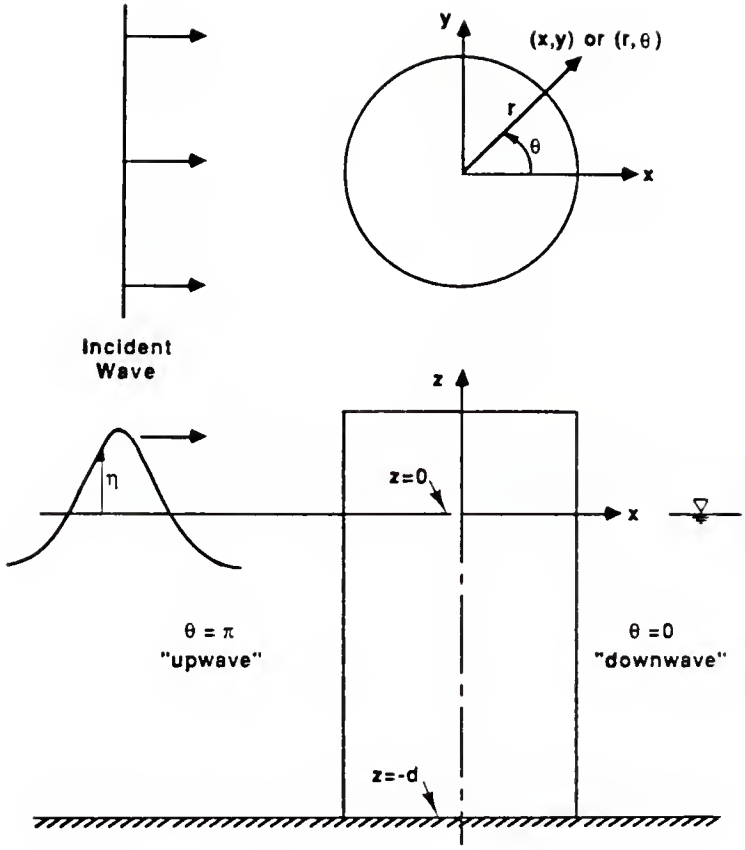

Figure 1.1: Definition sketch

The governing partial differential equation is the equation for conservation of fluid mass which, for an incompressible fluid, is given by the Laplace equation

$$\nabla^2 \Phi = 0 \tag{1.4}$$

In cylindrical coordinates this is

$$\Phi_{rr} + \frac{1}{r}\Phi_r + \frac{1}{r^2}\Phi_{\theta\theta} + \Phi_{zz} = 0 \tag{1.5}$$

In addition, appropriate boundary conditions must be satisfied. These include kinematic conditions governing the flow field along the bottom, the cylinder, and the free surface, as well as dynamic conditions which require the free surface to deform in order to maintain a uniform pressure. As a consequence of the deformable free surface, the position of the upper fluid boundary is an additional unknown and is given by the equation

$$z = \eta(r, \theta, t) \tag{1.6}$$

The derivations of the boundary conditions are well known, e.g. Stoker (1957), Mei (1983), or Dean and Dalrymple (1984). Kinematic boundary conditions are

Kinematic Bottom Boundary Condition (KBBC) for a flat bottom

$$\Phi_z = 0 \qquad \text{on } z = -d \tag{1.7}$$

Kinematic Structural Boundary Condition (KSBC) for a circular cylinder

$$\Phi_r = 0 \qquad \text{on } r = a \tag{1.8}$$

Kinematic Free Surface Boundary Condition (KFSBC)

$$\eta_t + \Phi_r \eta_r + \frac{1}{r^2}\Phi_\theta \eta_\theta - \Phi_z = 0 \qquad \text{on } z = \eta \tag{1.9}$$

The dynamic boundary condition is

Dynamic Free Surface Boundary Condition (DFSBC)

$$\Phi_t + g\eta + \frac{1}{2}\left[(\Phi_r)^2 + (\frac{1}{r}\Phi_\theta)^2 + (\Phi_z)^2\right] = C(t) \qquad \text{on } z = \eta \tag{1.10}$$

where the external atmospheric pressure along $z = \eta$, is taken to be zero. The Bernoulli function, $C(t)$, may be specified to be zero such that the solution is referenced to the mean water level datum in deep water which is identical to the still water level.

An additional boundary condition which must be specified is a proper form of the so-called radiation condition. This condition ensures that mathematical solutions for cylindrical waves physically represent waves that radiate outward away from the cylinder rather than waves that radiate inward toward the cylinder from sources at infinity. Sommerfeld (1949, p. 193) gives the radiation condition as

$$\lim_{r\to\infty} r^{\frac{1}{2}} \left(\Phi_r^s - i\kappa\Phi^s\right) = 0 \tag{1.11}$$

where κ is the scattered wavenumber which satisfies a dispersion relationship relating the wavenumber, the water depth, and the frequency of the oscillation.

The nonlinearity of the boundary value problem, imposed by the free surface boundary conditions, effectively prevents an exact solution from being obtained. In order to obtain an approximate solution, a perturbation expansion is employed which is identical to the usual perturbation solution for two-dimensional Stokes waves, e.g. Dean and Dalrymple (1984, pp. 296-305). The velocity potential and the free surface elevation are approximated in power series form as

$$\Phi = \sum_{n=1}^{\infty} \epsilon^n \Phi_n \tag{1.12}$$

$$\eta = \sum_{n=1}^{\infty} \epsilon^n \eta_n \tag{1.13}$$

where ϵ is equal to the nondimensional wave steepness; i.e. $\epsilon = kH$. In addition, since the location of the water surface, $z = \eta$, in the free surface boundary conditions is unknown, the KFSBC and DFSBC are expanded in a Taylor series about the known reference datum, $z = 0$. Substitution of the power series representations for Φ and η into the governing equation and the boundary conditions, including the expanded free surface conditions, results in separate boundary value problems for each order ϵ term in the power series. In this study, only solutions through the second order are considered.

At order ϵ, the first-order boundary value problem is

$$\nabla^2 \Phi_1 = 0 \tag{1.14}$$

$$\Phi_{1z} = 0 \qquad \text{on } z = -d \tag{1.15}$$

$$\eta_{1t} - \Phi_{1z} = 0 \qquad \text{on } z = 0 \tag{1.16}$$

$$\Phi_{1t} + g\eta_1 = 0 \qquad \text{on } z = 0 \tag{1.17}$$

$$\Phi_{1r} = 0 \qquad \text{on } r = a \tag{1.18}$$

$$\lim_{r \to \infty} r^{1/2} \left(\Phi^s_{1r} - i\kappa \Phi^s_1 \right) = 0 \tag{1.19}$$

along with symmetry conditions on θ. Elimination of η_1 from Equations 1.16 and 1.17 gives a single Combined Free Surface Boundary Condition (CFSBC) for Φ_1

$$\Phi_{1tt} + g\Phi_{1z} = 0 \qquad \text{on } z = 0 \tag{1.20}$$

At order ϵ^2, the second-order boundary value problem is

$$\nabla^2\Phi_2 = 0 \tag{1.21}$$

$$\Phi_{2z} = 0 \qquad \text{on } z = -d \tag{1.22}$$

$$\eta_{2t} + \Phi_{1r}\eta_{1r} + \frac{1}{r^2}\Phi_{1\theta}\eta_{1\theta} - \Phi_{2z} - \Phi_{1zz}\eta_{1z} = 0 \qquad \text{on } z = 0 \tag{1.23}$$

$$\Phi_{2t} + g\eta_2 + \frac{1}{2}\left[(\Phi_{1r})^2 + (\frac{1}{r}\Phi_{1\theta})^2 + (\Phi_{1z})^2\right] + \Phi_{1tz}\eta_1 = 0 \qquad \text{on } z = 0 \tag{1.24}$$

$$\Phi_{2r} = 0 \qquad \text{on } r = a \tag{1.25}$$

and where Φ_2 satisfies symmetry conditions on θ. While the first-order radiation condition may be written in closed form, the second-order radition condition is not well-posed; additional conditions on the far-field behavior of Φ_2 are required. Elimination of η_2 from Equations 1.23 and 1.24 yields the second-order Combined Free Surface Boundary Condition (CFSBC)

$$\Phi_{2tt} + g\Phi_{2z} = - \eta_1\left[\Phi_{1tt} + g\Phi_{1z}\right]_z - \left[(\Phi_{1r})^2 + (\frac{1}{r}\Phi_{1\theta})^2 + (\Phi_{1z})^2\right]_t \qquad \text{on } z = 0 \tag{1.26}$$

At first-order, the right-hand side of the CFSBC is identically equal to zero and the CFSBC may be termed homogeneous. At second-order, non-zero quadratic forcing terms appear on the right side of the CFSBC which render the problem nonhomogeneous. These forcing terms, mathematically, contain nonlinear products of derivatives of the first-order solution. Physically, they may be interpreted as an oscillatory pressure applied to the free surface which generates second-order forced waves in order to more closely satisfy the exact nonlinear free surface boundary conditions, e.g. Lighthill (1979).

As discussed by Stoker (1957), the linear water wave problem, with a homogeneous CFSBC, is analogous to a spring-mass system in which the oscillation of a mass, m, attached to a spring with a force constant, c, is given by

$$mx_{tt} + cx = 0 \tag{1.27}$$

The resulting motions are simple harmonic oscillations that are "free" in the sense that the modes of oscillation are determined only by the characteristics of the system. For the mechanical system, the natural period of oscillation is determined by the ratio c/m, while for the linear water waves, the free or natural wavelength is related to the wave period and water depth through the linear dispersion relationship

$$\sigma^2 = gk \tanh kd \tag{1.28}$$

In contrast, the second-order water wave problem is analogous to a forced spring-mass system described by

$$mx_{tt} + cx = f \tag{1.29}$$

where f is an externally applied oscillatory force. For forced systems, the resulting motion is composed of two types of oscillations: (1) a unique forced oscillation imposed by the applied forcing and (2) free oscillations that satisfy the homogeneous free surface boundary condition, and which correspond to the natural modes of oscillation of the system. At second-order, the free wave modes oscillate at frequency 2σ but the wavelength is governed by the homogeneous form of the second-order CFSBC which gives the second-order dispersion relationship

$$4\sigma^2 = gk_2 \tanh k_2 d \tag{1.30}$$

where k_2 is the wavenumber of the free second harmonic. In deep water, k_2 approaches $4k$ while in shallow water, k_2 approaches $2k$.

1.3 First-Order Solution

The solution for the order ϵ boundary value problem in Equations 1.14 to 1.19 has been given by Havelock (1940) for deep water and by MacCamy and Fuchs (1954) for finite water depth. The solution is obtained by a separation of the potential, Φ_1, into the sum of the specified incident wave and a scattered wave

$$\Phi_1 = \Phi_1^i + \Phi_1^s \tag{1.31}$$

This separation is typical in diffraction problems and leads directly to the solution of the total first order potential. At second-order, however, such a separation does not simplify the problem in the same way since additional wave motions are generated by the quadratic forcing in the free surface boundary condition.

The first-order incident potential, representing a plane wave propagating in the $+x$ direction independent of the presence of the cylinder, must satisfy the usual boundary value problem for linear wave theory

$$\nabla^2 \Phi_1^i = 0 \tag{1.32}$$

$$\Phi_{1z}^i = 0 \qquad \text{on } z = -d \tag{1.33}$$

$$\Phi_{1tt}^i + g\Phi_{1z}^i = 0 \qquad \text{on } z = 0 \tag{1.34}$$

The solution is given by

$$\Phi_1^i = -\frac{igH}{2\sigma} \frac{\cosh k(d+z)}{\cosh kd} \frac{e^{i(kx-\sigma t)}}{2} + c.c. \tag{1.35}$$

where the "c.c." denotes the complex conjugate quantity. The wavenumber, k, and the wave frequency, σ, satisfy the linear dispersion relationship

$$\sigma^2 = gk \tanh kd \tag{1.36}$$

obtained by substituting Φ_1 into the CFSBC, Equation 1.34.

In cylindrical coordinates, the incident plane wave may be represented by a partial wave expansion in terms of cylindrical standing waves, eg. Mei (1983), as

$$\Phi_1^i = -\frac{igH}{2\sigma} \frac{\cosh k(d+z)}{\cosh kd} \sum_{n=0}^{\infty} \beta_n J_n(kr) \cos n\theta \frac{e^{-i\sigma t}}{2} + c.c. \tag{1.37}$$

based on the identity, e.g. Abramowitz and Stegun (1972)

$$e^{ikx} = e^{ikr\cos\theta} = \sum_{n=0}^{\infty} \beta_n J_n(kr) \cos n\theta \tag{1.38}$$

where

$$\beta_n = (2 - \delta_{n0})i^n \tag{1.39}$$

and δ_{n0} is the Kronecker delta function.

The boundary value problem for the scattered wave potential, Φ_1^s, is given by

$$\nabla^2 \Phi_1^s = 0 \tag{1.40}$$

$$\Phi_{1z}^s = 0 \qquad \text{on } z = -d \tag{1.41}$$

$$\Phi_{1tt}^s + g\Phi_{1z}^s = 0 \qquad \text{on } z = 0 \tag{1.42}$$

$$\Phi_{1r}^s = -\Phi_{1r}^i \qquad \text{on } r = a \tag{1.43}$$

$$\lim_{r\to\infty} r^{\frac{1}{2}} \left(\Phi_{ir}^s - i\kappa\Phi_1^s\right) = 0 \tag{1.44}$$

where the scattered wavenumber, κ, is so far not specified. The scattered wave motions are "generated" by the nonhomogeneous boundary condition on the cylinder, in which there is an apparent velocity, $-\Phi_{1r}^i$, at $r = a$ as a result of the interaction of the incident plane wave with the fixed cylinder. In this way, the scattered wave problem is like a cylindrical wavemaker problem; this analogy may be applied equally at first and second-order.

The solution to the Laplace equation by separation of variables yields the following complete set of eigensolutions which satisfy the kinematic bottom boundary condition, the radiation condition, and symmetry conditions on θ, e.g. Mei (1983) or Dean and Dalrymple (1984)

$$\begin{aligned}\Phi_1^s &= \sum_{n=0}^{\infty} a_n H_n(\kappa r)\cos n\theta \cosh \kappa(d+z)\frac{e^{-i\sigma t}}{2} + c.c. \\ &+ \sum_{n=0}^{\infty}\sum_{j=1}^{\infty} a_{nj} K_n(\kappa_j r)\cos n\theta \cos \kappa_j(d+z)\frac{e^{-i\sigma t}}{2} + c.c.\end{aligned} \tag{1.45}$$

where $H_n(\kappa r)$ is understood to be the Hankel function of the first kind that represents an outwardly propagating wave while $K_n(\kappa_j r)$ is the modified Bessel function of the second kind that represents local standing wave motion. Substitution of Φ_1^s into the CFSBC in Equation 1.42 yields two dispersion relationships: (1) for real eigenvalues

$$\sigma^2 = g\kappa \tanh \kappa d \tag{1.46}$$

which has one positive root, k, identical to the incident free wave number, and (2) for imaginary eigenvalues

$$\sigma^2 = -g\kappa_j \tan \kappa_j d \tag{1.47}$$

which has many roots , κ_j, with

$$(j - \frac{1}{2})\pi < \kappa_j < j\pi \tag{1.48}$$

Applying the boundary condition on the cylinder, Equation 1.43, yields the following condition relating the unknown coefficients in the scattered wave solution, a_n and a_{nj}, to the incident wave solution

$$a_n k H_n'(ka) \cosh k(d+z) + \sum_{j=1}^{\infty} a_{nj}\kappa_{nj} K_n'(\kappa_j a) \cos \kappa_j (d+z) = \frac{igH}{2\sigma} \frac{\cosh k(d+z)}{\cosh kd} \beta_n k J_n'(ka) \tag{1.49}$$

where $J_n'(ka)$ is understood to be the derivative of $J_n(kr)$ with respect to the argument kr, evaluated at $r = a$. Since $\cosh k(d+z)$ and $\cos k_j(d+z)$ form an orthogonal set, the unknown coefficients in Equation 1.49, are found as

$$a_n = \frac{igH}{2\sigma} \frac{1}{\cosh kd} \frac{\beta_n k J_n'(ka)}{k H_n'(ka)} \tag{1.50}$$

$$a_{nj} = 0 \tag{1.51}$$

Substituting Equation 1.50 into Equation 1.45 gives the linear scattered wave solution as

$$\Phi_1^s = \frac{igH}{2\sigma} \frac{\cosh k(d+z)}{\cosh kd} \sum_{n=0}^{\infty} \beta_n \frac{J_n'(ka)}{H_n'(ka)} H_n(kr) \cos n\theta \frac{e^{-i\sigma t}}{2} + c.c. \tag{1.52}$$

which is the result of MacCamy and Fuchs (1954). The first-order scattered wave solution is represented exactly by an outwardly propagating wave since a_{nj} equals zero. This result, that the local standing modes vanish identically for the linear problem, is well known; the same result does not apply to the second-order scattered potential.

By adding the incident and scattered solutions from Equations 1.37 and 1.52, the total first order potential may now be written as

$$\Phi_1 = -\frac{igH}{2\sigma}\frac{\cosh k(d+z)}{\cosh kd}\sum_{n=0}^{\infty}\beta_n\left[J_n(kr) - \frac{J_n'(ka)}{H_n'(ka)}H_n(kr)\right]\cos n\theta\frac{e^{-i\sigma t}}{2} + c.c. \tag{1.53}$$

By redefining the radial dependence as

$$A_n(kr) = J_n(kr) - \frac{J_n'(ka)}{H_n'(ka)}H_n(kr) \tag{1.54}$$

the first-order solution becomes

$$\Phi_1 = -\frac{igH}{2\sigma}\frac{\cosh k(d+z)}{\cosh kd}\sum_{n=0}^{\infty}\beta_n A_n(kr)\cos n\theta\frac{e^{-i\sigma t}}{2} + c.c. \tag{1.55}$$

1.4 Second-Order Problem Formulation

Since the solution for Φ_1 includes the sum of the incident plus scattered waves, the quadratic terms in the second-order CFSBC, Equation 1.26, have the following general form

$$\Phi_{2tt} + g\Phi_{2z} = f^{ii} + f^{is} + f^{ss} \tag{1.56}$$

where each forcing term on the right hand side may be defined physically as

f^{ii} = due to nonlinear self-interaction of the first-order incident plane wave

f^{is} = due to nonlinear cross-interaction of the incident and scattered waves

f^{ss} = due to nonlinear self-interaction of the first-order scattered wave

Solutions for the second-order potential, Φ_2, must conceptually include three particular solutions which represent the forced wave motions due to the nonhomogeneous forcing on the free surface as

$$\Phi_2^P = \Phi_{2P}^{ii} + \Phi_{2P}^{is} + \Phi_{2P}^{ss} \tag{1.57}$$

These forced waves may be thought of as the ambient or "incident" waves at second-order, although only the Φ_{2P}^{ii} term is really incident in the sense that it is a second-order plane

wave propagating in the x direction with uniform amplitude everywhere. These forced wave motions exist only because of nonlinear wave-wave interactions. They also exist without further regard for the cylinder; therefore, they do not, by themselves, satisfy the KSBC requiring no-flow through the cylinder boundary.

In order to satisfy the no-flow condition at the cylinder boundary, a second set of solutions must exist which, when added to the particular solutions, compensates for the apparent velocity of the forced waves through the cylinder. These additional solutions are the complementary or homogeneous solutions of the corresponding boundary value problem with a homogeneous free surface boundary condition

$$\Phi^H_{2tt} + g\Phi^H_{2z} = 0 \tag{1.58}$$

These honogeneous solutions are the second-order scattered waves, and, conceptually, one homogeneous component is associated with each component of the forced wave motion as

$$\Phi^H_2 = \Phi^{ii}_{2H} + \Phi^{is}_{2H} + \Phi^{ss}_{2H} \tag{1.59}$$

While the forced waves arise because of nonlinear wave-wave interactions, the scattered waves arise because of wave-structure interactions. Just as the first-order scattered wave potential, Φ^s_1, was "generated" by an apparent motion of the cylinder boundary, $-\Phi^i_{1r}$, so too are the second-order scattered wave motions "generated" by an apparent motion of the cylinder, $-\Phi^P_{2r}$. Furthermore, the second-order scattered wave solutions may be determined by exactly the same methods used to obtain the first-order scattered wave solution.

CHAPTER 2
REVIEW OF THE LITERATURE

2.1 Introduction

Since 1972, numerous solutions for the second-order velocity potential have been proposed; however, after 15 years of research, it is not clear whether any solutions correctly represent the physics of the nonlinear wave-structure interaction problem. The first group of solutions, developed between 1972 and 1979, generally failed to (1) satisfy the nonhomogeneous combined free surface boundary condition, or (2) recognize that the solution must contain both forced wave motions, due to the quadratic terms in the CFSBC, as well as scattered free wave motions, due to the interaction of the forced waves with the cylinder. The solutions proposed since 1979 have seemingly corrected these deficiencies; however, while they mathematically satisfy the CFSBC and the KSBC, the solutions differ substantially in the way in which these boundary conditions are satisfied. Likewise, the proposed solutions incorporate the radiation condition in different ways and it is not certain that any of the methods contain a unique description of the second-order wave motions.

2.2 Solutions Prior to 1979

Chakrabarti (1972) appears to be the first to explicitly propose a solution for a higher-order velocity potential for the problem of nonlinear wave interaction with a large vertical cylinder. Using a Stokes 5th order incident wave, a series solution was assumed for the total potential which, at each order, m, had a form similar to that of the first-order solution as

$$\Phi_2 = \sum_{m=1} \lambda_m \cosh mk(d+z) \sum_{n=0} \beta_n \left[J_n(mkr) - \frac{J_n'(mka)}{H_n'(mka)} H_n(mkr) \right] \cos n\theta e^{-im\sigma t} \tag{2.1}$$

The coefficients, λ_m, are those associated with the mth order component of the incident Stokes 5th order wave. While this solution satisfies the kinematic structural boundary condition, it does not satisfy the nonhomogeneous free surface boundary condition since it does not include the effects of all nonlinear self-and cross-interaction terms.

Chakrabarti (1975) reviews the solution of Yamaguchi and Tsuchiya (1974) in which the second-order potential is given by

$$\Phi_2 = \cosh 2k(d+z) \sum_{n=0} C_n \left[Y_n'(2ka) J_n(2kr) - J_n'(2ka) Y_n(2kr) \right] \cos n\theta e^{-i2\sigma t} \tag{2.2}$$

This solution also satisfies the KSBC automatically but it assumes that all wave motion is forced with wavenumber $2k$, neglecting any second-order free wave components. The complex coefficients, C_n are determined by substituting Φ_2 into the CFSBC and evaluating at $r = a$; thus, the solution does not satisfy the required free surface conditions over the full domain.

The form of the solution for second-order terms assumed by Chakrabarti (1972) and Yamaguchi and Tsuchiya (1974) is based on a radial dependence like

$$J_n(2kr) - \frac{J_n'(2ka)}{H_n'(2ka)} H_n(2kr) \tag{2.3}$$

This form is valid at first-order since the wavenumber of the free scattered wave is identical to that of the incident wave. It is also useful mathematically since it automatically satisfies the no-flow condition on the cylinder. At second and higher-orders, however, this form of the solution is not valid since it neglects the change in wavenumber required after the nonlinear forced wave components scatter from the pile.

A standard solution technique, identical to that employed at first-order, has been to separate the second-order potential into incident and "scattered" components. Mathematically, the second-order incident wave is found from a separated boundary value problem in which no structure is present

$$\nabla^2 \Phi_2^i = 0 \tag{2.4}$$

$$\Phi^i_{2z} = 0 \qquad \text{on } z = -d \tag{2.5}$$

$$\Phi^i_{2tt} + g\Phi^i_{2z} = f^{ii} \qquad \text{on } z = 0 \tag{2.6}$$

The solution is easily obtained to be the usual Stokes second-order plane wave component since f^{ii} represents the familiar plane wave forcing.

The remaining problem for the "scattered" wave motion is

$$\nabla^2\Phi^s_2 = 0 \tag{2.7}$$

$$\Phi^s_{2z} = 0 \qquad \text{on } z = -d \tag{2.8}$$

$$\Phi^s_{2tt} + g\Phi^s_{2z} = f^{is} + f^{ss} \qquad \text{on } z = 0 \tag{2.9}$$

$$\Phi^s_{2r} = -\Phi^i_{2r} \qquad \text{on } r = a \tag{2.10}$$

Note that the nonhomogeneity in the CFSBC is not removed, and a second nonhomogeneous boundary condition is now present on the cylinder boundary. With this formulation the so-called "scattered" wave potential, Φ^s_2, must not only represent the true scattering of the incident component, Φ^i_2, but it must also represent the remaining forced wave motion generated by f^{is} and f^{ss}, as well as any interactions of these forced waves with the cylinder. This separation into second-order incident and "scattered" waves is not wrong; however, all components of wave motion must be carefully accounted for in Φ^s_2.

Raman and Venkatanarasaiah (1976a, 1976b) employ the separation outlined above and attempt to solve for the remaining "scattered"potential by taking the finite Fourier cosine transforms of the governing boundary value problem for Φ^s_2. The final solution is found to have the form

$$\Phi^s_2 = C\cosh k_2(d+z)\sum_{n=0} h_n(kr, k_2 r)\cos n\theta e^{-i2\sigma t} \tag{2.11}$$

where the function $h_n(kr, k_2 r)$ contains combinations of Bessel functions, Hankel functions, and their derivatives. The solution was the first to display the second-order free wavenumber, k_2, which satisfies the second-order dispersion relationship

$$4\sigma^2 = gk_2 \tanh k_2 d \tag{2.12}$$

As pointed out by Chakrabarti (1977,1978) and Isaacson (1977c), however, the solution with only the wavenumber, k_2, satisfies only the homogeneous CFSBC and cannot satisfy the remaining quadratic forcing in the CFSBC.

2.3 Asymptotic Solutions

Molin (1979) proposes a solution for the second-order wave forces based on Haskind's reciprocal relationship, e.g. Mei (1983), in which only an asymptotic form of the second-order velocity potential is required. Asymptotic forms of the "scattered" potential are proposed based on the leading asymptotic form of the quadratic forcing terms. For large r, the f^{is} forcing is found to behave like

$$f^{is} = \frac{1}{r^{1/2}} e^{i(kr(1+\cos\theta)-2\sigma t)} \tag{2.13}$$

Molin proposes an asymptotic solution for Φ_{2P}^{is} in the form

$$\Phi_{2P}^{is} = \frac{h(\theta)}{r^{1/2}} \left[\cosh(k(2+2\cos\theta)(d+z))\right] e^{i(kr(1+\cos\theta)-2\sigma t)} \tag{2.14}$$

which represents forced wave motion, propagating away from the cylinder everywhere, but which does not satisfy the Laplace equation. The f^{ss} forcing is found to behave asymptotically like

$$f^{ss} = \frac{1}{r} e^{i(2kr-2\sigma t)} \tag{2.15}$$

but Molin assumes a form for Φ_{2P}^{ss} like

$$\Phi_{2P}^{ss} = \frac{h(\theta)}{r^{1/2}} \cosh k_2(d+z) e^{i(k_2 r-2\sigma t)} \tag{2.16}$$

Molin argues that since Φ_{2P}^{ss} is forced by an outwardly radiating motion that decays rapidly, the wave motion far from the cylinder should be a second-order free wave satisfying the radiation condition. On the other hand, Molin assumes that the solution for Φ_{2P}^{is} should not satisfy a radiation condition, even though it too results from an oscillatory and outwardly propagating forcing applied to the free surface.

Lighthill (1979) proposes a solution for the second-order wave force which, like Molin's, does not require a solution for the second-order velocity potential. Green's theorem is applied to two potentials, the first, Φ_2, representing the second-order potential due to the presence of the fixed cylinder in waves, the other, Ψ, due to the unit oscillation of a cylinder in otherwise calm water. Four surface integrals are obtained; however, one is zero due to the bottom boundary condition and another is zero since Lighthill assumes that the "scattered" potential satisfies the radiation condition.

Of the remaining two integrals, one along the cylinder boundary is shown to be identical to the desired depth-integrated force on the cylinder, while the other may be reduced to an integral of the quadratic forcing from the CFSBC multiplied by the vertical velocity at $z = 0$ resulting from the unit oscillation of a cylinder in calm water. The method is attractive since forces may be computed without a solution for Φ_2; however, the method is also limited in that only the integrated force is obtained and other quantities, such as the wave runup or wave kinematics, cannot be determined. Lighthill (1979) applies the method for deep water and for small piles; general solutions for finite depth are given by Rahman (1984), Demirbilek and Gaston (1985), and Eatock Taylor and Hung (1987).

2.4 Green's Function Solutions

Garrison (1979) proposes a numerical solution for the second-order velocity potential based on a source distribution method using Green's functions. By introducing the Green's function, $G(\xi,\gamma,\varsigma)$, which represents a source of unit strength at $x = \xi$, $y = \gamma$, and $z = \varsigma$, the solution for the "scattered" potential is found by applying Green's theorem to Φ_2^s and G. Contributions to Φ_2^s are found from the surface integral over the cylinder at $r = a$ and from the surface integral over the free surface at $z = 0$; the radiation condition applied to Φ_2^s and G ensures no contribution from the surface integral around an imaginary outer cylinder at some large value of r.

The resulting integral solution for Φ_2^s is

$$\Phi_2^s(x,y,z) = \frac{1}{4\pi}\int_{r=a} f_s(\xi,\gamma,\varsigma)G(x,y,z;\xi,\gamma,\varsigma)dS$$

$$+ \quad \frac{1}{4\pi}\int_{z=0}(f^{is}(\xi,\gamma,0)+f^{ss}(\xi,\gamma,0))G(x,y,z;\xi,\gamma,0)dS \tag{2.17}$$

where $f_s(\xi,\gamma,\varsigma)$ is an unknown source strength distribution function over the cylinder at $r=a$, while the source strength distribution along the free surface is given exactly by the quadratic terms in the CFSBC, f^{is} and f^{ss}. The solution for $f_s(\xi,\gamma,\varsigma)$ and Φ_2^s proceeds by discretizing the cylinder boundary and the free surface into area elements and then numerically approximating the kinematic structural boundary condition using Equation 2.17. For later reference, the form of the Green's function used to represent the sources along the free surface is

$$\begin{aligned} G(x,y,0;\xi,\gamma,0) &= 2\cdot PV\int_0^\infty \frac{\kappa\cosh\kappa(d+z)}{\cosh\kappa d(\kappa\tanh\kappa d-k_2\tanh k_2 d)}J_0(\kappa R)d\kappa \\ &\quad + i4\pi\frac{k_2\cosh k_2 d\cosh k_2(d+z)}{\sinh 2k_2 d+2k_2 d}J_0(k_2 R) \end{aligned} \tag{2.18}$$

where the "PV" signifies the Cauchy Principal Value of the singular integral and R is the distance from the individual source at $(\xi,\gamma,0)$ to the field point of interest $(x,y,0)$.

Chen (1979) and Chen and Hudspeth (1982) propose a second-order diffraction solution based on an eigenfunction expansion for Green's functions. The second-order problem is first separated into the incident Stokes plane wave potential and the remaining "scattered" potential, which is further separated into two potentials as

$$\Phi_2^s = \Phi_2^{sh} + \Phi_2^{sf} \tag{2.19}$$

The potential Φ_2^{sh} satisfies the homogeneous CFSBC, the radiation condition, and a non-homogeneous structural boundary condition; this represents the scattering of free waves produced by the interaction of the incident plane wave component with the cylinder. This solution is obtained from an integral equation with a Green's function defined to include outwardly propagating free waves as well as local evanescent modes. This component is analogous to the Φ_{2H}^{ii} solution discussed in Chapter 1 and, for later reference, the solution for Φ_2^{sh} is

$$\Phi_2^{sh} = \frac{3i\sigma H^2 k}{8\sinh^4 kd}\frac{\cosh k_2 d\cosh 2kd}{(4k^2-k_2)(\sinh 2k_2 d+2k_2 d)}(2k\tanh 2kd-\frac{4\sigma^2}{g})$$

$$\cdot \cosh k_2(d+z) \sum_{n=0} \beta_n \frac{J_n'(2ka)}{H_n'(k_2a)} H_n(k_2r) \cos n\theta e^{-i2\sigma t} + c.c.$$

$$+ \frac{3\sigma H^2 k}{8 \sinh^4 kd} \sum_{j=1} \frac{\cos \kappa_{2j} d \cosh 2kd}{(4k^2 + \kappa_{2j}^2)(\sin 2\kappa_{2j} d + 2\kappa_{2j} d)} (2k \tanh 2kd - \frac{4\sigma^2}{g})$$

$$\cdot \cos \kappa_{2j}(d+z) \sum_{n=0} \beta_n \frac{J_n'(2ka)}{K_n'(\kappa_{2j}a)} K_n(\kappa_{2j}r) \cos n\theta e^{-2\sigma t} + c.c. \qquad (2.20)$$

where κ_{2j} denotes the second-order evanescent wavenumbers.

The potential Φ_2^{sf} is assumed to satisfy the remaining non-homogeneous forcing terms in the CFSBC, but is not required to satisfy a radiation condition. A Green's function solution is obtained in the form of double summations of products of Bessel functions. Unknown coefficients are determined by satisfying the CFSBC; however, eigenvalues, i.e. wavenumbers, are found by satisfying $\Phi_{2r}^{sf} = 0$ on $r = a$ based on zeros of

$$J_n'(q_j a) = 0 \qquad (2.21)$$

In this way, a set of discrete wavenumbers, q_j, are found, which satisfy the no-flow conditions for an interior boundary value problem and correspond to the irregular frequencies that occur in numerical Green's function solutions.

2.5 Fourier-Bessel Integral Solutions

Hunt and Baddour (1980a,1980b), Hunt and Baddour (1981), and Hunt and Williams (1982) proposed solutions for the second order velocity potential based on a Fourier-Bessel integral method for the conditions of deep water standing waves, deep water progressive waves, and progressive waves in finite depth, respectively. Rahman and Heaps (1983) also proposed a solution for progressive waves in finite depth that is identical in content to that of Hunt and Williams (1982).

Upon substituting the first-order solution into the second-order CFSBC, the quadratic forcing terms are ultimately represented by a single sum with separable harmonics in θ as

$$\Phi_{2tt} + g\Phi_{2z} = \sum_{n=0} f_n(r) \cos n\theta \frac{-i2\sigma t}{2} + c.c. \qquad (2.22)$$

where $f_n(r)$ is a complicated function of r that includes sums and products of $A_n(kr)$ and $A_n'(kr)$, with A_n defined in Equation 1.54.

A solution for Φ_2 is then sought in the form of an integral over a continuum of wavenumbers as

$$\Phi_2 = \sum_{n=0} \cos n\theta \left[\int_0^\infty D_n(\kappa) A_n(\kappa r) \cosh \kappa(d+z) d\kappa \right] \frac{e^{-i2\sigma t}}{2} + c.c. \tag{2.23}$$

This form satisfies the Laplace equation, the KBBC, and, since $A_n(\kappa r)$ is defined as in Equation 1.54 for each wavenumber κ, it also automatically satisfies the KSBC. By substituting Equation 2.23 into the CFSBC and equating harmonics in θ, integral equations are obtained for the spectrum of unknown coefficients $D_n(\kappa)$. Inversion of these integral equations yields the final solution for Φ_2 as

$$\begin{aligned} \Phi_2 \;=\; & \sum_{n=0} \cos n\theta \int_0^\infty \frac{m \cosh \kappa(d+z) A_n(\kappa r)}{\cosh \kappa d(\kappa \tanh \kappa d - k_2 \tanh k_2 d)} \\ & \cdot \int_0^\infty r' f_n(r') A_n(\kappa r') dr' d\kappa \frac{e^{-i2\sigma t}}{2} + c.c. \end{aligned} \tag{2.24}$$

The integral over all wavenumbers κ is singular at the second-order free wavenumber, k_2. A singular integral of this type represents local standing waves which are forced wave motions concentrated where the value of the forcing, $f_n(r)$, is greatest. Farther away, however, these forced wave modes die out and only one standing wave, with the free wavenumber, k_2, survives. The solution method requires that the prescribed forcing, $f_n(r)$ be sufficiently localized to permit a Fourier transform. Without explanation, the method is applied to all forcing terms, including the incident plane wave term, f^{ii}, which has uniform amplitude everywhere and which should not be transformable. The question of appropriate far field conditions is not fully addressed, and the solution given in Equation 2.24 does not satisfy a radiation condition, since it represents both inward and outward radiating cylindrical waves.

2.6 Other Recent Solutions

Chakrabarti (1983) presents a solution for the second-order potential based on a separation of the boundary value problem similar to that used by Chen and Hudspeth (1982). The "scattered" potential is separated into a "structural" problem (homogeneous CFSBC with

nonhomogeneous structural boundary condition) and a "free surface" problem (nonhomogeneous CFSBC but with a homogeneous structural boundary condition). For the structural problem, Chakrabarti adopts the solution of Chen and Hudspeth as given in Equation 2.20. For the free surface problem, a solution similar to that of Yamaguchi and Tsuchiya (1974) is assumed which automatically satisfies the homogeneous structural boundary condition and which has wavenumber dependence $2k$, therefore neglecting the scattered free wave components. Unknown coefficients are determined by satisfying the free surface boundary condition at $r = a$ only.

Sabuncu and Goren (1985) derive a solution for the second-order potential based on a direct eigenfunction expansion. The incident plane wave component was first separated; however, the scattering of this component was assumed to also have a $2k$ wavenumber dependence, unlike the more complete scattered solution given in Equation 2.20 by Chen and Hudspeth (1982). The remaining forced wave motions were termed the "particular" solutions and were assumed to have the form

$$\begin{aligned}\Phi_{2P} &= \sum_{n=0} \cos n\theta \left[E_{n0} \frac{H_n(2kr)}{H_n'(2ka)} \cosh 2k(d+z) \right. \\ &+ \left. \sum_{j=1} E_{nj} \frac{K_n(2\kappa_j r)}{K_n'(2\kappa_j a)} \cos 2\kappa_j (d+z) \right] \frac{e^{-i2\sigma t}}{2} + c.c. \end{aligned} \tag{2.25}$$

where a $2k$ wavenumber dependence is assumed but additional local evanescent motions are also included. The unknown coefficients are determined by numerically fitting the CFSBC through the method of collocation, in which Equation 2.25 is forced to satisfy the CFSBC at a series of discrete points on the free surface in the vicinity of the cylinder. The scattering of these forced wave motions is described by a series of homogeneous solutions which includes outwardly radiating free waves and local evanescent modes in an eigenfunction expansion form similar to that used at first-order.

2.7 Irregularity of Second-Order Solution

A controversy over the formal extension of the Stokes perturbation solution to second-order was initiated by Isaacson (1977b) who asserted that the CFSBC and the KSBC are

"incompatible" in the overlap region at $z = 0$ and $r = a$. By differentiating the CFSBC with respect to r and then evaluating at $r = a$, one obtains

$$\left(\frac{\partial^2}{\partial t^2} + g\frac{\partial}{\partial z}\right)\left(\frac{\partial \Phi_r}{\partial r}\right)_{r=a} = \frac{\partial}{\partial t}\left(\frac{2}{r^3}\left(\frac{\partial \Phi}{\partial \theta}\right)^2\right)_{r=a} \tag{2.26}$$

Isaacson found that, since $\Phi_r \equiv 0$ on $r = a$, the resulting irregular condition occurs

$$\frac{\partial}{\partial t}\left[\frac{2}{r^3}\left(\frac{\partial \Phi}{\partial \theta}\right)^2\right]_{r=a} \stackrel{?}{=} 0 \tag{2.27}$$

In general, this statement is not true, indicating an inconsistency in the solution at the juncture of the two boundaries. Isaacson (1977b, p. 169) concluded that the theory for wave diffraction "may not be extended formally to a second approximation by the usual perturbation procedure for Stokes wave."

A great deal of discussion subsequently occurred in the literature, with various authors claiming that the Isaacson irregularity was either wrong or misinterpreted. The most salient points seem to have been made by (1) Hunt and Baddour (1980b), who noted that in potential flow, discontinuities are to be expected in the tangential velocity at solid boundaries as found by Isaacson, and by (2) Wehausen (1980), who provided further proof that such an irregularity exists along the circlular water line contour and who showed that such an irregularity occurs at any order whenever a junction of nonhomogeneous boundary conditions is present. Wehausen continues to state, however, that such a solution does not prevent a useful solution from being attained. Miloh (1980, p. 281) examined the mathematical form of the irregularity and concluded that "such an irregularity must be present . . . any purported solution that is not singular on the line of intersection must be incorrect."

In summary, it seems that a concensus has been reached that Φ_2 must exhibit an irregularity along the water line contour since the KSBC requires the radial velocity to be zero there while the CFSBC is nonhomogeneous and contains nonzero tangential velocity terms at $r = a$. The irregularity, however, does not mean that Φ_{2r} is discontinuous or that a solution does not exist at second-order, but only that through the limiting process, the irregularity must be present in any second-order solution.

2.8 Discussion of Literature

Based on a review of the literature, various differences and inconsistencies between the previous solutions may be identified. In general, it is difficult to identify a single "correct" theory. However, Garrison's (1979) numerical solution, based on the method of Green's functions, seems to rigorously incorporate all of the physical elements of (1) forced wave motion due to the quadratic forcing applied to the free surface, as well as (2) the free wave motion due to the scattering of the forced waves from the cylinder.

One major source of difficulty in obtaining a consistent and complete solution has been the separation of Φ_2 into the incident plane Stokes wave potential and the "scattered" potential, as presented in Equations 2.4 through 2.10. At first-order, this separation is natural and clearly displays the origin of the scattered waves. At second-order, however, the same separation does not reduce the complexity of the problem or aid in the interpretation of the physics. As noted, the "scattered" potential must satisfy a combination of nonhomogeneous boundary conditions, including (1) the remaining quadratic terms in the CFSBC as well as (2) the apparent velocity at $r = a$ due to the interaction of the second-order plane wave component with the cylinder.

If the plane wave component, Φ_2^i, is separated as above, then the scattered wave motion due to the interaction of Φ_2^i (or Φ_{2P}^{ii} as defined in Chapter 1) with the cylinder may be found by methods identical to those employed at first-order. At both orders, the incident plane wave components, Φ_1^i and Φ_2^i (or Φ_{2P}^{ii}), lead to apparent motions of the cylinder boundary, $-\Phi_{1r}^i$ and $-\Phi_{2r}^i$ (or $-\Phi_{2Pr}^{ii}$). The scattered wave components, Φ_1^s and Φ_{2H}^{ii}, are then free waves required to compensate for this apparent motion and should consist of outwardly propagating waves as well as possibly local evanescent wave modes. The correct solution to this portion of the problem seems to have been determined in closed form by Chen (1979) and Chen and Hudspeth (1982), and in integral form, with a numerical solution, by Garrison (1979).

For the remaining wave motions, which include the forced waves generated by f^{is} and f^{ss}, as well as the free waves due to the interactions of these forced wave motions with the cylinder, the previous solutions may be classified into two catagories: (1) those that represent forced wave motion by discrete wavenumber solutions and (2) those that represent forced wave motions by the continuum of wavenumbers. In the first catagory, Chakrabarti (1972,1983), Yamaguchi and Tsuchiya (1974), and Sabuncu and Goren (1985) all represent forced wave motion with a $2k$ wavenumber dependence. Chen and Hudspeth (1982) represent the motion by a set of discrete wavenumbers corresponding to the eigenvalues of the interior Newman boundary value problem. The second method, based on a Fourier-Bessel integral incorporating the spectrum of wavenumbers, is used by Garrison (1979), Hunt and Baddour (1981), Hunt and Williams (1982), and Rahman and Heaps (1983).

As will be discussed in later chapters, the asymptotic forms of the forcing terms f^{is} and f^{ss} seem to have have strong $2k$ wavenumber dependence; however, other spatial oscillations and decay terms are also present, especially near the cylinder. It is therefore not possible to represent the forcing by a simple $2k$ wavenumber solution; repeated numerical tests by the author using the method of collocation and the method of least squares have confirmed that satisfaction of the CFSBC requires more freedom than is obtained from a simple $2k$ wavenumber solution. The Fourier-Bessel integral methods are required since they have sufficient generality to fit the complicated free surface forcing. These methods are also preferable based on knowledge of similar exterior boundary value problems in which the domain extends to infinity. In these cases, no discrete eigenvalues are physically suggested by the geometry and a continuum of wavenumbers is required, e.g. Sommerfeld (1949, p. 188) and Courant and Hilbert (1961, p. 339).

Several methods represent the velocity potential by a function that automatically satisfies the no-flow condition in the KSBC while the CFSBC is satisfied as a last step. This form of the solution is adopted by Chakrabarti (1972, 1983), Yamaguchi and Tsuchiya (1974), Hunt and Baddour (1981), Hunt and Williams (1982), Rahman and Heaps (1983),

and Chen and Hudspeth (1982). In these cases, the scattered wave motions have the same wavenumber dependence as the forced wave motions. However, the process of scattering of nonlinear waves is expected to lead to a change of wavenumber unlike the result at first-order. In addition, since the scattered waves are physically present only because of the reflection of the forced waves from the cylinder, it seems that the KSBC should be the last boundary condition to be mathematically satisfied. In this regard, the solutions of Garrison (1979) and Sabuncu and Goren (1985) clearly first satisfy the CFSBC then determine the scattered wave solutions by satisfying the KSBC; these solutions also reflect a change of wavenumber due to the scattering process with scattered solutions that are outwardly propagating second-order free waves.

A final aspect that differentiates the proposed solutions is the degree to which the Sommerfeld radiation condition is satisfied. For the wave motion generated directly by the quadratic forcing in the CFSBC, the proper far field condition is not clearly specified. The incident plane wave, generated by the f^{ii} forcing, certainly is not required to satisfy a radiation condition. As noted by Molin (1979), the other quadratic forcing terms have an outwardly propagating form but with rapid radial decay, such that waves are generated that radiate outward. Most proposed solutions, including those of Chakrabarti (1972,1983), Yamaguchi and Tsuchiya (1974), Raman and Venkatanarasaiah (1976a, 1976b), Hunt and Baddour (1981), Hunt and Williams (1982), Chen and Hudspeth (1982), Rahman and Heaps (1983), and Sabuncu and Goren (1985), do not require the forced wave motions to satisfy a radiation condition. Molin (1979) does not require the wave motion generated by the f^{is} forcing to satisfy the radiation condition; however, the wave motion due to the f^{ss} forcing is assumed to satisfy the radiation condition. Garrison (1979) and Lighthill (1979), on the other hand, require the wave motions generated by f^{is} and f^{ss} to satisfy the radiation condition.

CHAPTER 3
SOLUTION FOR SECOND-ORDER VELOCITY POTENTIAL

3.1 Introduction

The proposed solution for the second-order velocity potential is obtained in a complete and physically consistent fashion with the final result expressed in closed integral form. The solution is complicated and contains numerous terms; however, the physical origin of each term in the solution, including the forced wave motions due to the quadratic forcing in the CFSBC, and the free wave motions due to the scattering from the cylinder, are clearly displayed. Although it is derived in an independent way, the solution for forced wave motion is found to be identical to that proposed by Garrison (1979), through application of Green's theorem, in that forced wave motions are found based on a distribution of wave sources over the free surface with the source strengths and phases defined by the quadratic terms in the CFSBC. Garrison then obtains the scattered wave solutions in terms of an integral equation of a Green's function and an unknown source distribution function on the cylinder, which must be found numerically. The scattered wave motions in the proposed solution are obtained in closed-form based on the complete set of eigenfunction solutions which satisfy the exterior boundary value problem with a homogeneous free surface boundary condition.

3.2 General Solution Procedure

A complete statement of the second-order boundary value problem is

$$\nabla^2 \Phi_2 = 0 \tag{3.1}$$

$$\Phi_{2tt} + g\Phi_{2z} = f^{ii} + f^{is} + f^{ss} \qquad \text{on } z = 0 \tag{3.2}$$

$$\Phi_{2z} = 0 \qquad \text{on } z = -d \tag{3.3}$$

$$\Phi_{2r} = 0 \qquad \text{on } r = a \tag{3.4}$$

along with symmetry conditions on Φ_2 plus a form of the radiation condition that may be applied to all terms except the incident plane wave.

The quadratic forcing terms in the CFSBC in Equation 3.2 are

$$\begin{aligned} f^{ii} + f^{is} + f^{ss} &= \frac{1}{g}\Phi_{1t}\left\{\Phi_{1ttz} + g\Phi_{1zz}\right\} \\ &\quad - 2\left\{\Phi_{1r}\Phi_{1rt} + \frac{1}{r^2}\Phi_{1\theta}\Phi_{1\theta t} + \Phi_{1z}\Phi_{1zt}\right\} \end{aligned} \tag{3.5}$$

In Appendix A, the complete first-order solution is substituted into Equation 3.5 to obtain expressions for f^{ii}, f^{is}, and f^{ss}. One general feature of the quadratic forcing is that all forcing is periodic in time with frequency 2σ. The first-order potential has frequency σ; therefore, the quadratic forcing is expected to contain sum frequencies at 2σ, and possibly difference frequencies that are independent of time. As shown in Appendix A.2, all terms with difference frequencies vanish identically such that there are no steady or time-independent forcing terms. As a consequence, the time dependence of the second-order forcing may be separated; and, as shown in Appendix A.3, the quadratic forcing may be separated into a series form with harmonics of $\cos n\theta$ as

$$f^{ii} + f^{is} + f^{ss} = \sum_{n=0}\left[f_n^{ii}(r) + f_n^{is}(r) + f_n^{ss}(r)\right]\cos n\theta\frac{e^{-i2\sigma t}}{2} + c.c. \tag{3.6}$$

The time-dependence of the second-order potential may also be removed as

$$\Phi_2(r,\theta,z,t) = \phi_2(r,\theta,z)\frac{e^{-i2\sigma t}}{2} + c.c. \tag{3.7}$$

The nonhomogeneous combined free surface boundary condition from Equation 3.2 can then be rewritten as

$$\phi_{2z} - \frac{4\sigma^2}{g}\phi_2 = \frac{1}{g}\sum_{n=0}\left[f_n^{ii} + f_n^{is} + f_n^{ss}\right]\cos n\theta \tag{3.8}$$

Following conceptual developments presented in Chapter 1, the general solution for ϕ_2 can be obtained in terms of <u>particular</u> solutions, ϕ_2^P and complementary or <u>homogeneous</u> solutions, ϕ_2^H as

$$\phi_2 = \phi_2^P + \phi_2^H \tag{3.9}$$

The particular solutions ,ϕ_2^P, represent the second-order ambient forced wave motions due to the nonlinear wave-wave interactions of the first-order incident and scattered waves. These solutions must satisfy the Laplace equation, the bottom boundary condition, the nonhomogeneous free surface boundary condition, and some components must satisfy a form of the radiation condition. The particular solutions do not, by themselves, satisfy the no-flow condition on the cylinder boundary. As discussed in Chapter 1, the particular solution, ϕ_2^P, may be further separated as

$$\phi_2^P = \phi_{2P}^{ii} + \phi_{2P}^{is} + \phi_{2P}^{ss} \tag{3.10}$$

The component, ϕ_{2P}^{ii}, represents the forced wave motion generated by the f^{ii} forcing; this is the usual Stokes second-order plane wave component whose solution is well known. In the same way, two other forced wave components exist in the ambient or "incident" wave field due to the remaining f^{is} and f^{ss} forcing terms.

The homogeneous solutions, ϕ_2^H, represent free wave motions that exist due to the wave-structure interaction of the second-order ambient forced waves with the circular cylinder. These solutions must satisfy the Laplace equation, the bottom boundary condition, the radiation condition, and the homogeneous free surface boundary condition. The homogeneous solutions may be determined to within a set of unknown constant coefficients. Like the particular solutions, the homogeneous solutions do not satisfy the kinematic boundary condition on the cylinder.

Once the complete solution is specified, i.e. $\phi_2^P + \phi_2^H$, the unknown coefficients in the homogeneous solutions are determined by requiring the total solution to satisfy the kinematic condition of no-flow normal to the cylinder boundary. Determination of these unknown coefficients as a final step in the solution is correct mathematically and physically, as the homogeneous free wave motions exist at second-order only because of the reflection or scattering of the forced waves from the cylinder.

3.3 Far-Field Boundary Condition

Mathematically, the second-order boundary value problem is well posed with the exception of the conditions to be applied in the far field. It is known that Φ_2 must be bounded, i.e. finite, in the far field; but, the correct form of the radiation condition is not known with certainty. As noted in Chapter 2, previous solutions have variously invoked or ignored the radiation condition with little discussion or physical reasoning as to its proper form. The radiation condition, as posed by Sommerfeld (1949, p. 193), is a far field boundary condition required to distinguish physically relevant cylindrical wave solutions from solutions which are mathematically possible. In the context of linear diffraction theory, the incident wave is prescribed as a plane wave propagating in the x direction, for which a radiation condition is not required. For the scattered wave problem, finite solutions to the governing equations and boundary conditions include inward radiating waves in addition to the physically expected outward radiating modes. The radiation condition is applied to the scattered wave solution as

$$\lim_{r\to\infty} r^{\frac{1}{2}} \left(\Phi^s_{1r} - ik\Phi^s_1\right) = 0 \tag{3.11}$$

which can only be satisfied by outwardly propagating waves. It requires the vanishing of any inward radiating wave components and imposes a uniqueness to ensure that the mathematical solution agrees with the physics.

For the second-order problem, the radiation condition must be considered for two types of "disturbances" which generate waves at the fluid boundaries: (1) the direct quadratic forcing applied to the free surface, and (2) the apparent forcing at $r = a$ due to reflection of the forced wave motions with the cylinder. In the latter case, it is clear by analogy to the first-order problem, that a radiation condition is required to obtain proper homogeneous solutions which represent outwardly radiating scattered free waves. The far field condition

$$\lim_{r\to\infty} r^{\frac{1}{2}} \left(\Phi^H_{2r} - ik_2\Phi^H_2\right) = 0 \tag{3.12}$$

is therefore adopted.

The correct far field behavior of the particular solutions, Φ_2^P, may be investigated in part by considering the asymptotic form of the quadratic forcing terms. In Appendix A.5, the asymptotic forms of the forcing terms are found as

$$f^{ii} \approx a_1 e^{i2kr\cos\theta} e^{-i2\sigma t} \tag{3.13}$$

$$f^{is} \approx \left[\frac{a_2}{r^{\frac{1}{2}}} e^{ikr(1+\cos\theta)} + \frac{a_3}{r^{\frac{3}{2}}} e^{ikr(1+\cos\theta)}\right] e^{-i2\sigma t} \tag{3.14}$$

$$f^{ss} \approx \left[\frac{a_4}{r} e^{i2kr} + \frac{a_5}{r^2} e^{i2kr} + \frac{a_6}{r^3} e^{i2kr}\right] e^{-i2\sigma t} \tag{3.15}$$

The leading coefficients are generally complex and are functions of the three dimensionless parameters, kH, kh, and ka, as well as functions of θ. The forcing term f^{ii} is in the form of a periodic plane wave propagating in the $+x$ direction at wavenumber $2k$ with uniform amplitude. This forcing is associated with the usual Stokes second harmonic plane wave component for which the Sommerfeld radiation condition is certainly not required.

The general form of the f^{ss} forcing is that of an outwardly propagating oscillation; however, the radial decay is quite rapid and the forcing is concentrated in the vicinity of the cylinder. The wave motion generated by this forcing is expected to be composed of local forced wave motion, to satisfy the rapid radial decay; but far from the cylinder, the forced wave motions should decay such that only freely dispersive wave motions survive. The far field wave motion should, therefore, consist of free waves radiating outward from the region of localized forcing and, as Molin (1979) proposed, the particular solution due to the f^{ss} forcing should satisfy a form of the radiation condition.

The f^{is} forcing appears to have a radial decay like $r^{-1/2}$ to leading order, but like the f^{ss} forcing, also has higher order terms which give a more concentrated forcing near the cylinder; the decay rate also varies with θ. The propagation characteristics are quite complicated and, as noted by Mei (1983), range from an outward propagation with phase speed $c = \sigma/k$ along $\theta = 0$ side to a simple radially-decaying oscillation along $\theta = \pi$ side. The forcing propagates away from the cylinder over all angular positions and it is expected that the resulting wave motion will also be outwardly propagating but with significant local standing wave components in the region of most intense forcing. Far from this region,

forced oscillations should again die out and the resulting wave potential is expected to be composed of outwardly propagating free waves. While Molin (1979) assumed that the asymptotic wave motions should have the same form as the forcing, it appears, instead, that the wave motions generated by the nonuniform forcing f^{is} should satisfy a form of the radiation condition.

The physical arguments outlined above may be supported graphically by displaying the amplitude envelope of the free surface forcing. In Figures 3.1 and 3.2, the amplitude of the forcing is shown for the f^{ss} and f^{is} forcing respectively, with a side view at the top of the page, for $\theta = 0$, $\theta = \pi$, and the circumference of the cylinder, and a front view at the bottom of each page, for $\theta = \pm\pi/2$ and the circumference of the cylinder. For the f^{ss} forcing, the amplitudes are clearly concentrated near the cylinder and are expected to generate waves that radiate away from the cylinder.

For the f^{is} forcing, the behavior is quite different. Along $\theta = \pi$, the first-order scattered wave opposes the incident wave to produce a standing wave system that, in turn, produces large free surface forcing magnitudes. Along $\theta = 0$, however, the first-order scattered wave propagates in the same direction as the incident wave with the same frequency and wavenumber. The resulting quadratic forcing is small but also decays away from the cylinder as the strength of the nonlinear interactions decreases. A general feature of the f^{is} forcing is that the amplitude of the forcing in the upwave region is larger than the forcing in the downwave region. Around the cylinder, gradients are found in the forcing amplitudes, and large forcing magnitudes are also found along the sides of the cylinder. Generally, waves are generated near the front and sides of the cylinder, and then propagate both outward and around to the rear. It is expected that due to the concentrated nature of the forcing, and due to the spatial gradients of the forcing, free waves will radiate from the region of most intense forcing.

The application of the radiation condition to the wave potentials generated by the f^{is} and f^{ss} forcing is supported implicitly by Lighthill (1979) and directly by Garrison

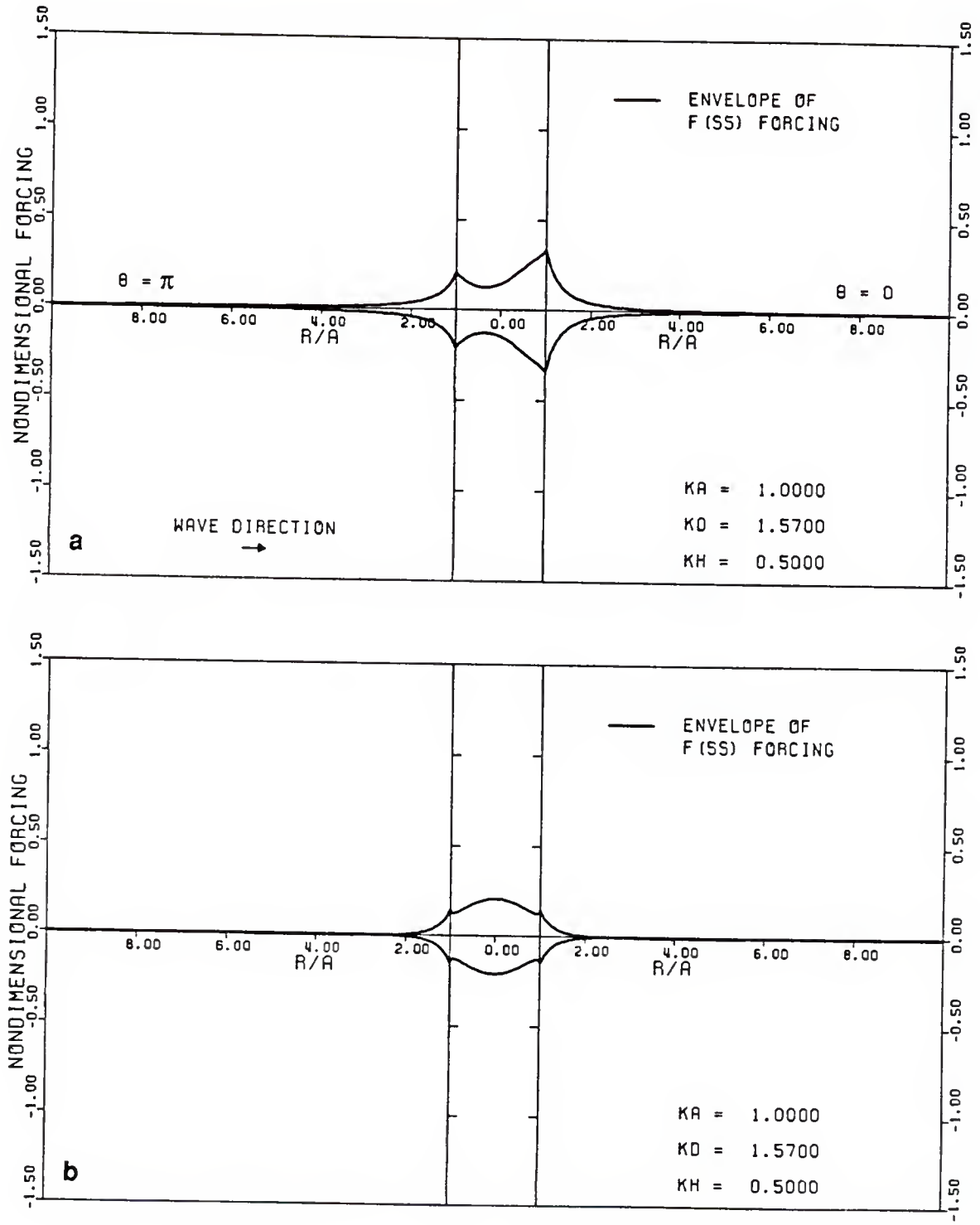

Figure 3.1: Amplitude of f^{ss} quadratic forcing applied to free surface, (a) side view, (b) front view

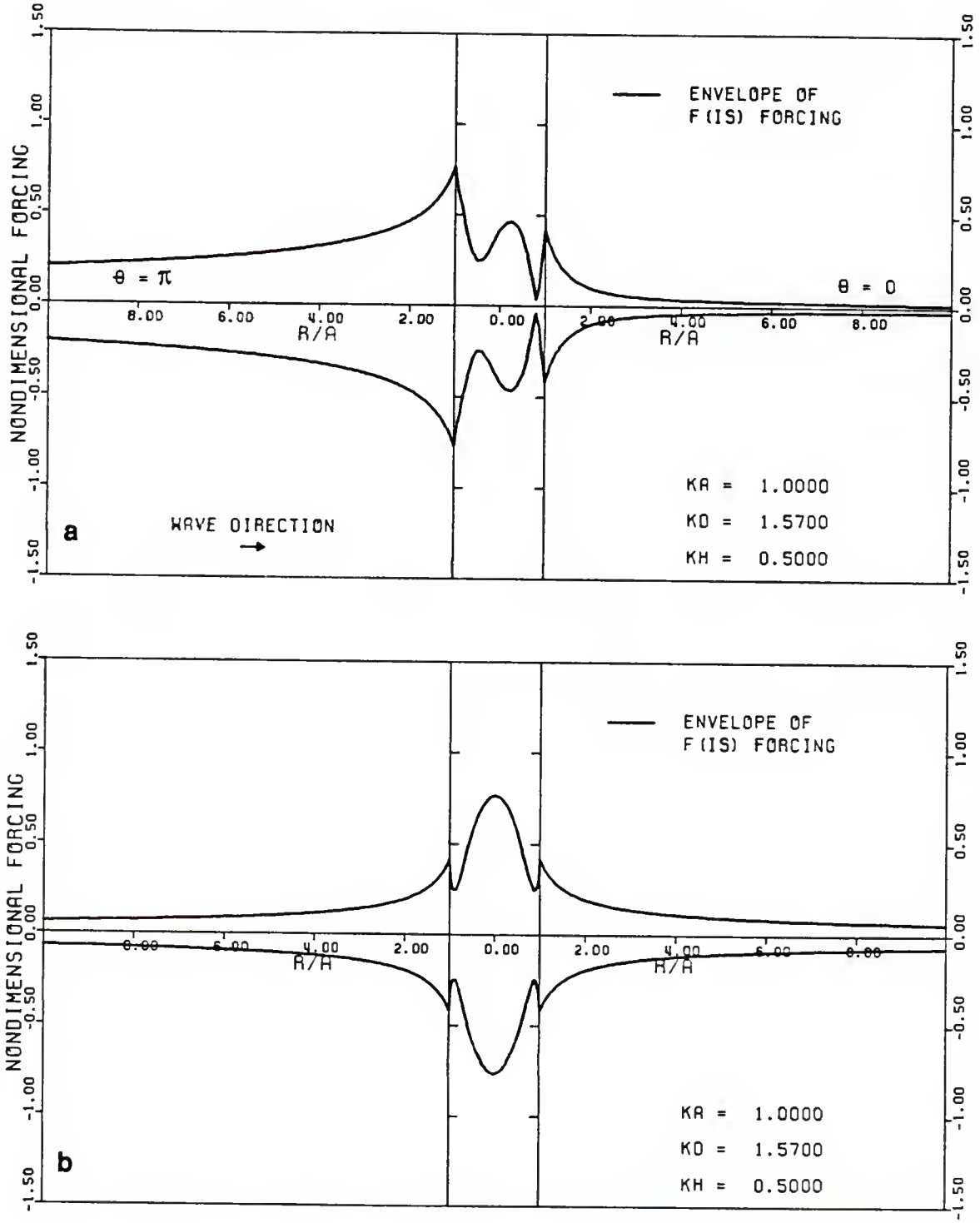

Figure 3.2: Amplitude of f^{is} quadratic forcing applied to free surface, (a) side view, (b) front view

(1979). As noted, Garrison's solution is based on application of a Green's function, which represents the wave motion generated by an individual source of unit strength and which must satisfy a radiation condition. The associated source distribution function specifies the strength, phasing, and spatial distribution of the unit sources; from Green's theorem the source distribution function is given exactly by the quadratic forcing terms f^{is} and f^{ss}. From Green's theorem, the wave potential does not have the same form as the forcing, but instead is composed of the contributions from infinitely many individual sources which may reinforce or cancel depending on their spatial distribution and phasing but which lead to outwardly radiating free wave motion in the far field. Since the radial decay of the forcing varies over θ, the amplitude of the radiated free waves is expected to vary over θ as well; thus, the radiation condition cannot be applied in closed form to the total solution but, rather, must be applied to each elemental point source.

3.4 Second-Order Solution

3.4.1 Solution for Scattered Potential ϕ_2^H

At first-order, the scattered wave solutions are obtained from the general set of eigenfunction solutions that satisfy the governing equation and the boundary conditions for the region exterior to the cylinder and oscillating at frequency σ. At second-order, the same method will be employed to determine the homogeneous solutions; however, since all forcing is found to oscillate at frequency 2σ, the associated free wave motions must also oscillate at frequency 2σ as in Equation 3.7. The homogeneous form of the CFSBC in Equation 3.8, which is satisfied by the second-order scattered free waves, is then

$$\phi_{2z}^H - \frac{4\sigma^2}{g}\phi_2^H = 0 \tag{3.16}$$

As given by Mei (1983) or Dean and Dalrymple (1984), the solution to the Laplace equation in cylindrical coordinates which satisfies the homogeneous free surface boundary condition, the bottom boundary condition, the Sommerfeld radiation condition, and which

is symmetric in θ, is given by the complete set of eigenfunction solutions

$$\begin{aligned}\phi_2^H &= \sum_{n=0} a_{n0} \cosh \kappa(d+z) H_n(\kappa r) \cos n\theta \\ &+ \sum_{n=0}\sum_{j=1} a_{nj} \cos \kappa_j(d+z) K_n(\kappa_j r) \cos n\theta \end{aligned} \tag{3.17}$$

The second-order free wavenumbers associated with the homogeneous solutions are found by substituting Equation 3.17 into the homogeneous CFSBC in Equation 3.16. Two second-order dispersion relationships result: (1) for the propagating free waves

$$4\sigma^2 = gk_2 \tanh k_2 d \tag{3.18}$$

which has a single positive root equal to the second-order free wavenumber, k_2, and (2) for the standing or evanescent wave modes

$$4\sigma^2 = -g\kappa_{2j} \tan \kappa_{2j} d \tag{3.19}$$

which has infinitely many positive roots, κ_{2j}, given by

$$(j - \frac{1}{2})\pi \leq \kappa_{2j} h \leq j\pi \tag{3.20}$$

The evanescent modes vanished identically at first-order since the depth dependence of the scattered wave was identical to that of the incident waves; i.e. both incident and scattered waves were free waves with wavenumber k. At second-order, the ambient or "incident" forced waves have a more complicated vertical distribution of water particle motion that differs from that of the freely propagating second-order scattered waves. This mismatch along the cylinder boundary requires the existence of the evanescent modes at second-order, in the same sense that the evanescent modes are required to satisfy the mismatch between the motion of a vertical wavemaker paddle and the fluid motion of the waves which are generated.

For later application, it will be useful to define a nondimensional form of the free wave solutions. By normalizing by the amplitude of the first-order velocity potential as

$$\tilde{\phi}_2^H = \frac{2\sigma}{gH} \phi_2^H \tag{3.21}$$

and by defining normalized amplitude coefficients as

$$\tilde{a}_{n0} = \frac{2\sigma}{gH} a_{n0} \tag{3.22}$$

$$\tilde{a}_{nj} = \frac{2\sigma}{gH} a_{nj} \tag{3.23}$$

the nondimensional homogeneous solution for the second-order scattered waves is given as

$$\begin{aligned} \tilde{\phi}_2^H &= \sum_{n=0}^{\infty} \tilde{a}_{n0} \cosh k_2(d+z) H_n(k_2 r) \cos n\theta \\ &+ \sum_{n=0}^{\infty} \sum_{j=1}^{\infty} \tilde{a}_{nj} \cos \kappa_{2j}(d+z) K_n(\kappa_{2j} r) \cos n\theta \end{aligned} \tag{3.24}$$

3.4.2 Solution for Incident Potential ϕ_{2P}^{ii}

The solution for the forced wave motion generated by the f^{ii} forcing is well-known and may be shown to be the usual second-order plane wave component obtained from the Stokes perturbation expansion. From Equation A.60 in Appendix A.4, the free surface boundary condition for the ϕ_{2P}^{ii} component may be written as

$$\phi_{2Pz}^{ii} - \frac{4\sigma^2}{g} \phi_{2P}^{ii} = -i \frac{3}{8} \frac{gH^2k^2}{\sigma} (\tanh^2 kd - 1) \sum_{n=0}^{\infty} \beta_n J_n(2kr) \cos n\theta \tag{3.25}$$

A solution is assumed for ϕ_{2P}^{ii} that satisfies the Laplace equation and the bottom boundary condition as

$$\phi_{2P}^{ii} = A^{ii} \cosh 2k(d+z) \sum_{n=0}^{\infty} \beta_n J_n(2kr) \cos n\theta \tag{3.26}$$

The amplitude A^{ii} is completely specified by the free surface boundary condition, and substitution of Equation 3.26 into Equation 3.25 yields

$$A^{ii} = -i \frac{3}{8} \frac{gH^2k^2}{\sigma} \frac{(\tanh^2 kd - 1)}{(2k \tanh 2kd - k_2 \tanh k_2 d) \cosh 2kd} \tag{3.27}$$

which is singular in shallow water when the free wave number, k_2, equals $2k$ such that the free surface forcing is resonant. The amplitude coefficient may also be written as

$$A^{ii} = -i \frac{3}{32} \sigma H^2 \frac{1}{\sinh^4 kdh} \tag{3.28}$$

The solution for Φ_{2P}^{ii}, including the time dependence, may then be given as

$$\Phi_{2P}^{ii} = -i\frac{3}{32}\sigma H^2 \frac{\cosh 2k(d+z)}{\sinh^4 kd} \sum_{n=0}^{\infty} \beta_n J_n(2kr)\cos n\theta \frac{e^{-i2\sigma t}}{2} + c.c. \tag{3.29}$$

Using the partial wave expansion, e.g. Abramowitz and Stegun (1972)

$$\sum_{n=0}^{\infty} \beta_n J_n(2kr)\cos n\theta = e^{i2kr\cos\theta} = e^{i2kx} \tag{3.30}$$

this becomes

$$\Phi_{2P}^{ii} = \frac{3}{32}\sigma H^2 \frac{\cosh 2k(d+z)}{\sinh^4 kd} \sin 2(kx - \sigma t) \tag{3.31}$$

which is the familiar Stokes second-order incident plane wave component, e.g. Dean and Dalrymple (1984, p. 301).

For later application, ϕ_{2P}^{ii} is normalized by the amplitude of the first-order velocity potential as

$$\tilde{\phi}_{2P}^{ii} = \frac{2\sigma}{gH}\phi_{2P}^{ii} \tag{3.32}$$

If the form of the second-order amplitude A^{ii} given in Equation 3.27 is used, the nondimensional form of ϕ_{2P}^{ii} becomes

$$\tilde{\phi}_{2P}^{ii} = -i\frac{3}{4}kH \frac{k(\tanh^2 kd - 1)}{(2k\tanh 2kd - k_2 \tanh k_2 d)} \frac{\cosh 2k(d+z)}{\cosh 2kd} \sum_{n=0}^{\infty} \beta_n J_n(2kr)\cos n\theta \tag{3.33}$$

3.4.3 Solutions for ϕ_{2P}^{is} and ϕ_{2P}^{ss}

The solutions for ϕ_{2P}^{is} and ϕ_{2P}^{ss} are based on a general solution for water waves due to a pressure distribution applied to the free surface. First, the solution is obtained for a single point source of pressure applied to the free surface. Next, the solution for an arbitrary two-dimensional pressure distribution is obtained by summing the effects of elemental point sources over the entire free surface. The quadratic forcing in the CFSBC is functionally equivalent to an external pressure applied to the free surface; and, by specifying the form of the pressure distribution, based on the derivation for the quadratic forcing in Appendix A.2, several simplifications may be made to obtain a closed-form integral solution for Φ_{2P}^{is} and Φ_{2P}^{ss}.

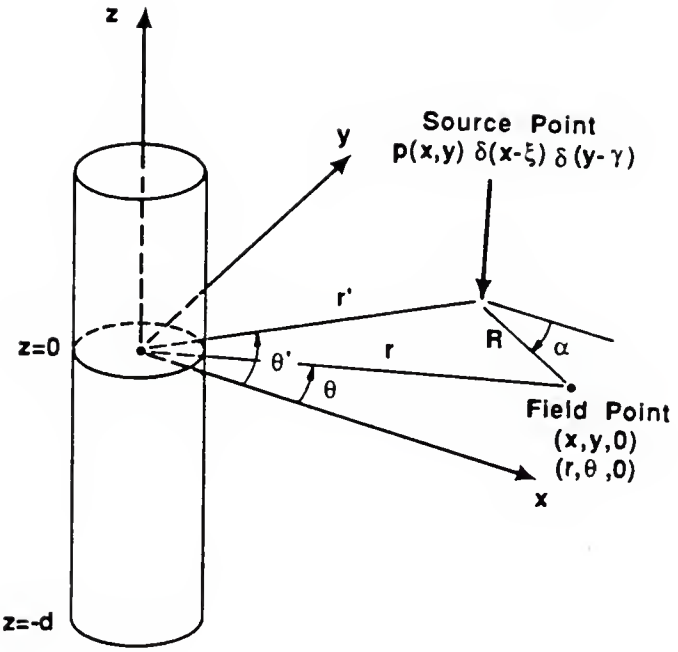

Figure 3.3: Definition sketch for point-source of applied surface pressure

Let the center of the vertical cylinder be at $x = 0$ and $y = 0$ in a global coordinate system, where $z = 0$ defines the still water level. At some point on the free surface, $x = \xi$, $y = \gamma$ and $z = 0$, let a point source of pressure oscillate at a frequency 2σ with a magnitude and spatial distribution defined by a Dirac delta function as $P(x,y)\delta(x-\xi)\delta(y-\gamma)$, where $P(x,y)$ is a complex quantity. In global cylindrical coordinates, the point source is located at $(r',\theta',0)$. From the point of application of the source, define a local coordinate system, (R,α,z), such that R is the radial distance from the point source to the field point $(x,y,0)$ as

$$R = \left((x-\xi)^2 + (y-\gamma)^2\right)^{\frac{1}{2}} = \left(r^2 + r'^2 - 2rr'\cos(\theta-\theta')\right)^{\frac{1}{2}} \tag{3.34}$$

as defined in Figure 3.3.

The boundary value problem for the velocity potential resulting from this oscillating point source is

$$\nabla^2\Phi = 0 \tag{3.35}$$

$$\Phi_z = 0 \qquad \text{on } z = -d \tag{3.36}$$

$$\Phi_{tt} + g\Phi_z = -\frac{1}{\rho}\frac{\partial}{\partial t}\left(P(x,y)\delta(x-\xi)\delta(y-\gamma)\frac{e^{-i2\sigma t}}{2}\right) + c.c. \qquad \text{on } z = 0 \tag{3.37}$$

$$\lim_{R\to\infty} R^{\frac{1}{2}}\left(\Phi_R - ik_2\Phi\right) = 0 \tag{3.38}$$

The radiation condition may be easily written in closed form since it is applied with respect to the point of application of the pressure, not the center of the cylinder.

A solution is sought in the form

$$\Phi(x,y,z,t) = \phi^F(x,y,z)\frac{e^{-i2\sigma t}}{2} + c.c. + \phi^R(x,y,z)\frac{e^{-i2\sigma t}}{2} + c.c. \tag{3.39}$$

where ϕ^F represents forced wave motion while, as suggested by Wehausen and Laitone (1960), ϕ^R is required to ensure that the total solution, Φ, satisfies the radiation condition. Substituting Equation 3.39 into the boundary value problem in Equations 3.35 to 3.38 gives two separate boundary value problems that are identical except for their free surface boundary conditions

$$\phi^F_z - \frac{4\sigma^2}{g}\phi^F = \frac{i2\sigma}{\rho g}P(x,y)\delta(x-\xi)\delta(y-\gamma) \qquad \text{on } z = 0 \tag{3.40}$$

and

$$\phi^R_z - \frac{4\sigma^2}{g}\phi^R = 0 \qquad \text{on } z = 0 \tag{3.41}$$

The radiation condition is applied to the total solution as

$$\lim_{R\to\infty} R^{\frac{1}{2}}\left[(\phi^F_R + \phi^R_R) - ik_2(\phi^F + \phi^R)\right] = 0 \tag{3.42}$$

The solution for ϕ^F may be obtained by applying the two-dimensional Fourier transform which is defined by the transform pair

$$\hat{\phi}^F(\mu,\nu,z) = \frac{1}{2\pi}\int_{-\infty}^{+\infty}\int_{-\infty}^{+\infty}\phi^F(x,y,z)e^{-i(\mu x+\nu y)}dxdy \tag{3.43}$$

$$\phi^F(x,y,z) = \frac{1}{2\pi}\int_{-\infty}^{+\infty}\int_{-\infty}^{+\infty}\hat{\phi}^F(\mu,\nu,z)e^{+i(\mu x+\nu y)}d\mu d\nu \tag{3.44}$$

Transforming the Laplace equation for ϕ^F gives a governing ordinary differential equation as

$$\hat{\phi}^F_{zz} - \kappa^2\hat{\phi}^F = 0 \tag{3.45}$$

where

$$\kappa^2 = \mu^2 + \nu^2 \tag{3.46}$$

Solutions to Equation 3.45 which also satisfy the transformed bottom boundary condition are

$$\hat{\phi}^F(\mu,\nu,z) = A(\mu,\nu)\cosh\kappa(d+z) \tag{3.47}$$

Transforming the CFSBC, in Equation 3.40, gives

$$\hat{\phi}^F_z - \frac{4\sigma^2}{g}\hat{\phi}^F = \frac{i2\sigma}{\rho g}\frac{P(\xi,\gamma)}{2\pi}e^{-i(\mu\xi+\nu\gamma)} \tag{3.48}$$

Substitution of Equation 3.47, into Equation 3.48, determines the coefficient $A(\mu,\nu)$ and, after applying the inverse transform in Equation 3.44, the fundamental solution for ϕ^F is obtained as

$$\phi^F(x,y,z;\xi,\gamma) = \frac{i2\sigma}{\rho g}\frac{P(\xi,\gamma)}{(2\pi)^2} \cdot \int_{-\infty}^{+\infty}\int_{-\infty}^{+\infty}\frac{\cosh\kappa(d+z)}{\cosh\kappa d(\kappa\tanh\kappa d - k_2\tanh k_2 d)}e^{i(\mu(x-\xi)+\nu(y-\gamma))}d\mu d\nu \tag{3.49}$$

This solution may be expressed in simpler form, first by changing spatial variables to local coordinates, then by changing the variables of integration as

$$x-\xi = R\cos\alpha \qquad \mu = \kappa\cos\theta$$

$$y-\gamma = R\sin\alpha \qquad \nu = \kappa\sin\theta$$

such that the solution is

$$\phi^F(R,\alpha,z;\xi,\gamma) = \frac{i2\sigma}{\rho g}\frac{P(\xi,\gamma)}{(2\pi)^2} \cdot \int_0^{+\infty}\int_{-\pi}^{+\pi} \frac{\kappa\cosh\kappa(d+z)}{\cosh\kappa d(\kappa\tanh\kappa d - k_2\tanh k_2 d)} e^{i\kappa R\cos(\theta-\alpha)} d\theta d\kappa \tag{3.50}$$

The identity, e.g Watson (1962)

$$\int_{+\pi}^{-\pi} e^{i\kappa R\cos(\theta-\alpha)} d\theta = 2\pi J_0(\kappa R) \tag{3.51}$$

may be used to obtain the simple result

$$\phi^F(R,\alpha,z;\xi,\gamma) = \frac{i2\sigma}{\rho g}\frac{P(\xi,\gamma)}{2\pi} PV\int_0^{+\infty} \frac{\kappa\cosh\kappa(d+z)}{\cosh\kappa d(\kappa\tanh\kappa d - k_2\tanh k_2 d)} J_0(\kappa R) d\kappa \tag{3.52}$$

Because of the singularity of the integral at the free wavenumber, k_2, the integral must be interpreted in the Cauchy Principal Value sense, e.g. Wehausen and Laitone (1960).

The solution for the additional term, ϕ^R, required to satisfy the radiation condition may be obtained from the general set of solutions which satisfy the Laplace equation, the bottom boundary condition, the homogeneous free surface boundary condition, and which are finite at $R = 0$. This solution is found as

$$\phi^R(R,\alpha,z) = C\cosh k_2(d+z) J_0(k_2 R) \tag{3.53}$$

In order to establish the free coefficient, C, the entire solution, $\phi^F + \phi^R$, is required to satisfy the radiation condition. To do this, the far field behavior of the forced wave motion, ϕ^F, must be considered; this is accomplished by evaluating the singular integral for large R using the Cauchy Integral Theorem. The desired integral may be obtained from the real part of the complex integral with $J_0(\kappa R)$ replaced by the Hankel function, $H_0(\kappa R)$. In addition, the singular function may be expanded about the singularity and leading order terms retained as

$$\begin{aligned} \kappa\tanh\kappa d - k_2\tanh k_2 d &\simeq (\kappa - k_2)\left[\tanh k_2 d + \frac{k_2 d}{\cosh^2 k_2 d}\right] + \cdots \\ &\simeq \frac{\kappa - k_2}{2\cosh^2 k_2 d}\left[\sinh 2k_2 d + 2k_2 d\right] + \cdots \end{aligned} \tag{3.54}$$

Carrying out the contour integration, e.g. Wehausen and Laitone (1960, p. 477), the asymptotic form for ϕ^F may be found as

$$\begin{aligned}\phi^F &= \lim_{R\to\infty} \Re\left[\frac{i2\sigma}{\rho g}\frac{P(\xi,\gamma)}{2\pi}\frac{2\cosh^2 k_2 d}{(\sinh 2k_2 d + 2k_2 d)}\int_0^\infty \frac{\kappa\cosh\kappa(d+z)}{(\kappa-k_2)\cosh\kappa d}H_0(\kappa R)d\kappa\right] \\ &= -\frac{i2\sigma}{\rho g}\frac{P(\xi,\gamma)}{2\pi}\left\{\pi\frac{2k_2\cosh k_2 d}{\sinh 2k_2 d + 2k_2 d}\cosh k_2(d+z)Y_0(k_2 R)\right\} \qquad (3.55)\end{aligned}$$

In order to satisfy the radiation condition, the total solution, $\phi^F + \phi^R$, must behave as an outgoing free wave; thus, the value of the coefficient, C, in Equation 3.53 may be found as

$$C = \frac{i2\sigma}{\rho g}\frac{P(\xi,\gamma)}{2\pi}\left[i\pi\frac{2k_2\cosh k_2 d}{\sinh 2k_2 d + 2k_2 d}\right] \qquad (3.56)$$

The final solution for the velocity potential due to a single point source of strength, $P(x,y)$, oscillating at frequency 2σ, is found by summing ϕ^F and ϕ^R to obtain

$$\begin{aligned}\Phi(R,\alpha,z;\xi,\gamma) &= \frac{i2\sigma}{\rho g}\frac{P(\xi,\gamma)}{2\pi}\left[i\pi\frac{2k_2\cosh k_2 d}{\sinh 2k_2 d + 2k_2 d}\cosh k_2(d+z)J_0(k_2 R)\right. \\ &+ \left. PV\int_0^\infty \frac{\kappa\cosh\kappa(d+z)}{\cosh\kappa d(\kappa\tanh\kappa d - k_2\tanh k_2 d)}J_0(\kappa R)d\kappa\right]\frac{e^{-i2\sigma t}}{2} \\ &+ c.c. \qquad (3.57)\end{aligned}$$

This elemental solution may be interpreted as follows. The singular integral represents forced wave motion that is composed of contributions from all wavenumbers, κ, and which represents cylindrical standing waves. From the Cauchy Integral Theorem, the standing waves have a strong local source-like behavior but, farther from the source, dispersion selectively filters all wavenumbers such that only the contribution at k_2, the second-order free wavenumber, survives. This term is a cylindrical standing wave and, by itself, cannot satisfy the radiation condition; therefore, a second standing wave solution, represented by ϕ^R, is required to ensure outward progressive wave motion. The solution is therefore a combination of forced and radiated wave motions.

A mathematical description of the effects of a two-dimensional applied surface pressure distribution is given by Wehausen and Laitone (1960, pp. 592-595). Application of the two-dimensional Fourier transform to an arbitrary but transformable, i.e. sufficiently localized, applied pressure distribution gives a two-term solution that represents local forced wave

motion, but with a selective radiation of an outwardly propagating free waves. As proved by Hudimac (1958), the same result may be obtained by solving the more general problem of an arbitrary distribution of wave sources anywhere in the fluid and then taking the limit as the source distribution approaches the free surface. In this study, a more intuitive approach is used, but the same result is obtained by summing an infinite number of point sources, each with an elemental solution given in Equation 3.57, but with pressure amplitudes and phases given by the quadratic forcing in the CFSBC. The result turns out to be equivalent to that obtained by application of Green's theorem, as found by Garrison (1979). The fundamental solution in Equation 3.57 is identical to the Green's function used by Garrison (1979) to represent surface wave sources, in Equation 2.18, with a source strength of

$$\frac{i2\sigma}{\rho g} P(\xi, \gamma) \tag{3.58}$$

The solution at a given field point due to a distribution of applied surface pressure is obtained by a straightforward integration of the solution for $\phi(R, \alpha, z; \xi, \gamma)$ over the spatial domain for all ξ and γ, as

$$\phi(R, \alpha, z) = \int_{-\infty}^{+\infty} \int_{-\infty}^{+\infty} \phi(R, \alpha, z; \xi, \gamma) d\xi d\gamma \tag{3.59}$$

By introducing the change of variables of integration into Equation 3.57 as

$$\begin{aligned} x &= r\cos\theta & \xi &= r'\cos\theta' \\ y &= r\sin\theta & \gamma &= r'\sin\theta' \end{aligned} \tag{3.60}$$

and recognizing that the limits of the physical domain over which the forcing is applied are $a \le r \le \infty$ and $-\pi \le \theta \le \pi$, it is found that

$$\begin{aligned} \phi(r, \theta, z) \;=\; & \frac{1}{2\pi} \frac{i2\sigma}{\rho g} \left[i\pi \frac{2k_2 \cosh k_2 d}{\sinh 2k_2 d + 2k_2 d} \cosh k_2(d+z) \right. \\ & \cdot \int_a^{\infty} \int_{-\pi}^{\pi} P(r', \theta') J_0(k_2 \sqrt{r^2 + r'^2 + 2rr'\cos(\theta - \theta')}) r' dr' d\theta' \\ & + \int_a^{\infty} \int_{-\pi}^{\pi} P(r', \theta') PV \int_0^{\infty} \frac{\kappa \cosh \kappa(d+z)}{\cosh \kappa d (\kappa \tanh \kappa d - k_2 \tanh k_2 d)} \\ & \left. \cdot J_0(\kappa \sqrt{r^2 + r'^2 + 2rr'\cos(\theta - \theta')}) r' d\kappa dr' d\theta' \right] \end{aligned} \tag{3.61}$$

Simplifications may be achieved by first introducing the Addition Theorem for Bessel functions, e.g. Watson (1962)

$$J_0(\kappa\sqrt{r^2+r'^2+2rr'\cos(\theta-\theta')}) = \sum_{n=0}^{\infty} \varepsilon_n J_n(\kappa r) J_n(\kappa r') \cos n(\theta-\theta') \tag{3.62}$$

where

$$\varepsilon_n = 2 - \delta_{n0} \tag{3.63}$$

Next, the applied pressure distribution may be related to the quadratic forcing terms in the second-order CFSBC. In Appendix A.2, it is shown that the quadratic forcing may replace the generic pressure such that

$$\frac{i2\sigma}{\rho g} P(r',\theta') = \frac{1}{g}\sum_{m=0}^{\infty} f_m(r') \cos m\theta' \tag{3.64}$$

The solution may then be written as

$$\begin{aligned}
\phi(r,\theta,z) &= \frac{1}{2\pi g}\left[i\pi \frac{2k_2 \cosh k_2 d}{\sinh 2k_2 d + 2k_2 d} \cosh k_2(d+z) \right. \\
&\quad \cdot \int_a^{\infty}\int_{-\pi}^{\pi} \sum_{n=0}^{\infty}\sum_{m=0}^{\infty} \varepsilon_n \cos m\theta' \cos n(\theta-\theta') f_m(r') J_n(k_2 r') J_n(k_2 r) r' dr' d\theta' \\
&+ \int_a^{\infty}\int_{-\pi}^{\pi} \sum_{n=0}^{\infty}\sum_{m=0}^{\infty} \varepsilon_n \cos m\theta' \cos n(\theta-\theta') f_m(r') d\theta' \\
&\quad \cdot \left. PV \int_0^{\infty} \frac{\kappa \cosh \kappa(d+z)}{\cosh \kappa d(\kappa \tanh \kappa d - k_2 \tanh k_2 d)} J_n(\kappa r') J_n(\kappa r) r' d\kappa dr' \right]
\end{aligned} \tag{3.65}$$

Carrying out the integration over θ', it is found that

$$\int_{-\pi}^{\pi} \sum_{n=0}^{\infty}\sum_{m=0}^{\infty} \varepsilon_n \cos m\theta' \cos n(\theta-\theta') d\theta' = \begin{cases} 0 & \text{if } m \neq n \\ 2\pi \sum \cos n\theta & \text{if } m = n \end{cases} \tag{3.66}$$

Finally, the solution $\phi(r,\theta,z)$, due to an arbitrarily distributed applied forcing in the CFSBC is found to be

$$\begin{aligned}
\phi(r,\theta,z) &= \frac{1}{g}\sum_{n=0}^{\infty} \cos n\theta \left[i\pi \frac{2k_2 \cosh k_2 d \cosh k_2(d+z)}{\sinh 2k_2 d + 2k_2 d} J_n(k_2 r) \right. \\
&\quad \cdot \int_a^{\infty} r' f_n(r') J_n(k_2 r') dr' \\
&+ PV \int_0^{\infty} \frac{\kappa \cosh \kappa(d+z)}{\cosh \kappa d(\kappa \tanh \kappa d - k_2 \tanh k_2 d)} J_n(\kappa r) \\
&\quad \cdot \left. \int_a^{\infty} r' f_n(r') J_n(\kappa r') dr' d\kappa \right]
\end{aligned} \tag{3.67}$$

The integrals over r' may be conveniently redefined as

$$D_n(\kappa) = \int_a^\infty r' f_n(r') J_n(\kappa r') dr' \tag{3.68}$$

where $D_n(\kappa)$ represents a wavenumber spectrum for cylindrical wave motion. This term is analogous to the usual spectrum obtained by the Fourier transform and is equal to the Hankel transform of the applied quadratic forcing, e.g. Sneddon (1951). In order to obtain the solutions ϕ_{2P}^{is} and ϕ_{2P}^{ss}, corresponding to the wave potentials generated by the f^{is} and f^{ss} forcing, the generic forcing in Equation 3.67 may be replaced by specific values of the forcing. In this way the wavenumber spectra $D_n^{is}(\kappa)$ and $D_n^{ss}(\kappa)$ may be defined individually as

$$D_n^{is}(\kappa) = \int_a^\infty r' f_n^{is}(r') J_n(\kappa r') dr' \tag{3.69}$$

$$D_n^{ss}(\kappa) = \int_a^\infty r' f_n^{ss}(r') J_n(\kappa r') dr' \tag{3.70}$$

Since the potentials ϕ_{2P}^{is} and ϕ_{2P}^{ss} always have the same mathematical form, they will always be taken together in this study with the single wavenumber spectrum $D_n(\kappa)$, as

$$D_n(\kappa) = D_n^{is}(\kappa) + D_n^{ss}(\kappa) \tag{3.71}$$

The solution for $\phi_{2P}^{is} + \phi_{2P}^{ss}$ may be made nondimensional by dividing by the amplitude of the first order potential. The wavenumber spectrum is normalized based on the nondimensional forcing, e.g Appendix A.2, as

$$\frac{2\sigma k}{g^2 H} D_n(\kappa) = \frac{2\sigma k}{g^2 H} \int_a^\infty r' f_n(r') J_n(\kappa r') dr' \tag{3.72}$$

$$= \frac{2\sigma k}{g^2 H} \int_a^\infty r' \left(\frac{-ig^2 k^2 H^2}{8\sigma} \right) \tilde{f}_n(r') J_n(\kappa r') dr' \tag{3.73}$$

$$= \frac{-ikH}{4} \int_a^\infty k^2 r' \tilde{f}_n(r') J_n(\kappa r') dr' \tag{3.74}$$

$$= -i\frac{kH}{4} \tilde{D}_n(\kappa) \tag{3.75}$$

The nondimensional particular solution for the forced-radiated wave motion $\phi_{2P}^{is} + \phi_{2P}^{ss}$ is then given by

$$\tilde{\phi}_{2P}^{is} + \tilde{\phi}_{2P}^{ss} = -i\frac{kH}{4} \sum_{n=0}^{\infty} \cos n\theta \left[i2\pi \frac{k_2}{k} \frac{\cosh k_2 d \cosh k_2 (d+z)}{\sinh 2k_2 d + 2k_2 d} J_n(k_2 r) \tilde{D}_n(k_2) \right.$$

$$+ \quad PV \int_0^\infty \frac{\kappa \cosh \kappa(d+z)}{k \cosh \kappa d(\kappa \tanh \kappa d - k_2 \tanh k_2 d)} J_n(\kappa r) \tilde{D}_n(\kappa) d\kappa \Bigg] \tag{3.76}$$

3.4.4 Summary of Forced Wave Motion

The solution for the portion of the second-order velocity potential generated by the quadratic forcing in the CFSBC may now be summarized from Equations 3.33 and Equation 3.76. The nondimensional particular solutions are

$$\begin{aligned}
\tilde{\phi}_2^P &= \tilde{\phi}_{2P}^{ii} + \tilde{\phi}_{2P}^{is} + \tilde{\phi}_{2P}^{ss} \\
&= -ikH \sum_{n=0}^{\infty} \cos n\theta \\
&\cdot \Bigg[\frac{3}{4} \frac{k(\tanh^2 kd - 1)}{(2k \tanh 2kd - k_2 \tanh k_2 d)} \frac{\cosh 2k(d+z)}{\cosh 2kd} \beta_n J_n(2kr) \\
&+ \frac{i\pi}{2} \frac{k_2}{k} \frac{\cosh k_2 d \cosh k_2(d+z)}{\sinh 2k_2 d + 2k_2 d} \tilde{D}_n(k_2) J_n(k_2 r) \\
&+ \frac{1}{4} PV \int_0^\infty \frac{\kappa \cosh \kappa(d+z)}{k \cosh \kappa d(\kappa \tanh \kappa d - k_2 \tanh k_2 d)} \tilde{D}_n(\kappa) J_n(\kappa r) d\kappa \Bigg]
\end{aligned} \tag{3.77}$$

3.5 Complete Solution Satisfying the No-Flow Condition

The solution to the complete second-order potential is determined by adding the homogeneous solution, in Equation 3.24, to the particular solutions for the forced wave motion, in Equation 3.77. The unknown coefficients, $\tilde{a}_{n0}$ and $\tilde{a}_{nm}$ in the homogeneous solution are determined by requiring the total solution to satisfy the kinematic boundary condition on the cylinder as

$$\tilde{\phi}_{2r}^P + \tilde{\phi}_{2r}^H = 0 \tag{3.78}$$

Details of the derivation are presented in Appendix B, but the procedure is identical to that at first order where the coefficients were determined by utilizing the orthogonality properties of $\cosh k(d+z)$ and $\cos \kappa_j(d+z)$. With $\tilde{a}_{n0}$ and $\tilde{a}_{nj}$ determined by Equations B.4 and B.6 in Appendix B respectively, the homogeneous solutions are obtained as

$$\tilde{\phi}_2^H = ikH \sum_{n=0}^{\infty} \cos n\theta$$

$$
\begin{aligned}
&\cdot \left[\frac{\cosh k_2 d}{\sinh 2k_2 d + 2k_2 d}\cosh k_2(d+z)H_n(k_2 r)\left\{6k^2\frac{(\tanh^2 kd - 1)}{(4k^2 - k_2^2)}\beta_n\frac{J_n'(2ka)}{H_n'(k_2 a)}\right.\right.\\
&\quad \left.\left. + \frac{1}{kH_n'(k_2 a)}PV\int_0^\infty \frac{\kappa^2\tilde{D}_n(\kappa)J_n'(\kappa a)}{(\kappa^2 - k_2^2)}d\kappa + \frac{i\pi}{2}\frac{k_2}{k}\tilde{D}_n(k_2)\frac{J_n'(k_2 a)}{H_n'(k_2 a)}\right\}\right.\\
&+ \sum_{j=1}\frac{\cos\kappa_{2j}d}{\sin 2\kappa_{2j}d + 2\kappa_{2j}d}\cos\kappa_{2j}(d+z)K_n(\kappa_{2j}r)\left\{6k^2\frac{(\tanh^2 kd - 1)}{(4k^2 + \kappa_{2j}^2)}\frac{J_n'(2ka)}{K_n'(\kappa_{2j}a)}\right.\\
&\quad \left.\left. + \frac{1}{kK_n'(\kappa_{2j}a)}\int_0^\infty \frac{\kappa^2\tilde{D}_n(\kappa)J_n'(\kappa a)}{(\kappa^2 + \kappa_{2j}^2)}d\kappa\right\}\right] \qquad (3.79)
\end{aligned}
$$

The <u>total</u> solution for the second-order velocity potential may now be given in nondimensional form, based on the sum of $\phi_2^P + \phi_2^H$. Combining Equation 3.77 and Equation 3.79 and adding the time dependence gives the final solution for the second-order velocity potential as

$$
\begin{aligned}
\tilde{\Phi}_2 = &-ikH\frac{e^{-i2\sigma t}}{2}\sum_{n=0}^{\infty}\cos n\theta\\
&\cdot \left[\left\{\frac{3}{4}\frac{k(\tanh^2 kd - 1)}{(2k\tanh 2kd - k_2\tanh k_2 d)}\frac{\cosh 2k(d+z)}{\cosh 2kd}\beta_n J_n(2kr)\right.\right.\\
&\quad - 6k^2\frac{(\tanh^2 kd - 1)}{(4k^2 - k_2^2)}\frac{\cosh k_2 d\cosh k_2(d+z)}{\sinh 2k_2 d + 2k_2 d}\beta_n\frac{J_n'(2ka)}{H_n'(k_2 a)}H_n(k_2 r)\\
&\quad \left.\left. - \sum_{j=1}6k^2\frac{(\tanh^2 kd - 1)}{(4k^2 + \kappa_{2j}^2)}\frac{\cos\kappa_{2j}d\cos\kappa_{2j}(d+z)}{\sin 2\kappa_{2j}d + 2\kappa_{2j}d}\beta_n\frac{J_n'(2ka)}{K_n'(\kappa_{2j}a)}K_n(\kappa_{2j}r)\right\}\right.\\
&+ \left\{\frac{1}{4}PV\int_0^\infty \frac{\kappa\cosh\kappa(d+z)}{k\cosh\kappa d(\kappa\tanh\kappa d - k_2\tanh k_2 d)}\tilde{D}_n(\kappa)J_n(\kappa r)d\kappa\right.\\
&\quad - \frac{\cosh k_2 d\cosh k_2(d+z)}{\sinh 2k_2 d + 2k_2 d}\frac{H_n(k_2 r)}{kH_n'(k_2 a)}\int_0^\infty \frac{\kappa^2\tilde{D}_n(\kappa)J_n'(\kappa a)}{(\kappa^2 - k_2^2)}d\kappa\\
&\quad - \sum_{j=1}\frac{\cos\kappa_{2j}d\cos\kappa_{2j}(d+z)}{\sin 2\kappa_{2j}d + 2\kappa_{2j}d}\frac{K_n(\kappa_{2j}r)}{kK_n'(\kappa_{2j}a)}\int_0^\infty \frac{\kappa^2\tilde{D}_n(\kappa)J_n'(\kappa a)}{(\kappa^2 + \kappa_{2j}^2)}d\kappa\\
&+ \frac{i\pi}{2}\frac{k_2}{k}\frac{\cosh k_2 d\cosh k_2(d+z)}{\sinh 2k_2 d + 2k_2 d}\tilde{D}_n(k_2)\left(J_n(k_2 r) - \frac{J_n'(k_2 a)}{H_n'(k_2 a)}H_n(k_2 r)\right)\left.\right\}\Big]\\
&+ c.c \qquad (3.80)
\end{aligned}
$$

In order to discuss the physical features of the solution, it is first convenient to define several nondimensional coefficients as

$$C_0 = \frac{\cosh k_2 d}{\sinh 2k_2 d + 2k_2 d} \qquad (3.81)$$

$$C_j = \frac{\cos\kappa_{2j}d}{\sin 2\kappa_{2j}d + 2\kappa_{2j}d} \qquad (3.82)$$

$$C_1 = \frac{3}{4}\frac{k(\tanh^2 kd - 1)}{\cosh 2kd(2k\tanh 2kd - k_2 \tanh k_2 d)} \tag{3.83}$$

$$C_{10} = 6\frac{k^2(\tanh^2 kd - 1)}{4k^2 - k_2^2} \tag{3.84}$$

$$C_{1j} = 6\frac{k^2(\tanh^2 kd - 1)}{4k^2 + \kappa_j^2} \tag{3.85}$$

$$C_2 = \frac{1}{4}\frac{\kappa \tilde{D}_n(\kappa)}{\cosh \kappa d(\kappa \tanh \kappa d - k_2 \tanh k_2 d)} \tag{3.86}$$

$$I_{20} = \int_0^\infty \frac{\kappa^2 \tilde{D}_n(\kappa) J_n'(\kappa a)}{(\kappa^2 - k_2^2)} d\kappa \tag{3.87}$$

$$I_{2j} = \int_0^\infty \frac{\kappa^2 \tilde{D}_n(\kappa) J_n'(\kappa a)}{(\kappa^2 + \kappa_{2j}^2)} d\kappa \tag{3.88}$$

$$C_3 = \frac{i\pi}{2}\frac{k_2}{k}\tilde{D}_n(k_2) \tag{3.89}$$

With this notation, the complete second order solution is

$$\begin{aligned}
\tilde{\Phi}_2 = -ikH\frac{e^{-i2\sigma t}}{2}\sum_{n=0}^{\infty}\cos n\theta \\
\cdot \Bigg[\Bigg\{ & C_1 \cosh 2k(d+z)\beta_n J_n(2kr) - C_{10}C_0 \cosh k_2(d+z)\beta_n \frac{J_n'(2ka)}{H_n'(k_2a)} H_n(k_2 r) \\
& - \sum_{j=1} C_{1j}C_j \cos \kappa_{2j}(d+z)\beta_n \frac{J_n'(2ka)}{K_n'(\kappa_{2j}a)} K_n(\kappa_{2j} r) \Bigg\} \\
+ \Bigg\{ & PV\int_0^\infty \frac{C_2}{k}\cosh \kappa(d+z) J_n(\kappa r) d\kappa - C_0 I_{20} \cosh k_2(d+z)\frac{H_n(k_2 r)}{kH_n'(k_2 a)} \\
& - \sum_{j=1} C_j I_{2j} \cos \kappa_{2j}(d+z)\frac{K_n(\kappa_{2j} r)}{kK_n'(\kappa_{2j})} \\
+ \quad & C_3 C_0 \cosh k_2(d+z)\left(J_n(k_2 r) - \frac{J_n'(k_2 a)}{H_n'(k_2 a)} H_n(k_2 r)\right)\Bigg\}\Bigg] + c.c.
\end{aligned} \tag{3.90}$$

3.6 Discussion of Solution for Φ_2

In the solution given in Equation 3.80 or Equation 3.90, terms enclosed in the first bracket on the right hand side represent (1) the forced Stokes incident plane wave component at wavenumber 2k and (2) the free cylindrical wave motion due to the scattering of the Stokes plane wave. Although notation is different, these terms are identical to the partial solution given in Equation 2.20 which was derived in a different way by Chen (1979, p.104) and Chen and Hudspeth (1982) using the method of Green's functions. In deep water, the terms, C_1, C_{10}, and C_{1j}, vanish rapidly with increasing kd; this is in agreement with the

known behavior of the Stokes second-order plane wave velocity potential in deep water. In shallow water, the second-order free wavenumber, k_2, approaches $2k$ and resonant quadratic forcing occurs in the CFSBC. Mathematically, C_1 and C_{10} become singular in shallow water and the solution "blows up" as expected.

The second bracket includes terms that represent the remaining forced-radiated wave motion due to nonlinear wave-wave interactions through the forcing terms f^{is} and f^{ss}, as well as free scattered waves which are due to the interaction of these forced-radiated waves with the cylinder. While interpretation is more difficult, the forced wave motions are composed of local cylindrical standing waves with amplitudes given by the wavenumber spectrum, based on the integrated effects of the quadratic forcing. The associated scattered wave motions are free cylindrical waves with an amplitude that is defined in terms of contributions from all wavenumbers as well. The last components, with the coefficient C_3 in Equation 3.90, represent the "radiated" wave motions that are required to ensure that the waves generated by f^{is} and f^{ss} satisfy a radiation condition. These motions must also interact with the cylinder to produce additional scattered wave components.

In deep and shallow water, the behavior of the cylindrical forced-radiated waves, and the associated scattered waves, is difficult to interpret explicitly. Since all wavenumbers are present, some long wave motions may be in relatively shallow water even though the dimensionless depth, kd, may be quite large. Some second-order motions associated with the f^{is} forcing have very slow depth decay and give the appearance of a "microseism." As noted earlier, on the upwave side, the f^{is} forcing has the leading order form

$$f^{is} \approx \frac{1}{\sqrt{r}} e^{-i2\sigma t} \tag{3.91}$$

The resulting wave motion, together with other quadratic terms in the equation for the second-order pressure, is a long standing wave with radial decay (and decay over θ), without radial oscillation, but with temporal oscillation at frequency 2σ. This is the cylindrical analog to the microseism associated with plane standing waves.

As may be verified from the solution procedure, all governing equations and boundary conditions are satisfied by the solution for Φ_2. The boundary condition of most interest, the nonhomogeneous CFSBC, is satisfied as follows. Remembering that all terms in the solution that have $\cosh k_2(d+z)$ or $\cos \kappa_{2j}(d+z)$ behavior satisfy the homogeneous CFSBC, substitution of Φ_2, from Equation 3.90, into the CFSBC, Equation 3.2 yields the condition

$$C_1(2k \tanh 2kd - k_2 \tanh k_2 d) \cosh 2kd \beta_n J_n(2kr) + \int_0^\infty \frac{C_2}{k}(\kappa \tanh \kappa d - k_2 \tanh k_2 d) \cosh \kappa d J_n(\kappa r) d\kappa = \frac{1}{4}\left[\tilde{f}_n^{ii} + \tilde{f}_n^{is} + \tilde{f}_n^{ss}\right] \quad (3.92)$$

From Appendix A.4, the forcing term $\tilde{f}^{ii}$ is equal to

$$\tilde{f}_n^{ii} = 3(\tanh^2 kd - 1)\beta_n J_n(2kr) \quad (3.93)$$

Based on the definition of C_1 in Equation 3.83, the first term on the left hand side of Equation 3.92 satisfies the first nonhomogeneous forcing term on the right hand side of Equation 3.92. From the definition for C_2 in Equation 3.86, the remaining condition is then found to be

$$\int_0^\infty \kappa \tilde{D}_n(\kappa) J_n(\kappa r) d\kappa = \tilde{f}_n^{is} + \tilde{f}_n^{ss} \quad (3.94)$$

where substitution of the expression for $\tilde{D}_n(\kappa)$ yields

$$\int_0^\infty \kappa J_n(\kappa r) \int_a^\infty r' \left(\tilde{f}_n^{is}(r') + \tilde{f}_n^{ss}(r')\right) J_n'(\kappa r') dr' d\kappa = \tilde{f}_n^{is}(r) + \tilde{f}_n^{ss}(r) \quad (3.95)$$

From the theorem of Hankel transforms, e.g. Watson (1962) or Sneddon (1951), it is verified that the integrals on the left hand side represent those on the right hand side; thus the CFSBC is satisfied.

The solution in Equation 3.90 is found to exhibit the irregularity in the overlap region of the boundary conditions, at $r = a$ and $z = 0$, as first observed by Isaacson (1977a). The irregular nature may be confirmed by considering the equivalence of the following derivatives in the limit as the overlap is approached from different directions

$$\lim_{r \to a} \frac{\partial}{\partial r}\left[(\Phi_{2tt} + g\Phi_{2z})_{z=0}\right] \stackrel{?}{=} \lim_{z \to 0}\left(\frac{\partial^2}{\partial t^2} + g\frac{\partial}{\partial z}\right)\left[(\Phi_{2r})_{r=a}\right] \quad (3.96)$$

The solution guarantees that the no-flow requirement is satisfied at $r = a$; therefore, the right hand side is identically zero. Substitution of Φ_2 into the CFSBC yields the result

$$(\Phi_{2tt} + g\Phi_{2z})_{z=0} \simeq \Re\left[e^{-i2\sigma t}\sum_{n=0}\cos n\theta f_n(r)\right] \tag{3.97}$$

Thus, taking the derivative with respect to r and then taking the limit as $r \to a$ gives Isaacson's inequality in a different form

$$\lim_{r\to a}\sum_{n=0}\cos n\theta\left(\frac{\partial f_n(r)}{\partial r}\right) \stackrel{?}{=} 0 \tag{3.98}$$

3.7 Numerical Computation of Φ_2

The theoretical second-order velocity potential is derived in closed integral form; however, numerical integration techniques are required for evaluation. The integrals that must be evaluated may be separated into two types: (1) the integration from $a \leq r \leq \infty$ which yields the wavenumber spectrum, $\tilde{D}_n(\kappa)$ and (2) the integration over wavenumber space, $0 \leq \kappa < \infty$, of three sparate integrands, two of which have singularities at the free wavenumber, k_2. Various methods of computing the integrals are available and several methods are discussed by Monacella (1966), Garrison (1978), Hunt and Baddour (1981), Hunt and Williams (1982), and Rahman and Heaps (1983). In this study, all integrals are evaluated with the Simpson's rule.

The r-integrations are difficult since both $\tilde{f}_n(r)$ and $J_n(\kappa r)$ are oscillatory functions; thus the integrand is oscillatory and sensitive to the cutoff limit on the upper limit of integration. In lieu of carrying the integrations out to exceedingly large distances in r, the method used here is to replace the upper limit by an indefinite limit, r. The integration may then be carried out from $r = a$ to any distance, r , yielding a function of r as

$$\tilde{D}_n(\kappa, r) = k^2\int_a^r r'\tilde{f}_n(r')J_n(\kappa r')dr' \tag{3.99}$$

The function, $\tilde{D}_n(\kappa, r)$, is oscillatory, but beyond several pile radii, any additional net contribution to the integral is found to be very small. By applying a moving filter to $\tilde{D}_n(\kappa, r)$, the asymptotic value of the oscillatory integral can be obtained with a smaller cutoff limit, R_o, as

$$\tilde{D}_n(\kappa) = \lim_{r \to R_o} \int_{r-R_w}^{r+R_w} w(r) \tilde{D}_n(\kappa, r) dr \tag{3.100}$$

A triangular window

$$w(r) = \frac{1}{R_w} \left(1 - \frac{| r - R_w |}{R_w} \right) \tag{3.101}$$

where R_w equal to $5a$ has been used. A cutoff, $R_o = 15a$, has been found to be accurate for cylinder sizes up to $ka = 1.5$; for larger cylinder sizes the cutoff must be increased.

The evaluation of the κ-integrals is surprisingly straightforward. The numerical integration of the Cauchy Principal Value integrals is performed by removing the singularity as suggested by Monacella (1966, p. 246). The integrand is first written in terms of a general function, $g(\kappa)$, as

$$I = PV \int_0^\infty \frac{g(\kappa)}{\kappa \tanh \kappa d - k_2 \tanh k_2 d} d\kappa \tag{3.102}$$

Then, the value of the integrand at the singularity is removed as

$$I = \int_0^\infty \frac{g(\kappa) - g(k_2)}{\kappa \tanh \kappa d - k_2 \tanh k_2 d} d\kappa + g(k_2) \cdot PV \int_0^\infty \frac{1}{\kappa \tanh \kappa d - k_2 \tanh k_2 d} d\kappa \tag{3.103}$$

The behavior of the first integral is now regular across the singularity and may be integrated directly. The second integrand is sufficiently linear near the singularity that in the Principal Value sense, the positive and negative contributions on some small distance, ε, either side of the singularity cancel each other, and a contribution exists only for regions away from the singularity. The singularity in the integrand, at $\kappa = k_2$, always occurs between $k_2 = 2k$ at the shallow water limit and $k_2 = 4k$ at the deep water limit. The contribution to the integrals is found to be most significant from $\kappa = 0$ to beyond $\kappa = 4k$; a cutoff wavenumber $\kappa_c = 12k$ was found to be required for adequate convergence.

A final numerical feature of the theoretical solution is the appearance of the Gibb's phenomenon, e.g. Courant and Hilbert (1961), in the numerical transforms involved in fitting the CFSBC. As noted, substituting the solution for $\tilde{\Phi}_2$ into the CFSBC yields the Hankel transform of the quadratic free surface forcing as given in Equation 3.95. While

this transform identity is generally true, at points of discontinuity in the forcing, $f_n(r)$, the transform can only recover the mean value of the function from either side of the jump. In this case, the transform method is applied to the quadratic forcing from $r = a$ to $r = R_o$, with the forcing being zero inside the cylinder; i.e. there is no wave-generating forcing applied to the free surface inside the cylinder. At $r = a$, the forcing experiences a jump discontinuity from zero at $r = a^-$ to $f_n(a)$ at $r = a^+$, and the Gibb's phenomenon occurs at the point of most interest in the solution.

An example of this phenomenon is depicted in Figure 3.4 for one order in the solution, $n = 1$. The amplitude of the quadratic forcing is shown in the solid curve. By application of the integral solution, the wavenumber spectrum, $\tilde{D}_n(\kappa)$ is first computed, then the solution is substituted into the CFSBC. From the Hankel transform identity in Equation 3.95, the exact form of the quadratic forcing should be recovered. It is found instead that due to numerically performing a continuous transform with discrete calculations over a finite interval, there is an error in the reconstructed forcing as

$$\tilde{\varepsilon}_n(r) = \tilde{f}_n(r) - \frac{1}{k^2}\int_a^\infty \kappa \tilde{D}_n(\kappa) J_n(\kappa r) d\kappa \tag{3.104}$$

In Figure 3.4, the reconstructed forcing is shown in the dashed line and clearly displays the Gibb's phenomenon where one-half of the value of the function is recovered at $r = a$, while the approximation then overshoots and undershoots the exact value while the error decreases as r increases.

An intuitive procedure has been used to reduce the effects of the Gibb's phenomena. The method is based on the repeated application of the transform method to successively obtain better reconstructions of the quadratic forcing and the velocity potential. From the initial approximation of the solution, an error is found in the reconstruction of the CFSBC as in Equation 3.104. This error in the quadratic forcing must be accounted for to obtain an exact fitting of the CFSBC; therefore, a correction to the wavenumber spectrum, $\Delta\tilde{D}_n(\kappa)$, may be obtained by transforming the error as

$$\Delta\tilde{D}_n(\kappa) = k^2 \int_a^\infty r' \tilde{\varepsilon}_n(r') J_n(\kappa r') dr' \tag{3.105}$$

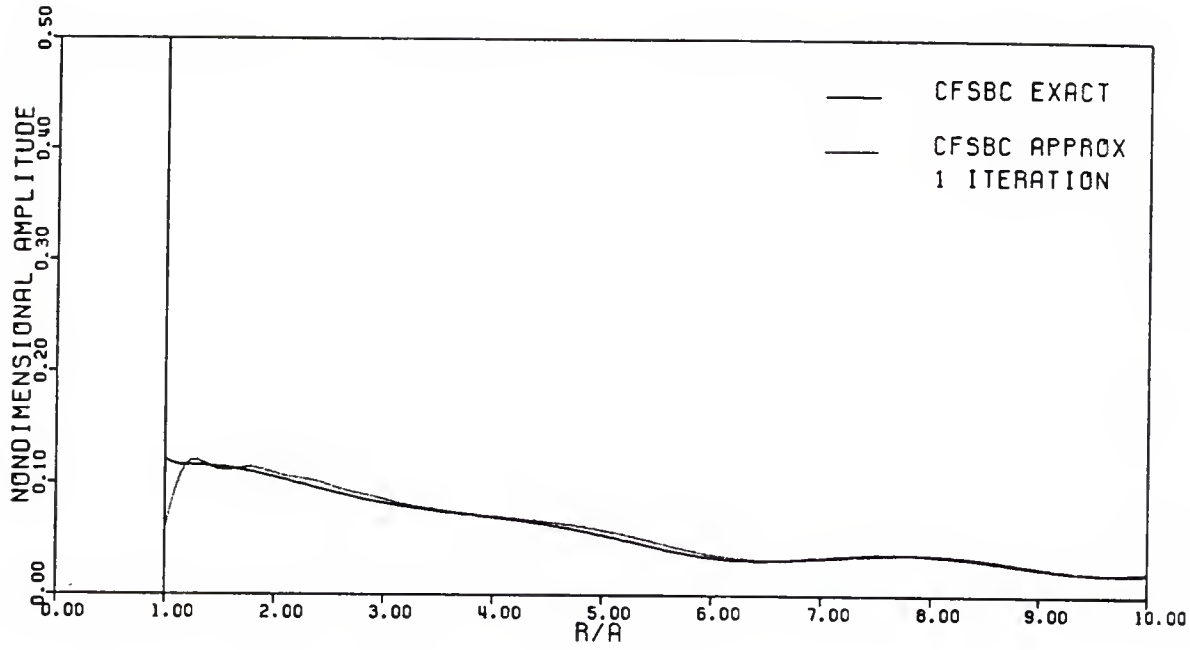

Figure 3.4: Amplitude of $\tilde{f}_1^{is}$ forcing with Gibb's phenomenon after one iteration

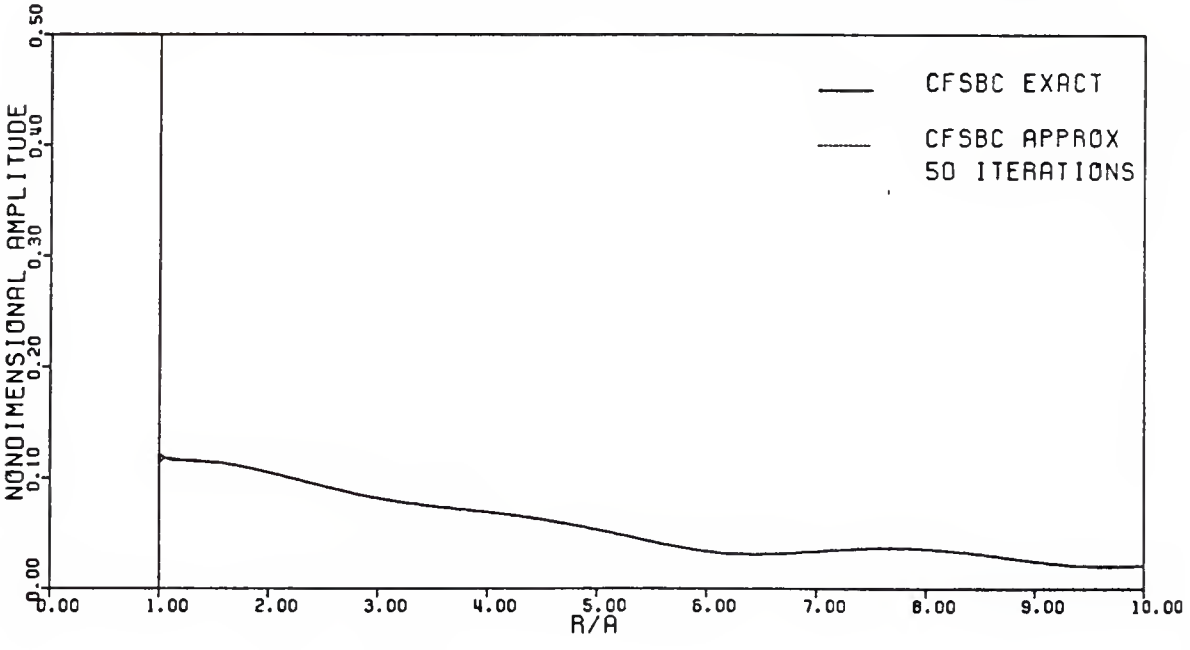

Figure 3.5: Amplitude of $\tilde{f}_1^{is}$ forcing with reduced Gibb's phenomenon after 50 iterations

This correction to the wavenumber spectrum may then be added to the initial estimate of the wavenumber spectrum, to obtain a better approximation as

$$\tilde{D}_n^*(\kappa) = \tilde{D}_n(\kappa) + \Delta\tilde{D}_n(\kappa) \tag{3.106}$$

By applying the inverse transform using the new wavenumber spectrum, a better fitting of the CFSBC is achieved with a new smaller error as

$$\tilde{\varepsilon}_n^*(r) = \tilde{f}_n(r) - \frac{1}{k^2}\int_a^\infty \kappa\tilde{D}_n^*(\kappa)J_n(\kappa r)d\kappa \tag{3.107}$$

By successively applying the transform to each error term, additional corrections are obtained for the wavenumber spectrum. In Figure 3.5, after, 50 iterations, the CFSBC is satisfied almost exactly and the effects of the Gibb's phenomenon are nearly eliminated. From repeated numerical testing, the effects of the Gibb's phenomenon are of importance near the cylinder, as expected; but, differences between the solution after, say 5 iterations and 50 iterations are typically only a few percent. Other proposed solutions that have been based on a Fourier-Bessel integral, such as those of Garrison (1979), Hunt and Baddour (1981), Hunt and Williams (1982), and Rahman and Heaps (1983), certainly contain the same Gibb's phenomena problem; however, none of the authors mention its existence.

CHAPTER 4
FREE SURFACE ELEVATIONS AND WAVE RUNUP

4.1 Introduction

One of the primary goals of this study is to determine the second-order water surface elevations surrounding a large circular cylinder. Despite all of the previous studies of the second-order velocity potential and the resulting wave forces, only Raman and Venkatanarasaiah (1976b), Raman et al. (1977), and Chakrabarti (1978) have applied second-order solutions for Φ_2 to obtain the second-order water surface; and, they only considered the runup distribution around the cylinder for 2 to 4 test cases. No previous solutions have been used to calculate the three-dimensional wave field around the pile.

The water surface elevation is obtained from the dynamic free surface boundary condition, Equation 1.10, as

$$\eta = -\frac{P}{\rho g} - \frac{1}{g}\Phi_t - \frac{1}{2g}(\nabla\Phi)^2 - \frac{C(t)}{g} \qquad \text{on } z = \eta \qquad (4.1)$$

which is an unsteady form of the Bernoulli equation. Based on the perturbation expansion technique, Φ and η are expanded in power series form, and Equation 4.1 is expanded in a Taylor series about $z = 0$. The water surface consistent to the second perturbation order may then be obtained as

$$\eta_1 + \eta_2 = -\frac{1}{g}\Phi_{1t} - \frac{1}{g}\Phi_{2t} + \frac{1}{g}\eta_1\Phi_{1tz} - \frac{1}{2g}\left[\Phi_{1r}^2 + \frac{1}{r^2}\Phi_{1\theta}^2 + \Phi_{1z}^2\right] \qquad (4.2)$$

where the external atmospheric pressure is taken to be zero.

At first order, the water surface is given by one term

$$\eta_1 = -\frac{1}{g}\Phi_{1t} \qquad \text{on } z = 0 \qquad (4.3)$$

such that the linear free surface depends only on the unsteady dynamic pressure associated with local accelerations of the linear incident and scattered waves. The second-order free surface elevation is found from

$$\eta_2 = -\frac{1}{g}\eta_1\Phi_{1tz} - \frac{1}{2g}\left[(\Phi_{1r})^2 + (\frac{1}{r}\Phi_{1\theta})^2 + (\Phi_{1z})^2\right] - \frac{1}{g}\Phi_{2t} \qquad \text{on } z = 0 \qquad (4.4)$$

At second order, the free surface elevation is given by two types of components: (1) quadratic terms that depend on products of derivatives of the first-order potential, associated with convective accelerations of the first-order fluid motion as well as the free surface displacement and (2) the local time derivative of the second-order velocity potential associated with the local accelerations of the second-order motions.

4.2 First-Order Water Surface

Substitution of the solution for Φ_1 in Equation 1.55, into Equation 4.3, yields the first-order linear wave field as

$$\eta_1 = \frac{H}{2}\sum_{n=0}^{\infty}\beta_n\left[J_n(kr) - \frac{J_n'(ka)}{H_n'(ka)}H_n(kr)\right]\cos n\theta\frac{e^{-i\sigma t}}{2} + c.c. \qquad (4.5)$$

The nondimensional water surface may be obtained by normalizing η_1 by the incident wave amplitude as

$$\tilde{\eta}_1 = \frac{2\eta_1}{H} \qquad (4.6)$$

to give

$$\tilde{\eta}_1 = \sum_{n=0}^{\infty}\beta_n\left[J_n(kr) - \frac{J_n'(ka)}{H_n'(ka)}H_n(kr)\right]\cos n\theta\frac{e^{-i\sigma t}}{2} + c.c. \qquad (4.7)$$

The incident and scattered waves are both represented by complex quantities that depend on the relative cylinder radius ka; therefore, a phase shift is introduced between the incident and scattered waves that also depends on the size of the cylinder relative to the wavelength.

At $r = a$, a useful identity may be introduced, e.g. Abramowitz and Stegun (1972)

$$J_n(kr) - \frac{J_n'(ka)}{H_n'(ka)}H_n(kr) = \frac{2i}{\pi ka}\frac{1}{H_n'(ka)} \qquad (4.8)$$

The nondimensional free surface elevation around the circumference of the cylinder, $\tilde{\eta}_{1c}$, is then

$$\tilde{\eta}_{1c} = \frac{2}{\pi ka} \sum_{n=0}^{\infty} (2 - \delta_{n0}) i^{n+1} \frac{1}{H_n'(ka)} \cos n\theta \frac{e^{-i\sigma t}}{2} + c.c. \tag{4.9}$$

The runup and rundown on the cylinder may be defined as the maximum and minimum free surface elevations that occur over one wave period at a given angular position, i.e. the maxima and minima of the wave envelope at $r = a$. Linear runup profiles around the circumference of the cylinder for various values of ka are depicted in Figure 4.1. The runup is greatest at the leading edge of the cylinder and decreases to a minimum between 30 and 60 degrees, or slightly aft of the shoulder; this is shifted farther to the rear as ka is increased. For small piles, runup amplitudes at the rear of the pile approaches unity, while for larger piles, the runup amplitude at the rear of the pile decreases as the sheltering effects of the pile become more important.

The behavior of the maximum runup at the front of the cylinder over the range of cylinder sizes may be represented by a single curve as a function of ka as shown in Figure 4.2. For small piles, with $ka < 0.2$, the incident wave crest is not significantly interrupted by the pile. As the cylinder radius increases, the cylinder reflects more of the incident wave energy and an antinode of a partial standing wave system forms at the front of the cylinder giving larger runup. With increased wave reflection, the maximum wave runup amplitude approaches twice that of the incident wave.

In Figure 4.3, a vertical cross-section of the free surface region is depicted to show the linear wave envelope in the upwave and downwave regions, and to show a projection of the wave envelope around the circumference of the cylinder, for a reference case with $ka = 1.0$. The linear wave field is observed to be a partial standing wave system on the upwave side, with antinodes and nodes that become less pronounced away from the cylinder. On the downwave side, few diffraction effects are evident. In this region the incident and scattered wave are propagating in nearly the same direction and produce no modulated wave envelope, unless ka is very large. Since Φ_1 is composed of terms at frequency σ only, the linear water

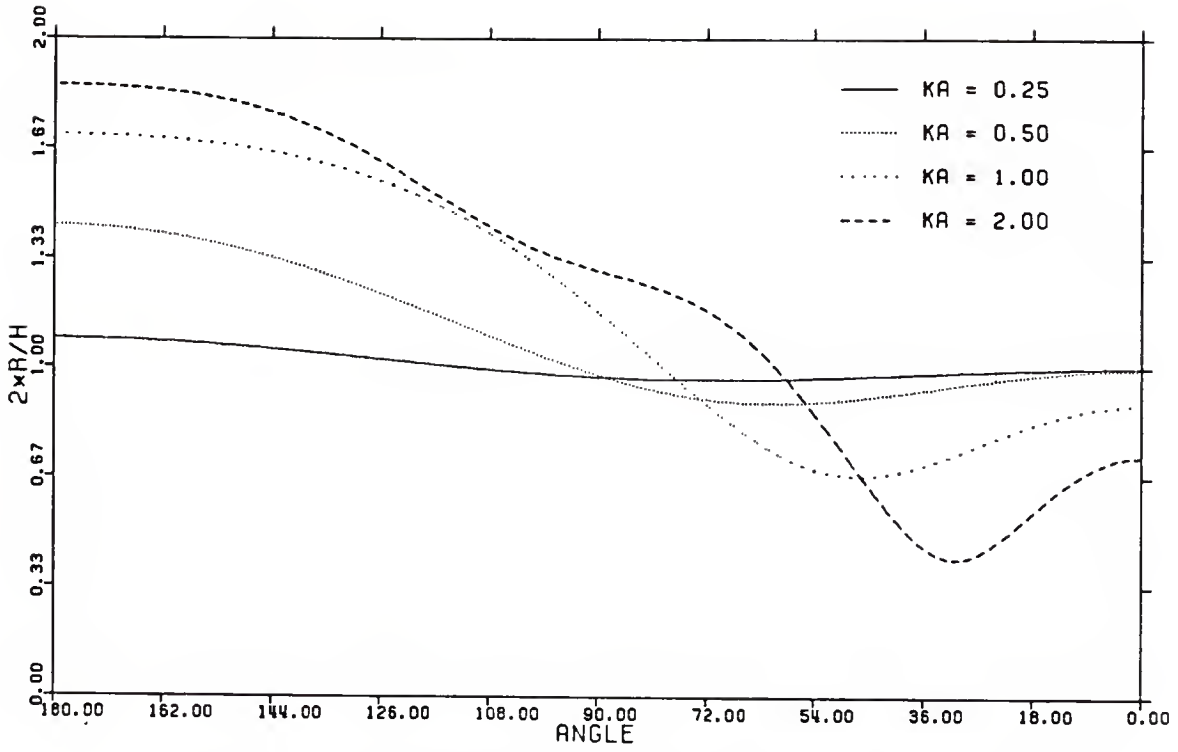

Figure 4.1: Runup profiles from linear theory for various values of ka.

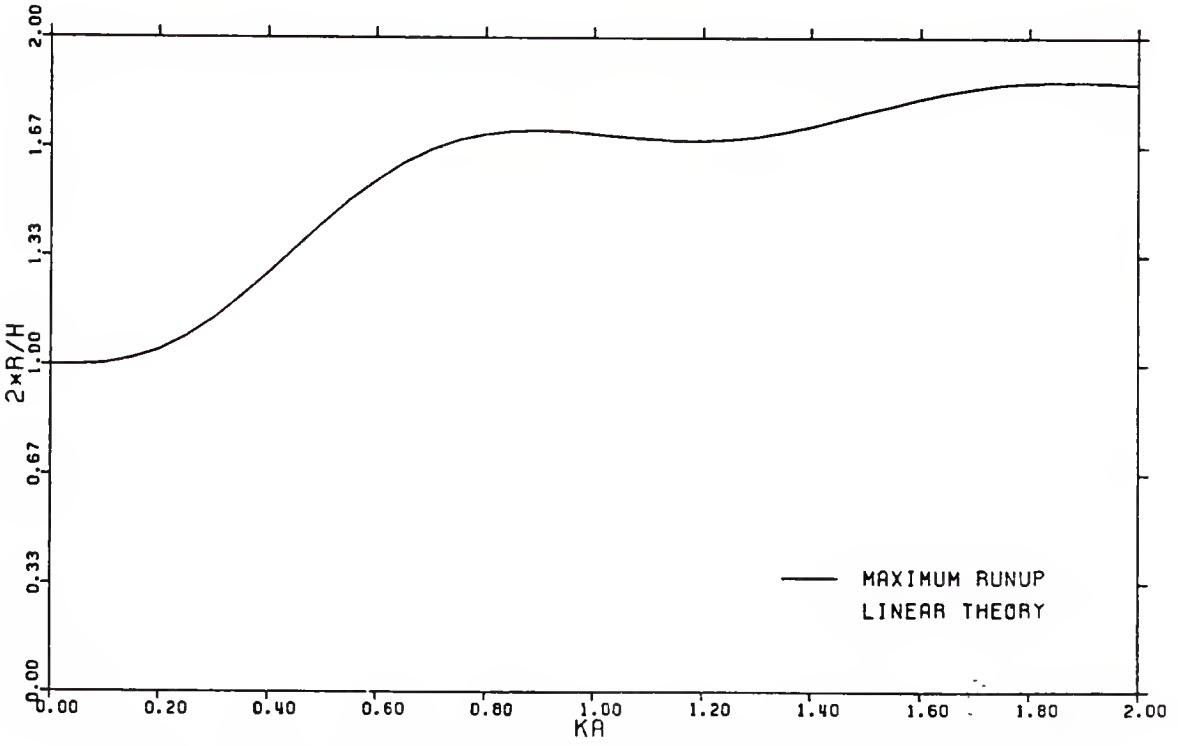

Figure 4.2: Maximum wave runup as a function of diffraction parameter, ka.

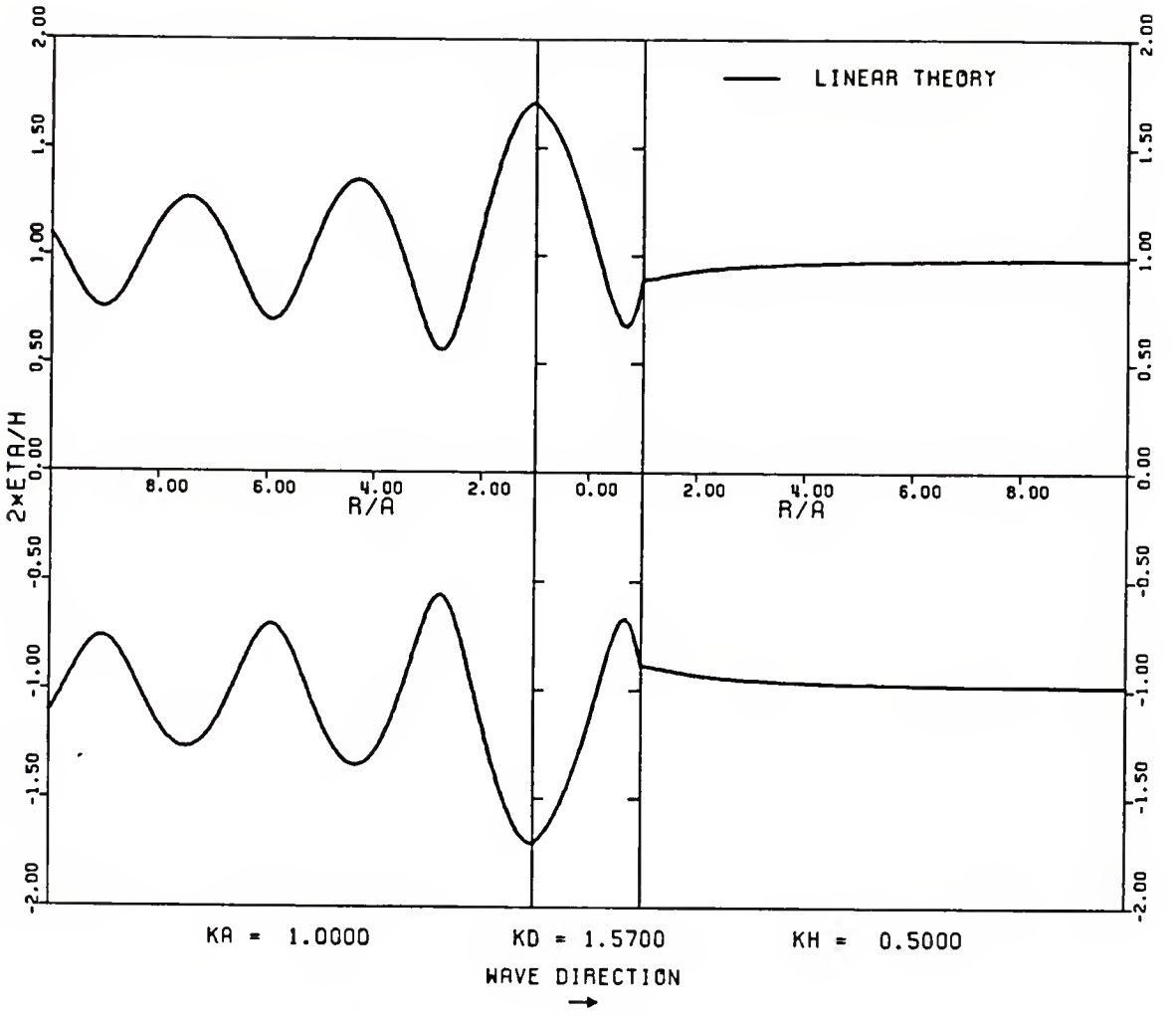

Figure 4.3: Envelope of first-order free surface along axis of wave propagation, $ka = 1.0$

surface oscillates about $z = 0$ with equal trough and crest amplitudes.

In Figure 4.4, contours of equal wave amplitude are shown in planform for an area extending out 7 to 10 times the pile radius for the same reference case. The partial standing wave system on the upwave side is observed to be fairly uniform along the x axis and decays gradually as θ decreases and as r increases. In the downwave region, diffraction effects are now evident as simple zones of constructive and destructive wave interference. The most evident diffraction effects are at approximately $\pm 30^o$ to 60^o. In the region behind the cylinder, the linear theory does not predict any spatially periodic amplitude modulation, but nondimensional wave amplitudes are reduced at $r = a$ and approach unity as r increases.

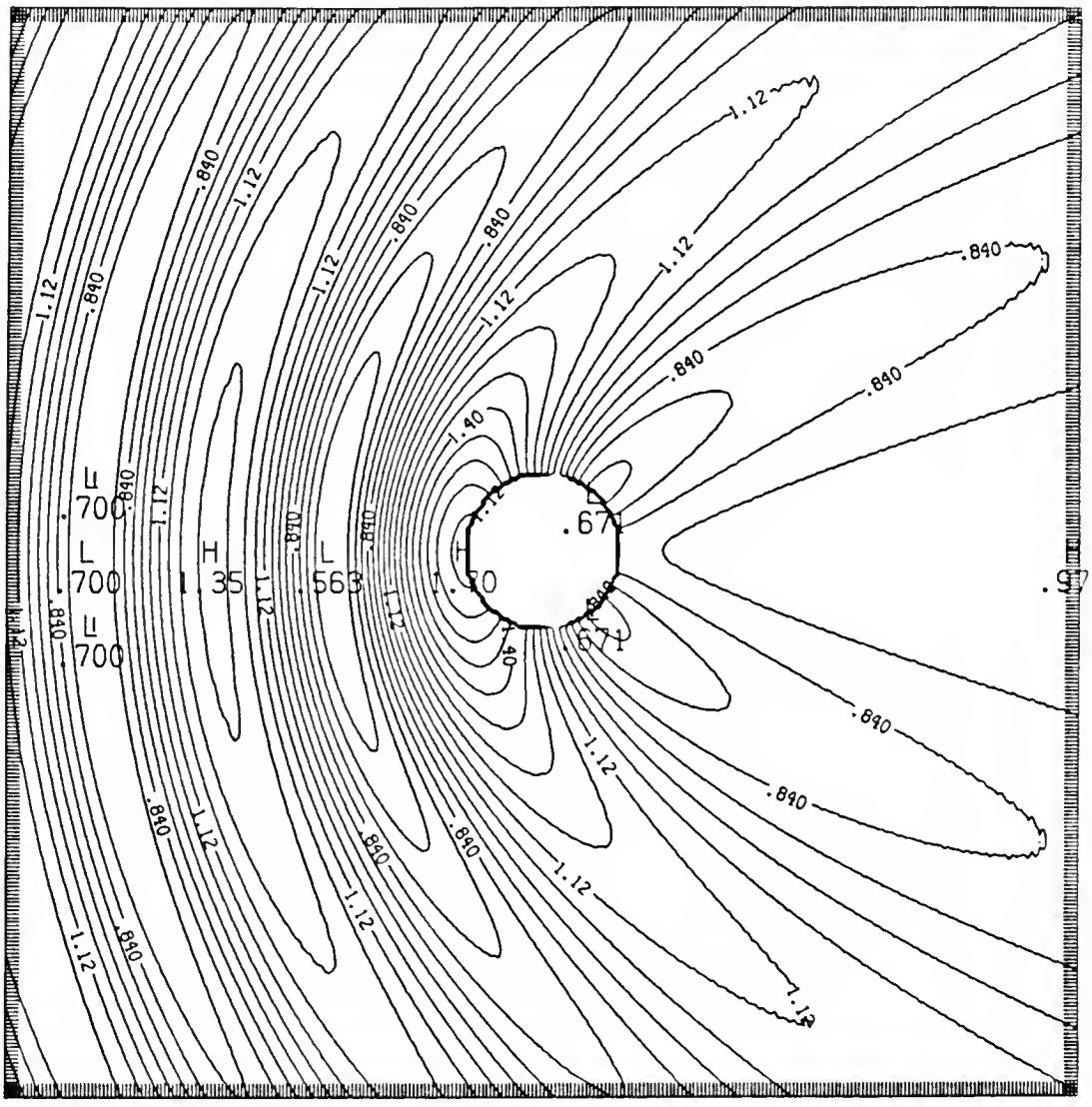

Figure 4.4: Contours of first-order wave crest envelope, $ka = 1.0$

Based on the linear solution, some insight may be gained into the nature of the quadratic free surface forcing which, in turn, generates the second-order wave field. On the upwave side, the linear scattered waves oppose the incident plane waves and a partial standing wave field is developed. This region is reflection-dominated, and quadratic interactions of the incident and scattered linear waves are strong such that this region serves as a generating area for many second-order wave components. Along the sides of the cylinder, a node forms in the first-order wave envelope and large quadratic pressures are found near to the cylinder. In the downwave region, the linear scattered wave propagates in much the same direction as the incident wave and the linear wave envelope is not strongly modulated. The quadratic forcing in the CFSBC is weak; and, rather than being a wave generation area, wave motions in this region originate largely from the front and side regions. The downwave region is, therefore, diffraction-dominated.

4.3 Quadratic Components of the Second-Order Water Surface

From Equation 4.4, the quadratic terms in the second-order free surface are

$$\eta_{21} = +\frac{1}{g^2}\Phi_{1t}\Phi_{1tz} - \frac{1}{2g}\left[(\Phi_{1r})^2 + (\frac{1}{r}\Phi_{1\theta})^2 + (\Phi_{1z})^2\right] \tag{4.10}$$

In Appendix A.6, these terms are reduced to simpler forms suitable for numerical computation. From Equation A.88, the reduced form of the nondimensional quadratic free surface terms, $\tilde{\eta}_{21}$, is found to be

$$\begin{aligned}\tilde{\eta}_{21} &= \frac{kH}{8\tanh kd}\sum_{n=0}^{\infty} G_n^s(r)\cos n\theta \\ &\quad + \frac{kH}{8\tanh kd}\sum_{n=0}^{\infty} G_n^o(r)\cos n\theta \frac{e^{-i2\sigma t}}{2} + c.c.\end{aligned} \tag{4.11}$$

The radial functions $G_n^s(r)$ and $G_n^o(r)$ are defined as in Equations A.89 and A.90 in Appendix A.6. Features of $\tilde{\eta}_{21}$ are (1) the second-order quadratic components include terms that oscillate in time at frequency 2σ and terms that are independent of time, and (2) the second-order quadratic terms depend on all three nondimensional parameters, ka, kd, and kH; the dependence on ka and kd is incorporated in the spatial functions $G_n^s(r)$ and $G_n^o(r)$.

4.3.1 Mean Water Levels

The steady components of $\tilde{\eta}_{21}$ are

$$\tilde{\eta}^s_{21} = \frac{kH}{8\tanh kd} \sum_{n=0}^{\infty} G^s_n(r) \cos n\theta \tag{4.12}$$

where $G^s_n(r)$ is a real quantity. This term includes (1) a uniform setdown due to the self-interaction terms from the first-order incident plane wave, as well as (2) spatially varying mean water levels due to the cross and self-interactions of the first-order incident and scattered waves. In Equation A.85 from Appendix A.6, if no structure is present, then $\tilde{\eta}^s_{21}$ may be shown to reduce to

$$\tilde{\eta}^s_{21} = -\frac{kH}{8\sinh 2kd} \tag{4.13}$$

which is the expected second-order uniform setdown, e.g Dean and Dalrymple (1984, p. 302).

In Figure 4.5, a vertical cross-section of the mean water surface is given to show the steady water levels on the upwave and downwave side as well as around the circumference of the cylinder. This figure is based on a set of reference conditions with the dimensionless radius $ka = 1.0$, the dimensionless depth $kd = 1.57$, and the wave steepness $kH = 0.5$. In Figure 4.6, the mean water level contours are shown in planform for the same wave conditions.

General features of the second-order mean water levels are

1. On the upwave side, there is a spatially varying setup and setdown pattern related to the first-order partial standing wave system. The setup-setdown pattern is completely analogous to that observed in front of a plane barrier due to standing plane waves, except that in the present case the amplitudes of the mean water level variations decrease as $r^{-\frac{1}{2}}$ and with θ. This "corrugated" mean water level is superimposed on the usual uniform setdown associated with the incident plane wave.

2. On the downwave side, the mean water level varies monotonically from a small net setup at the rear of the cylinder to a uniform setdown farther away. The first-order

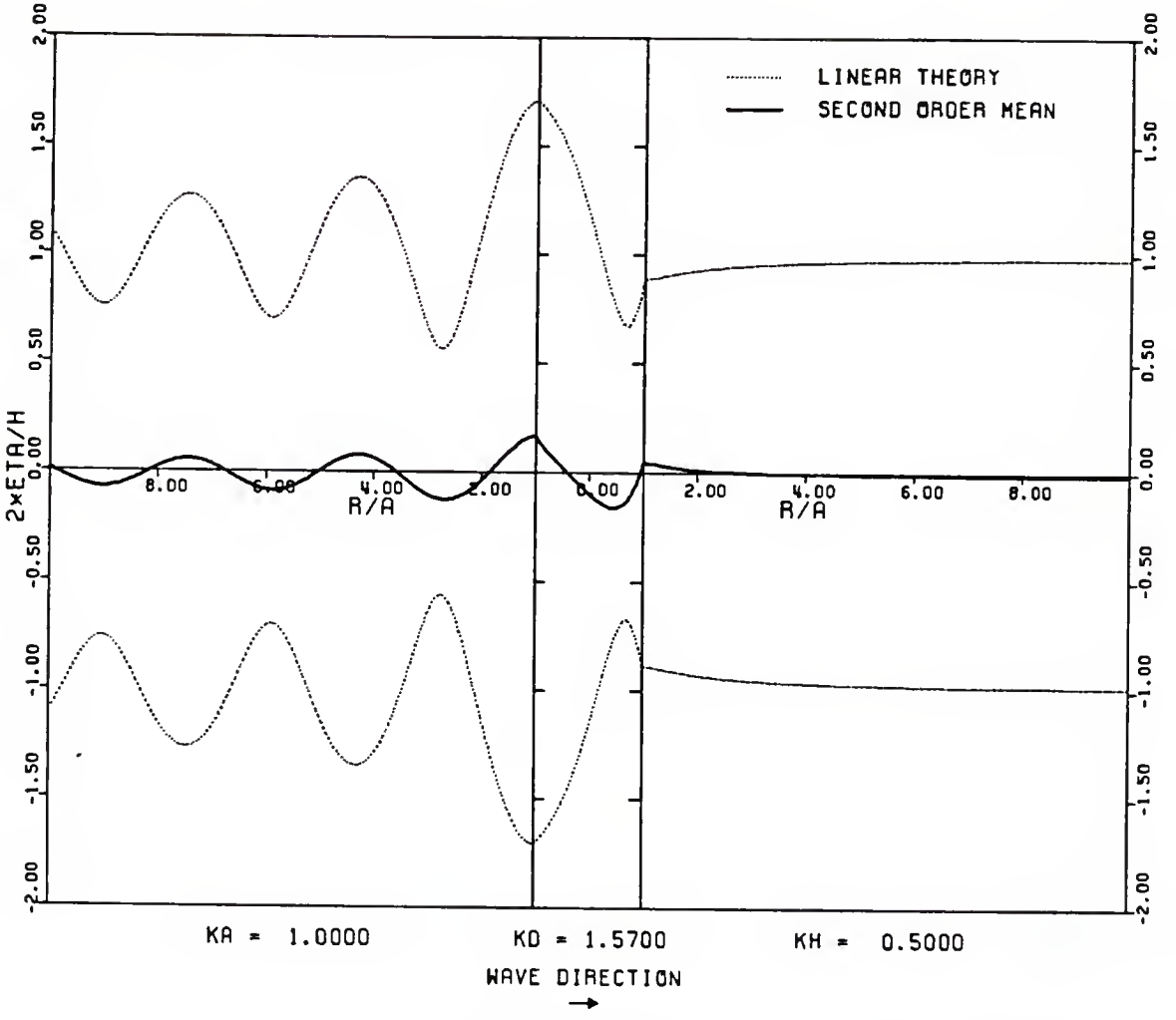

Figure 4.5: Second-order mean water levels along x axis for reference case, $ka = 1.0$, $kd = 1.57$, and $kH = 0.5$

wave field does not exhibit nodes or antinodes; therefore, the second-order mean water level does not have spatial periodicity.

3. On the sides of the cylinder, a smooth transition occurs from maximum setup at the front, to maximum setdown aft of the shoulder, to a secondary setup at the rear. The large setdown near the shoulder of the cylinder is quite localized and is due to the low pressures associated with the node of the first-order wave envelope at the shoulder.

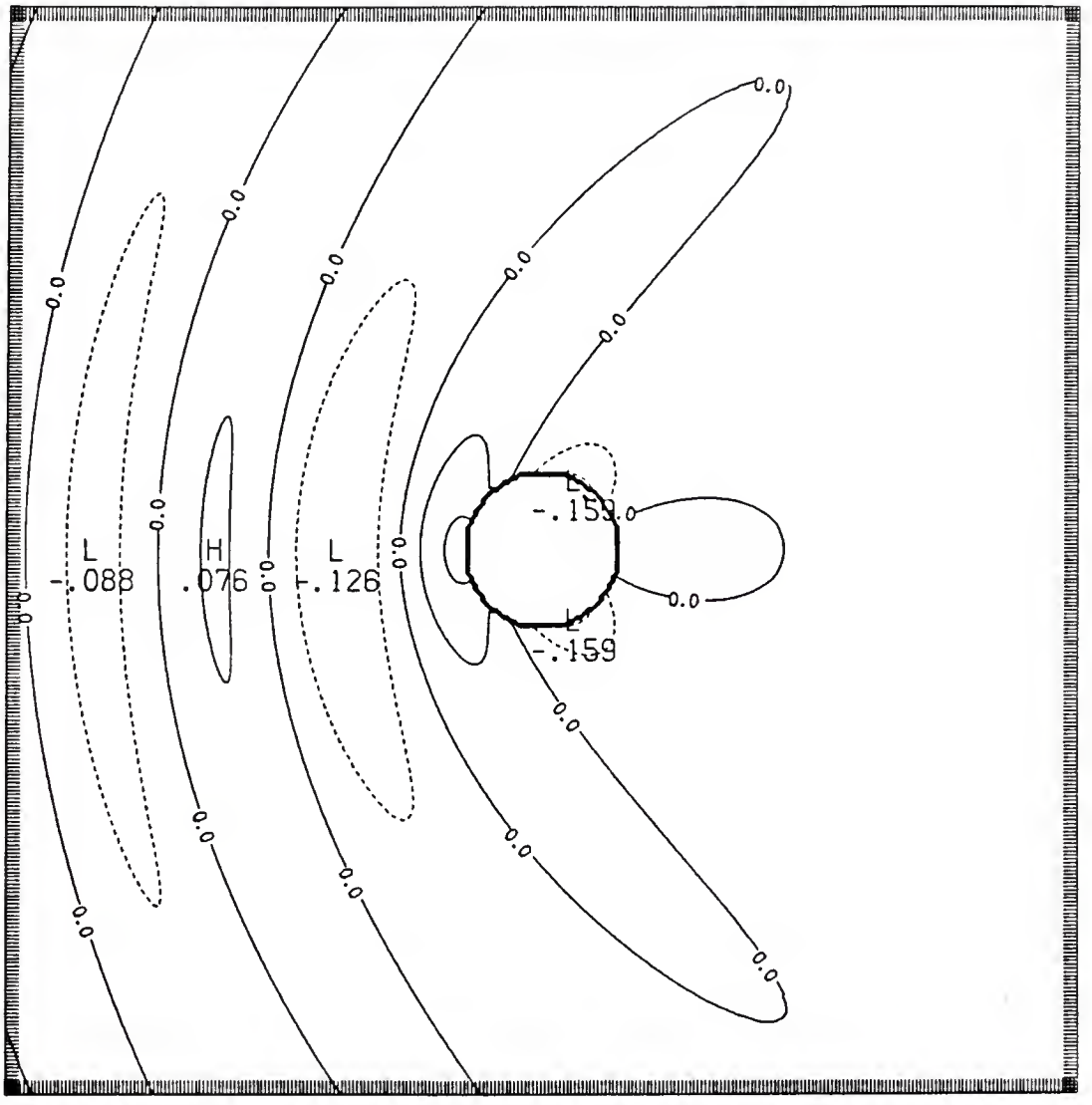

Figure 4.6: Contours of second-order mean water level for reference case, $ka = 1.0$, $kd = 1.57$, and $kH = 0.5$

4.3.2 Oscillatory Quadratic Free Surface

The time-dependent terms in $\tilde{\eta}_{21}$ are

$$\tilde{\eta}^o_{21} = \frac{kH}{8\tanh kd} \sum_{n=0}^{\infty} G^o_n(r) \cos n\theta \frac{e^{-i2\sigma t}}{2} + c.c. \tag{4.14}$$

where $G^o_n(r)$ is a complex quantity. Like the steady water level term, the oscillatory term consists of components due to the nonlinear self and cross-interactions of the first-order incident and scattered waves. If no structure is present, then the plane wave components of $\tilde{\eta}^o_{21}$ may be algebraically reduced to the form

$$\tilde{\eta}^o_{21} = \frac{kH}{8\tanh kd} \left[3\tanh^2 kd - 1\right] \cos 2(kx - \sigma t) \tag{4.15}$$

which is presented in Appendix A.6. In a later section, this expression will be combined with the plane wave component from the second-order velocity potential to verify that the series form in Equation 4.14 yields the familiar Stokes second-order plane wave component.

In Figure 4.7, an example of the wave envelope due to the second-order quadratic terms is given for the same wave conditions used to illustrate the second-order mean water levels in Figure 4.5. General features of the second-order oscillatory quadratic water levels are

1. On the upwave side, the wave envelope for the oscillatory quadratic components is similar in form to the envelope of the first-order terms. One component of the quadratic wave envelope is the usual second-order plane wave, given in Equation 4.15. The remaining nonlinear interactions of the first-order incident and scattered waves produce a second-order partial standing wave system with antinodes and nodes located at the same spatial positions as those of the first-order partial standing wave system.

2. On the down-wave side, the second-order quadratic envelope is similar to the first-order envelope, and represents a near-plane wave at wavenumber $2k$ with no spatial modulation. The amplitude in this region is almost identical to that obtained from two-dimensional Stokes theory; nonlinearity associated with the first-order scattered wave is usually small in this region.

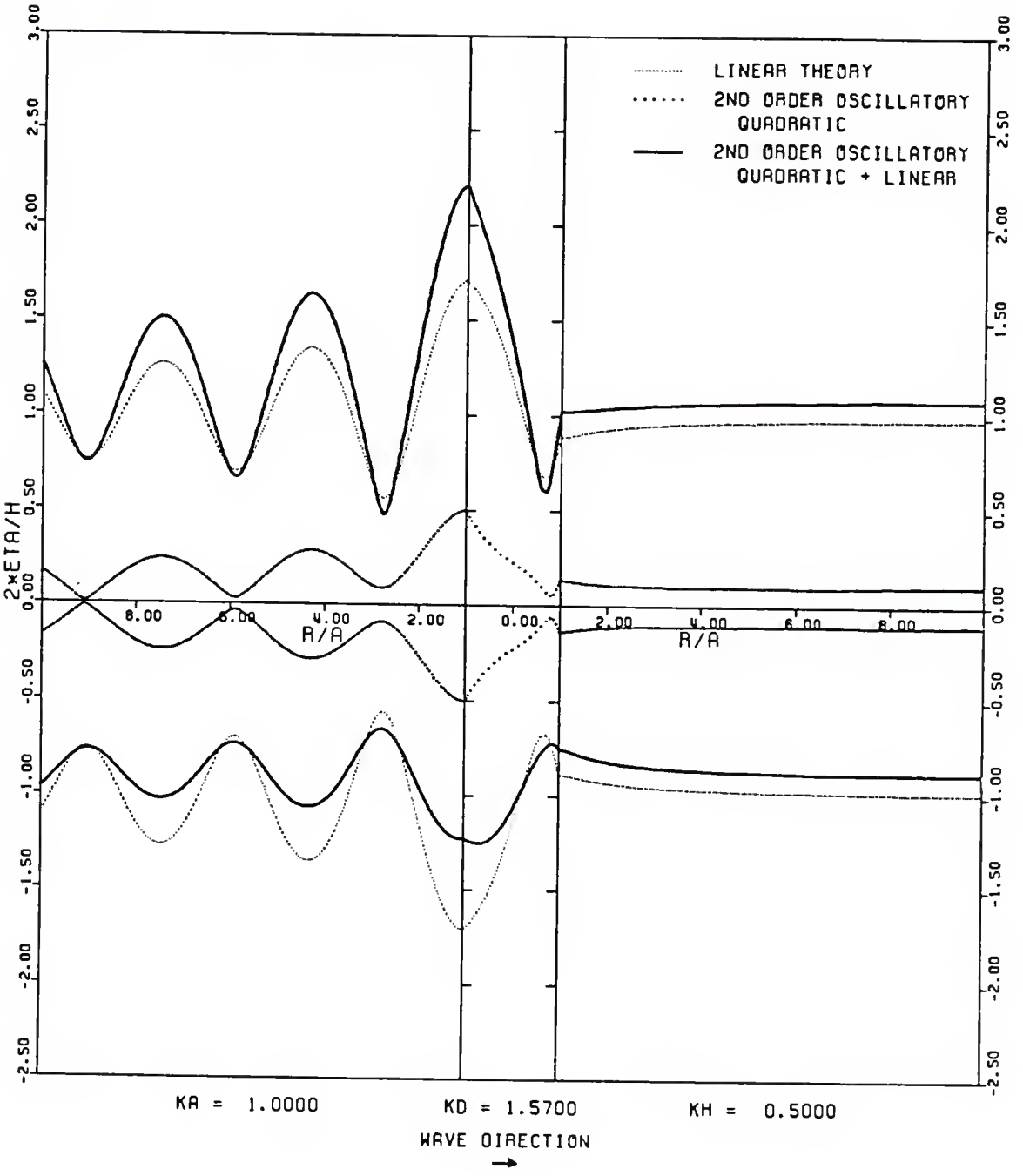

Figure 4.7: Envelope of second-order oscillatory quadratic components, $ka = 1.0$, $kd = 1.57$, and $kH = 0.5$

3. On the sides of the cylinder, a smooth transition occurs from maximum amplitude at the front, to minimum amplitude aft of the shoulder, to a secondary maximum at the rear. The node of the second-order envelope is in the same position as the node in the linear envelope.

When the oscillatory quadratic terms are added to the first-order solution, also shown in Figure 4.7, it is evident they are locked in phase relative to the first-order waves. Since the second-order terms oscillate at twice the frequency, they contribute to increase the wave crest amplitudes compared to first-order while they decrease the wave trough amplitudes. These effects are analogous to the phase-locked effects of the second-order plane wave components from the usual Stokes plane wave theory. Quadratic free surface terms tend to substantially increase wave runup and crest elevations compared to first-order.

4.4 Free Surface from Second-Order Velocity Potential

The second-order free surface components from the second-order velocity potential, Φ_2, are given in Equation 4.4 as

$$\eta_{22} = -\frac{1}{g}\Phi_{2t} \qquad \text{on } z = 0 \tag{4.16}$$

Evaluating the derivative and normalizing by the first-order wave amplitude, the nondimensional form of η_{22} is

$$\tilde{\eta}_{22} = \frac{2\eta_{22}}{H} = 2i\tilde{\Phi}_2 \qquad \text{on } z = 0 \tag{4.17}$$

From Equation 4.17 and from the equation for $\tilde{\phi}_2$ given as Equation 3.80 in Chapter 3, the nondimensional free surface from the second-order velocity potential is

$$\begin{aligned}
\tilde{\eta}_{22} = {} & kH\frac{e^{-i2\sigma t}}{2}\sum_{n=0}^{\infty}\cos n\theta \\
& \cdot \left[\left\{\frac{3}{2}\frac{k(\tanh^2 kd - 1)}{(2k\tanh 2kd - k_2\tanh k_2 d)}\beta_n J_n(2kr)\right.\right. \\
& -12\frac{k^2(\tanh^2 kd - 1)}{(4k^2 - k_2^2)}\frac{\cosh^2 k_2 d}{(\sinh 2k_2 d + 2k_2 d)}\beta_n\frac{J_n'(2ka)}{H_n'(k_2 a)}H_n(k_2 r) \\
& \left.\left.-12\sum_{j=1}\frac{k^2(\tanh^2 kd - 1)}{(4k^2 + \kappa_{2j}^2)}\frac{\cos^2 \kappa_{2j} d}{(\sin 2\kappa_{2j} d + 2\kappa_{2j} d)}\beta_n\frac{J_n'(2ka)}{K_n'(\kappa_{2j} a)}K_n(\kappa_{2j} r)\right\}\right.
\end{aligned}$$

$$
\begin{aligned}
+ \quad & \left\{ \frac{1}{2} PV \int_0^\infty \frac{\kappa \tilde{D}_n(\kappa) J_n(\kappa r)}{k(\kappa \tanh \kappa d - k_2 \tanh k_2 d)} d\kappa \right. \\
& -2 \frac{\cosh^2 k_2 d}{(\sinh 2k_2 d + 2k_2 d)} \frac{H_n(k_2 r)}{k H_n'(k_2 a)} PV \int_0^\infty \frac{\kappa^2 \tilde{D}_n(\kappa) J_n'(\kappa a)}{(\kappa^2 - k_2^2)} d\kappa \\
& -2 \sum_{j=1} \frac{\cos^2 \kappa_{2j} d}{(\sin 2\kappa_{2j} d + 2\kappa_{2j} d)} \frac{K_n(\kappa_{2j} r)}{k K_n'(\kappa_{2j} a)} \int_0^\infty \frac{\kappa^2 \tilde{D}_n(\kappa) J_n'(\kappa a)}{(\kappa^2 + \kappa_{2j}^2)} d\kappa \\
+ \quad & \left. i\pi \frac{k_2}{k} \frac{\cosh^2 k_2 d}{(\sinh 2k_2 d + 2k_2 d)} \tilde{D}_n(k_2) \left(J_n(k_2 r) - \frac{J_n'(k_2 a)}{H_n'(k_2 a)} H_n(k_2 r) \right) \right\} \Bigg] \\
+ \quad & c.c.
\end{aligned}
\tag{4.18}
$$

The terms in the first bracket on the right-hand side in Equation 4.18 represent the contribution from the incident Stokes second-order plane wave as well as its associated scattered wave components. If no structure were present, the only non-zero term in Equation 4.18 would be the leading term in the first bracket

$$
\tilde{\eta}_{22} = \Re \left[kH \frac{3}{2} \frac{k(\tanh^2 kd - 1)}{(2k \tanh 2kd - k_2 \tanh k_2 d)} \sum_{n=0}^{\infty} \beta_n J_n(2kr) \cos n\theta e^{-i2\sigma t} \right] \tag{4.19}
$$

which may also be written as

$$
\tilde{\eta}_{22} = kH \frac{3}{4} \frac{(\tanh^2 kd - 1)}{(\tanh 2kd - 2 \tanh kd)} \cos 2(kx - \sigma t) \tag{4.20}
$$

Combining Equation 4.20, the plane-wave term from the second-order velocity potential, with Equation 4.15, the plane-wave quadratic component $\tilde{\eta}_{21}^o$, yields

$$
\tilde{\eta}_2 = \frac{kH}{8} \frac{\cosh kd(2 + \cosh 2kd)}{\sinh^3 kd} \cos 2(kx - \sigma t) \tag{4.21}
$$

which is verified to be the usual Stokes second-order plane wave component at wavenumber $2k$, e.g. Dean and Dalrymple (1984, p. 303). This plane wave term is always phase-locked to the first-order incident wave, while its associated scattered components, especially the outwardly scattered free wave at wavenumber k_2, are shifted in phase with a phase shift that depends on the relative cylinder radius.

The terms in the second bracket represent the remaining forced-radiated wave motions and their associated scattered waves. These terms are all related to the presence of the first-order scattered wave and may be traced to both f^{is} and f^{ss} forcing in the second-order CFSBC. It should be remembered that all of these terms yield local standing wave

motion in the vicinity of the free surface quadratic forcing, but far away, give an outwardly propagating wave motion with wavenumber k_2. All terms, the forced-radiated motions and the scattered motions, become more important as the cylinder size increases.

In Figure 4.8, the wave envelope from the second-order velocity potential is depicted for the reference wave conditions $ka = 1.0$, $kd = 1.57$ and $kH = 0.5$. General features of the free surface components from the second-order velocity potential are as follows

1. Along $\theta = \pi$, the free surface contribution from the second-order velocity potential appears as a complicated partial standing wave system with generally decreasing amplitude as r increases. The asymptotic behavior of these terms is a combination of the uniform amplitude incident plane wave component, a standing long wave, and outwardly propagating free waves.

2. Along $\theta = 0$, the direct quadratic forcing applied to the free surface is small; however, a substantial outwardly propagating wave field is predicted. This is a manifestation of diffraction effects in which waves are generated by the strong forcing along $\theta = \pi$ but then propagate around the cylinder into the shadow region. Since the waves that propagate outward from the region of large quadratic forcing are second-order free waves, the dominant wavenumber in the diffraction-dominated region is k_2.

3. Around the cylinder, the wave amplitudes from the second-order velocity potential are more complicated. One feature of the second-order velocity potential is that large wave amplitudes occur along the shoulders of the cylinder, at the location of the node in the first-order envelope. The quadratic forcing on the free surface is large in this area due to the convective accelerations from the first-order flow field, and this acts as a generating mechanism for second-order waves.

The free surface terms from the second-order potential are added to the first-order terms in Figure 4.8 to investigate the phasing relationship. Except for the incident plane wave term, the remaining components of the second-order velocity potential are mostly

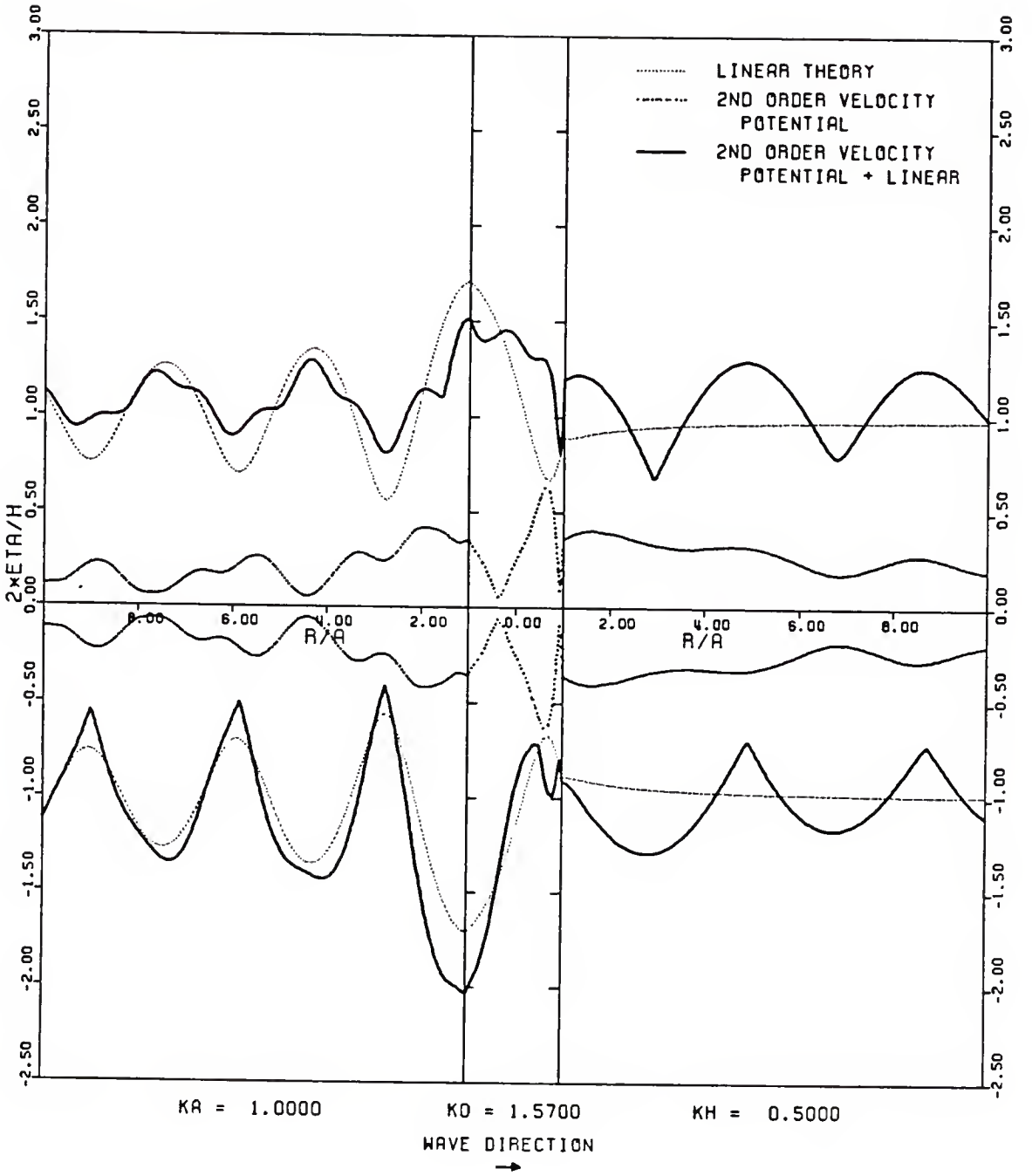

Figure 4.8: Envelope from second-order velocity potential and effect of second-order potential on free surface, $ka = 1.0$, $kd = 1.57$, and $kH = 0.5$

out-of-phase with the first-order solution. Along $\theta = \pi$, the second-order terms are strongly out-of-phase near the cylinder such that the trough amplitudes are accentuated while the crest amplitudes are reduced. Comparing Figures 4.7 and 4.8, it is found that the oscillatory quadratic terms and the components from the second-order potential are generally out of phase near the cylinder and will partially cancel each other. As a general conclusion, the second-order velocity potential is not exactly out-of-phase with the quadratic second-order terms or the linear solution; but it seems to always act to reduce the overall second-order effects.

On the down-wave side, the combination of free surface terms from the second-order potential and the terms from the first-order potential leads to a substantial change in the form of the free surface envelope, unlike the effects of the oscillatory quadratic terms. The wave envelope in this region is characteristic of a wave system in which a free second harmonic, with wavenumber k_2 and frequency 2σ, is added to a first-order wave, with wavenumber k and frequency σ, and its bound second harmonic at wavenumber $2k$ and frequency 2σ, e.g. Buhr Hansen and Svendsen (1974).

4.5 Free Surface Complete to Second-Order

The complete theoretical solution for the free surface, consistent to the second perturbation order, is obtained by superimposing the following components

1. The first-order solution, $\tilde{\eta}_1$, given in Equation 4.7.

2. The second-order quadratic mean water levels, $\tilde{\eta}^s_{21}$, given in Equation 4.12.

3. The second-order oscillatory quadratic terms, $\tilde{\eta}^o_{21}$, given in Equation 4.14.

4. The terms from the second-order velocity potential, $\tilde{\eta}_{22}$, given in Equation 4.18.

For the reference conditions, $ka = 1.0$, $kd = 1.57$, and $kH = 0.5$, the cross-section of the total wave envelope to second-order is given in Figure 4.9. General features of the complete solution are as follows

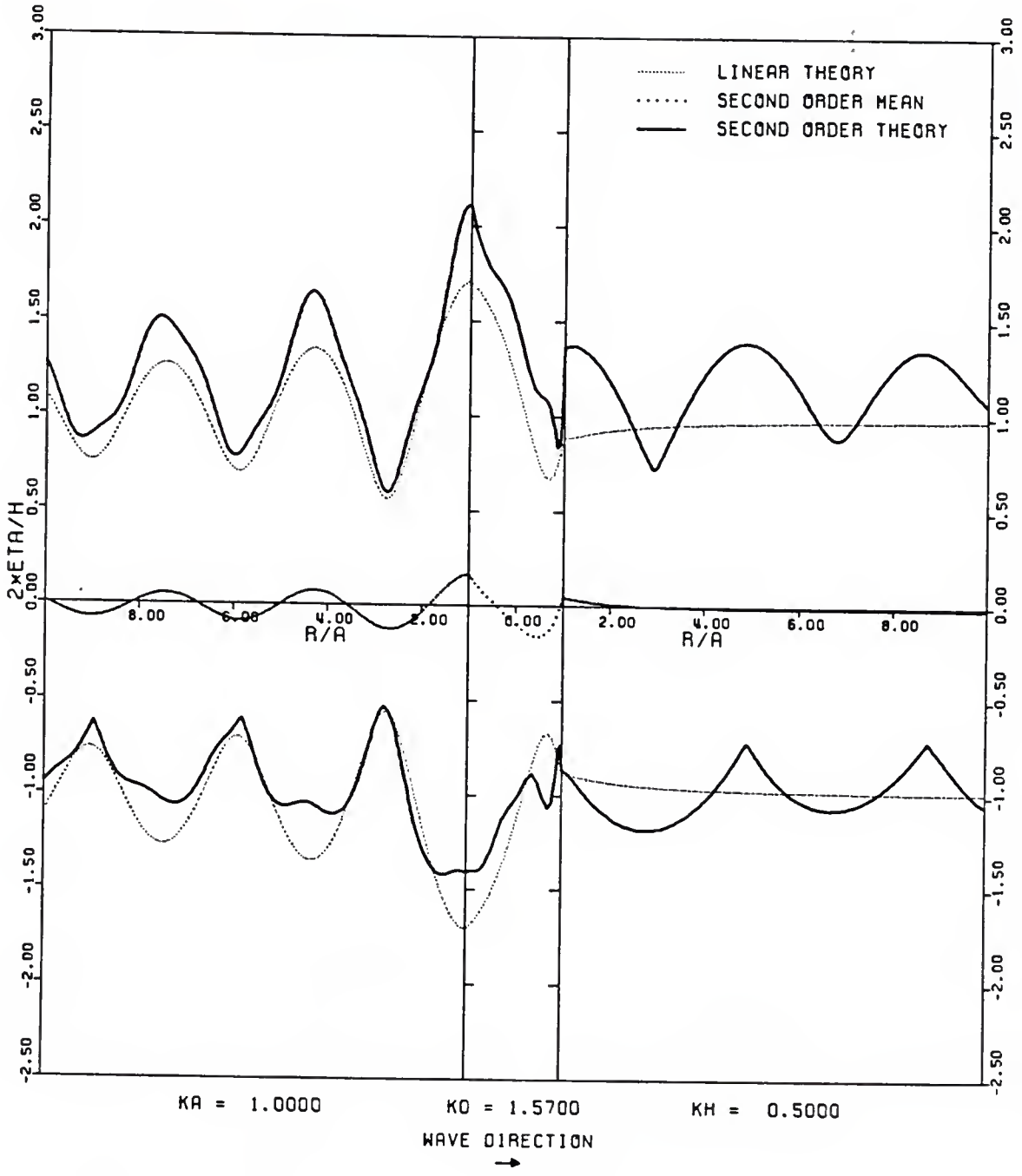

Figure 4.9: Total wave envelope to second-order for reference case $ka = 1.0$, $kd = 1.57$, and $kH = 0.5$

1. All second-order oscillatory terms are complex quantities such that phase shifts exist between the various components. The plane wave terms are phase-locked to the first-order wave, while the quadratic terms also generally in phase, especially near the cylinder. The forced-radiated waves and their scattered components, in the second-order potential, are generally out-of-phase with the first-order solution. As a result, partial cancellation occurs to reduce the net second-order contribution to the total wave envelope.

2. Along $\theta = \pi$, the partial standing wave system at first-order is largely preserved; however, wave crest amplitudes are increased and trough amplitudes are decreased. For smaller values of ka, additional nodes and antinodes associated with the second-order velocity potential components may be introduced (see Appendix E). The maximum wave runup at the cylinder is increased substantially, and in this example the maximum crest amplitude also exceeds twice that of the linear crest amplitude; this is partly due to the increased incident crest heights at second-order and partly due to the nonlinear reflection process. Maximum wave rundown on the cylinder is reduced relative to the linear theory and, in general, trough amplitudes become more uniform everywhere.

3. Along $\theta = 0$, the second-order terms alter the diffraction pattern significantly to produce a modulated wave envelope, unlike that obtained from linear theory. Again, crest amplitudes are generally increased while trough amplitudes are decreased. For larger values of ka, like the example shown, the envelope will be modulated due to significant diffracted and scattered second-order free waves. For smaller cylinder sizes, the scattered and diffracted terms are small. Plane wave and oscillatory quadratic terms dominate at second-order such that the resulting envelope will not be strongly modulated, although crest elevations will still be increased. The maximum runup at the rear of the cylinder is increased due to second-order diffraction. Maximum wave rundown may be greater or less than that at first-order.

4. Around the circumference of the cylinder, the wave runup profile is generally increased relative to the linear solution, except that for small cylinders, runup is often less than that predicted by linear theory in the region between 30 and 60 degrees. Runup maxima at both the front and back of the cylinder are much greater than the linear maxima, a feature that is in qualitative agreement with laboratory data. Wave rundown is more complicated and rundown amplitudes are generally smaller than those predicted by linear theory, except at the position of the first-order node. Much of the departure from linear theory at this point seems to be due to the second-order mean water levels which, according to potential flow theory, experience their largest setdown in this region.

In Figure 4.10, the total wave crest envelope to second-order is shown in planform for the example case; and, by comparing Figure 4.10 to Figure 4.4, differences in the first and second-order theories may be identified. As second-order waves radiate and scatter away from the cylinder, the interaction of second-order crests with the first-order crests occurs at different distances from the cylinder at each angular position. This leads to more localized and isolated maxima and mimima; this is more dramatic for somewhat smaller cylinder sizes as observed in Appendix E. The most striking diffrences between linear and nonlinear theories is in the diffraction pattern at the rear of the cylinder. While linear theory contained only a broad region with nearly uniform amplitude in the downwave region, second-order theory predicts distinct and localized maxima and minima due to nonlinear diffraction, with locations where the crest amplitudes are nearly 50 percent smaller and 50 percent larger than the incident wave amplitude.

As a more detailed illustration of the theoretical second-order effects, Figures 4.11 through 4.12 present an oblique view of the wave field for two wave phases before and at the phase of maximum runup. In Figure 4.11, the cylinder is in the wave trough and a wave crest is approaching from the left while a previous wave crest moves away from the cylinder to the right. The incident crest is distorted by scattered waves such that its height is not

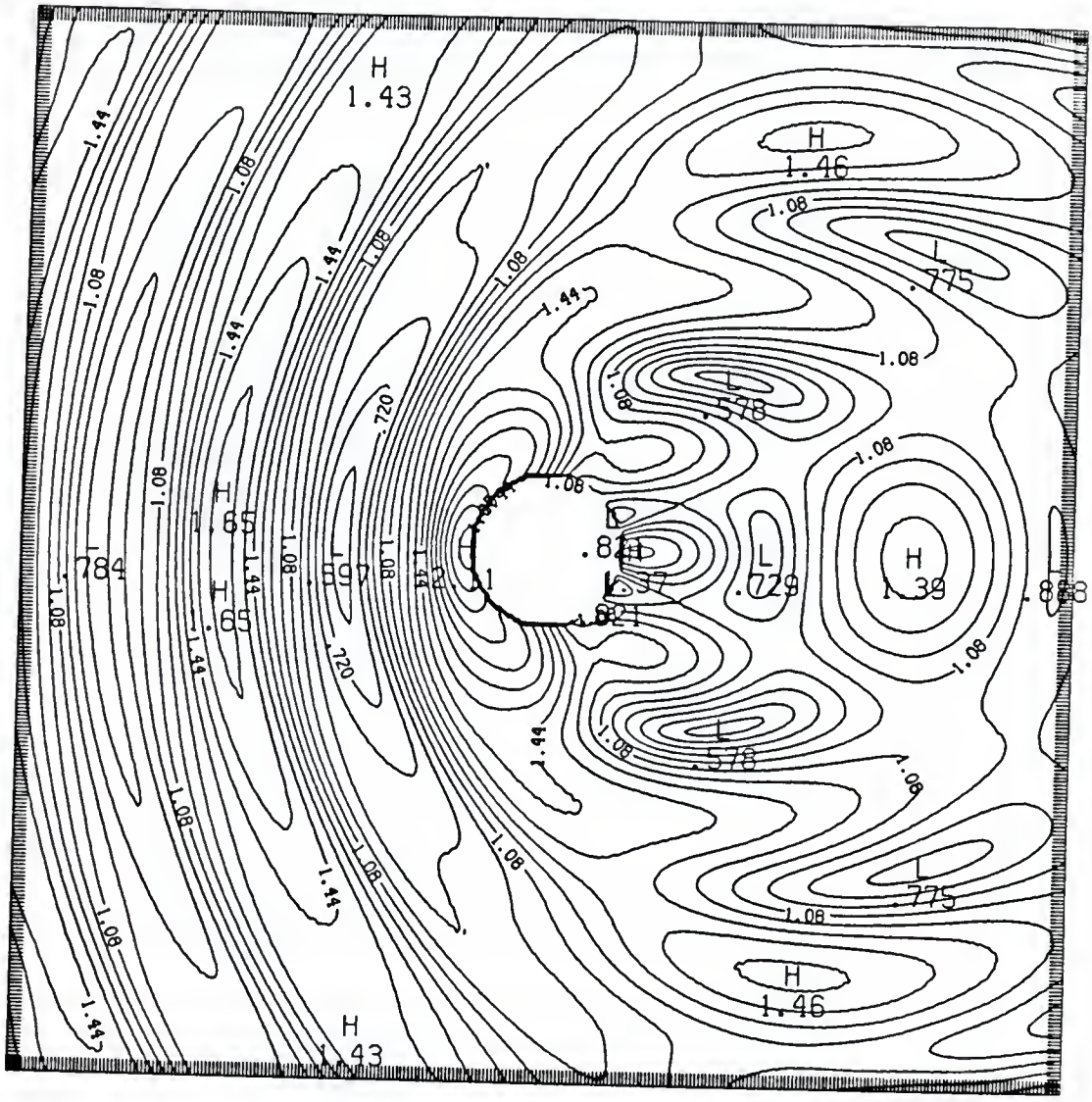

Figure 4.10: Contours of total wave crest amplitude to second-order for reference case $ka = 1.0$, $kd = 1.57$, and $kH = 0.5$

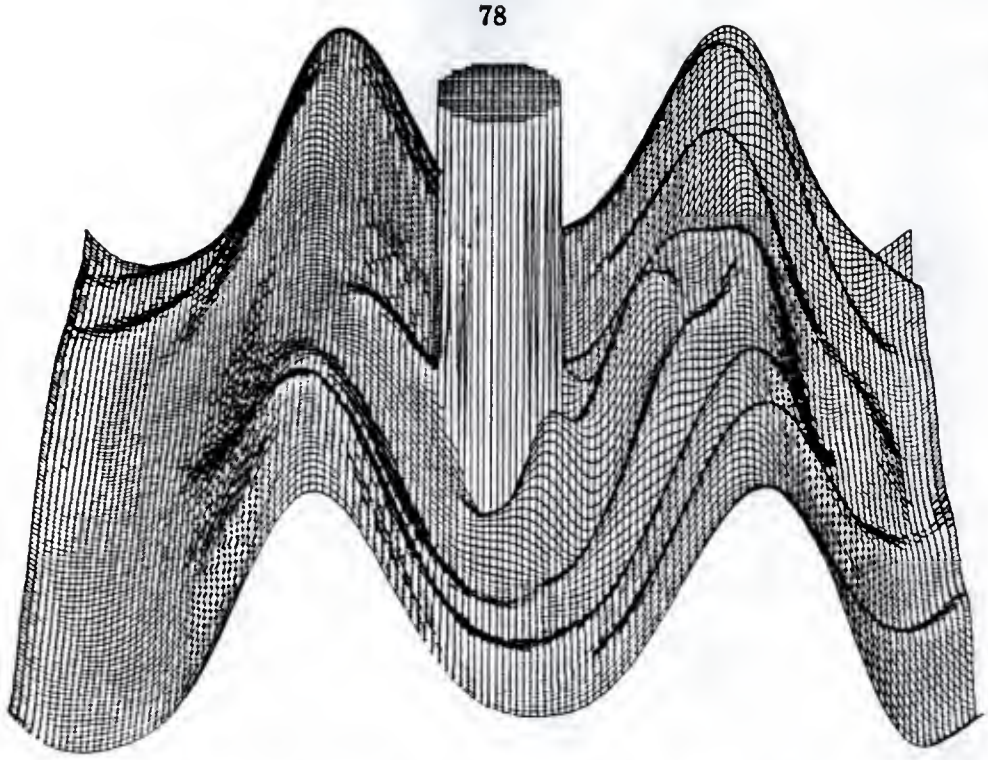

Figure 4.11: Oblique view of wave field near cylinder to second- order, phase of maximum runup$-\pi/2$, for reference case $ka = 1.0$, $kd = 1.57$, and $kH = 0.57$

uniform along the crest but is lower along the $\theta = \pi$ axis as it passes into a node of the wave envelope. The wave form is asymmetrical as the face of this wave in the direction of propagation is steepened while the back side of the wave is elongated by the superposition of the scattered waves. The previous crest is also highly distorted, with significant amplitude variation along the crest due to the second-order scattered and diffracted waves. This crest is no longer straight but is bowed behind the cylinder due to diffraction of the wave crests from each side.

In Figure 4.12, the wave crest is at the phase of maximum wave runup. The crest runup is highly localized on the front of the cylinder. Water surface slopes along the shoulders of the cylinder are near their maximum and, the solution shows that water particles near the cylinder moves faster than those in the wave crest farther away. For very steep incident waves, localized breaking is often observed at or near this phase position. Second-order free waves are evident in both figures moving away from the cylinder. These are not too pronounced on the upwave side as second-order motion is dominated by long standing waves

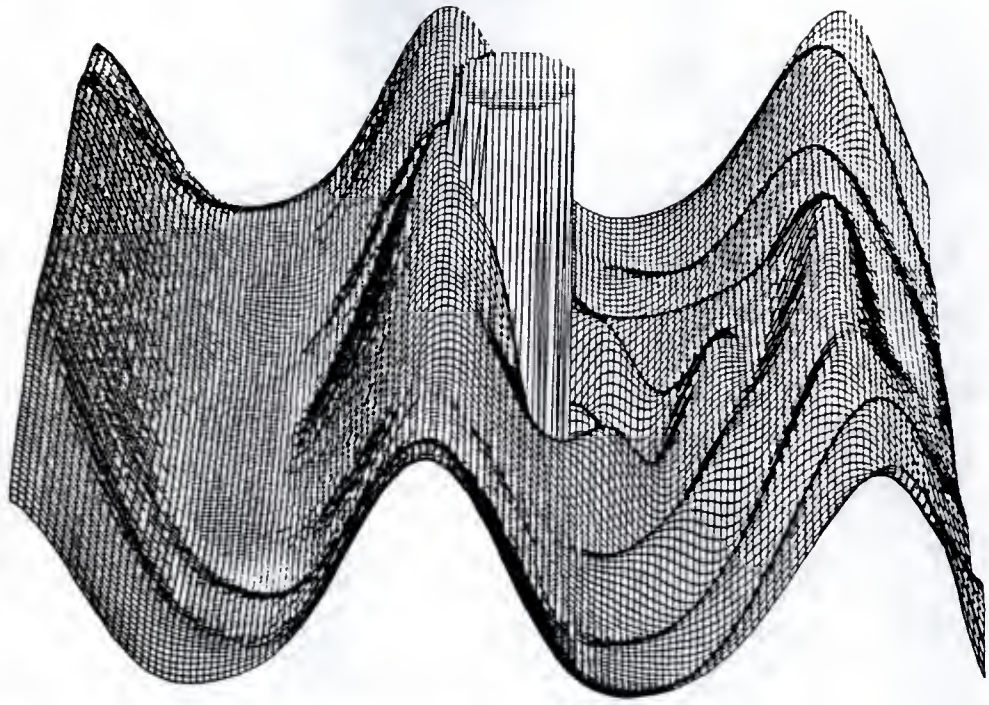

Figure 4.12: Oblique view of wave field near cylinder to second- order, phase of maximum runup, for reference case $ka = 1.0$, $kd = 1.57$, and $kH = 0.5$

for large cylinders. In the downwave direction, the radiated-scattered free waves are quite significant; it is also evident that their phase speeds are much slower than linear wave. For smaller relative depths, the phase speed of these waves approches the linear phase speed as the free wavenumber, k_2, approaches $2k$.

4.6 Summary of Nonlinear free surface

The reference case cited above serves as a useful example of the principal features of the second-order solution; however, the second-order free surface is dependent on the relative magnitudes and phases of several independent components, which vary with the cylinder size, ka, and the relative depth, kd. In Figures 4.13 through 4.16, examples are given for the free surface envelopes for the following additional cases (1) large cylinder, intermediate depth, in Figure 4.13, (2) small cylinder, intermediate depth, in Figure 4.14, (3) deep water, moderate cylinder size, in Figure 4.15, and (4) near-shallow water, moderate cylinder size, in Figure 4.16.

Varying the pile radius, ka, for a given water depth and wave steepness has a great effect on the second-order solution. In Figure 4.13, large cylinders are associated with more pronounced scattered wave components at first-order and; therefore, larger nonlinear quadratic pressure terms in the CFSBC and the Bernoulli equation on the upwave side. This is manifested in (1) larger spatially varying mean water levels (2) larger quadratic corrections to the free surface due to increased convective fluid accelerations, and (3) larger contributions from the second-order velocity potential. Due to the sheltering effects of large cylinders, the wave amplitudes on the rear of the cylinder also vary greatly with ka; for ka greater than about 0.8, wave amplitudes decrease in the downwave region.

In Figure 4.14, small cylinders do not disturb the linear wave field significantly and the resulting wave envelope has little modulation anywhere. The wave crest elevations are nearly uniformly increased in the front and rear; however, the wave crests are locally disturbed at the cylinder, leading to second-order runup elevations that are larger than would be expected simply from the increased nonlinear incident crest height. Plane wave terms in the solution are not effected by the cylinder size. However, as these plane waves reflect from the cylinder, their resulting scattered components introduce additional modulations in the wave envelope. These scattered effects are most readily observed for small cylinders where the other forced-radiated motions are not as large.

The behavior of the nonlinear theory from deep to shallow water is depicted in Figures 4.15 and 4.16. Plane wave terms, found in Equation 4.15 and in the first terms on the right-hand-side of the second-order velocity potential in Equation 4.18, increase rapidly from deep to shallow water. The remaining second-order terms tend to be of comparable magnitude in deep or shallow water; the cylinder size has more of an effect on these than does the depth. It is noted that since the plane wave terms become singular due to resonant free surface forcing, the entire second-order theory is limited in shallow water by exactly the same conditions that limit the usual two-dimensional Stokes theory at second-order.

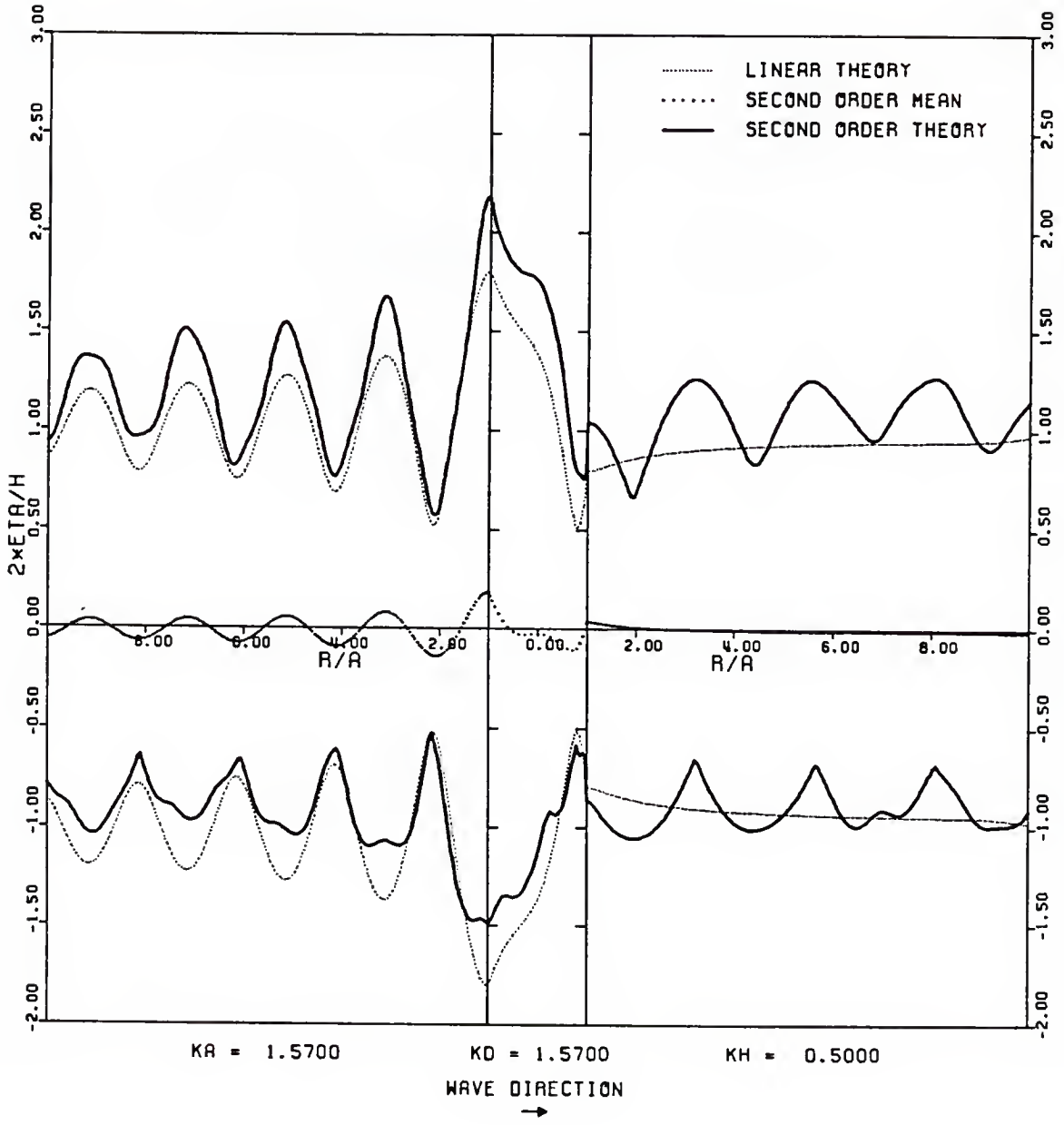

Figure 4.13: Example of second-order wave envelope for large cylinder, $ka = 1.57$, $kd = 1.57$, $kH = 0.5$

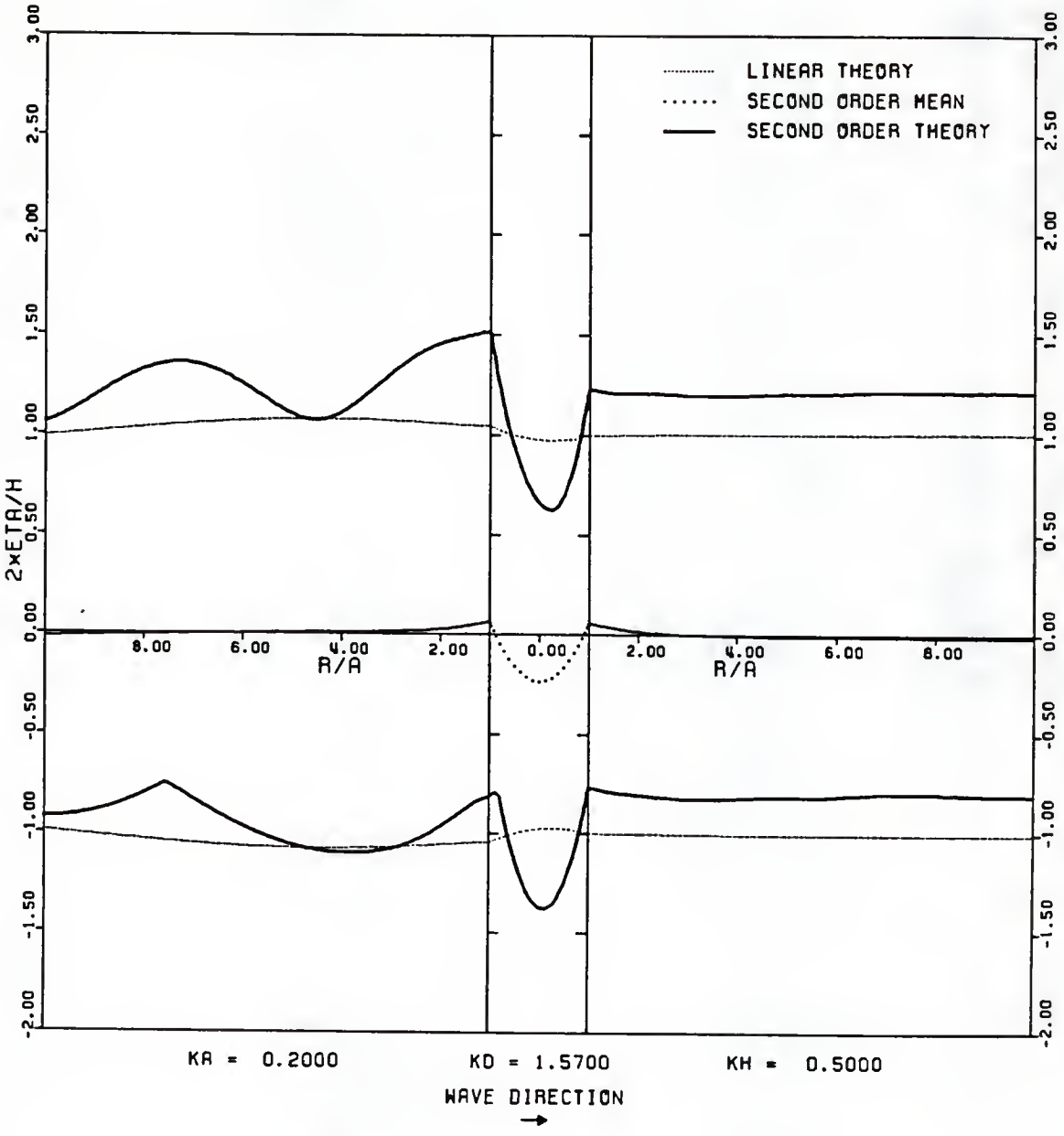

Figure 4.14: Example of second-order wave envelope for small cylinder, $ka = 0.2$, $kd = 1.57$, $kH = 0.5$

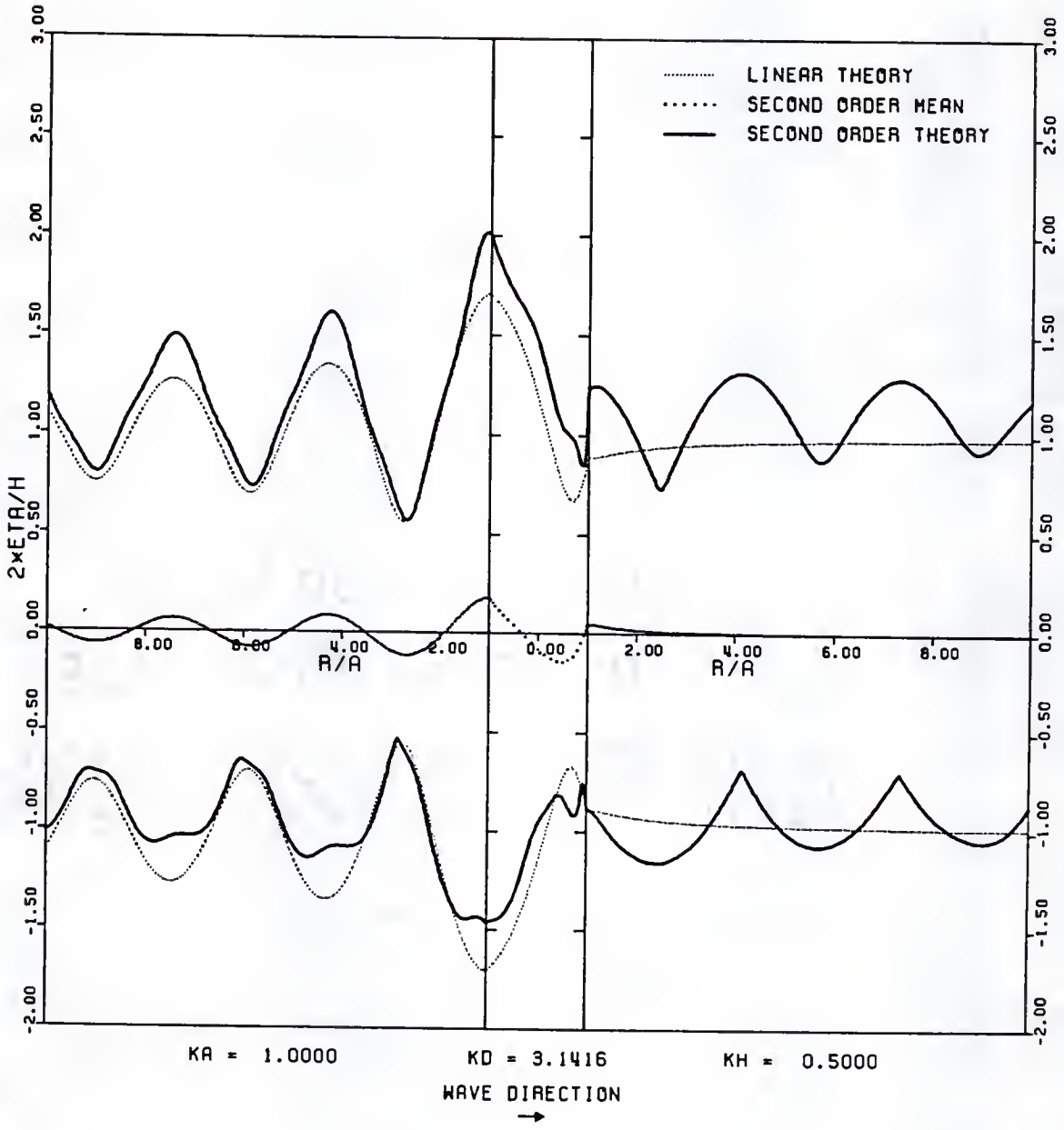

Figure 4.15: Example of second-order wave envelope for deep water, $ka = 1.0$, $kd = 3.14$, $kH = 0.5$

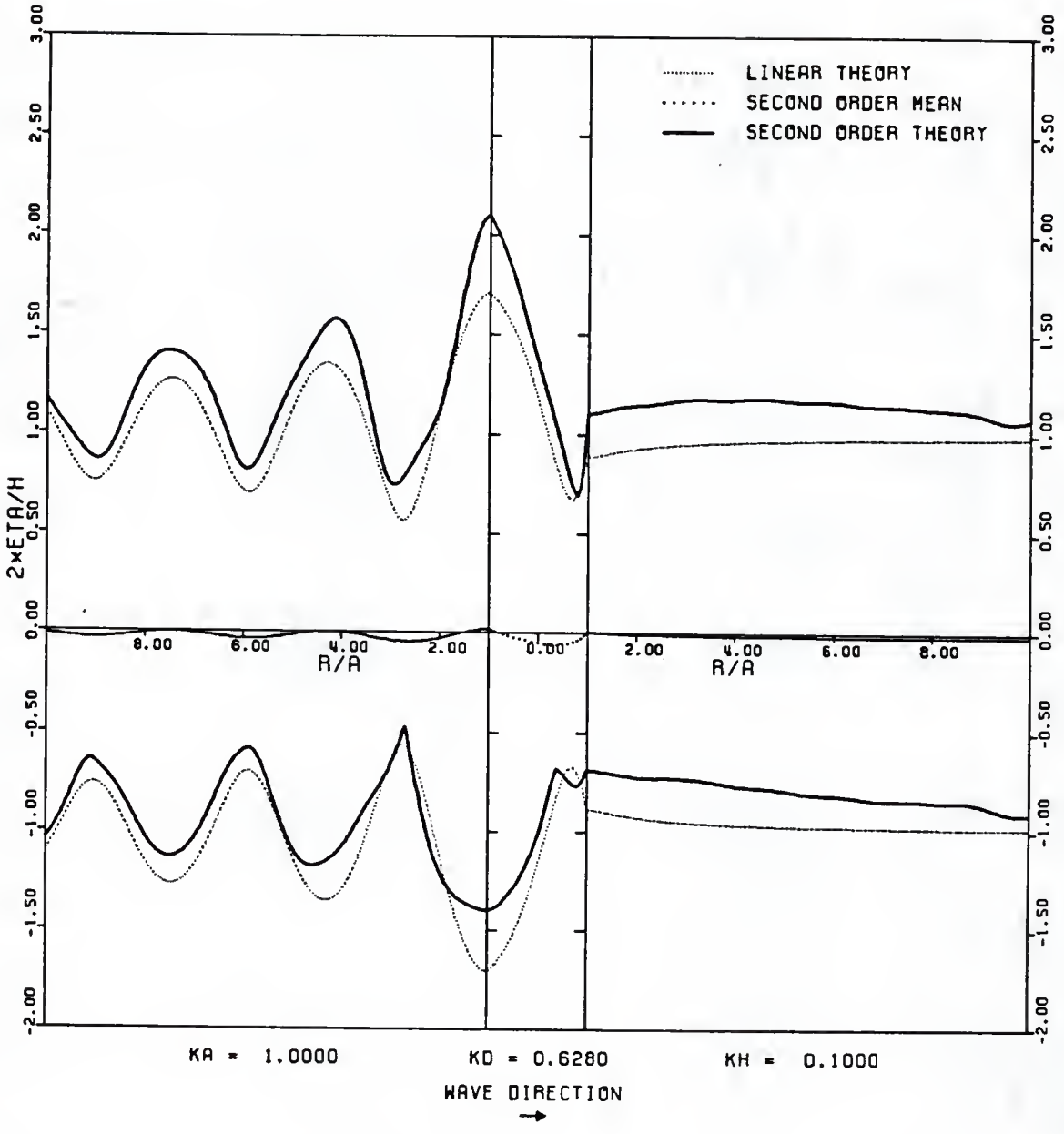

Figure 4.16: Example of second-order wave envelope for near-shallow water, $ka = 1.0$, $kd = 0.628$, $kH = 0.1$

Another effect of depth is that for a given ka, based on the first-order wavelength, the second-order free wavenumber in deep water may be up to twice the shallow water free wavenumber. Therefore, the pile "appears" to be twice as large relative to the second-order free waves in deep water; hence, second-order scattering and diffraction may be more effected in deep water. The spatial variation of the wave envelope in the diffraction region is also effected as the second order free wavenumber changes from $4k$ to $2k$ from deep to shallow water. In deep water the envelopes exhibit many maxima and minima, while in near-shallow water, when the phase speed of the second-order free waves is equal to that of the linear wave, the envelopes have little or no modulation.

A useful application of the solution for the nonlinear free surface is a determination of the maximum wave crest elevations at the front of the cylinder. In Figures 4.17 and 4.18, the linear and nonlinear maximum runup amplitudes at $\theta = \pi$ are presented in two ways for a fixed depth-to-radius ratio, $d/a = 2.77$, which corresponds to the laboratory conditions used in the experimental phase of this study. In Figure 4.17, the maximum runup amplitudes are presented as a function of the diffraction parameter, ka, for various wave steepnesses for which the second-order theory may be valid. For smaller relative depths, the Stokes second-order theory is limited by the convergence of the power series expansion. In Figure 4.17, the limiting steepness at a given relative depth is labelled the "Limit of Stokes Theory" and corresponds to a steepness at which the amplitude of the second-order plane wave term is equal to one-quarter of the linear wave amplitude. Below and to the right of this curve, a Stokes wave has a smooth trough, while above and to the left, the trough develops a secondary crest as the theory becomes invalid.

For smaller cylinders (and smaller relative depths in this format), the nonlinear runup is increased substantially over the linear runup. In this region, the plane wave and its scattered components dominate the runup distribution; however, other contributions from the forced-radiated waves and the quadratic terms are also measurably important and contribute from 10 to 40 percent of the second-order runup amplitude. As ka increases, the forced and

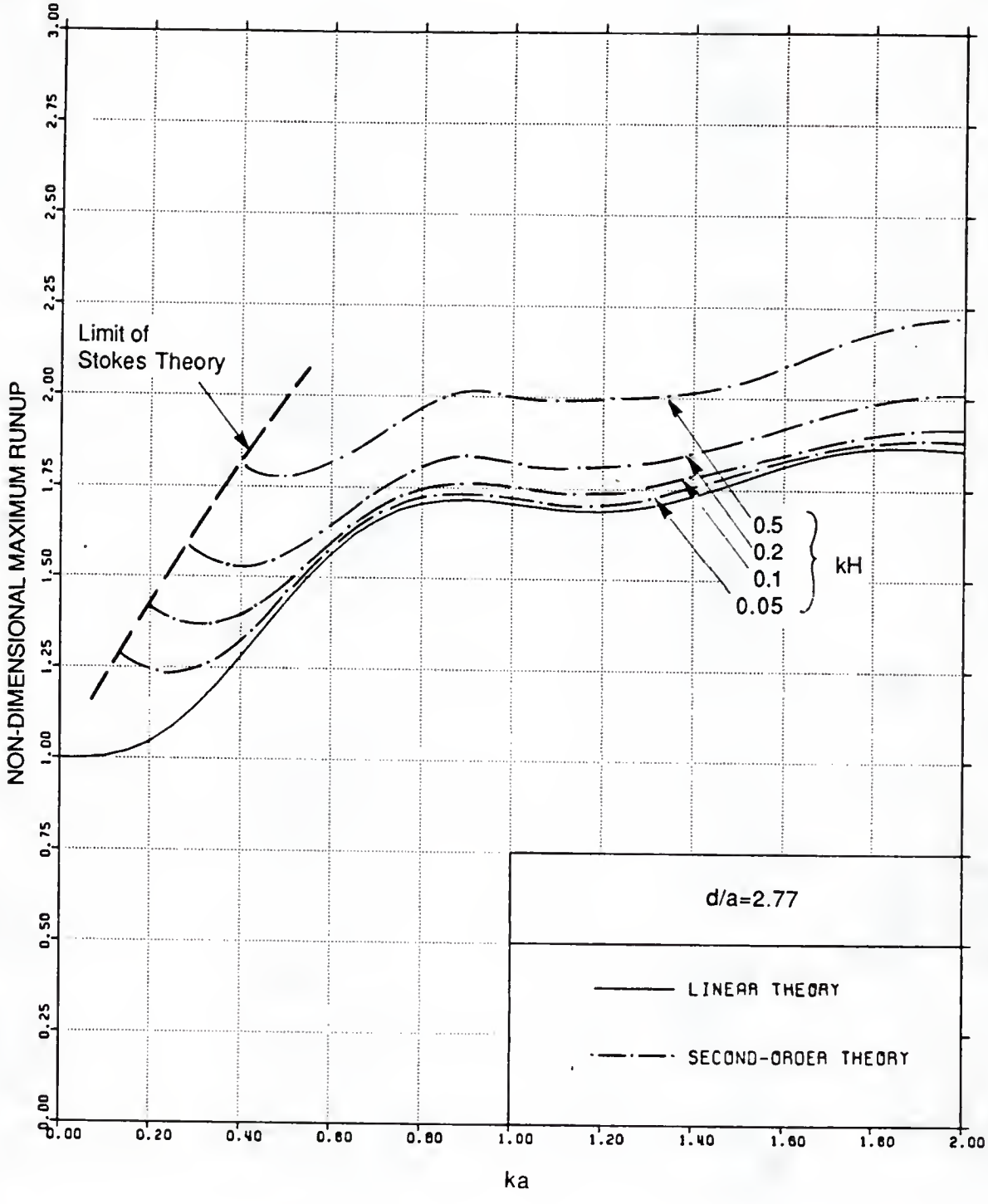

Figure 4.17: Comparison of first and second-order wave runup at $\theta = \pi$ as a function of the diffraction parameter and wave steepness

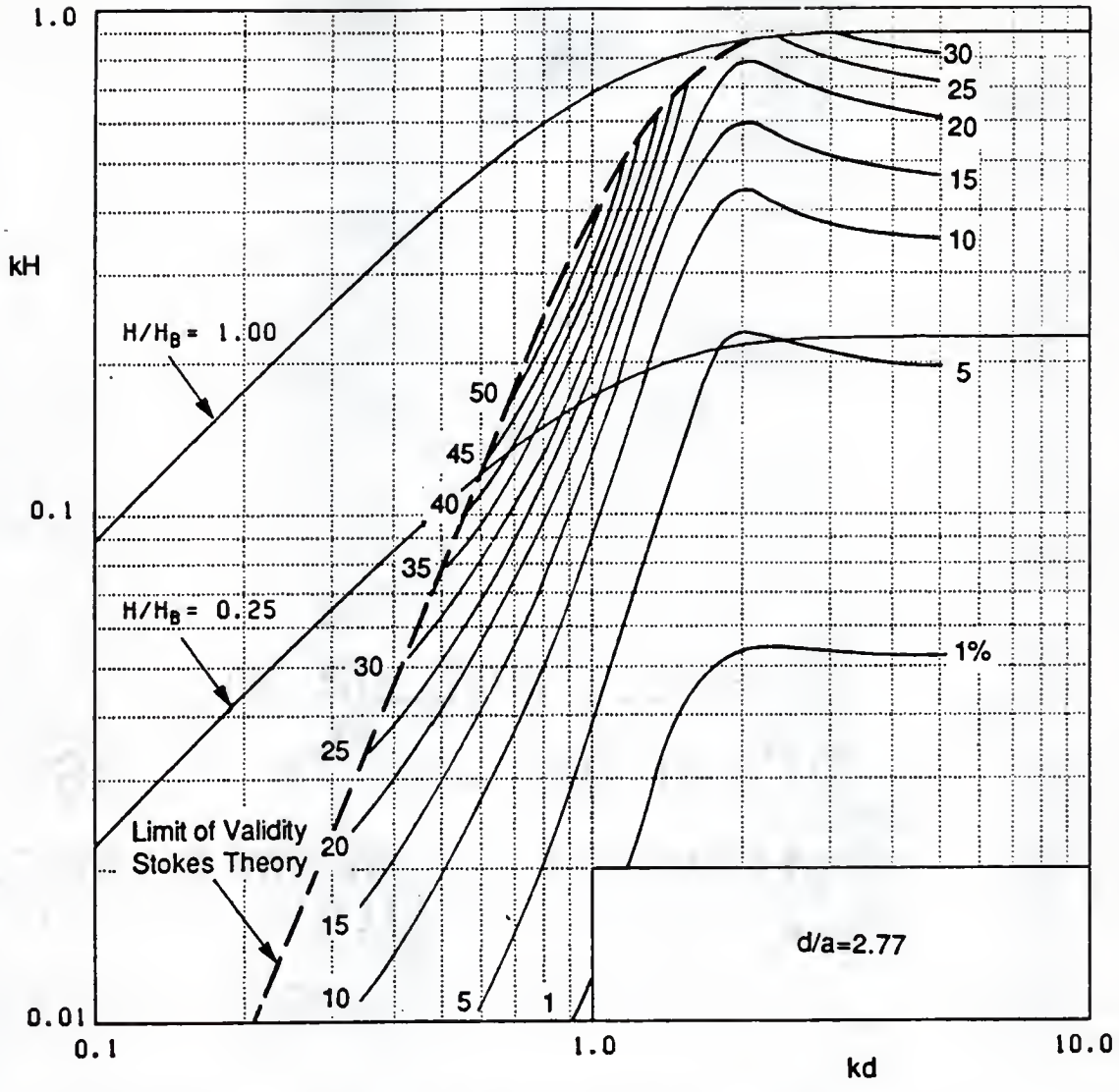

Figure 4.18: Percent difference between second and first order maximum runup

radiated components become more important and reduce the runup, since they are mostly out-of-phase with the other components. As ka continues to increase, the second-order contribution increases only slightly. For a wide range of cylinder sizes and wave steepnesses, maximum runup exceeds twice the incident wave amplitude.

In Figure 4.18, the percent difference between the second and first-order theories is presented. This percentage is defined as

$$\frac{\tilde{R}_2 - \tilde{R}_1}{\tilde{R}_1} \cdot 100\% \tag{4.22}$$

where $\tilde{R}$ is the nondimensional runup for a given order. In this format, the approximate

breaking wave steepness, based on the Miche criterion, i.e. U.S. Army Corps of Engineers (1977)

$$kH_B = \frac{2\pi}{7} \tanh kd \tag{4.23}$$

is included. The upper curve represents this breaking steepness, while the lower curve is at one-quarter of the theoretical breaking steepness. The second-order diffraction theory indicates that maximum runup elevations may exceed those predicted by linear theory by 10 to 50 percent for a wide range of wave and water depth conditions, again for the ratio $d/a = 2.77$. The differences are greatest, as expected, for steep waves, and as waves move into shallow water, where the second-order runup may be 20 to 40 percent larger than the linear theory even for waves of low steepness, i.e. at less than one-quarter of the breaking steepness. The largest differences occur along the limiting steepness for the validity of the Stokes theory. The region near $kd = 2.0$ corresponds to the theoretical conditions where there is significant cancellation of the various second-order components.

CHAPTER 5
WAVE FORCES

5.1 Introduction

The second application of the proposed second-order velocity potential is the determination of depth-integrated wave forces. The forces that are exerted by waves on a large vertical cylinder have traditionally been estimated according to linear diffraction theory. Other numerical design methods have been developed for arbitrary geometries, e.g wave source or integral equation methods and finite element methods; however, these methods have been based on linear wave theories where the effects of quadratic forcing in the nonlinear combined free surface boundary condition have been neglected. A comprehensive review of these methods is given by Sarpkaya and Isaacson (1981, pp. 396-449). Additional solutions have been proposed for second-order forces by Kurata and Ijima (1974) and Herfjord and Nielsen (1986) based the quadratic second-order pressure terms that can be derived from linear theory; these methods neglect the contributions from the second-order velocity potential.

More complete solutions for the forces of nonlinear waves on circular cylinders in the diffraction regime, have followed from the proposed forms of the second-order velocity potential reviewed in Chapter 2. The derivation of second-order forces, given a second-order velocity potential, is fairly straightforward; however, the same inconsistencies noted in the discussion of the proposed solutions for the velocity potential also apply to the proposed solutions for the second-order forces. These usually include (1) failure to satisfy the required free surface boundary conditions, (2) failure to include both free and forced wave motions, and (3) failure to properly satisfy a form of the radiation condition. At present, none of these solution methods has achieved widespread acceptance as a design method.

In potential flow, the total force on a vertical cylinder may by found by integrating the fluid pressure over the immersed surface of the cylinder. For an incident plane wave propagating in the $+x$ direction, the only force component is found to be in the x direction as

$$F(t) = -\int_{-d}^{\eta}\int_{-\pi}^{\pi} P(a,\theta,z,t)a\cos\theta d\theta dz \tag{5.1}$$

where $P(a,\theta,z,t)$ is the fluid pressure on the surface of the cylinder. From the unsteady form of the Bernoulli equation, the pressure at $r = a$ is

$$P(a,\theta,z,t) = -\rho g z - \rho\Phi_t - \frac{1}{2}\rho\left(\nabla\Phi\right)^2 \tag{5.2}$$

Based on the perturbation expansion in Chapter 1, the pressure may also be expressed in powers of ϵ; to the second perturbation order, the fluid pressure is

$$P(a,\theta,z,t) = -\rho g z - \rho\Phi_{1t} - \rho\Phi_{2t} - \frac{1}{2}\rho\left(\nabla\Phi_1\right)^2 \tag{5.3}$$

where ϵ is implied in Φ_1 and Φ_2.

Substitution of Equation 5.3 into Equation 5.1, with the free surface expanded in a Taylor series about $z = 0$, yields the potential flow force to the second perturbation order

$$\begin{aligned} F &= \rho a\int_{-d}^{\eta_1}\int_{-\pi}^{+\pi}(gz+\Phi_{1t})\cos\theta d\theta dz \\ &+ \frac{\rho a}{2}\int_{-d}^{0}\int_{-\pi}^{\pi}\left(\nabla\Phi_1\right)^2\cos\theta d\theta dz \\ &+ \rho a\int_{-d}^{0}\int_{-\pi}^{\pi}\Phi_{2t}\cos\theta d\theta dz \end{aligned} \tag{5.4}$$

Since Φ_{2t} and $\left(\nabla\Phi_1\right)^2$ are already of order ϵ^2, integration is carried out only to $z = 0$, while the hydrostatic and first-order terms are integrated to the first-order free surface. The leading term may be further separated into an integral up to the still water level, $z = 0$, plus an integral of the pressure in the free surface region as

$$\begin{aligned} \rho a\int_{-d}^{\eta_1}\int_{-\pi}^{\pi}(gz+\Phi_{1t})\cos\theta d\theta dz &= \rho a\int_{-d}^{0}\int_{-\pi}^{\pi}\Phi_{1t}\cos\theta d\theta dz \\ &+ \rho a\int_{0}^{\eta_1}\int_{-\pi}^{\pi}(gz+\Phi_{1t})\cos\theta d\theta dz \end{aligned} \tag{5.5}$$

Since Φ_{1t} is not defined above $z = 0$ the second integrand must be expanded about $z = 0$ in a Taylor series as

$$\begin{aligned} gz + \Phi_{1t} &= gz + (\Phi_{1t})_{z=0} + \cdots \\ &= gz - g\eta_1 + \cdots \end{aligned} \tag{5.6}$$

such that the pressure in the free surface region is assumed to be hydrostatic between $z = 0$ and the first-order water surface for the purposes of computing forces to second-order. Carrying out the required integration over $0 \leq z \leq \eta_1$ gives

$$\int_0^{\eta_1} (gz - g\eta_1)\, dz = -\frac{1}{2} g\eta_1^2 \tag{5.7}$$

The depth-integrated wave forces, consistent to second-order, are then given by Equation 5.4, as

$$\begin{aligned} F &= \rho a \int_{-d}^{0} \int_{-\pi}^{\pi} \Phi_{1t} \cos\theta\, d\theta\, dz \\ &- \frac{1}{2} g a \int_{-\pi}^{\pi} \eta_1^2 \cos\theta\, d\theta \\ &+ \frac{\rho a}{2} \int_{-d}^{0} \int_{-\pi}^{\pi} (\nabla\Phi_1)^2 \cos\theta\, d\theta\, dz \\ &+ \rho a \int_{-d}^{0} \int_{-\pi}^{\pi} \Phi_{2t} \cos\theta\, d\theta\, dz \end{aligned} \tag{5.8}$$

The second-order force, like the second-order water surface, is composed of three types of terms (1) the first-order force based on the local accelerations of the first-order flow, (2) second-order forces based on quadratic or product terms from convective acceleration of the first-order flow and from the displacement of the first-order free surface at $r = a$, and (3) second-order forces based on the local acceleration of the second-order flow field.

5.2 First-Order Wave Forces

From Equation 5.8, the first-order contribution to the wave force is given by the integral

$$F_1 = \rho a \int_{-d}^{0} \int_{-\pi}^{\pi} \Phi_{1t}(a, \theta, z, t) \cos\theta\, d\theta\, dz \tag{5.9}$$

The radial dependence of the first-order velocity potential, evaluated at $r = a$ is found to be

$$A_n(ka) = J_n(ka) - \frac{J_n'(ka)}{H_n'(ka)} H_n(ka) = \frac{2i}{\pi ka H_n'(ka)} \tag{5.10}$$

such that at the cylinder boundary

$$\Phi_{1t} = -\frac{gH}{2} \frac{\cosh k(d+z)}{\cosh kd} \sum_{n=0} \beta_n \frac{2i}{\pi ka H_n'(ka)} \cos n\theta \frac{e^{-i\sigma t}}{2} + c.c. \tag{5.11}$$

Substituting Equation 5.11 into Equation 5.9, and carrying out the integrations over depth and over θ gives

$$F_1 = \frac{\rho g a H}{k} \tanh kd \frac{2}{ka H_1'(ka)} \frac{e^{-i\sigma t}}{2} + c.c. \tag{5.12}$$

where, due to the orthogonality of $\cos n\theta \cos\theta$, only the dipole-like term associated with $n = 1$ contributes to the net force.

The nondimensional force may be obtained in several ways depending on the choice of normalizing parameters. As shown by Sarpkaya and Isaacson (1981), if the first-order force is normalized as

$$\tilde{F}_1 = \frac{F_1}{\rho g a H d(\tanh kd/kd)} \tag{5.13}$$

then the nondimensional linear force amplitude is a function of ka only

$$\tilde{F}_1 = \frac{2}{ka H_1'(ka)} \frac{e^{-i\sigma t}}{2} + c.c. \tag{5.14}$$

The first-order force has equal positive (in the direction of wave propagation) and negative amplitudes and, when time-averaged, has a zero mean. The variation of the nondimensional first-order force amplitude with ka is shown in Figure 5.1.

A useful interpretation of the linear force is obtained by considering the inertial force for a linear plane wave, obtained by evaluating the linear dynamic pressure due to the local fluid acceleration at the center of the cylinder as

$$\begin{aligned} F_I &= C_m \rho \pi a^2 \int_{-d}^{0} \left(\Phi_{1xt}^i\right)_{x=0} dz \\ &= -C_m \frac{1}{2} \rho g \pi a^2 H \tanh kd \sin \sigma t \end{aligned} \tag{5.15}$$

In nondimensional form using the normalizing parameter used in Equation 5.13 this is

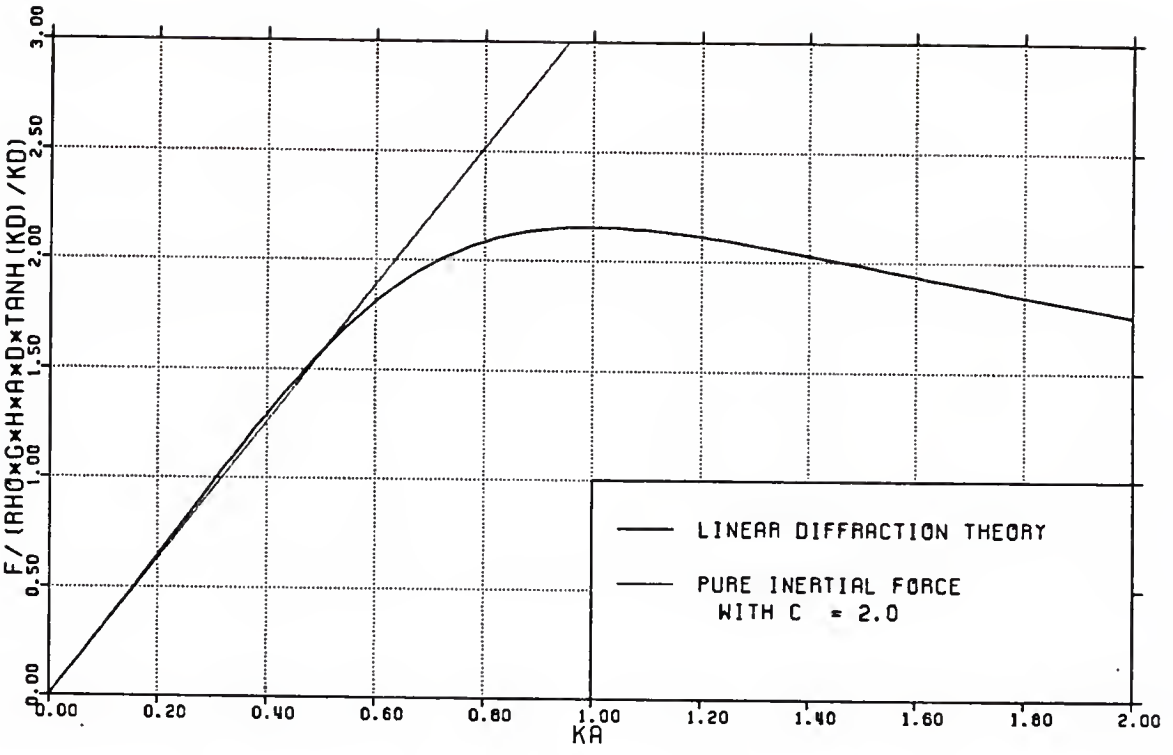

Figure 5.1: Maximum linear wave force as a function of the diffraction parameter ka

$$\tilde{F}_I = -C_m \frac{\pi}{2} ka \sin \sigma t \tag{5.16}$$

The inertial force varies linearly with ka except for the unknown, and in practice empirically determined, behavior of the coefficient C_m. From two-dimensional plane oscillatory flow, C_m is found to be equal to 2.0; this nondimensional linear force is shown as a straight line in Figure 5.1.

From Figure 5.1, it is apparent that for ka up to 0.5, linear scattering and diffraction are not too important and the resulting forces from linear diffraction theory are nearly inertial, and in-phase with the local acceleration of the linear wave. As ka increases, the cylinder redirects part of the flow. Phase shifts occur such the potential flow force is not purely in-phase with the local fluid acceleration of the undisturbed incident wave and the maximum force is skewed more toward the wave crest phase. In addition, total forces are reduced relative to pure inertial forces. For large piles, linear potential flow theory predicts C_m to be much less than 2.0, apparently due to the integrating or averaging effects of large

piles, in which the fluid acceleration past the pile no longer resembles unidirectional flow. For very large cylinders, positive and negative accelerations may occur over the surface of the cylinder that counteract to reduce the net force on the cylinder from its value in a unidirectionally accelerating flow.

5.3 Quadratic Components of Second-Order Force

The quadratic components of the second-order force are given in Equation 5.8 as

$$\begin{aligned} F_{21} &= -\frac{1}{2}ga\int_{-\pi}^{\pi}\eta_1^2\cos\theta d\theta \\ &\quad + \frac{\rho a}{2}\int_{-d}^{0}\int_{-\pi}^{\pi}(\nabla\Phi_1)^2\cos\theta d\theta dz \end{aligned} \tag{5.17}$$

In Appendix A.7, the quadratic force components in Equation 5.17 are derived separately for the two integrals which may be defined as: (1) the quadratic free surface force, F_{21f} from the first integral in Equation 5.17, and (2) the quadratic velocity-squared or convective force, F_{21v} from the second integral. It is noted that each component contains terms that are independent of time as well as terms that oscillate at frequency 2σ. Thus the second-order quadratic force may be separated as

$$F_{21} = F_{21f} + F_{21v} \tag{5.18}$$

$$= F^s_{21f} + F^s_{21v} + F^o_{21f} + F^o_{21v} \tag{5.19}$$

$$= F^s_{21} + F^o_{21} \tag{5.20}$$

where

F^s_{21f} = steady free surface force

F^s_{21v} = steady velocity-squared force

F^o_{21f} = oscillatory free surface force

F^o_{21v} = oscillatory velocity-squared force

F^s_{21} = total steady quadratic force

F^o_{21} = total oscillatory quadratic force

5.3.1 Mean Drift Forces

The steady quadratic force components are given in Equations A.110 and A.142 in Appendix A.7 as

$$F^s_{21f} = -\frac{\rho g a H^2}{\pi (ka)^2} \sum_{n=1}^{\infty} A_n A_{n-1} \sin(\psi_n - \psi_{n-1}) \tag{5.21}$$

$$\begin{aligned} F^s_{21v} &= +\frac{\rho g a H^2}{2\pi (ka)^2} \left[\left(1 + \frac{2kd}{\sinh 2kd}\right) \sum_{n=1}^{\infty} \frac{n(n-1)}{(ka)^2} A_n A_{n-1} \sin(\psi_n - \psi_{n-1}) \right. \\ &\quad \left. + \left(1 - \frac{2kd}{\sinh 2kd}\right) \sum_{n=1}^{\infty} A_n A_{n-1} \sin(\psi_n - \psi_{n-1}) \right] \end{aligned} \tag{5.22}$$

where

$$A_n = \frac{1}{|H'_n(ka)|} \tag{5.23}$$

$$\psi_n = \tan^{-1}\left(Y'_n(ka)/J'_n(ka)\right) \tag{5.24}$$

Combining the two components yields the total second-order steady quadratic force, popularly called the mean drift force, as

$$\begin{aligned} F^s_{21} &= F^s_{21f} + F^s_{21v} \\ &= \frac{\rho g a H^2}{2\pi (ka)^2} \left(1 + \frac{2kd}{\sinh 2kd}\right) \sum_{n=1}^{\infty} \left[\frac{n(n-1)}{(ka)^2} - 1\right] A_n A_{n-1} \sin(\psi_n - \psi_{n-1}) \end{aligned} \tag{5.25}$$

As a check on computations, the limits of the drift force may be considered. In deep water

$$\frac{2kd}{\sinh 2kd} \to 0 \tag{5.26}$$

Expanding the last terms as in the series as

$$A_n A_{n-1} \sin(\psi_n - \psi_{n-1}) = \Re\left\{ i A_n e^{-i\psi_n} A_{n-1} e^{+i\psi_{n-1}} \right\} \tag{5.27}$$

$$= \Re\left\{ i \frac{1}{(J'_n + iY'_n)} \frac{1}{(J'_n - iY'_n)} \right\} \tag{5.28}$$

and applying the identities for the derivatives of Bessel functions eventually leads to

$$A_n A_{n-1} \sin(\psi_n - \psi_{n-1}) = \left[\frac{n(n-1)}{(ka)^2} - 1\right] \frac{2}{\pi ka} A_n^2 A_{n-1}^2 \tag{5.29}$$

such that in deep water

$$F_{21}^{s} = \frac{\rho g a H^2}{\pi^2 (ka)^3} \sum_{n=1}^{\infty} \left[\frac{n(n-1)}{(ka)^2} - 1 \right]^2 A_n^2 A_{n-1}^2 \tag{5.30}$$

This expression agrees with the deep water drift force derived by Havelock (1940, p. 419) and Chakrabarti (1984).

The drift force can be related to the second-order incident momentum flux. The incident wave energy per unit length is, to second-order

$$E = \frac{1}{8} \rho g H^2 \tag{5.31}$$

Since the ratio of the group velocity to the wave celerity is

$$\frac{C_g}{C} = \frac{1}{2} \left(1 + \frac{2kd}{\sinh 2kd} \right) \tag{5.32}$$

the drift force may be written as

$$F_{21}^{s} = (2a) \frac{E C_g}{C} \frac{8}{\pi^2 (ka)^3} \sum_{n=1}^{\infty} \left[\frac{n(n-1)}{(ka)^2} - 1 \right]^2 A_n^2 A_{n-1}^2 \tag{5.33}$$

Since $C_g/C = \frac{1}{2}$ in deep water and $C_g/C = 1$ in shallow water, the ratio of deep to shallow water drift forces is related to the rate at which wave energy is transferred relative to the wave celerity; in shallow water, the drift force is found to equal twice the the deep water drift force. As shown by Havelock (1940, p.419) when ka is large, the series terms in Equation 5.33 reduce to $\pi^2 (ka)^3/6$ such that the drift force reduces further to

$$F_{21}^{s} = \frac{2}{3} (2a) \left(2 \frac{E C_g}{C} \right) \tag{5.34}$$

The drift force may be interpreted in terms of a reversal or re-direction of the incident mean momentum flux (given by $2EC_g/C$) over the plane projection of the cylinder cross section with the factor of 2/3 being obtained by resolving the actual momentum flux normal to the cylinder into the x direction. As stated by Havelock, this assumption is based on a large cylinder which redirects all of the incident momentum over the front half of the cylinder and which has no wave momentum over the rear half.

The theoretical second-order drift force may be most conveniently normalized by the force amplitude $\rho g a H^2$ such that the drift force may be expressed independently of the

wave steepness. In keeping with a standard way of normalizing forces for comparison to the first-order force magnitude, however, in this study the drift force will be normalized as

$$\tilde{F}^s_{21} = \frac{F^s_{21}}{\rho g a H d(\tanh kd/kd)} \tag{5.35}$$

such that the nondimensional drift force is

$$\tilde{F}^s_{21} = \frac{1}{2\pi(ka)^2}\frac{kH}{\tanh kd} \cdot \left(1+\frac{2kd}{\sinh 2kd}\right)\sum_{n=1}^{\infty}\left[\frac{n(n-1)}{(ka)^2}-1\right]A_nA_{n-1}\sin(\psi_n-\psi_{n-1}) \tag{5.36}$$

It is noted that the theoretical drift forces are always positive, i.e. in the direction of wave advance, consistent with the redirection of momentum flux.

5.3.2 Oscillatory Quadratic Forces

The oscillatory quadratic force components are given in Equations A.119 and A.143 in Appendix A.7 as

$$F^o_{21f} = +\frac{\rho g a H^2}{\pi(ka)^2}\sum_{n=1}^{\infty}A_nA_{n-1}e^{i\left[(2n-1)\frac{\pi}{2}-\psi_n-\psi_{n-1}\right]}\frac{e^{-i2\sigma t}}{2}+c.c. \tag{5.37}$$

$$\begin{aligned} F^o_{21v} &= +\frac{\rho g a H^2}{2\pi(ka)^2}\left[\left(1+\frac{2kd}{\sinh 2kd}\right)\sum_{n=1}^{\infty}\frac{n(n-1)}{(ka)^2}A_nA_{n-1}e^{i\left[(2n-1)\frac{\pi}{2}-\psi_n-\psi_{n-1}\right]}\right. \\ &\quad \left.+\left(1-\frac{2kd}{\sinh 2kd}\right)\sum_{n=1}^{\infty}A_nA_{n-1}e^{i\left[(2n-1)\frac{\pi}{2}-\psi_n-\psi_{n-1}\right]}\right]\frac{e^{-i2\sigma t}}{2} \\ &\quad +c.c \end{aligned} \tag{5.38}$$

Combining the two components yields the second-order oscillatory quadratic force as

$$\begin{aligned} F^o_{21} &= F^o_{21f}+F^o_{21v} \\ &= \frac{\rho g a H^2}{2\pi(ka)^2}\left[\left(1+\frac{2kd}{\sinh 2kd}\right)\sum_{n=1}^{\infty}\frac{n(n-1)}{(ka)^2}A_nA_{n-1}e^{i\left[(2n-1)\frac{\pi}{2}-\psi_n-\psi_{n-1}\right]}\right. \\ &\quad \left.+\left(3-\frac{2kd}{\sinh 2kd}\right)\sum_{n=1}^{\infty}A_nA_{n-1}e^{i\left[(2n-1)\frac{\pi}{2}-\psi_n-\psi_{n-1}\right]}\right]\frac{e^{-i2\sigma t}}{2} \\ &\quad +c.c. \end{aligned} \tag{5.39}$$

The oscillatory quadratic force and the mean drift force in Equation 5.36 have nearly the same form and are of the same order of magnitude. As shown by Herfjord and Nielsen

(1986) and Eatock Taylor and Hung (1987), the magnitude of the oscillatory terms are typically only two or three times larger than the magnitude of the mean drift force, and for small piles or in near-shallow water, the magnitude of the oscillatory quadratic force may be smaller than the drift force.

In order to compare the amplitude and phase relationship of the oscillatory force, F_{21}^o, to the first-order force, the standard normalization will be used as

$$\tilde{F}_{21}^o = \frac{F_{21}^o}{\rho g a H d(\tanh kd/kd)} \tag{5.40}$$

such that the normalized second-order oscillatory quadratic force is

$$\begin{aligned}\tilde{F}_{21}^o &= \frac{kH}{2\pi(ka)^2 \tanh kd} \\ &\cdot \left[\left(1+\frac{2kd}{\sinh 2kd}\right)\sum_{n=1}^{\infty}\frac{n(n-1)}{(ka)^2}A_nA_{n-1}e^{i\left[(2n-1)\frac{\pi}{2}-\psi_n-\psi_{n-1}\right]}\right. \\ &\left. + \left(3-\frac{2kd}{\sinh 2kd}\right)\sum_{n=1}^{\infty}A_nA_{n-1}e^{i\left[(2n-1)\frac{\pi}{2}-\psi_n-\psi_{n-1}\right]}\right]\frac{e^{-i2\sigma t}}{2} \\ &+ c.c.\end{aligned} \tag{5.41}$$

In Figure 5.2, the oscillatory quadratic force is compared to the first-order force for the reference conditions, $ka = 1.0$, $kd = 1.57$, and $kH = 0.5$, used throughout Chapter 4. A general feature of the second-order oscillatory quadratic force is displayed; like the second-order oscillatory free surface components, the quadratic forces are phased such that they tend to increase the maximum force in the positive direction, i.e. in the direction of wave propagation, and decrease the peak force in the negative direction. Physically, the quadratic forces are the result of pressure gradients induced by (1) the variation of the first-order free surface around the cylinder and (2) convective acceleration of the first-order flow field around the cylinder. Since each of these effects are related to the wave crest phase, the maximum oscillatory quadratic force occurs between the phase of the maximum horizontal acceleration and the maximum horizontal velocity. The exact phasing depends on the relative cylinder size and relative depth.

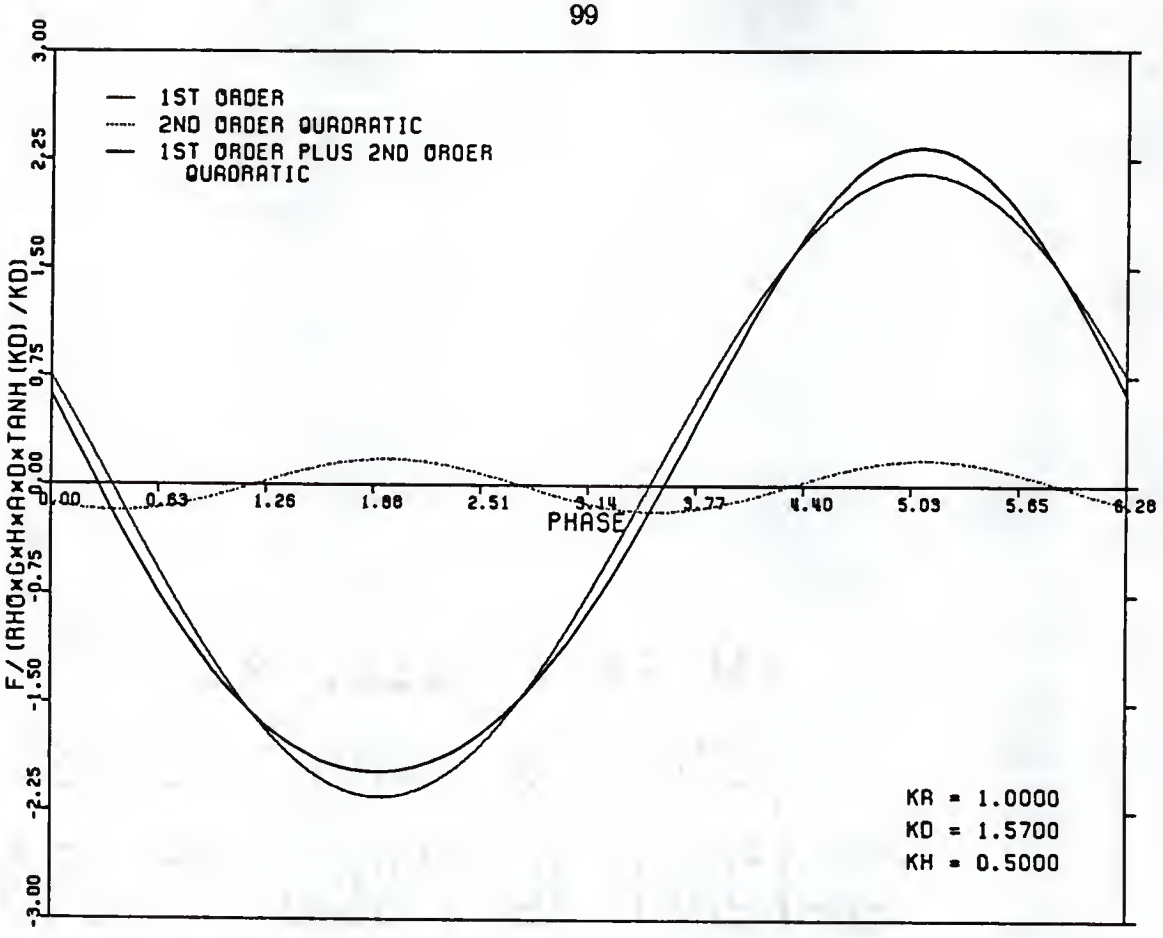

Figure 5.2: Oscillatory quadratic force compared to linear force for reference conditions

5.4 Forces from Second-Order Velocity Potential

The second-order force contributions from the second-order velocity potential are found directly by substituting the solution for Φ_2, given in Equation 3.80 in Chapter 3, into the expression for the second-order force

$$F_{22} = \rho a \int_{-d}^{0} \int_{-\pi}^{\pi} (\Phi_{2t})_{r=a} \cos\theta \, d\theta \, dz \tag{5.42}$$

Since Φ_2 is separable into functions of r, θ, z, and t, the integrations over θ and over depth are straightforward. Once again, since Φ_2 is expressed in terms of a series with terms like $\cos n\theta$, the integration over θ eliminates all orders, n, except the dipole-like term at $n = 1$.

Once the integrations are complete, the resulting expression for the force may be normalized in the standard way as

$$\tilde{F}_{22} = \frac{F_{22}}{\rho g a H d(\tanh kd/kd)} \tag{5.43}$$

The nondimensional second-order force contribution from the second-order velocity potential is then found to be

$$
\begin{aligned}
\tilde{F}_{22} \;=\; & -\pi \frac{kH}{\tanh kd} \frac{e^{-i2\sigma t}}{2} \\
& \cdot \left[\left\{ \frac{3i}{8} \frac{k(\tanh^2 kd - 1)\tanh 2kd}{(2k \tanh 2kd - k_2 \tanh k_2 d)} J_1(2ka) \right.\right. \\
& - 6i \frac{k}{k_2} \frac{k^2(\tanh^2 kd - 1)}{(4k^2 - k_2^2)} \frac{\sinh 2k_2 d}{(\sinh 2k_2 d + 2k_2 d)} \frac{J_1'(2ka)}{H_1'(k_2 a)} H_1(k_2 a) \\
& \left.\left. -6i \sum_{j=1} \frac{k}{\kappa_{2j}} \frac{k^2(\tanh^2 kd - 1)}{(4k^2 + \kappa_{2j}^2)} \frac{\sin 2\kappa_{2j} d}{(\sin 2\kappa_{2j} d + 2\kappa_{2j} d)} \frac{J_1'(2ka)}{K_1'(\kappa_{2j} a)} K_1(\kappa_{2j} a) \right\} \right. \\
& + \left\{ \frac{1}{4} PV \int_0^\infty \frac{\tanh \kappa d}{\kappa \tanh \kappa d - k_2 \tanh k_2 d} \tilde{D}_1(\kappa) J_1(\kappa a) d\kappa \right. \\
& - \frac{1}{2} \frac{k}{k_2} \frac{\sinh 2k_2 d}{(\sinh 2k_2 d + 2k_2 d)} \frac{H_1(k_2 a)}{k H_1'(k_2 a)} PV \int_0^\infty \frac{\kappa^2 \tilde{D}_1(\kappa) J_1'(\kappa a)}{\kappa^2 - k_2^2} d\kappa \\
& - \frac{1}{2} \sum_{j=1} \frac{k}{\kappa_{2j}} \frac{\sin 2\kappa_{2j} d}{(\sin 2\kappa_{2j} d + 2\kappa_{2j} d)} \frac{K_1(\kappa_{2j} a)}{k K_1'(\kappa_{2j} a)} \int_0^\infty \frac{\kappa^2 \tilde{D}_1(\kappa) J_1'(\kappa a)}{\kappa^2 + \kappa_{2j}^2} d\kappa \\
& \left.\left. + \frac{i\pi}{4} \frac{\sinh 2k_2 d}{(\sinh 2k_2 d + 2k_2 d)} \tilde{D}(k_2) \left(J_1(k_2 a) - \frac{J_1'(k_2 a)}{H_1'(k_2 a)} H_1(k_2 a) \right) \right\} \right] \\
& + \; c.c.
\end{aligned}
\tag{5.44}
$$

The origin of each of these terms is as follows. The terms in the first bracket repesent the second-order incident plane wave at wavenumber $2k$ and its two associated scattered components, one an outwardly radiating wave at wavenumber k_2 and the other given by a series of local standing waves. The plane wave component is exactly phase-locked with the first-order incident wave, therefore its force components are maximum at a phase of $-\pi/4$; its scattered components are shifted in phase depending on the relative cylinder size. Since the linear force is maximum at a phase of $-\pi/2$ (for small cylinders) or closer to the wave crest (for large cylinders), the terms in the first bracket may increase or decrease the maximum force in the positive direction compared to linear theory, depending on the relative cylinder size.

The groups of force components in the second bracket in Equation 5.44 represent the other forced and radiated waves generated by the applied forcings f^{is} and f^{ss} in the CFSBC,

as well as the scattered waves resulting from the interaction of the forced-radiated waves with the cylinder. As noted, these terms do not have a simple variation from deep to shallow water, due to the contributions from all wavenumbers in the integral terms. The resulting forces generally increase as ka increases since the quadratic forcing in the CFSBC is stronger for larger cylinders. In particular, forces due to the long wave terms in the solution, associated with the long standing wave forcing in the upwave region, become more important as the cylinder size increases and as the depth increases.

A general feature of the forced-radiated force terms, however, is that they are mostly out-of-phase relative to all other force components. The free surface contribution resulting from the f^{is} and f^{ss} forcing in the CFSBC is out-of-phase relative to other second-order free surface components, such that the various second-order components tended to cancel each other. The same result applies to the second-order forces. Terms resulting from the f^{is} and f^{ss} forcing in the CFSBC increase the force in the negative direction (opposing the direction of wave propagation) and reduce the force in the positive direction, tending to compensate for, or dominate over, the effects of the second-order incident plane wave and the oscillatory quadratic terms.

In Figure 5.3. the behavior of the nondimensional second-order force component, $\tilde{F}_{22}$, is compared to the linear force for the reference conditions. In this case the amplitude of the second-order terms from the second-order potential is similar to the amplitude of the oscillatory quadratic terms, however, the phasings are different, with the $\tilde{F}_{22}$ terms increasing the force in the negative direction. It is noted that the force component $\tilde{F}_{22}$ is itself the resultant of two competing terms. For the reference case with $ka = 1.0$, the plane wave terms (first bracket in Equation 5.44) increase the force in the direction of wave advance, while the remaining forces from the forced-radiated terms (second bracket) are generally out-of-phase with the first-order forces and act to increase the force in the negative direction.

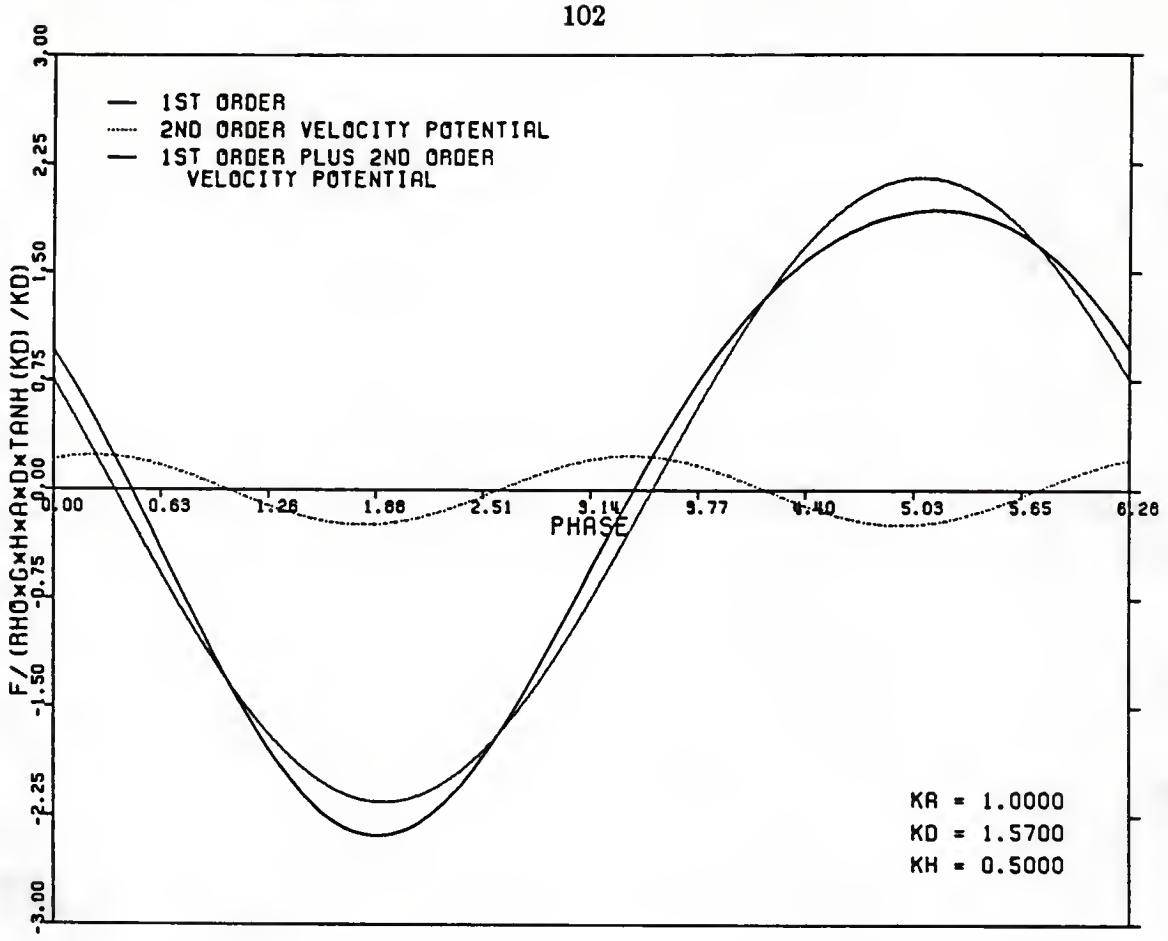

Figure 5.3: Second-order forces from the second-order velocity potential for reference condition

5.5 Wave Forces Complete to Second-Order

The complete theoretical solution for the potential flow wave forces, complete to the second perturbation order, are obtained by adding the following components

1. The first-order solution, $\tilde{F}_1$, given in Equation 5.14.

2. The second-order steady or drift force, $\tilde{F}^s_{21}$, as given in Equation 5.36.

3. The second-order oscillatory quadratic force, $\tilde{F}^o_{21}$, given in Equation 5.41.

4. The second-order force from the second-order velocity potential, $\tilde{F}_{22}$, as given in Equation 5.44.

The force cancellations displayed in the reference case, with $ka = 1.0$, $kd = 1.57$, and $kH = 0.5$, are typical of the competing effects of the various force components. The sum

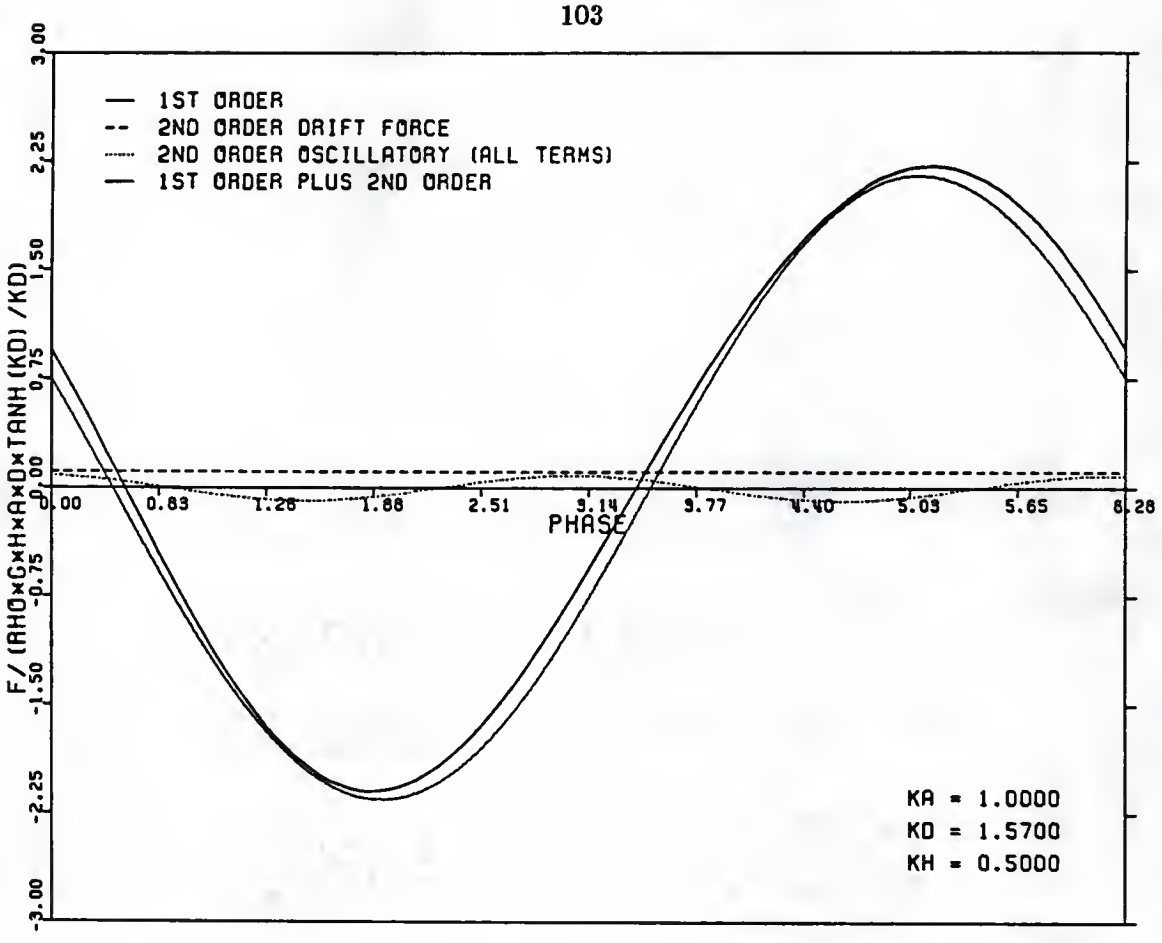

Figure 5.4: Total second-order wave forces for reference conditions

of the second-order oscillatory terms yields a force component at frequency 2σ that has an amplitude of only 4 percent of the linear force amplitude, as shown in Figure 5.4. The second-order oscillatory contribution is the result of (1) the oscillatory quadratic terms with an amplitude of 8.3 percent of the linear and no phase shift and (2) the terms from the second-order velocity potential which have an amplitude of 11.1 percent of the linear but which have a phase shift of 1.44 radians relative to the linear force. These two oscillatory force contributions, therefore, tend to partially cancel to reduce the overall second-order force contribution. Finally, the drift force, with a magnitude of 5.3 percent of the linear force, is added and the total force is increased by only 3.1 percent in the positive direction, and decreased in the negative direction.

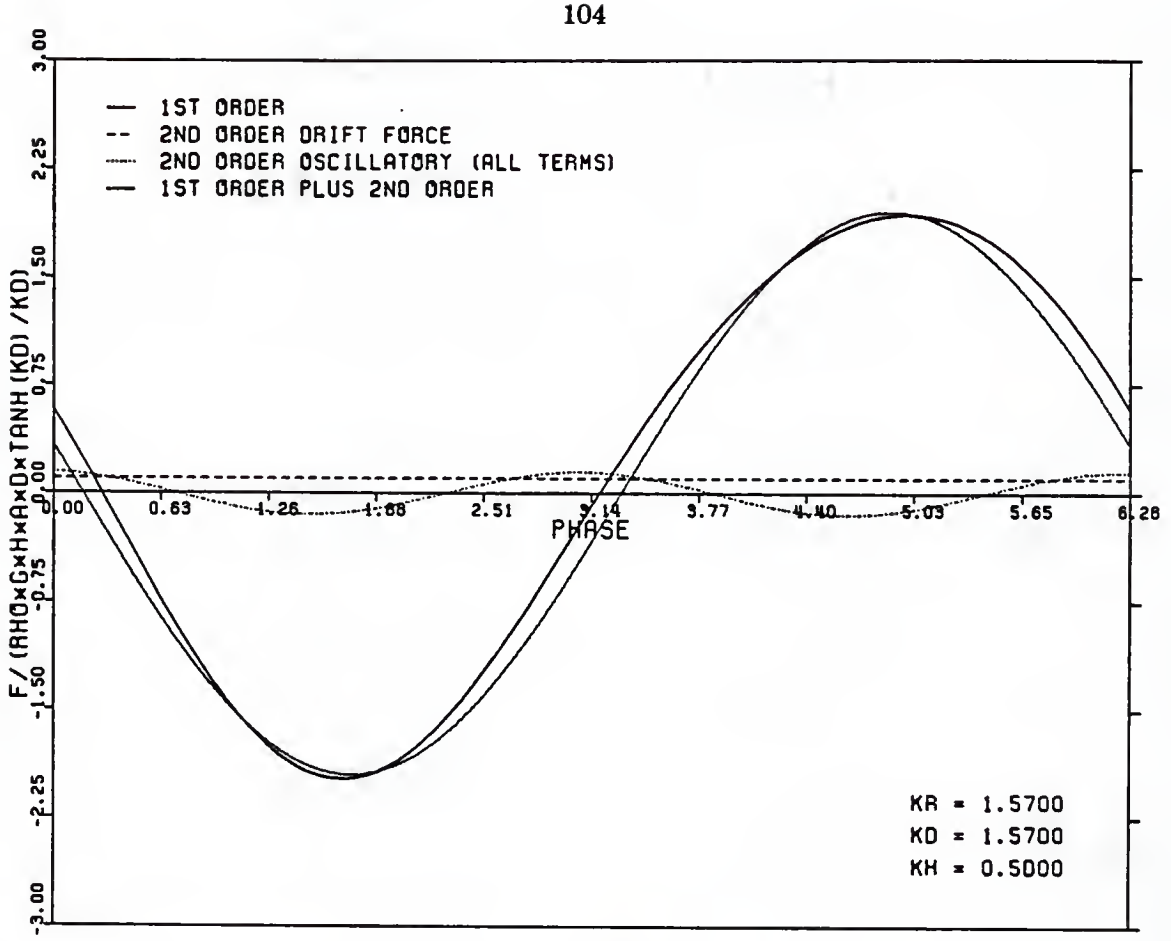

Figure 5.5: Example of second-order force for large cylinder, $ka = 1.57$, $kd = 1.57$, and $kH = 0.5$

5.6 Summary of Nonlinear Forces

Additional examples of nonlinear forces in the diffraction regime are presented in Figure 5.5 through 5.8 for the following cases (1) large cylinder, intermediate depth, in Figure 5.5, (2) small cylinder, intermediate depth, in Figure 5.6, (3) deep water, moderate cylinder size, in Figure 5.7, and (4) near-shallow water, moderate cylinder size, in Figure 5.8.

As is evident in Figures 5.5 and 5.6, the effect of cylinder size is most pronounced in terms of the nondimensional linear force, which reaches a maximum near $ka = 1.0$. Nondimensional second-order effects are more important, as a percentage of the linear force amplitude, for the smaller cylinder. However, the absolute force magnitudes are much greater for large cylinders, and the individual second-order force components are usually

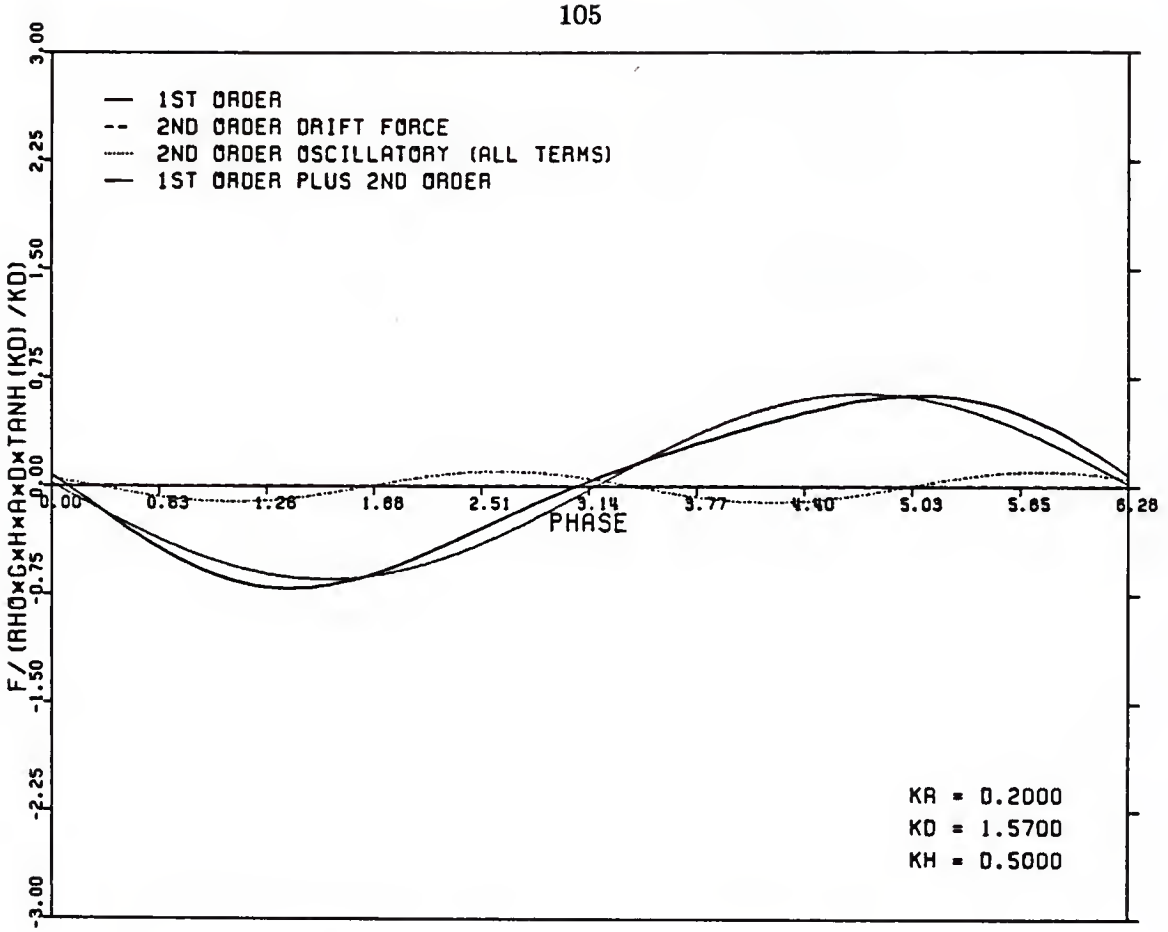

Figure 5.6: Example of second-order force for small cylinder, $ka = 0.2$, $kd = 1.57$, and $kH = 0.5$

larger for large cylinders due to increased scattering and sheltering.

For large cylinders, the increased scattering and diffraction cause the free surface force components to increase in importance; thus, quadratic forces tend to be more associated with the wave crest phase when the maximum first-order runup occurs. The forces due to the second-order velocity potential are also increased for large cylinders and it is found that the magnitude of these force components tends to be comparable to the magnitude of the quadratic terms. Since the quadratic terms and the terms from the velocity potential are nearly, but not completely, out-of-phase, the resulting second-order force component may have a wide range of effects on the total force. In the example in Figure 5.5, quadratic forces dominate and the second-order force is shifted toward the wave crest, causing forces in the positive direction to be decreased slightly while negative forces are increased.

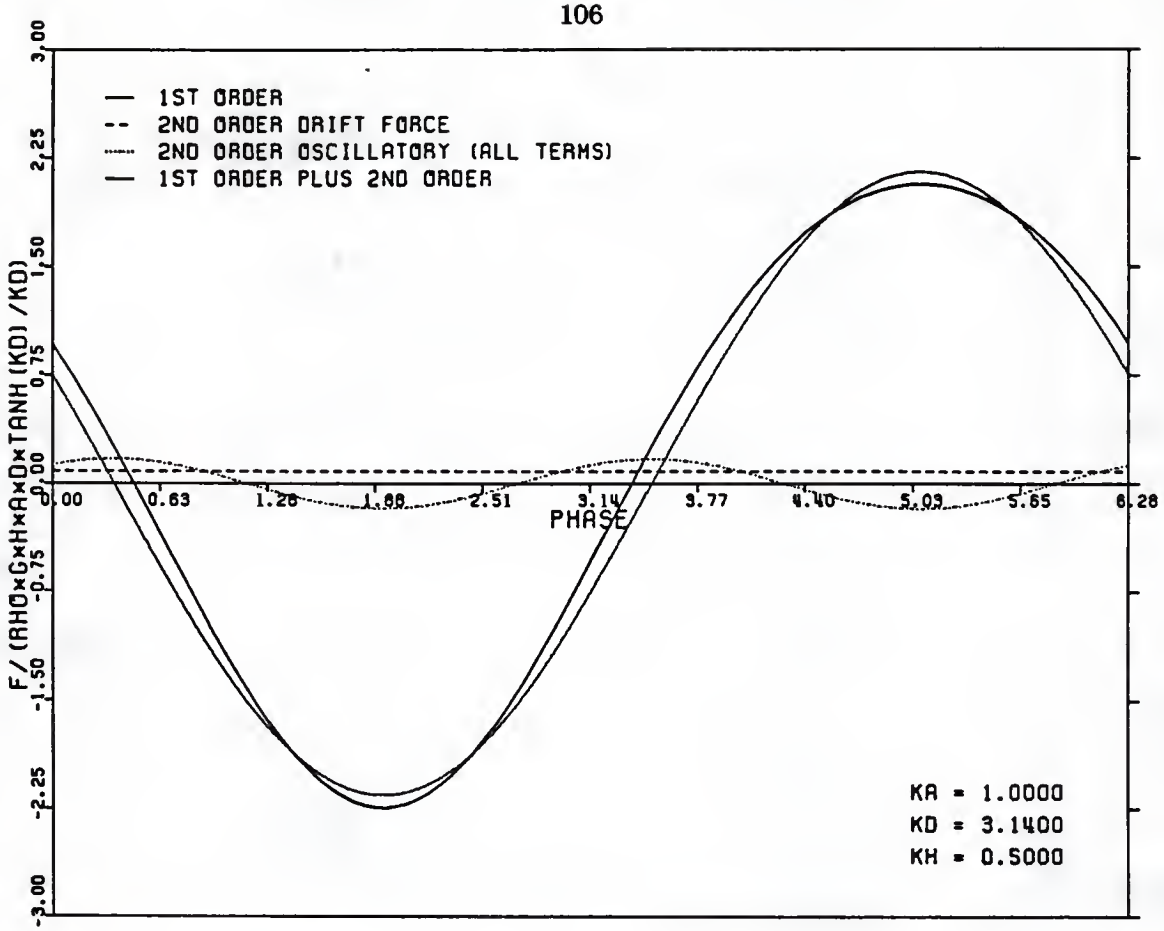

Figure 5.7: Example of second-order force for deep water, $ka = 1.0$, $kd = 3.14$, and $kH = 0.5$

For small cylinders, the plane wave terms typically dominate. The effect on the force trace is to shift both the positive and negative maxima closer to the wave crest, resulting in a more sudden reversal in the loading direction under the wave crest. For very small cylinders, this is consistent with only considering the convective acceleration terms in the equations of motion. As cylinder size increases, the scattered wave, due to the interaction of the plane wave with the cylinder, alters the second-order force to skew the force closer to the wave crest.

Between deep and shallow water, the total second-order force contribution is again based on the competing effects of the various second-order force terms. In deep water, the terms associated with the second-order plane wave are nearly zero, therefore the second-order force contribution is dominated by the other forced wave motions. These other forced-radiated

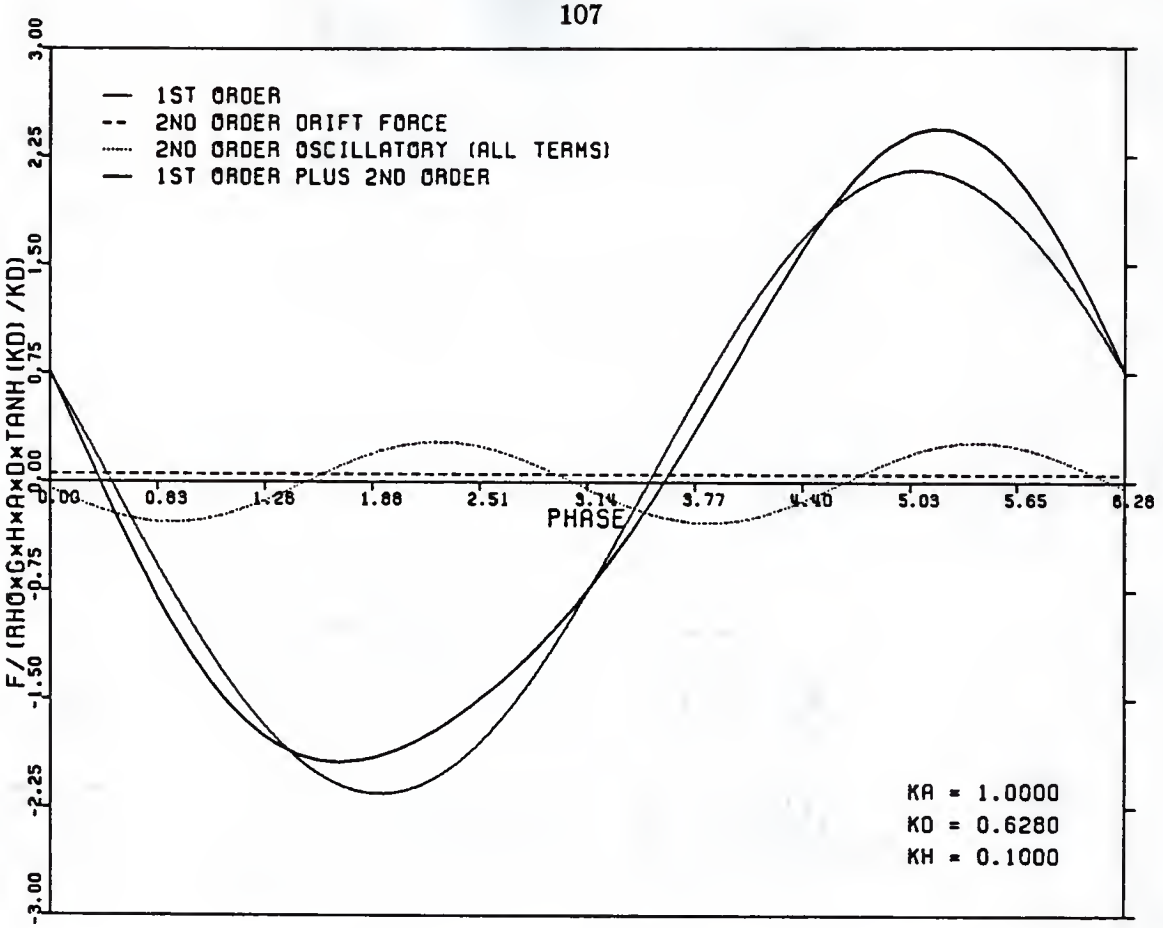

Figure 5.8: Example of second-order force for near-shallow water, $ka = 1.0$, $kd = 0.628$, and $kH = 0.1$

and scattered components do not vary strongly with water depth, although the long standing wave motion in the second-order velocity potential becomes important for large cylinders in deep water. In shallow water, the second-order force $\tilde{F}_{22}$ is usually dominated by the incident plane wave. Depending on the magnitudes and phasings of the first and second-order components, the total force maxima can be increased substantially from linear theory, as shown in Figure 5.8.

The overall effects of second-order terms on the maximum force exerted on the cylinder may be considered in Figure 5.9, in which the maximum nondimensional force is compared for various values of the diffraction parameter and wave steepness, for a fixed ratio of water depth to cylinder size, $d/a = 2.77$. For small cylinders (in smaller depths) the second-order forces exceed the linear force by more than twenty percent for the cases shown. The

predicted forces also exceed the inertial force based on $C_m = 2.0$ and the maximum fluid acceleration from linear wave theory; this loading regime is dominated by nonlinear inertial forces asociated with the second- order plane wave terms. In Chapter 6, it will be shown that the agreement of the theory to laboratory force data is excellent in this loading regime, even for steepnesses up to the limit of validity of the Stokes theory. For steepnesses larger than the limiting steepness shown, the forces increase further but the solution is not considered valid.

For moderate cylinder sizes, the predicted nonlinear forces are nearly equal to the linear force predictions, and net second-order effects are insignificant. In this region, from $ka = 0.5$ to $ka = 1.0$, the various second-order force components, individually are appreciable, but they are out-of-phase and cancel almost identically. As ka increases above 1.0, the second-order velocity potential forces begin to dominate, but the same cancellation effects are still present. As ka approaches 2.0, the long standing wave terms in the second-order velocity potential begin to dominate and predicted forces increase from linear theory.

In Figure 5.10, the same information is presented in terms of the percentage difference between the maximum forces predicted by the second-order theory and the much simpler first-order theory. This percentage, is defined as

$$\frac{\tilde{F}_2 - \tilde{F}_1}{\tilde{F}_1} \cdot 100\% \tag{5.45}$$

where $\tilde{F}$ represents the maximum force amplitude for either theory. With this information, the first-order force may be evaluated and then simply increased by the percentage shown to account for theoretical second-order effects.

The maximum differences between first and second-order theories occur for high steepness waves and for waves near the Stokes convergence limit. In deep water, the differences are typically between 5 and 20 percent, and up to 30 percent for highly nonlinear waves. At smaller kd values near the shallow water limit, the second-order theory predicts increased forces that are up to 25 percent larger than those predicted by linear theory. Even for waves at less than one-quarter of the breaking steepness, the differences are more than 10 percent

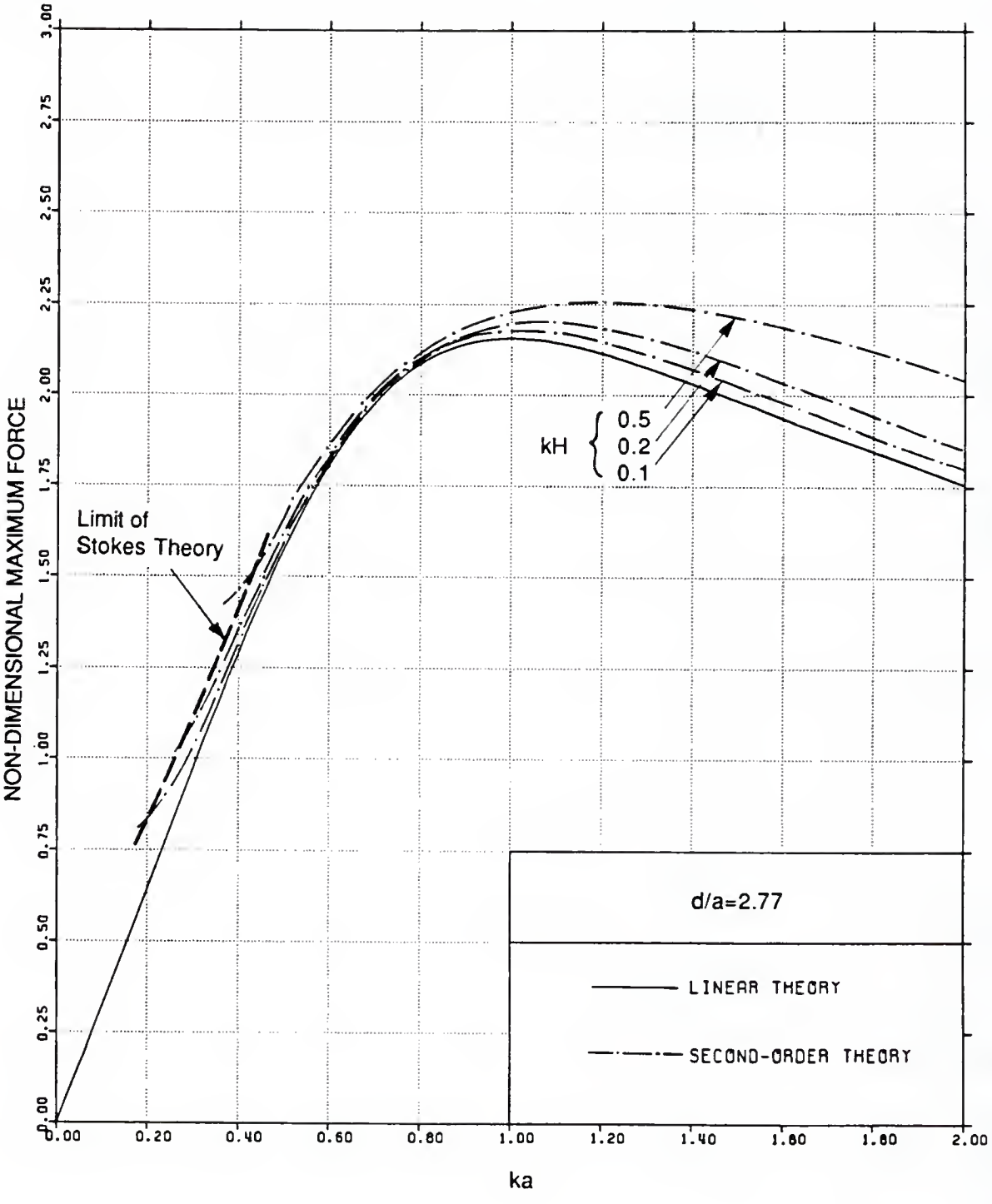

Figure 5.9: Comparison of first and second-order maximum forces as a function of the diffraction parameter and wave steepness

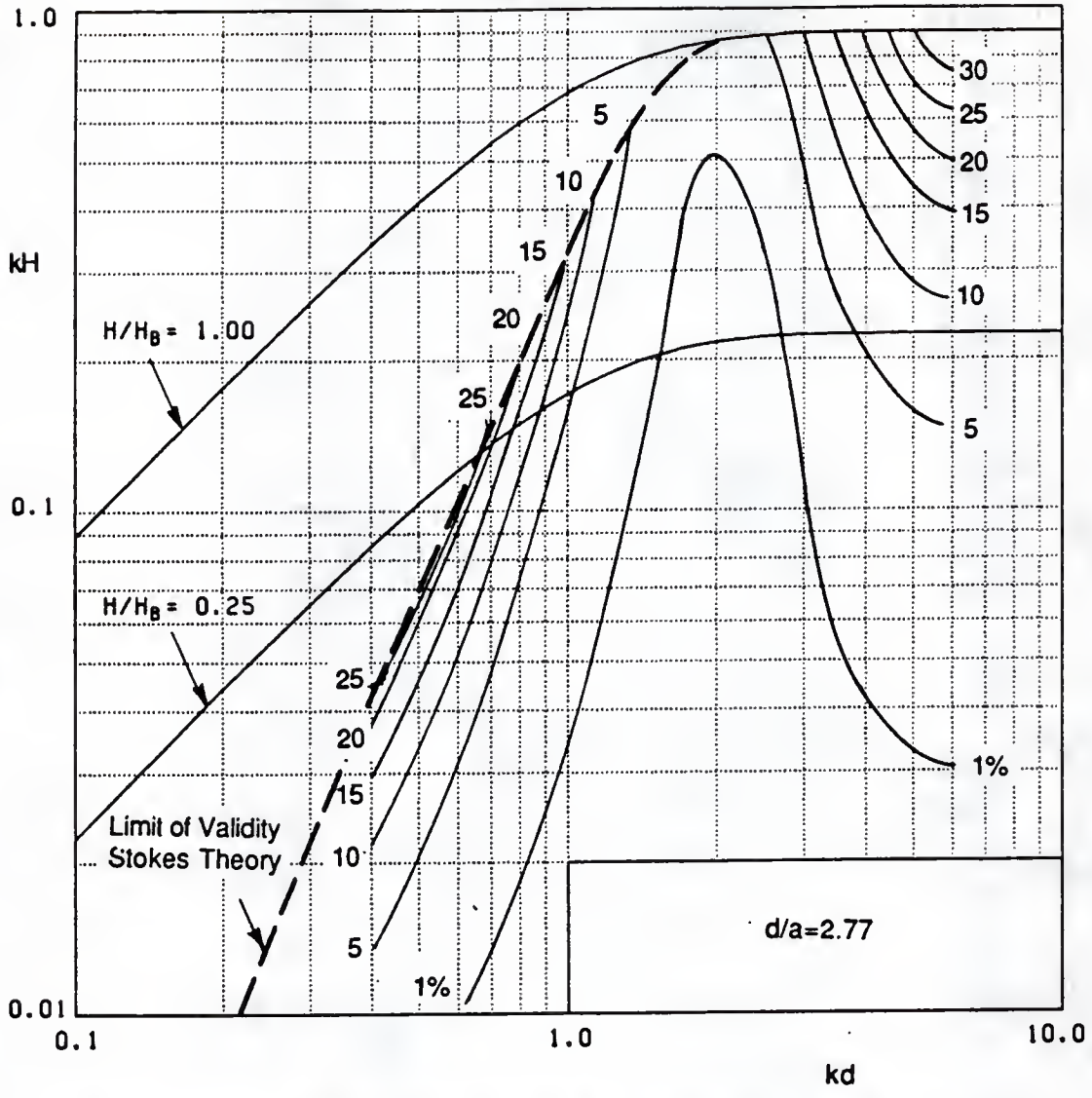

Figure 5.10: Percent difference between second and first-order maximum force

in some cases. The smallest differences occur for $kd = 2.0$ and $ka = 0.72$, corresponding to conditions where almost complete cancellation occurs between the second-order quadratic forces and the forces from the second-order velocity potential.

CHAPTER 6
EXPERIMENTAL VERIFICATION OF SECOND-ORDER THEORY

6.1 Description of Laboratory Experiments

The theoretical solutions for the second-order free surface and wave forces are evaluated through a series of small-scale laboratory experiments. The experiments were conducted in the directional wave basin at the University of Florida Coastal and Oceanographic Engineering Laboratory, as shown in Figure 6.1. The basin was selected over wave flumes in order to minimize side wall effects such as re-reflection of scattered waves. In addition, the basin contained a dissipative sand beach, placed on a 9 degree angle relative to the wavemaker, which eliminated wave reflection. A steel frame was erected in the basin and an instrumented test cylinder was supported in the center of the frame. The water depth was maintained at 45.0 centimeters and a cylinder with radius 16.25 centimeters was used, such that the depth-to-radius ratio, d/a, equaled 2.77 for all experiments.

The experiments were conducted with monochromatic long-crested waves and, as listed in Table 6.1, the test series included six wave periods and up to five wave heights at each period. A total of 22 experiments were carried out covering a broad range of the nondimensional parameters ka, kd, and kH, given in Table 6.2. Relative cylinder sizes remained in the diffraction regime with ka values from 0.271 to 0.917. Relative water depths remained in the intermediate depth regime where Stokes second-order theory should be valid; conditions ranged from near-deep water, with $kd = 2.536$, to near-shallow water, with $kd = 0.750$. Values of the wave steepness were selected such that Stokes second-order theory would remain convergent, although some waves with very high steepness were also tested; kH values ranged from 0.085 to 0.806. For the wave periods of 0.85, 1.05, and 1.25 seconds, a practical breaking steepness was reached. In these cases, waves were from 68 to 91 percent of

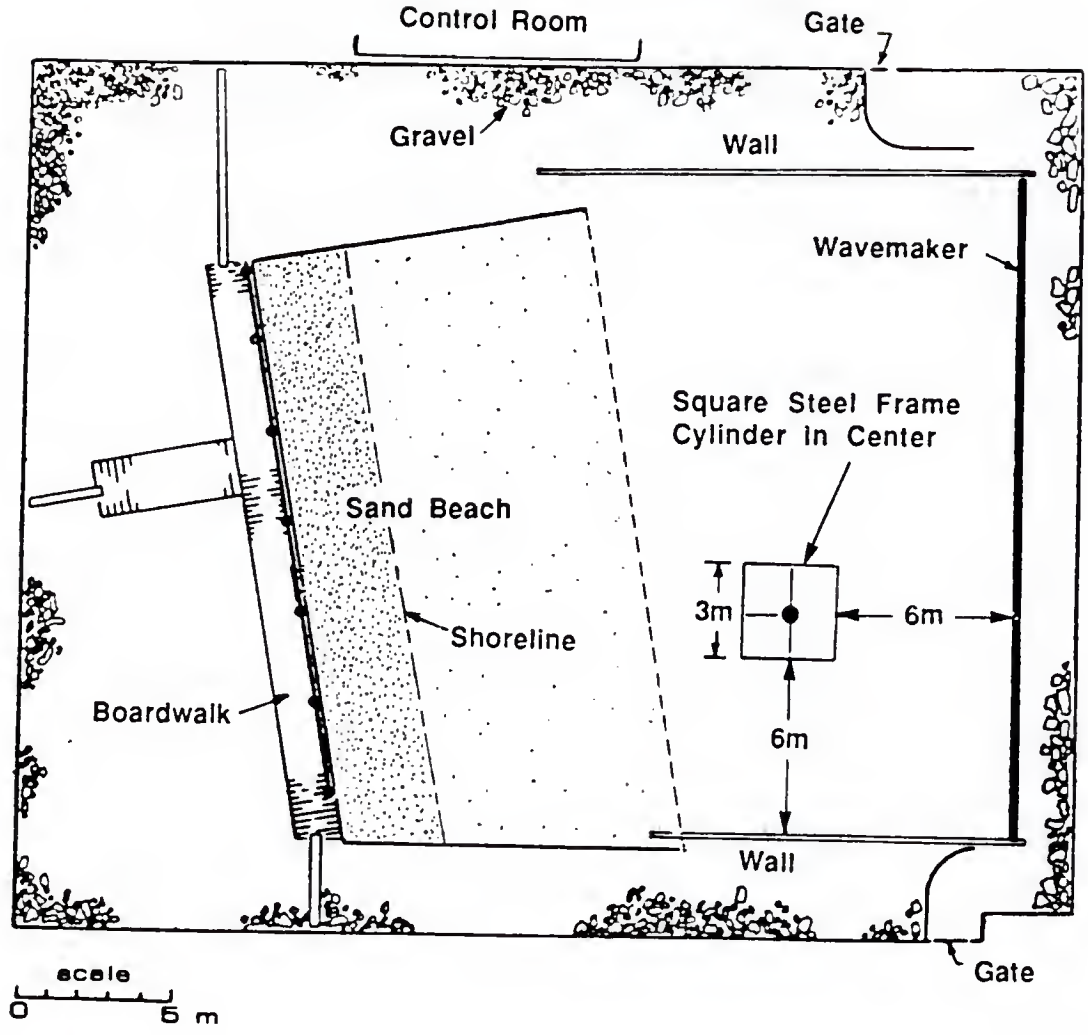

Figure 6.1: Model basin and experimental setup

the theoretical breaking steepness according to the Miche criterion; however, cross-waves became important in the basin and breaking occurred at isolated locations along the wave crest, rather than along the entire crest.

The test conditions are plotted in Figure 6.2, in a format suggested by LeMehaute (1969) and reproduced in the Shore Protection Manual (1977), in order to obtain an indication of the validity of Stokes second-order wave theory for each experiment. According to Figure 6.2, Stokes second-order theory is expected to be most appropriate for 8 of the 22 experiments, while another 5 or 6 tests are just out of this range. At the highest one or two values of the wave steepness at each period, conditions are in the regions in which either

Table 6.1: Wave Conditions for Laboratory Experiments

Wave Period (sec)	Wave Height (cm)				
	Wavemaker Stroke				
	2	3	4	5	6
0.85	11.2	14.3			
1.00	9.3	13.6			
1.05			17.6		
1.25	6.3	10.7	14.8	17.9	
1.50	5.3	8.9	12.4	16.7	17.4
1.75	4.5	7.2	9.6	13.2	15.6
1.95			7.9	10.7	12.9

Table 6.2: Nondimensional Parameters From Laboratory Experiments

ka	kd	kH				
		Wavemaker Stroke				
		2	3	4	5	6
0.917	2.536	0.631	0.806			
0.684	1.894	0.391	0.572			
0.631	1.745			0.683		
0.481	1.332	0.186	0.317	0.438	0.530	
0.374	1.036	0.122	0.205	0.286	0.385	0.402
0.308	0.853	0.085	0.137	0.182	0.250	0.296
0.271	0.750			0.132	0.178	0.215

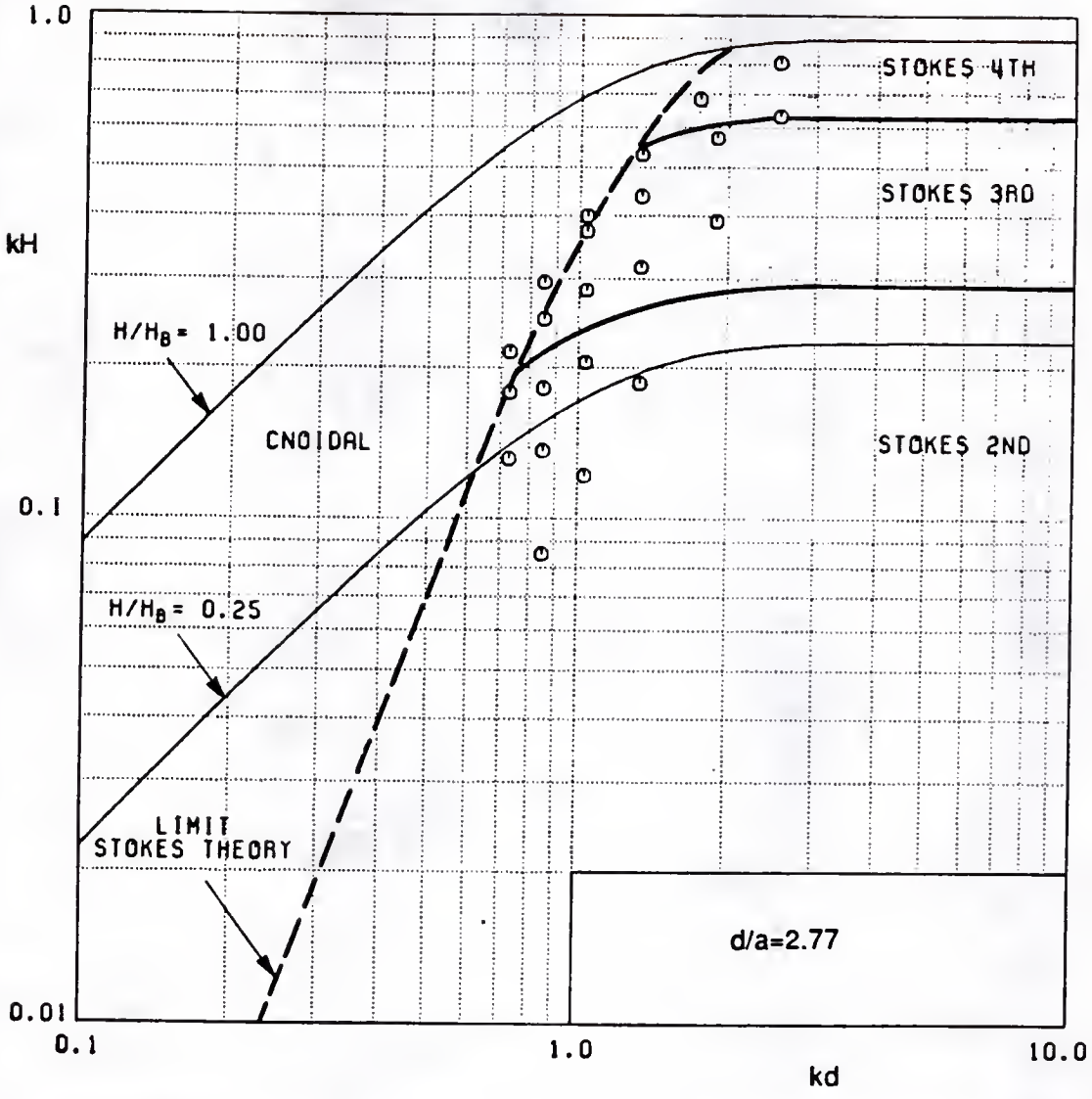

Figure 6.2: Test conditions compared to approximate limits of validity for Stokes theories

Stokes third or fourth-order theories are the most appropriate according to LeMehaute's qualitative criteria. Dean (1970) has shown that for these conditions, Stokes fifth-order theory or the numerical Stream Function theory is most appropriate.

A Stokes second-order wave develops a secondary crest or "bump" in the primary wave trough if the second-order wave amplitude exceeds one-quarter of the first-order amplitude. gives yields an upper limit on wave steepness, for which second-order theory is realistic, of

$$kH_{max} = \frac{2\sinh^3 kd}{\cosh kd(2\cosh^2 kd + 1)} \tag{6.1}$$

For values of the wave steepness exceeding this limit, Stokes second-order theory is not convergent and will be considered invalid. This condition, represented by a diagonal line in Figure 6.2, restricts the applicability of the second-order theory in near-shallow water. Of the 21 experimental conditions, 2 marginally exceeded this criterion and extend into the regime where cnoidal theory may be most appropriate, while Stokes theories are applicable for the rest of the experiments.

Three types of measurements were made for each set of wave conditions (1) total wave forces on the cylinder, (2) wave runup around the circumference of the cylinder, and (3) water surface elevations at selected locations around the cylinder.

Force measurements were obtained from a pair of load cells installed between the cylinder and the frame as shown in Figure 6.3. The load cells are the tension-compression type. Static calibrations were performed in both loading directions before each set of tests by hanging lead weights from each load cell. In general, the load cells were almost perfectly linear and were not sensitive to daily changes in temperature. Time series of free surface elevations at a given location were obtained from a capacitance-type wave gage. The wave gage was also calibrated before each set of experiments. The voltage signals from the load cells and the wave gage were filtered to eliminate interference from neighboring electrical systems. The signals were then amplified and passed to the analog-to-digital converter on a DEC PDP 11/03 computer and were sampled at a rate of 32 Hertz.

For each set of wave conditions, the water surface was initially quiescent, then waves were generated for 60 seconds. In most cases steady-state wave conditions around the cylinder seemed to be achieved after 10 to 20 seconds. Wave runup and force data were then collected for a 30 to 40 second period. Force data were phase-averaged over 10 waves for each experiment. For all tests, wave records were first obtained at the location of the center of the cylinder but with the cylinder removed in order to obtain the undisturbed incident wave heights. During tests with the cylinder in place, the wave gage was positioned in-line with the center of the cylinder, but off to the side at $\theta = \pi/2$ and at a distance $r = 10a$.

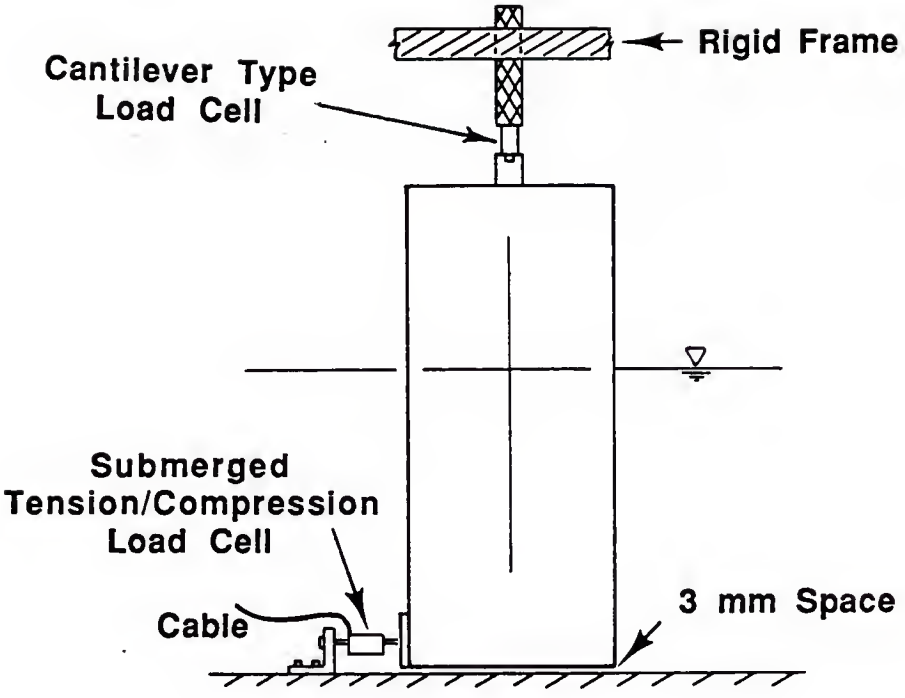

Figure 6.3: Instrumented cylinder for measuring total wave forces

Wave runup data were obtained by video-taping the water surface on the circumference of the cylinder. A grid was painted on the outside of the cylinder with vertical lines every 15 degrees and with horizontal lines every five centimeters. Data analysis for the video records was limited to (1) selecting a 20 to 30 second period in which steady state conditions seemed to have occurred and (2) averaging the wave crest runup and trough rundown for 10 waves for each of the 15 degree verticals. The maximum and minimum runup excursions were also obtained at 0, 45, 90, 135, and 180 degrees.

For 12 of the experiments a video record was also made of waves passing a "photopole" array, which consisted simply of 10 thin vertical rods placed in a linear array along the x axis on the upwave and downwave sides of the cylinder out to a distance of $r = 5a$, as depicted in Figure 6.4. The photopole data consists of the wave crest and trough envelopes at each pole location, averaged over 10 waves. The photopole experiments were conducted separately from the runup/rundown or and force experiments so that the presence of the poles would not disrupt the other measurments.

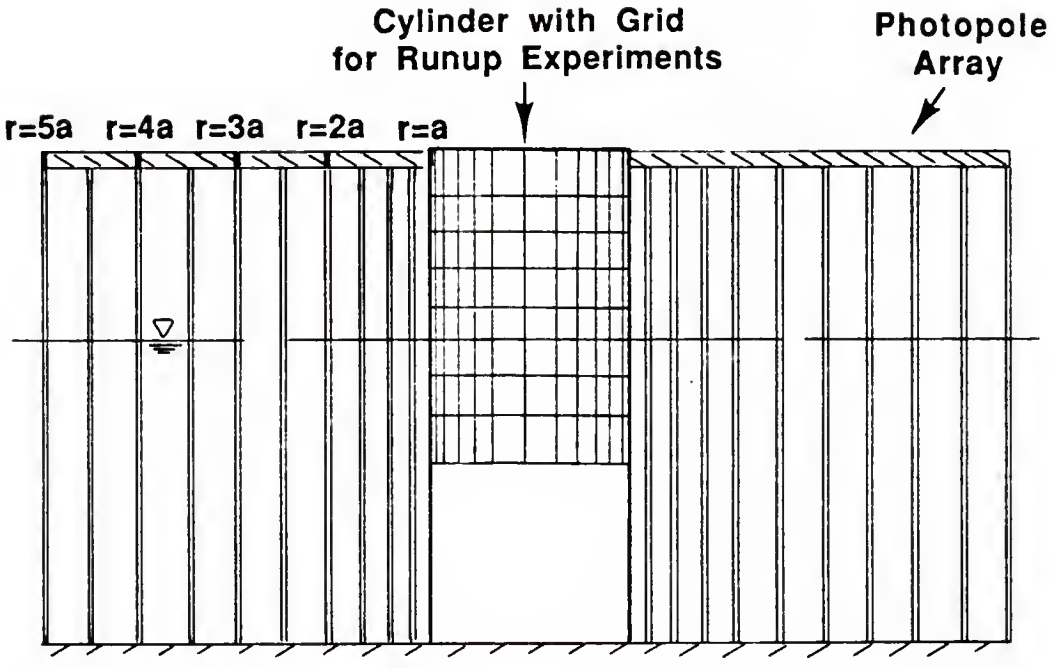

Figure 6.4: Side view of cylinder with photopole array

6.2 Literature Review of Previous Experiments

Previous experiments have been conducted to measure either wave forces or wave runup in the diffraction regime; however, the goal of most experiments has been to verify linear diffraction theory. Only one other study, that of Raman and Venkatanarasaiah (1976a, 1976b), has included both a second-order theory and a series of laboratory experiments designed to test the nonlinear theory. Other proposed second-order theories have used data from the literature for comparison, but usually only a few selected data points have been considered; therefore, no proposed second-order theory has been rigorously tested.

Data from wave runup experiments in the diffraction regime are extremely limited, and no data are available for wave scattering or diffraction patterns around the cylinder. Chakrabarti and Tam (1975) present the only significant data set for wave runup, with runup distributions published for 27 experiments. For ka less than 0.2, scattering was minimal and the runup distribution did not vary with changes in the wave period. As the relative cylinder

size, ka, increased (wave period decreased), the runup distributions changed, with larger runup occurring for larger cylinder sizes, although results did not show this consistently. At any fixed set of ka or kd values, runup always increased as the wave steepness increased. The observed runup was not compared to a theory.

Laird (1955), Nagai (1973), and Raman and Venkatanarasaiah (1976) each present runup data from a small number of experiments. Few definitive conclusions may be made except that the measured runup is found to be significantly larger than linear runup theory as wave steepness is increased. Nagai also found that in 8 of 9 cases, measured maximum runup exceeded twice the incident wave amplitude. The most extensive series of wave runup experiments are summarized by Hallermeier (1976); however, most tests were performed in shallow water and with small diameter piles. Isaacson (1978) compared measured runup data from large cylinders in shallow water to an approximate theory for diffraction of cnoidal waves and found that the cnoidal theory is much better than linear theory, although the nonlinear theory still underestimates the maximum runup.

The first experimental sudies of wave forces in the diffraction regime seem to be those of Laird (1955) and tests reported by Nagai (1973). Laird used waves of low steepness but found that measured pressures over depth were generally smaller than those predicted by linear theory. Nagai found that in 7 out of 9 experiments with higher wave steepness, the total wave forces were also smaller than those estimated by linear theory.

Chakrabarti and Tam (1973) measured total wave forces for a fixed depth-to-radius ratio, $d/a = 1.16$. Results are presented for the maximum forces measured at a given wave period, presumably associated with the largest wave steepness at each period; therefore, force data are presented for only 18 cases whereas runup data are given for 27 cases from the same test series. Results generally agreed with linear theory with 7 tests yielding measured forces larger than those predicted while 11 tests gave smaller measured forces. Maximum measured forces exceeded linear theory significantly, i.e. by more than 10 percent, in only three cases.

Hobgen and Standing (1975) measured total forces for 22 different wave conditions with $d/a = 5.0$. Only 4 of the test conditions gave measured forces that even marginally exceeded those predicted by linear theory; 18 cases gave forces that were equal to or less than the linear theory with 14 measured values being significantly less than the linear prediction.

Mogridge and Jamiesen (1976) performed the most extensive set of experiments concerning wave forces in the diffraction regime; results are presented for 91 experiments covering a range of intermediate water depths, with $d/a = 1.13$ to $d/a = 4.8$. Only the average force amplitude of the positive and negative maximum forces was reported. For given ka and kd conditions, measured average forces departed from linear theory as the wave steepness was increased. However, this departure was not certain nor systematic as in some cases measured forces increased, while in other cases measured forces decreased, relative to linear theory. The most systematic departure from linear theory was found for steep waves in relatively shallow water for the smallest relative cylinder sizes, where forces consistently exceeded linear theory. It was concluded that linear theory was generally valid for the range of conditions tested, but average forces that differed from linear theory by more than ± 20 percent were observed.

Raman and Venkatanarasaiah (1976a, 1976b) carried out 19 experiments and found a systematic deviation of measured forces from linear theory. For the largest dimensionless depths, measured nondimensional forces were smaller than linear theory and decreased further as the wave steepness was increased. For smaller ka values and in smaller dimensionless depths, measured forces were found to exceed linear theory and increased further as the wave steepness increased.

A comparison of all of the available wave force data is given in Figure 6.5 where 170 test results, including those from this study, are presented. The measured forces are normalized as

$$\tilde{F} = \frac{F}{\rho g a H d(\tanh kd/kd)} \tag{6.2}$$

which has been used throughout this study since linear theory collapses to a single curve

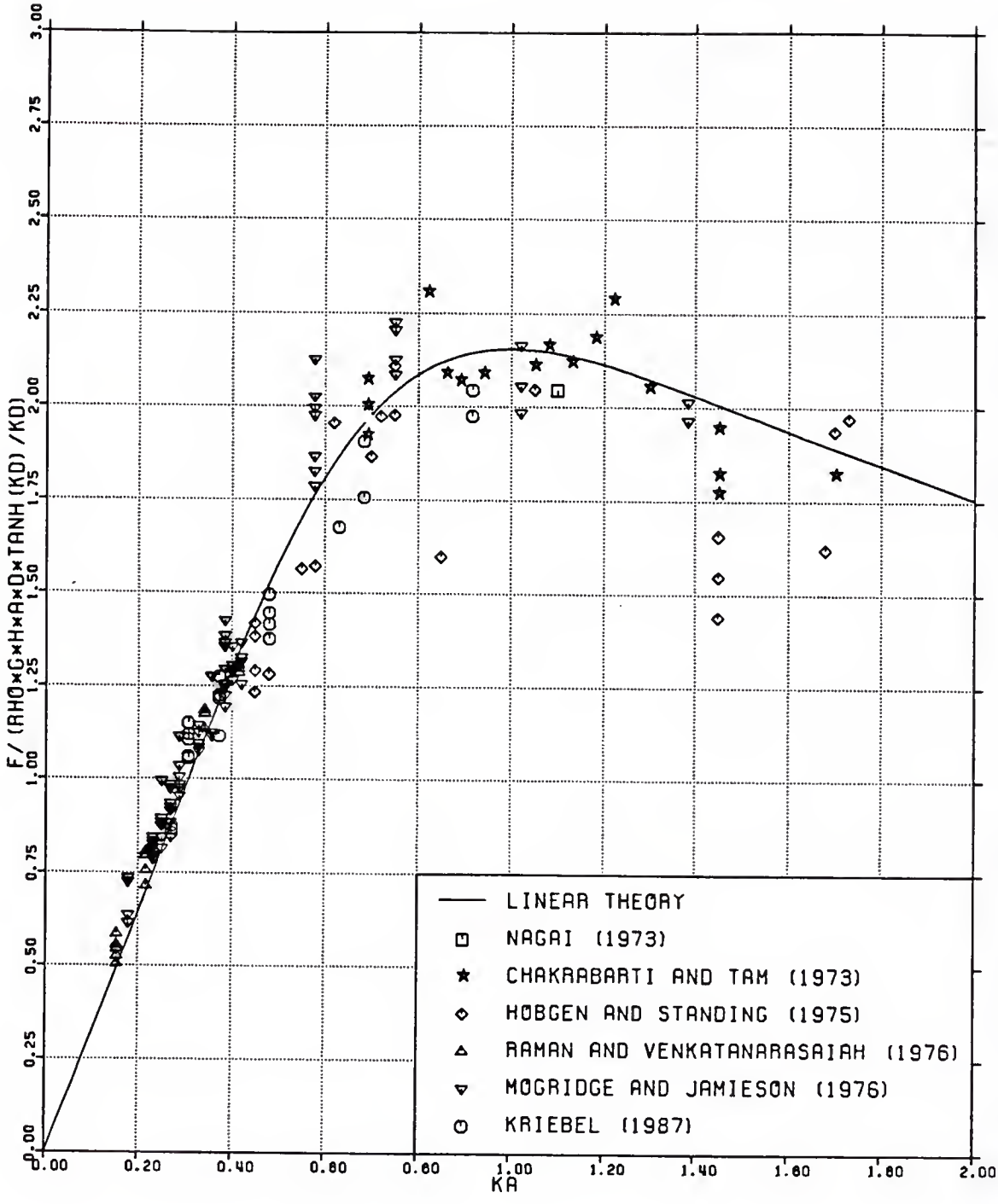

Figure 6.5: Comparison of linear theory to available force data in the diffraction regime

as a function of ka. The data have not been separated according to dimensionless depth or wave steepness effects, and it is not possible to distinguish between maximum or average forces based on information presented in published papers.

In spite of the lack of uniformity in the reported data, several aspects of measured forces are immediately evident. For ka values less than 0.4, the data are well-behaved. Consistent features of the measured forces in this regime are (1) an increase in nondimensional forces relative to linear theory, in some cases by more than 20 percent, (2) a unidirectional increase in nondimensional forces with increasing wave steepness, and (3) an increase in forces compared to the theoretical inertia force, based on local fluid accelerations from linear wave theory with $C_m = 2.0$. While most tests in this regime are dominated by nonlinear inertia forces, diffraction and nonlinear scattering become important in this regime as well.

For ka around 0.4 to 0.5, a transition seems to occur in the loading regime. At larger values of ka, measured forces are predominantly smaller than those predicted by linear theory; however, data are widely scattered about the linear curve and no clear trend is evident. For a given value of ka, measured forces vary from as much as 25 percent greater than linear theory to 35 percent less than linear theory. Approximately 35 percent of the measured forces are larger than the linear force estimate while 65 percent of the data are smaller than the predicted linear force maxima.

It is not clear whether the data scatter is due to laboratory measurement techniques or nonlinear features of the wave-structure interaction; possible explanations are discussed at the end of Chapter 7. Of the different data sets, the data of Mogridge and Jamieson (1976) are the most consistent and are generally greater than linear theory up to $ka = 1.0$. The data of Chakrabarti and Tam (1975) are also fairly consistent but are generally smaller than linear theory except for a few data points. The data of Hobgen and Standing (1975) have the most scatter and also show the smallest measured forces relative to linear theory.

Some data also exist for the time-averaged drift forces that occur for nonlinear wave loadings in the diffraction regime. Chakrabarti (1984b) presents results of 40 measurements

obtained from the same wave force data set analyzed by Chakrabarti and Tam (1973, 1975). In general, measured drift forces are found to be two to three times larger than the theoretical predictions. Herfjord and Nielsen (1985), on the other hand, found that the measured drift forces were in good agreement with the theory; out of 16 experiments, drift forces were larger than the theory for 8 tests, smaller than theory for 6 tests, and were in the opposite direction, i.e. opposing the direction of wave advance, for 2 tests. Otherwise, few definitive measurements of drift forces appear in the published literature.

6.3 Results of Wave Runup/Rundown Experiments

The results of the wave runup/rundown experiments and the comparison of the second-order theory to the laboratory data are presented in Figures D.1 through D.22 in Appendix D. The data in these figures include (1) the visually averaged runup/rundown envelopes at 15 degree intervals around the circumference of the cylinder, and (2) the maximum and minimum runup/rundown excursions observed at 45 degree intervals to give an indication of the regularity of the envelope. Each figure gives a comparison of the measured runup/rundown data to both linear and second-order theory.

Based on a comparison of the data to linear theory, several general conclusions may be reached. Maximum wave runup at the front of the cylinder is greater than that predicted by linear theory in all cases. The maximum runup also exceeds twice the incident wave amplitude for steep waves and for large relative cylinder sizes when significant scattering occurs. A highly nonlinear runup mechanism occurs for waves near breaking, as observed in Figures D.17, D.18, and D.22. In these cases, the wave steepness was near the practical breaking limit for the wave basin and runup occurred as a vertical jet, producing a thin film of water over the leading half of the cylinder. At the rear of the cylinder, the wave crest amplitude is greater than that predicted by linear theory in all cases, indicating that significant nonlinear diffraction effects are present. In general, runup distributions around the circumference are poorly predicted by linear theory. Finally, the rundown amplitudes in the front and rear of the cylinder are not as large as predicted by linear theory.

Nonlinear runup/rundown characteristics are now considered beginning with Figures D.1, D.2, and D.3, for the smallest relative cylinder size and depth. The measured runup profile is almost exactly predicted over all angular positions by the second-order theory for all three cases. For the first two tests, Stokes second-order theory is expected to be valid, while for the highest wave steepness, conditions are in the range where cnoidal theory may be more appropriate. For all cases, the predicted maximum runup amplitude is slightly larger than the measured runup; these are the only tests where the nonlinear theory overpredicts the maximum runup. Wave trough or rundown amplitudes are well predicted at the front and rear for the higher steepnesses; while linear theory predicts the rundown envelope better for the lowest steepness.

In Figures D.4, D.5, D.6, D.7, and D.8, for $ka = 0.308$ and $kd = 0.853$, second-order predictions for wave runup distributions are in good agreement with the data for the first three wave steepnesses tested, corresponding to the conditions where Stokes second-order theory is expected to be valid. At higher values of kH, the nonlinear theory predicts substantially larger runup than linear theory, however, the measured runup is even larger. The position of the minimum in the runup distribution is forward of its observed position, and the theory gives a smaller nodal amplitude at this point as the steepness increases while the data show a larger amplitude with increasing steepness. The maximum runup at the rear is higher and more localized in the data, although the nonlinear theory predicts a substantial localized recovery of the wave height in this area due to nonlinear diffraction. The rundown envelope is also predicted fairly well for the first three cases. The large trough amplitudes predicted near 60° are displayed erratically in the data and the rundown is usually not as large as predicted.

The same general observations apply to the next data set, given in Figures D.9, D.10, D.11, D.12, and D.13, for $ka = 0.374$ and $kd = 1.036$. The second-order theory is found to accurately predict the runup and rundown envelopes only for the smallest values of the wave steepness where second-order theory is expected to be most appropriate. For higher

steepnesses, where higher-order theories are better, the second-order diffraction theory again gives increasingly large runup but not as large as observed. The nonlinear theory again predicts a large rundown just aft of the shoulder which is not found in the data, except at low values of kH.

In Figures D.14, D.15, D.16, and D.17, corresponding to $ka = 0.481$ and $kd = 1.332$, the nonlinear theory shows good agreement for the conditions where Stokes second and third-order theories are valid according to Figure 6.2. The maximum runup is slightly underpredicted but the runup distribution has the correct form and the minimum runup location is predicted accurately. For this data set, the second-order theory indicates substantial cancellation of the various second-order wave components, giving fairly small theoretical runup amplitudes; the data seem to confirm this feature. For the last test, where a high-order theory is required, supercritial runup occurs in the form of a vertical jet and the second-order theory badly underestimates the runup distribution over the leading half of the cylinder. Once again, rundown is not well predicted, and the large rundown excursion near the shoulder is not displayed in the data.

In Figure D.18, for $ka = 0.631$ and $kd = 1.745$, supercritical runup again occurs as the wave steepness is near the breaking limit. Theoretical runup amplitudes over the sides and rear of the cylinder are in agreement with the data; however, as are the rundown amplitudes over the front half. In Figures D.19 and D.20, for $ka = 0.684$ and $kd = 1.894$, the nonlinear theory is very accurate for the smaller steepness where Stokes third-order theory should be applicable, but maximum runup is underpredicted for the higher steepness where high-order Stokes theories are most appropriate. For both cases, most of the predicted features of the runup distributions are predicted, including the slight increase in runup heights near 75°. Rundown amplitudes are also in agreement, except in the region near 60°.

Finally, in Figures D.21 and D.22, for $ka = 0.917$ and $kd = 2.536$, the runup/rundown envelope is predicted very accurately for the lowest steepness where, again, Stokes 3rd order theory is thought to be most appropriate and the wave steepness is fairly high, $kH = 0.631$.

In this case, both the maximum runup at the front and at the rear are predicted almost exactly. For the higher steepness, $kH = 0.806$, wave breaking occurred in the basin and supercritical runup occurred; this was the most erratic test condition as cross-waves became very important. While the average runup was more than three times the incident amplitude, the runup varied wildly depending on whether the incident wave was breaking or broken. The highest runup seemed to occur for waves just about to break. Interestingly, the rundown distribution is well-predicted over the leading half of the cylinder.

The overall agreement of first or second-order runup predictions is evaluated in Figures 6.6 through 6.8. In Figure 6.6, the measured maximum crest amplitude, at $\theta = \pi$, is compared to linear theory at the top of the page and to the second-order theory at the bottom of the page. Linear theory is found to underpredict runup in all cases. Measured maximum runup amplitudes exceed he linear runup prediction by 13 to 83 percent, and by 44 percent on average. In contrast, the agreement between the second-order theory and measured runup data is much better, although the nonlinear theory still underpredicts the highest runups, especially for waves near breaking. Measured runup amplitudes exceed the second-order theory by up to 43 percent for the highest steepness tested, but are smaller than the predicted runup by up to 5 percent in other cases. On average, measured runup exceeds the second-order theory by 11 percent.

In Figures 6.7 and 6.8, the measured maximum runup amplitudes are compared to the first and second-order theories in a different format as a function of wave steepness and relative depth. The percent difference between the observed maximum runup, R_{max}, and the first-order maximum runup, R_1, or the second-order maximum runup,R_2, is defined as

$$\frac{R_{max} - R_1}{R_1} \cdot 100\% \qquad \text{and} \qquad \frac{R_{max} - R_2}{R_2} \cdot 100\%$$

The numbers in the figures indicate the percentage difference for each test, with positive numbers indicating the percentage by which the measured data exceeds the theoretical prediction.

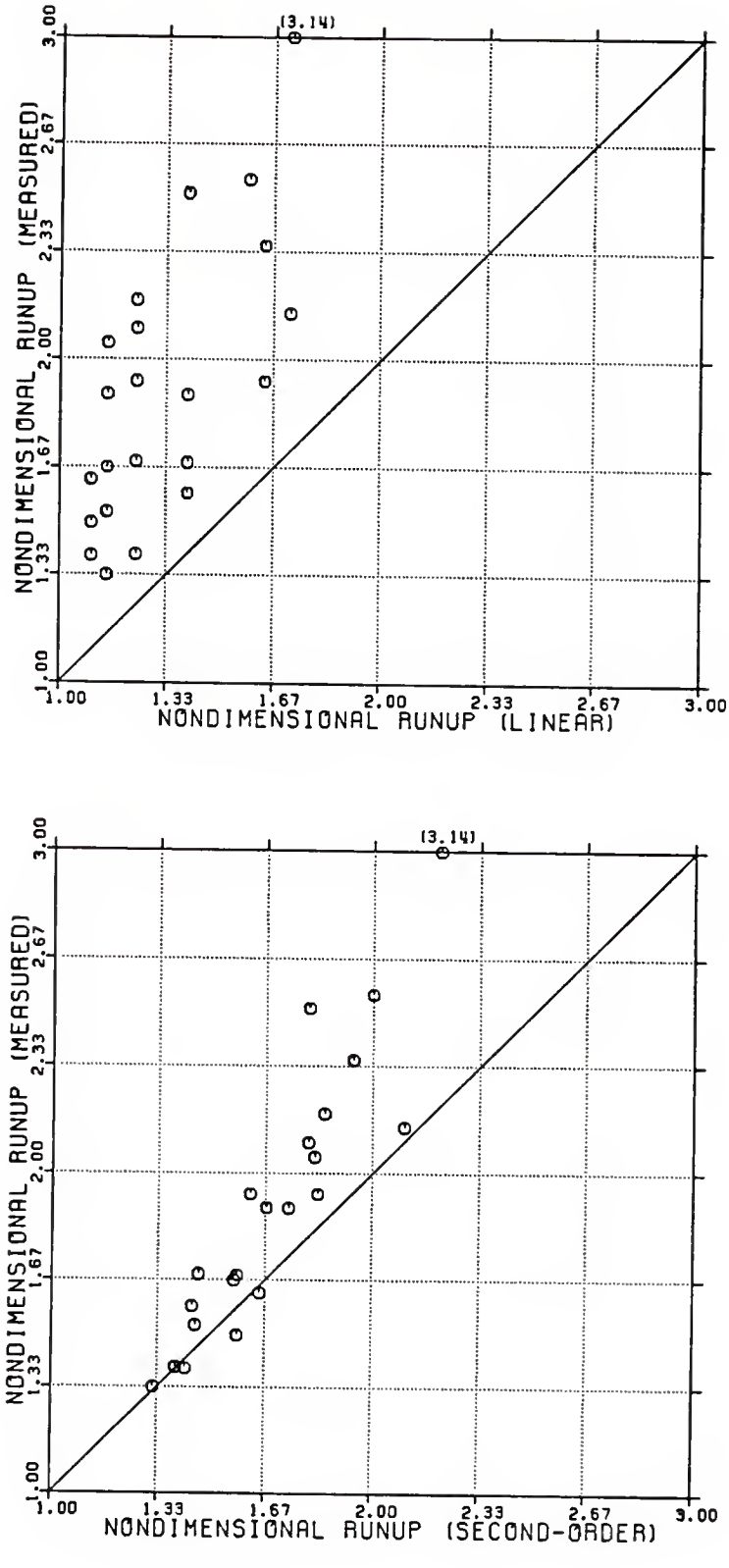

Figure 6.6: Comparison of measured runup to linear and second-order theories

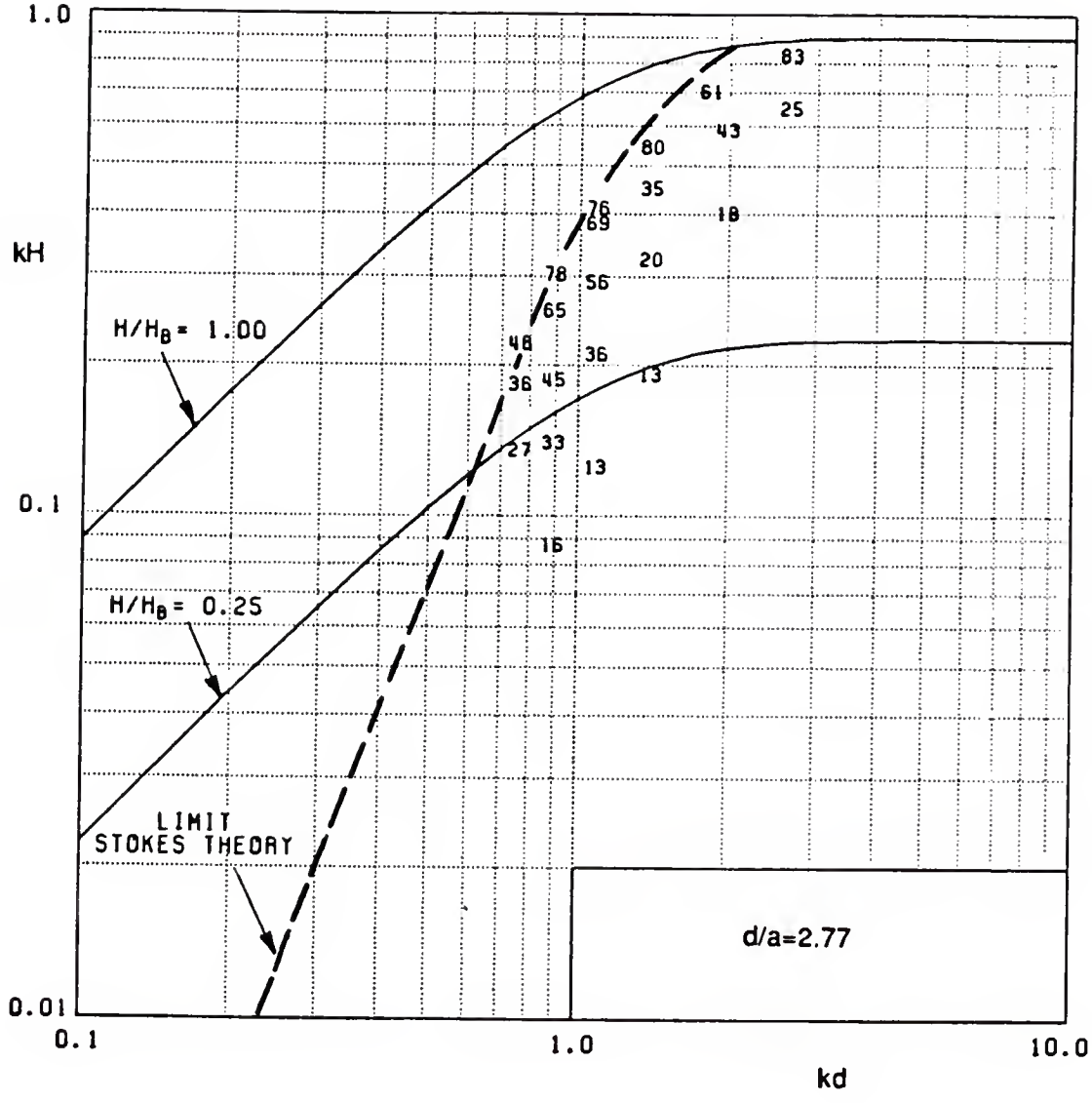

Figure 6.7: Percentage difference between measured maximum runup and linear theory

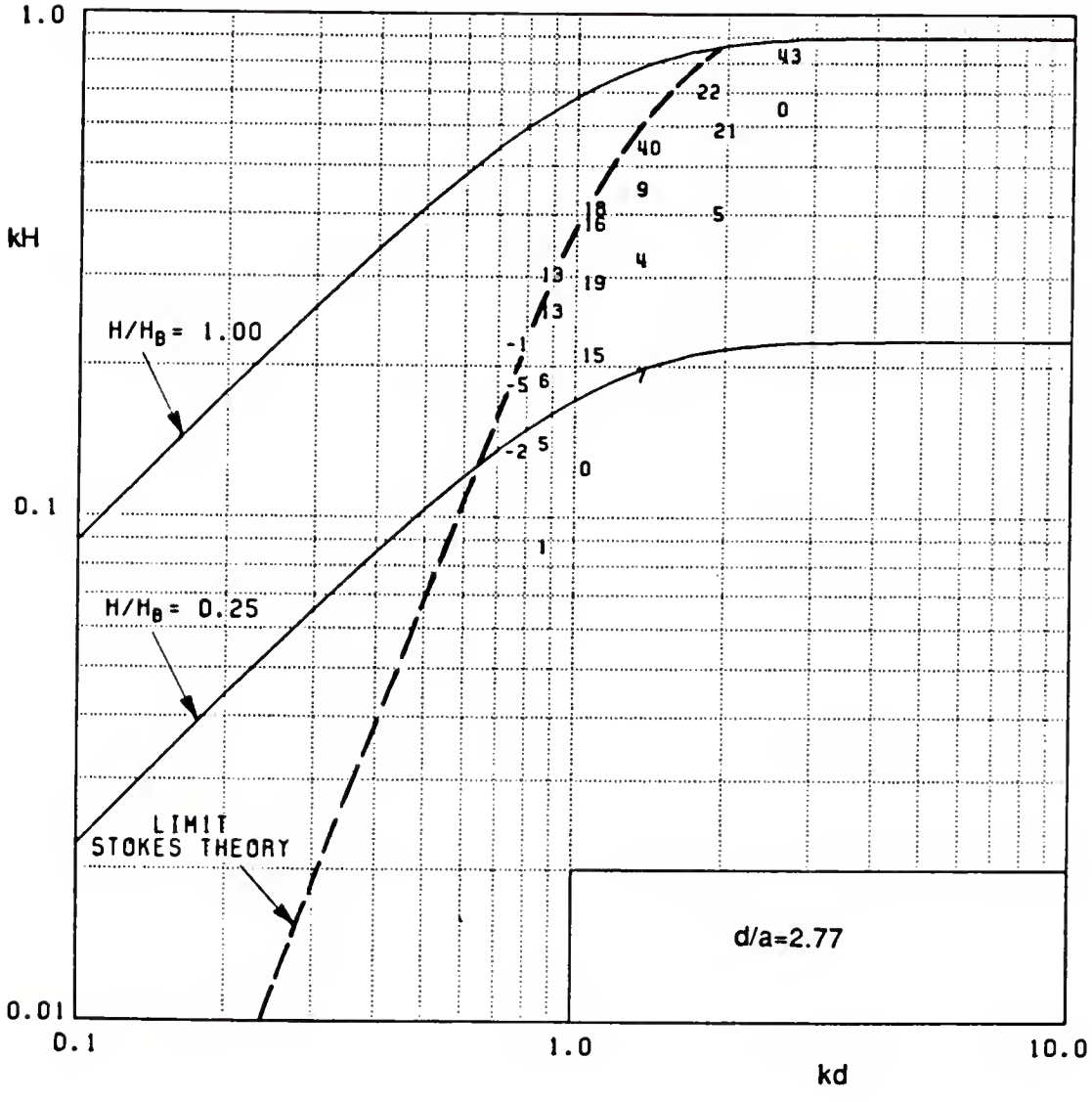

Figure 6.8: Percentage difference between measured maximum runup and second-order theory

As shown in Figure 6.7, linear theory consistently underpredicts the observed maximum runup, with errors on the order of 60 to 80 percent occurring for very steep waves near deep water but even for moderately steep waves as the relative depth decreases. In Figure 6.8, second-order theory overestimates the maximum runup in 3 cases at the smallest relative depth (and smallest relative cylinder size) tested while for the other 19 tests, the nonlinear theory underestimates the runup amplitude. For steep waves where higher-order Stokes theories are more appropriate, the measured data exceeds the second-order runup prediction by 20 to 40 percent, with the largest errors being associated with the jet-like runup which occurred on 3 tests. For smaller wave steepnesses and smaller relative depths (smaller values of ka), the nonlinear theory is exceeded by less than 5 to 10 percent in most cases. The agreement with the data is especially good for the conditions near the limit of validity of the Stokes theory, and within the region in which the Stokes second-order theory is normally considered valid.

6.4 Results for Photopole Experiments

The results for the photopole experiments are presented in Appendix E in Figures E.1 through E.12. The photopole experiments were conducted for 12 wave conditions, generally corresponding to the two or three lowest values of the wave steepness for each ka and kd pair, although this included some very steep waves. The visual observations of the wave crest and trough envelopes are compared to the first and second-order theoretical solutions, which have been extended out to $r = 10a$ to give a better indication of the overall scattering and diffraction patterns along the x axis.

The photopole data seem to verify the general features of the wave envelopes predicted by the second-order theory. For the smallest cylinder sizes tested, $ka = 0.308$ and $ka = 0.374$, in Figures E.1 through E.6, the second-order wave envelope is dominated by the second-order plane wave term and its associated scattered components, although other forced-radiated terms account for up to 40 percent of the variation in the wave envelope. Since the plane wave is locked in phase with the linear wave, crest amplitudes are uniformly

increased everywhere. The scattering of the plane wave (plus other forced-radiated and scattered waves) generates outwardly radiating free waves that interact with the incident wave field to produce secondary maxima and minima in the envelope compared to linear theory. The photopole data confirm the positions and magnitudes of these maxima and minima for both the wave crest and trough on the upwave side. On the downwave side, the second-order corrections do not produce significant modulations in the envelope; to within measurement accuracy, the data verify this theoretical prediction.

The data in Figures E.7 through E.9, for $ka = 0.481$, represent the transition condition where, on the upwave side, the nonlinear theory predicts significant cancellation of second-order components. This is especially important near the cylinder where it leads to reduced wave runup. Away from the cylinder, secondary maxima and minima are predicted in the envelope. The photopole data again confirm the locations and, approximately, the magnitudes of these envelope variations. On the downwave side, the superposition of the second-order free waves with the incident linear wave and its bound harmonics, produces a spatially varying envelope. The data agree with the theoretical crest elevations, while in the wave trough, the predicted envelope has the correct form but the measured magnitudes are much smaller than the predicted values, possibly due to flow interference from the submerged load cell.

At the largest ka values, $ka = 0.684$ and $ka = 0.917$ in Figures E.10 through E.12, the theoretical wave envelopes on the upwave side are dominated by the quadratic terms and long standing wave motion of the second-order velocity potential. The envelope is similar to the linear envelope except that the crest elevations are increased while troughs are reduced. No secondary maxima are predicted in between maxima of the first-order envelope, in contrast to the results at smaller values of ka. In general, the photopole data seem to strongly verify these envelope features. On the downwave side, significant spatially modulated envelopes are predicted. Data from the wave crest envelopes provide a rough verification of these nonlinear diffraction effects, as the presence and approximate spacing

of the predicted envelope maxima and mimima are confirmed, although the measured envelopes are more poorly defined. The trough envelopes are again found to differ from the theoretical prediction, although the general form of the predicted envelope is found.

6.5 Results of Wave Force Experiments

The results of the wave force measurements are presented in Figures F.1 through F.22 in Appendix F. Each figure contains two parts (1) a comparison of the theoretical solutions from first and second-orders for the depth-integrated forces as well as for the free surface elevation over one wave period at a position $\theta = \pi/2$ and $r = 10a$, and (2) a comparison of the phase-averaged laboratory measurements for wave forces and for the wave profile at $\theta = \pi/2$ and $r = 10a$. The figures in Appendix F provide a visual comparison of the agreement between the laboratory data and theory. In addition, the theoretical and phase-averaged time series are analyzed to obtain the spectral amplitudes of the first three Fourier components. The results of this analysis are presented in Table 6.3 where second and third-order amplitudes, i.e. at frequencies 2σ and 3σ, are normalized by the fundamental amplitude to facilitate comparison.

The data in Figure F.1 to F.3, for the smallest relative cylinder size, $ka = 0.271$, and relative depth, $kd = 0.750$, are the most irregular in the data set. The measured wave profiles are highly distorted on the front face, and the measured forces in the direction of wave propagation are smaller than predicted. The wavemaker was operated at the longest possible wave period in these tests and it is thought that mechanical irregularities in the wavemaker caused the unusual wave forms. During the reversal of the flow direction, measured and theoretical wave forms agree fairly well, and measured forces are of the same magnitude as those predicted, but shifted in phase. Measured second-order wave amplitudes are smaller than those predicted and third order amplitudes are fairly large. Measured second-order force amplitudes agree almost exactly with those predicted, but again significant force amplitudes are present at frequency 3σ. Drag forces would appear at odd harmonic frequencies, so it is possible that some flow separation occurred in these tests.

Table 6.3: Normalized Fourier Amplitudes for Wave and Force Data

		Wave Profile at $r = 10a$ and $\theta = \pi/2$			Force Trace		
		2nd Order Theory	Measured		2nd Order Theory	Measured	
ka	kH	a_2/a_1	a_2/a_1	a_3/a_1	a_2/a_1	a_2/a_1	a_3/a_1
0.271	0.132	0.15	0.10	0.05	0.21	0.20	0.06
	0.178	0.20	0.15	0.07	0.28	0.22	0.06
	0.215	0.25	0.18	0.09	0.33	0.30	0.07
0.308	0.085	0.08	0.09	0.05	0.10	0.15	0.01
	0.137	0.13	0.19	0.03	0.15	0.22	0.01
	0.182	0.18	0.23	0.03	0.20	0.27	0.03
	0.250	0.25	0.26	0.03	0.26	0.30	0.04
	0.296	0.29	0.31	0.01	0.30	0.32	0.05
0.374	0.122	0.09	0.11	0.00	0.06	0.11	0.01
	0.205	0.14	0.21	0.05	0.10	0.15	0.01
	0.286	0.20	0.23	0.04	0.13	0.17	0.01
	0.385	0.27	0.27	0.10	0.18	0.27	0.06
	0.402	0.28	0.29	0.10	0.19	0.23	0.06
0.481	0.186	0.09	0.13	0.02	0.03	0.05	0.00
	0.317	0.15	0.19	0.06	0.06	0.05	0.03
	0.438	0.21	0.27	0.05	0.08	0.10	0.03
	0.530	0.25	0.29	0.07	0.09	0.10	0.04
0.631	0.683	0.33	0.26	0.09	0.10	0.02	0.01
0.684	0.391	0.11	0.07	0.02	0.08	0.03	0.01
	0.572	0.16	0.10	0.06	0.12	0.07	0.03
0.917	0.631	0.14	0.14	0.04	0.04	0.08	0.04
	0.806	0.18	0.15	0.06	0.05	0.14	0.06

The next group of experiments, with $ka = 0.308$ and $kd = 0.853$ in Figure F.4 through F.8, provide good agreement between the second-order theory and measured data. Except for the lowest wave steepness, measured and predicted wave forms agree very well. Force traces also agree almost exactly for the three lowest values of wave steepness. In these cases, nonlinearities are apparent which cause a slow increase in forces in the positive direction, a sudden reversal in the force direction under the wave crest, and maximum force magnitudes in the negative direction. These nonlinearities are the result of the dominance of the second-order plane wave components and are common features of nonlinear inertial forces. For the two highest steepnesses, measured negative forces are smaller than those predicted and are smaller than positive forces. Fourier amplitudes of both forces and free surface show good agreement; however, measured force amplitudes are consistently smaller than those predicted.

In Figures F.9 to F.13, measured time series for $ka = 0.374$ and $kd = 1.036$ again provide verification of the second-order theory for the three lowest steepnesses where Stokes second-order theory is expected to be applicable. As in the previous data set, maximum negative forces are larger than positive forces in both the measured data and the second-order theory. Nonlinearities in the force traces are reproduced accurately, especially the more abrupt transition from positive to negative forces than is found in linear theory. Plane wave terms and their associated scattered waves again dominate the loading regime, although other forced-radiated terms are also important and account for about 25 to 40 percent of the total second-order force amplitudes. For the two highest steepnesses, predicted maximum force magnitudes agree with the data, but there is poor agreement over the complete wave period. Second-order Fourier amplitudes for the wave profile and force trace are in good agreement, but for the two highest steepnesses, large third order forces are measured.

As discussed previously, for the conditions $ka = 0.481$ and $kd = 1.332$, the second-order solution indicates nearly complete cancellation of the various second-order wave and force components. Measured wave runup data supported this theoretical result and measured

wave profiles and force traces seem to provide further confirmation. Predicted forces do not differ significantly from linear theory. Measured force maxima are also similar to the linear prediction and show no strong preference in direction. Although net second-order forces are small, individual second-order components are much larger. Quadratic terms and terms from the second-order velocity potential are each approximately twice as large as the net second-order force amplitude; but, due to phase shifts, they cancel to produce a small net second-order force correction. The amplitude of the Fourier components show that measured second-order force amplitudes are nearly identical to those predicted. In all four tests, measured force maxima are smaller than maximum forces predicted by linear theory.

For the remaining tests, with $ka = 0.631$, $ka = 0.684$, and $ka = 0.917$, measured force maxima are always smaller than those predicted by linear theory; therefore second-order theory consistently overestimates maximum force magnitudes. This occurs even though (1) very large wave steepnesses were tested, with kH from near 0.6 up to 0.8, and (2) incident waves were near or at the effective breaking limit. Force maxima are not modified significantly from linear theory, however, either in the second-order theory or in the measured data. Significant forces are found at a wave phase of 0.0, mostly due to phase shifts in the first and second-order scattered wave components as predicted by the nonlinear theory. For the highest steepness tested, however, it appears that separation probably occurred near the free surface due to local breaking along the sides of the cylinder; significant force amplitudes are found at frequency 3σ. For these tests, the fixed wave gage is at a different position relative to the nodes and antinodes of the free surface envelope for each ka condition, accounting for the variations in predicted and measured wave forms from one test to the next.

The overall comparison of the measured force data to first and second-order theories is presented in Figures 6.9 through 6.11. In Figure 6.9, measured maximum forces (positive or negative, whichever is larger) are compared to maximum forces predicted by linear theory

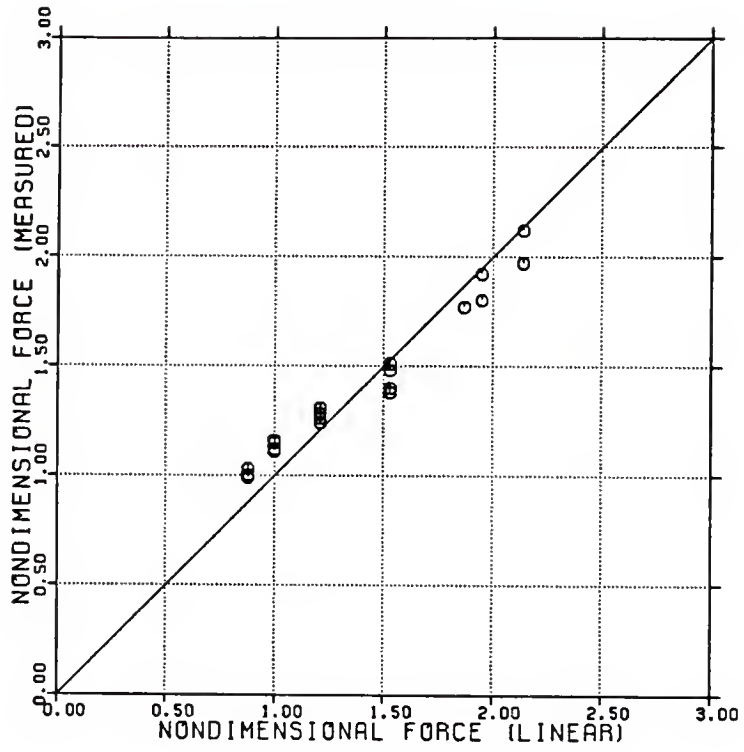

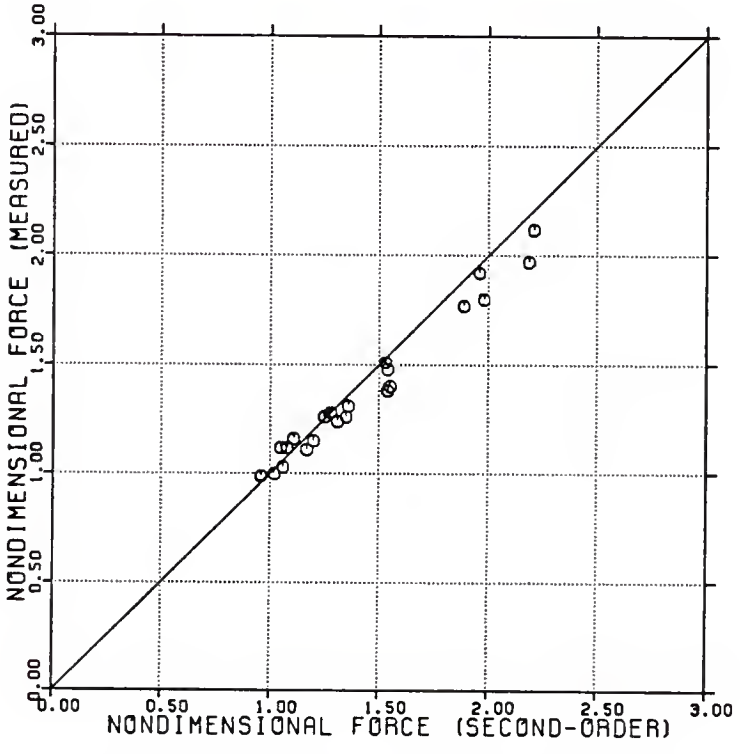

Figure 6.9: Comparison of measured maximum forces to linear and second-order theories

at the top of the page and to the second-order theory at the bottom of the page. For larger ka values, linear and nonlinear theories give comparable force estimates; however, linear theory provides better agreement since measured maximum forces are even smaller than the linear forces. For the smaller nondimensional forces, which correspond to the smallest ka values tested, linear theory consistently underpredicts the magnitude of maximum forces. For these same conditions, however, second-order theory makes significant improvements in force predictions, and even overestimates the force magnitudes slightly in some cases.

This same information is presented in Figures 6.10 and 6.11, in which the percentage differences between measured force maxima and first and second-order theories are given as

$$\frac{F_{max} - F_1}{F_1} \cdot 100\% \qquad \text{and} \qquad \frac{F_{max} - F_2}{F_2} \cdot 100\%$$

In Figure 6.10, linear theory is found to overpredict measured force maxima slightly for larger ka and kd values, but to underestimate maximum forces by 10 to 18 percent at lower ka and kd values. In contrast, in Figure 6.11, the second-order theory is found to give slightly larger errors for larger kd (and ka) values, but near-exact agreement for smaller relative depths and smaller cylinders. The second-order diffraction theory gives the smallest errors of 0 to 4 percent near the limit of validity of Stokes theory.

An additional comparison is made between the theoretical and measured drift forces, as shown in Figure 6.12. In this figure, measured mean forces and the second-order theory have been normalized by $\rho g a H^2$ in order to facilitate comparison, since for a fixed d/a ratio, the theory collapses to a single curve as a function of ka. The agreement of the data is remarkably good, considering that drift force magnitudes are approximately 5 percent of the dynamic force magnitudes. On a percentage basis the drift force theory differs from the data by up 45 percent, however, the data seem to confirm the validity of the second-order theory over a broad range of conditions, including the region of maximum nondimensional drift forces, near $ka = 0.9$.

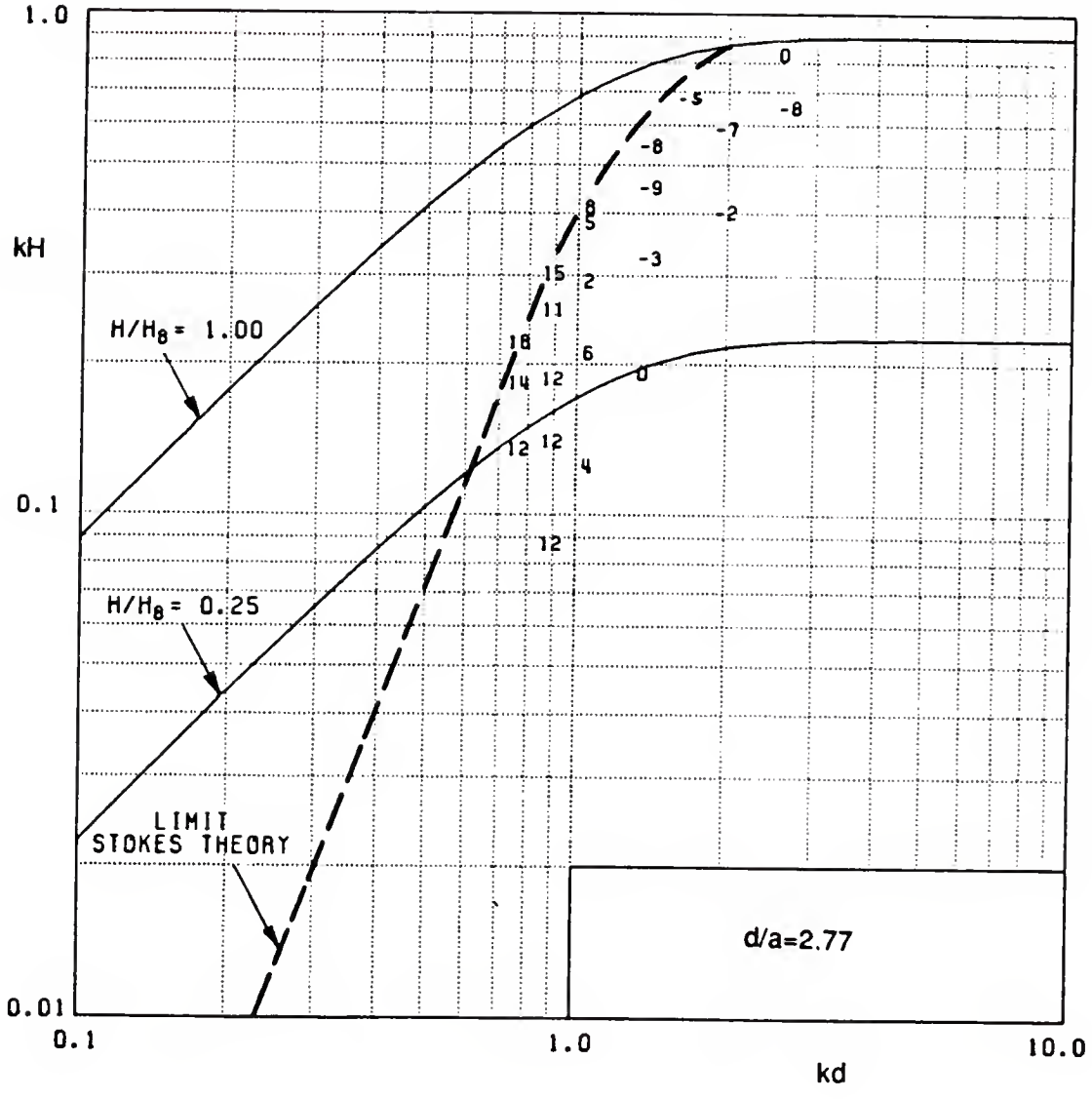

Figure 6.10: Percentage difference between measured maximum forces and linear theory

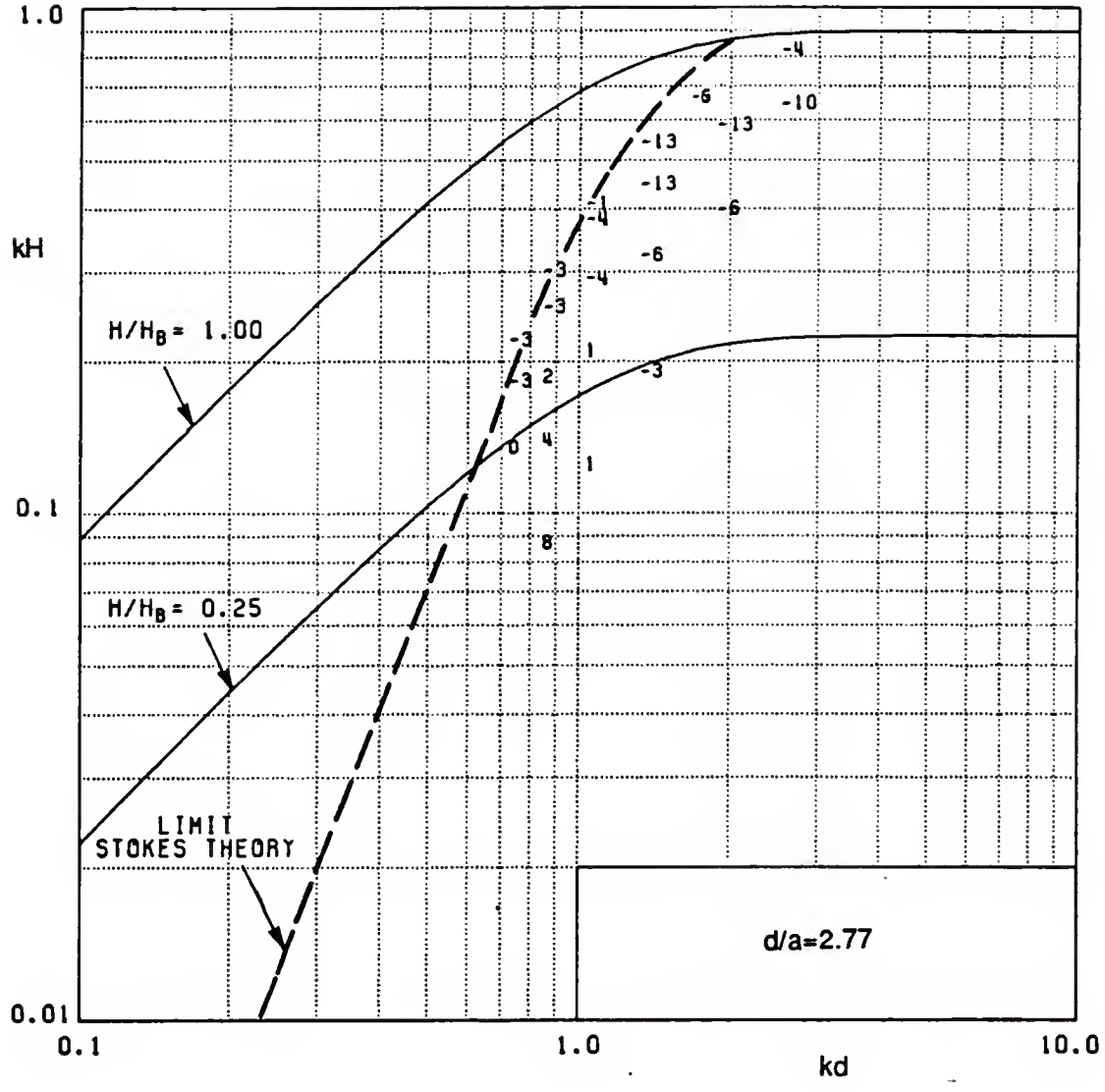

Figure 6.11: Percentage difference between measured maximum forces and second-order theory

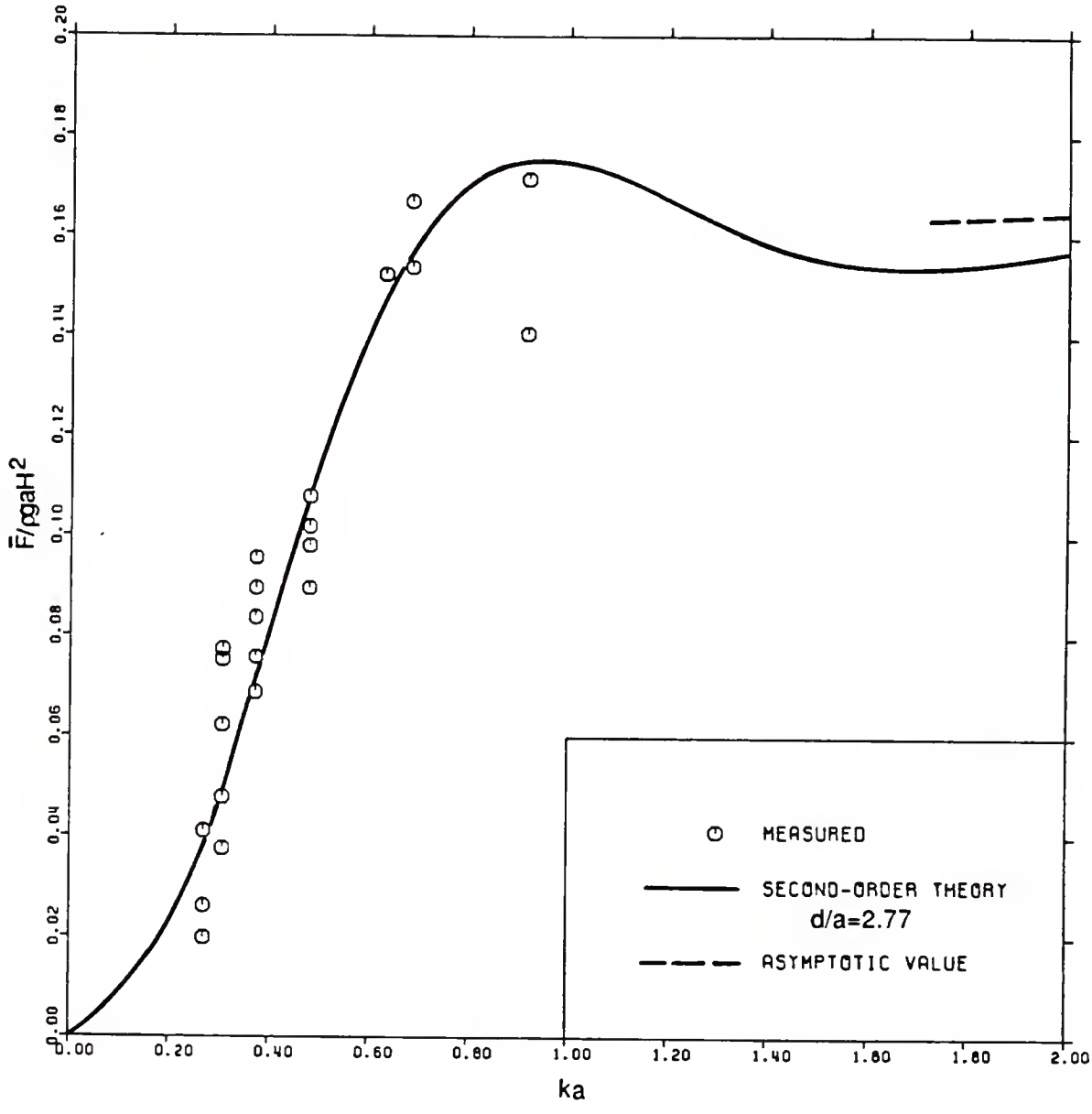

Figure 6.12: Comparison of measured drift forces to second-order theory

CHAPTER 7
SUMMARY AND CONCLUSIONS

A nonlinear diffraction theory has been developed for the interaction of second-order Stokes waves with a large vertical circular cylinder. The solution procedure is based on a perturbation expansion approach in which separate boundary value problems are obtained for the first and second perturbation orders. At first-order, the solution is the linear diffraction theory of MacCamy and Fuchs (1954) which consists of a linear incident plane wave plus a scattered wave which radiates outward away from the cylinder in all directions. Both the incident and scattered waves satisfy the linear dispersion relationship

$$\sigma^2 = gk \tanh kd$$

since they oscillate at frequency σ with the linear wavenumber k.

At second-order, the boundary value problem is complicated by (1) the presence of nonhomogeneous quadratic forcing terms in the free surface boundary condition and (2) the lack of a well-posed radiation condition. The quadratic forcing on the free surface is the result of nonlinear wave-wave interactions of the first-order incident and scattered waves. Three components of nonlinear interactions exist. One component is due to the nonlinear self-interaction of the first-order incident plane wave. This forcing generates the usual Stokes second-order plane wave component, at wavenumber $2k$ and at frequency 2σ. In addition, two other forcing terms exist due to the self-interaction of the first-order scattered wave and due to the cross-interaction between the first-order incident and scattered waves. Both forcings oscillate at frequency 2σ and propagate outward away from the cylinder, but not with a simple wavenumber behavior nor with a simple amplitude decay over r and θ. These forcing components are shown to have the same effect as an external pressure applied to the free surface which generates additional waves at second order.

The particular solutions for these forced wave motions are obtained by a source distribution method in closed integral form. First, the solution is obtained for a single isolated point source of pressure oscillating on the free surface with frequency 2σ. This solution is given in terms of local standing waves near the point source; however, far from the source, second-order free waves are found which radiate away from the source with a wavenumber, k_2, that satisfies the second-order dispersion relationship

$$4\sigma^2 = gk_2 \tanh k_2 d$$

The effects of an arbitrary two-dimensional pressure distribution are obtained by summing the wave components generated by an infinite number of elementary point sources over r and θ. The wave motions generated by the quadratic forcing in the free surface boundary condition are then found by relating the quadratic forcing to the general pressure distribution.

Based on the integrated effects of the quadratic forcing along the entire free surface, the particular solutions consist of (1) local standing waves concentrated in the vicinity of the most intense forcing on the free surface and given in terms of an integral over all wavenumbers plus (2) outwardly propagating second-order free waves which radiate away from the region of most intense forcing. The standing wave modes are forced waves, generated directly by the nonlinear ineractions of the first-order wave field in order to exactly satisfy the second-order combined free surface boundary condition. The radiated free waves, on the other hand, are waves of permanent form which are generated within the region of applied quadratic forcing but which then propagate away. These radiating free waves are analogous to second-order free waves that are generated by other nonlinear wave-wave interactions, for example over a localized shoal or at the entrance to a harbor, e.g. Biesel (1963).

The resulting forced-radiated wave motions satisfy a form of the radiation condition since the wave motions generated by each elemental point source solution satisfy the radiation condition. The variation in the quadratic forcing over r and θ leads to regions of constructive and destructive wave interference, but with a net outward radiation of second-

order free waves. In addition, it is found that the second-order wave motions are mostly generated on the upwave side of the cylinder, where strong nonlinear interactions occur as a result of the opposing motions of the first-order incident and scattered waves. The radiated waves then propagate both outward from this region as well as in the downwave direction, leading to the expected nonlinear diffraction effects.

The forced-radiated waves exist without regard for the presence of the cylinder; the solution assumes that the cylinder is "transparent" to these waves, in the same way that the cylinder is "transparent" to the first-order incident waves. In order to satisfy the no-flow requirement on the cylinder boundary, a second set of compensating wave motions must exist at second-order. These are the second-order scattered waves which are determined by exactly the same method employed at first-order. These wave motions satisfy the homogeneous form of the second-order boundary value problem and are found to consist of outwardly radiating second-order free waves, plus local evanescent or standing modes near the cylinder. While the forced-radiated motions are generated by nonlinear wave-wave interactions on the free surface, the scattered waves are generated by nonlinear wave-structure interactions between the forced-radiated waves and the vertical cylinder.

The total solution for the second-order velocity potential is found to consist, mathematically, of particular and complementary (homogeneous) solutions which physically represent (1) the Stokes plane wave component and its associated scattered waves plus (2) more complicated forced-radiated wave components and their associated scattered wave motions. The solution for the Stokes plane wave is well-known. The solution for its scattered components is identical to that proposed by Chen (1979) and Chen and Hudspeth (1982) using a Green's function approach. In this study, this solution is obtained in a more direct way through a direct eigenfunction expansion, i.e. separation of variables, that parallels the solution used at first-order and which seems to independently confirm the earlier solution of Chen and Hudspeth. The solution for the forced-radiated waves is then found to be equivalent to that obtained by Garrison (1979) through application of Green's Theorem,

also using the method of Green's functions. In this study, however, the solution is obtained in a more intuitive way that clearly displays the origin of each term in the solution. The solution is also reduced further through several simplifying integrations to obtain a closed integral form. In addition, the associated scattered waves are obtained in closed form by the same method used at first-order, unlike Garrison's integral equation solution, which must be solved numerically for an unknown source distribution function along the cylinder boundary.

The solution for the second-order velocity potential is then used to determine (1) the second-order free surface elevations around the cylinder, including wave runup on the cylinder, and (2) the depth-integrated forces on the cylinder to second-order. At first-order, linear free surface and force contributions are found from the dynamic pressure associated with the local acceleration of the first-order fluid motion. At second-order, contributions are found from dynamic pressures associated with (1) local fluid accelerations of the second-order velocity potential and (2) convective accelerations of the first-order solution (velocity-squared terms in the Bernoulli equation) plus variations of the first-order free surface above the still water level, both of which lead to quadratic terms in the second-order free surface or force expressions.

The first-order solution displays three regions of wave-wave and wave-structure interaction that, in turn, govern the behavior of the second-order solution. In the upwave region, the first-order incident and scattered waves propagate in essentially opposite directions to produce a partial standing wave system that leads to stong quadratic forcing in the second-order free surface boundary condition. Along the sides, the first-order scattered wave is small but leads to a substantial node in the first-order wave envelope, associated with the flow around the cylinder, which also produces large quadratic forcing terms. In the downwave region, the first-order incident and scattered waves propagate in the same general direction and do not produce a strongly modulated wave envelope; the resulting weak nonlinear interactions have little effect on the second-order free surface boundary condition.

At second-order the entire free surface experiences the usual uniform setdown associated with the incident plane wave. Superimposed upon this is a spatially varying setup/setdown pattern that varies around the cylinder. In the upwave region, mean water levels include alternating regions of setup and setdown, with setup occurring at antinodes of the first-order partial standing wave system. This "corrugated" mean water level pattern is analogous to the steady water levels caused by the reflection of plane waves from a vertical barrier, except in this case the amplitude of the setup/setdown decreases with distance from the cylinder and to the sides away from the x axis. On the sides of the cylinder, a deep but localized setdown occurs due to the low pressures associated with the first-order flow around the cylinder. In the downwave region, the first-order wave field has no spatially periodic modulation (except for very large cylinder sizes) but is reduced in height behind the cylinder. Mean water levels are elevated slightly at the rear of the cylinder and decrease monotonically with distance from the cylinder.

The net second-order oscillatory free surface contributions are found to depend on the relative magnitudes and phases of the various free surface components. The Stokes second-order plane wave terms are phase-locked to the first-order incident wave and increase crest heights everywhere. In addition, however, the second-order plane wave interacts with the cylinder and produces scattered free waves which may be in or out-of-phase with the incident plane wave terms, depending on the cylinder radius and relative water depth. As is well known the Stokes plane wave component in the second-order velocity potential is negligible in deep water, but becomes unrealistically large in shallow water due to resonant quadratic forcing in the free surface boundary condition. In general, the stability and convergence of the entire second-order solution is governed by the plane wave component so that the present solution seems to be limited by the same relative depth restrictions that apply to Stokes plane wave theory.

In the upwave region, second-order oscillatory quadratic terms form a partial standing wave system that decays away from the cylinder but that is mostly phase-locked to the

first-order wave field. The quadratic terms cause an increase in crest heights of the partial standing waves, and most importantly increase the runup at the front of the cylinder. The second-order velocity potential also gives a second-order partial standing wave system; and, for large ka, a long standing wave motion is found that is analogous to the plane wave microseism. These terms are generally out-of-phase with the linear and quadratic second-order terms. The overall impact of the second-order velocity potential is to reduce the wave crest heights, and especially the wave runup, from those predicted from the quadratic terms alone.

In the downwave region, quadratic free surface terms are small but behave much like a second-order locked plane wave to increase the wave crest height. The second-order velocity potential, on the other hand, is dominated by outwardly propagating free wave motions due to diffraction and scattering of the forced-radiated waves from the front of the cylinder. The combination of these second-order free waves with the linear wave and its bound second harmonic, produce a spatially modulated wave envelope in the downwave region, with localized maxima and minima and significant recovery of the wave amplitude at the rear of the cylinder.

Most of the predicted nonlinear features of the free surface are verified based on a series of 22 laboratory experiments conducted as part of the study. Wave envelopes measured for 12 of the experiments along the upwave and downwave x axes, provide confirmation that the second-order theory correctly estimates the positions and magnitudes of the wave crest (and to a lesser extent the wave trough) maxima and minima. On the upwave side, both the second-order theory and the laboratory data show that for larger cylinders, with $ka > 0.6$, nonlinearities in the partial standing wave envelope increase crest heights but do not form additional nodes or antinodes in the envelope. For smaller ka values, secondary antinodes are measured in between the primary antinodes of the first-order wave envelope; the magnitude and positions of these additional envelope features are correctly predicted by the second-order theory. In the downwave region, spatially modulated envelopes are

predicted by the second-order theory for larger cylinder sizes. Data are available for only a few cases, but measurements seem to confirm the location and magnitude of these envelope features, although not as distinctly as predicted by the theory.

The second-order wave runup and rundown envelopes around the circumference of the cylinder are found to agree with measured data for a wide range of relative depth, cylinder size, and wave steepness conditions. For wave conditions in which Stokes second or third-order theories are expected to be valid, the nonlinear diffraction theory predicts nearly exact runup and rundown distributions over the leading and trailing quadrants, while conditions near the shoulder are not as accurately predicted. The agreement of the maximum runup elevations at the front of the cylinder provide confirmation that nonlinear scattering mechanisms are correctly included while the agreement at the rear provides confirmation that nonlinear diffraction mechanisms are also realistically included.

The theoretical maximum nonlinear wave runup on the front of the cylinder is found to exceed the linear runup elevation substantially. In deep water (larger cylinder sizes) second-order runup exceeded linear runup by up to 30 percent. As relative depth decreased (and cylinder size decreased) nonlinear runup increased to exceed linear runup by more than 50 percent. Comparisons to laboratory data show that these nonlinear runup predictions are realistic and are much better than linear runup predictions. Linear theory underpredicted the maximum runup in every experiment, with measured runup exceeding the linear theory by up to 83 percent, and by 44 percent on average. The nonlinear runup predictions overestimated runup by up to 4 percent on three cases, underestmated by up to 43 percent in two cases with waves near breaking, but, on average, measured runup exceeded the second-order theory by only 11 percent.

At first-order, depth-integrated wave forces are nearly inertial and are in-phase with the linear wave acceleration for small cylinders, but are shifted to be more in-phase of the wave crest as scattering increases for larger cylinders. At second-order, additional force components again include (1) a mean or steady quadratic force, (2) oscillatory quadratic

components, and (3) oscillatory components from the second-order velocity potential. The time-averaged mean drift force is always positive (in the direction of wave propagation), and is related to the redirection of the time-averaged momentum flux by the fixed cylinder.

The dynamic forces at second-order are found to reflect the competing effects of the various wave components, like the solution for the second-order free surface. The forces resulting from the Stokes second-order plane wave are maximum in the positive direction just before the wave crest and are maximum in the negative direction just after the wave crest. For small cylinders, these force components tend to skew the resulting nonlinear force distribution to give sudden reversal in the force direction as the wave crest passes, but they change the force magnitude equally in the positive and negative directions. For larger cylinders, where the linear force is shifted closer to the wave crest, the plane wave forces tend to increase the positive force and reduce the negative force maxima. The plane wave motion in the second-order velocity potential also interacts with the cylinder to generate a scattered wave component, whose phase shift relative to the plane-wave terms depends on the cylinder size.

The oscillatory quadratic force components are mostly in-phase with the first-order force. Since these terms are associated with convective accelerations of the first-order flow field and the first-order free surface displacement, the forces tend to increase the force in the positive direction. The forces arising from the second-order velocity potential, like the free surface contributions from the second-order velocity potential, are mostly out-of-phase with the linear forces. Because of the many forced-radiated and scattered wave components, each of which has a unique phase shift relative to the linear wave, the associated force terms are not always or exactly out-of-phase. However, the effects of the second-order velocity potential are usually to reduce forces in the positive direction and increase forces in the direction contrary to the direction of wave advance. In general, these terms oppose the quadratic force terms to reduce or change the direction of the overall second-order dynamic force.

Measured forces from the 22 laboratory experiments confirm most of the features of the nonlinear forces as predicted by the second-order theory. For small relative cylinder sizes, the nonlinear features of the measured time series, including inflections in the force traces, the more-sudden reversal from maximum positive to maximum negative forces, and the magnitude and direction of the maximum force, are all predicted by the nonlinear diffraction theory. For larger cylinder sizes, predicted nonlinear force maxima are not significantly larger than linear force maxima; the second-order theory indicates an almost complete cancellation of second-order quadratic forces and forces from the second-order velocity potential. However, for these larger relative cylinder sizes, measured forces are smaller than those predicted by linear theory, so that the nonlinear theory provides worse agreement that does the linear theory.

Theoretical maximum nonlinear forces are found to exceed linear maximum forces by up to 30 percent for wave steepnesses up to near breaking and by 25 percent for low steepness waves in near- shallow water. When compared to laboratory data for the force maxima, linear theory provided a better estimate of forces for larger cylinders, but underestimated forces by 10 to 15 percent for smaller cylinders, in smaller relative depths, and for waves at about one-quarter of the breaking steepness. In this same loading regime, the nonlinear theory predicted maximum force amplitudes almost exactly, with errors of less than 3 to 4 percent. Measured second-order drift forces were found to give good agreement with the second-order theory. For incident wave conditions in which Stokes second-order wave theory is valid, and for most conditions in which Stokes third-order theory is more appropriate, the comparison of the second-order theory to laboratory data is superior to linear theory for smaller values of ka while for larger cylinder sizes, both linear and nonlinear theories overpredicted the maximum forces.

One caveat to the above conclusions is that the laboratory data covered a limited range of conditions. In this study, experiments cover a transition from loading dominated by nonlinear inertia forces to loading dominated by nonlinear scattering and diffraction. The

data do not extend into the regime of truly large cylinder sizes, where the cylinder diameter is greater than one half-third of the incident wavelength. In this regime, other laboratory data suggests a more confused loading regime where forces may depart significantly from linear theory, with the bulk of laboratory data showing nonlinear forces that are reduced relative to linear theory, while other data shows forces that exceed linear forces. The proposed theory is not tested in this regime and its applicablity is not certain.

In general, second-order effects on wave forces are not as significant as second-order effects on wave runup. Reasons for this are principally that maximum runup occurs as the crest reaches the leading edge of the cylinder, while maximum forces are related more closely to the phase of maximum acceleration of the flow. Since many second-order free surface terms are in-phase (or out-of-phase) with the wave crest, they have a substantial effect on the free surface elevation as the crest passes the cylinder. In contrast, forces due to these same wave components tend to be shifted in phase relative to the first-order force, and therefore do not have as great an effect. In addition, since second-order terms are mostly at wavenumbers from $2k$ to $4k$, their motions are mostly concentrated near the surface and may have little effect on overall depth-integrated forces. An exception to this occurs for very large cylinders, where significant scattering occurs at first-order and significant long standing wave motions are found in the theoretical second-order velocity potential.

In computing nonlinear wave loadings, if forces due to the second-order velocity potential are neglected, then the combination of linear forces and quadratic second-order forces lead to an overestimate of maximum force magnitudes. At least two proposed design methods, of Kurata and Ijima (1979) and of Herfjord and Nielsen (1986), have included the effects of quadratic terms, derived from the linear theory, while neglecting the effects of the more complicated second-order velocity potential. Comparisons to laboratory data by Herfjord and Nielsen show that measured second-order forces were, in fact, smaller than those predicted by their simplified second-order theory, by as much as 30 to 50 percent. This provides some confirmation that the neglect of the second-order velocity potential results

in overly conservative force predictions, and that the cancellation effects of the second-order velocity potential predicted by the present nonlinear diffraction theory are a realistic physical feature.

Results from 170 experiments of wave forces in the diffraction regime are compiled and for conditions where $ka > 0.4$, it is found that 65 percent of the measured maximum forces are smaller than the linear force maxima. Reasons for the predominance of measured forces that are smaller than linear theory are not known conclusively, but several explanations are possible.

Experimental error could contribute if, for example, force measuring devices do not respond instantly to the rapidly oscillating forces that occur in many of the laboratory tests with large values of ka. Smaller forces will also be recorded if test cylinders are not rigidly supported but can move slightly in response to the applied forces. Phase-averaging of forces also skews the reported force maxima downward relative to the largest forces that are measured for given test conditions. In addition, various artificial wave components may alter the wave field reproduced in laboratory basins or flumes. These include the presence of cross-waves, waves reflected from side walls, or secondary free waves from the wavemaker, all of which may reduce the effective wave heights at the cylinder, or, in the case of cross-waves and reflected waves, may impart an oblique or transverse loading. In this study, the incident wave conditions were recorded at the location of the center of the cylinder, without the cylinder in place, so that the effects of cross waves and secondary free waves from the wavemaker would be partially accounted for in the measured incident wave height.

Physical reasons for reduced force magnitudes in nonlinear waves may also be found. First, steep nonlinear waves have less total momentum than linear waves of the same height. Forces that result from a redirection or transfer of the wave momentum may, therefore, be reduced relative to the forces calculated by a linear theory. Second, these steep waves have larger maximum horizontal water particle accelerations, but for large cylinders, the resulting pressure gradients are concentrated over a small portion of the cylinder. These

forces may be opposed by other smaller pressure gradients acting over other larger portions of the cylinder circumference.

Third, for steep waves, other higher-order nonlinearities are usually present which may reduce maximum force magnitudes. Force components at twice the frequency of the linear force always act to either increase or maintain the maximum force magnitudes; they can never reduce the force magnitude from that predicted by linear theory. If significant odd harmonic frequencies are present, however, such as at a frequency of 3σ, these components can be phased such that they reduce the maximum force magnitudes; this will be especially important for conditions in which the second-order force contributions are already small.

A fourth possible explanation of reduced nonlinear force magnitudes relates to the presence of breaking waves that are often observed along the sides of the cylinder for steep waves. While breaking waves are associated with larger forces on small piles, local breaking along the sides of large cylinders occurs in between the phase of maximum acceleration and the phase of the wave crest, at the same phase position as the maximum linear forces exerted on the cylinder. This breaking may cause local separation near the free surface, with attendant increases in fluid pressures in the region of separated flow, leading to reduced net pressure gradients on the cylinder.

Additional research into second-order diffraction effects on large cylinders is warranted from the standpoint of gaining an understanding of basic wave-wave and wave-structure interaction phenomena. More rigorous measurements of wave envelopes in the upwave and downwave regions, and around the cylinder, are necessary. Experiments utilizing a wave gage which could be moved along radial lines extending from the cylinder would permit a more exact documentation of the nonlinear scattering and diffraction effects. A problem in data analysis which should be addressed is the separation and identification of the various second-order waves in a wave basin, which include the bound second harmonic travelling with the incident wave, free second-order waves originating from the wavemaker, and cylindrical second-order free waves radiating away from the cylinder. Subsurface pressure or

current measurements would also be useful for identifying near-bottom features, particularly the presence of the microseism or long standing wave on the upwave side.

Additional research is also needed to verify the design-oriented information on wave runup and wave loading. It is suggested that more exact numerical integration techniques be employed with the proposed theory. The solution procedure used here seems to lose accuracy for very large cylinders as ka approaches 2.0, particularly for deep water conditions. Comparison of the nonlinear theory to additional wave runup data, such as that of Chakrabarti and Tam (1975), would be useful for verifying the theory under a different set of conditions on the relative depth and relative cylinder size. Comparison of the theory to Isaacson's (1977a) approximate theory for diffraction of cnoidal waves would establish the usefulness of each design method in the transition region of intermediate to shallow water. A comparison of the present theory to Garrison's (1979) numerical Green's function method would also be useful for determining the equivalence of the two methods. In this regard, the proposed solution, if further substantiated by laboratory data, could serve as a benchmark for verifying other more versatile numerical techniques that can then be applied to arbitrary geometries. Finally, the predominance of measured wave forces that are smaller than those predicted by linear theory for very large cylinders is surprising and additional research is required, to determine whether this phenomenon is an experimental artifact or a realistic result of nonlinear wave-structure interaction.

In conclusion, the proposed second-order diffraction theory seems to rigorously account for all physically expected second-order wave motions. These include (1) forced waves, generated by nonlinear wave-wave interactions on the free surface and required to satisfy the second-order free surface boundary conditions, (2) radiated second-order free waves which are generated in the regions of strong wave-wave interactions but which then propagate away, and (3) scattered second-order free waves which are the result of wave-structure interaction of the forced-radiated waves with the fixed cylinder. The solution is found to incorporate elements of previous solutions of Chen (1979) and Chen and Hudspeth (1982),

as well as of Garrison (1979). This agreement is viewed as an important finding, since the present solution is obtained in an independent way and since no other proposed solutions have shown any apparent agreement. Finally, the proposed nonlinear diffraction solution is compared to laboratory data for (1) wave runup/rundown around the circumference of the cylinder, (2) the wave envelope in the upwave and downwave regions, and (3) depth-integrated wave forces on the cylinder, including mean drift forces. The agreement between the theory and the measured data provides confirmation of most of the features in the second-order solution and indicates that the proposed solution is valid for the same relative depth and wave steepness conditions for which the usual Stokes second-order theory is valid.

APPENDIX A
DERIVATION OF QUADRATIC TERMS

A.1 Notation

The physical solution for the first-order velocity potential, $\Phi_1(r,\theta,x,t)$, which includes incident and scattered components, may be written as

$$\Phi_1(r,\theta,z,t) = \frac{1}{2}\left\{\phi_1(r,\theta,z)e^{-i\sigma t} + \hat{\phi}_1(r,\theta,z)e^{+i\sigma t}\right\} \tag{A.1}$$

where $\hat{\phi}_1$ is the complex conjugate of ϕ_1. Based on Equation 1.55, the solution for Φ_1 is

$$\begin{aligned}\Phi_1 &= \frac{1}{2}\left\{-iC\frac{\cosh k(d+z)}{\cosh kd}\sum_{n=0}\beta_n A_n(kr)\cos n\theta e^{-i\sigma t}\right. \\ &\quad \left. + iC\frac{\cosh k(d+z)}{\cosh kd}\sum_{n=0}\hat{\beta}_n\hat{A}_n(kr)\cos n\theta e^{+i\sigma t}\right\}\end{aligned} \tag{A.2}$$

where the upper limit of the summation is implied as ∞ and where

$$C = \frac{gH}{2\sigma} \tag{A.3}$$

$$\beta_n = (2-\delta_{n0})e^{in\pi/2} \tag{A.4}$$

$$A_n(kr) = J_n(kr) - \frac{J_n'(ka)}{H_n'(ka)}H_n(kr) \tag{A.5}$$

Some new notation will be useful; therefore, the following quantities are defined

$$P = -i\sum_{n=0}\beta_n A_n(kr)\cos n\theta e^{-i\sigma t} \tag{A.6}$$

$$\hat{P} = +i\sum_{n=0}\hat{\beta}_n\hat{A}_n(kr)\cos n\theta e^{+i\sigma t} \tag{A.7}$$

$$R = -i\sum_{n=0}\beta_n A_n'(kr)\cos n\theta e^{-i\sigma t} \tag{A.8}$$

$$\hat{R} = +i\sum_{n=0}\hat{\beta}_n\hat{A}_n'(kr)\cos n\theta e^{+i\sigma t} \tag{A.9}$$

$$T = -i\sum_{n=0}\beta_n A_n(kr)n\sin n\theta e^{-i\sigma t} \tag{A.10}$$

$$\hat{T} = +i\sum_{n=0}\hat{\beta}_n\hat{A}_n(kr)n\sin n\theta e^{+i\sigma t} \tag{A.11}$$

The first-order solution may now be written as

$$\Phi_1 = \frac{C}{2}\frac{\cosh k(d+z)}{\cosh kd}\left\{P+\hat{P}\right\} \tag{A.12}$$

Derivatives of Φ_1, evaluated at z=0, which will be required are then

$$\Phi_{1t} = \frac{i\sigma C}{2}\left\{-P+\hat{P}\right\} \tag{A.13}$$

$$\Phi_{1r} = \frac{kC}{2}\left\{R+\hat{R}\right\} \tag{A.14}$$

$$\Phi_{1\theta} = -\frac{C}{2}\left\{T+\hat{T}\right\} \tag{A.15}$$

$$\Phi_{1z} = \frac{kC}{2}\tanh kd\left\{P+\hat{P}\right\} \tag{A.16}$$

$$\Phi_{1tt} = -\frac{\sigma^2 C}{2}\left\{P+\hat{P}\right\} \tag{A.17}$$

$$\Phi_{1rt} = \frac{i\sigma kC}{2}\left\{-R+\hat{R}\right\} \tag{A.18}$$

$$\Phi_{1\theta t} = \frac{i\sigma C}{2}\left\{T-\hat{T}\right\} \tag{A.19}$$

$$\Phi_{1zt} = \frac{i\sigma kC}{2}\tanh kd\left\{-P+\hat{P}\right\} \tag{A.20}$$

$$\Phi_{1zz} = \frac{k^2 C}{2}\left\{P+\hat{P}\right\} \tag{A.21}$$

$$\Phi_{1ttz} = -\frac{k\sigma^2 C}{2}\tanh kd\left\{P+\hat{P}\right\} \tag{A.22}$$

A.2 Quadratic Forcing in Combined Free Surface Boundary Condition

The quadratic forcing terms in the second-order combined free surface boundary condition, rewritten from Equation 3.67 are

$$f(r,\theta,t) = \frac{1}{g}\Phi_{1t}\left\{\Phi_{1ttz}+g\Phi_{1zz}\right\} - 2\left\{\Phi_{1r}\Phi_{1rt}+\frac{1}{r^2}\Phi_{1\theta}\Phi_{1\theta t}+\Phi_{1z}\Phi_{1zt}\right\} \tag{A.23}$$

Based on the definitions given in Equations A.13 through A.22, the quadratic forcing in Equation A.23 may be written as

$$f(r,\theta,t) = \frac{i\sigma k^2 C^2}{4}\left[(3\tanh^2 kd-1)(P^2-\hat{P}^2)+2(R^2-\hat{R}^2)+\frac{2}{(kr)^2}(T^2-\hat{T}^2)\right] \tag{A.24}$$

Since $f(r,\theta,t)$ may be represented as

$$f(r,\theta,t) = \frac{1}{2}\left\{f(r,\theta)+\hat{f}(r,\theta)\right\} \tag{A.25}$$

the forcing terms may be separated into complex and complex conjugate quantities as

$$f(r,\theta,t) = \frac{+i\sigma k^2 C^2}{2}\left[(3\tanh^2 kd - 1)P^2 + 2R^2 + \frac{2}{(kr)^2}T^2\right] \quad \text{(A.26)}$$

$$\hat{f}(r,\theta,t) = \frac{-i\sigma k^2 C^2}{2}\left[(3\tanh^2 kd - 1)\hat{P}^2 + 2\hat{R}^2 + \frac{2}{(kr)^2}\hat{T}^2\right] \quad \text{(A.27)}$$

Note that all cross-product terms such as $P\hat{P}$, $R\hat{R}$, and $T\hat{T}$, cancel identically; thus, no steady or non-oscillatory forcing terms are present. The second-order problem may therefore be separated into two problems, one for the complex forcing, $f(r,\theta,t)$ and the associated potential, $\Phi_2(r,\theta,z,t)$, and one for the complex conjugate quantities $\hat{f}(r,\theta,t)$ and $\hat{\Phi}_2(r,\theta,z,t)$.

Expanding the product terms, P^2, R^2, and T^2, yields products of infinite sums as

$$P^2 = -\sum_{n=0}\sum_{m=0}\beta_n\beta_m A_n(kr)A_m(kr)\cos n\theta \cos m\theta e^{-i2\sigma t} \quad \text{(A.28)}$$

$$R^2 = -\sum_{n=0}\sum_{m=0}\beta_n\beta_m A_n'(kr)A_m'(kr)\cos n\theta \cos m\theta e^{-i2\sigma t} \quad \text{(A.29)}$$

$$T^2 = -\sum_{n=0}\sum_{m=0}\beta_n\beta_m A_n(kr)A_m(kr)n\sin n\theta m\sin m\theta e^{-i2\sigma t} \quad \text{(A.30)}$$

and expanding the coefficient term yields

$$\frac{i\sigma k^2 C^2}{2} = \frac{ig^2k^2H^2}{8\sigma} \quad \text{(A.31)}$$

The quadratic forcing in Equation A.26 may now be written in expanded form as

$$\begin{aligned} f(r,\theta,t) = {} & \frac{-ig^2k^2H^2}{8\sigma} \\ & \cdot \left[(3\tanh^2 kd - 1)\sum_{n=0}\sum_{m=0}\beta_n\beta_m A_n(kr)A_m(kr)\cos n\theta\cos m\theta\right. \\ & + 2\sum_{n=0}\sum_{m=0}\beta_n\beta_m A_n'(kr)A_m'(kr)\cos n\theta\cos m\theta \\ & \left. + \frac{2}{(kr)^2}\sum_{n=0}\sum_{m=0}\beta_n\beta_m A_n(kr)A_m(kr)n\sin n\theta m\sin m\theta\right] e^{-i2\sigma t} \end{aligned} \quad \text{(A.32)}$$

Expanding the product terms $A_n(kr)A_m(kr)$ gives terms like

$$\begin{aligned} A_n(kr)A_m(kr) = {} & J_n(kr)J_m(kr) - \alpha_m J_n(kr)H_m(kr) \\ & - \alpha_n J_m(kr)H_n(kr) + \alpha_n\alpha_m H_n(kr)H_m(kr) \end{aligned} \quad \text{(A.33)}$$

where

$$\alpha_n = \frac{J_n'(ka)}{H_n'(ka)} \tag{A.34}$$

Substitution of these terms into Equation A.32 yields a lengthy expression that will not be reproduced here; however, it is evident that the quadratic forcing contains terms may be identified as follows:

1. Terms $J_n(kr)J_m(kr)$ and derivatives that result from the nonlinear self-interaction of the first-order incident wave.

2. Terms $J_n(kr)H_m(kr)$ and derivatives that result from the nonlinear cross-interaction of the first-order incident and scattered waves.

3. Terms $H_n(kr)H_m(kr)$ and derivatives that result from the nonlinear self-interaction of the first-order scattered wave.

Conceptually, the quadratic forcing, f, may then be separated into three individual forcing terms as

$$f = f^{ii} + f^{is} + f^{ss} \tag{A.35}$$

where f^{ii} represents the forcing due to the self interaction of the first-order incident wave, f^{is} represents the forcing due to the cross-interaction of the incident and scattered waves, and f^{ss} represents the forcing due to the self-interaction of the first-order scattered wave.

For later application, the f^{ii} forcing term, which leads to the generation of the forced second-order plane wave associated with the usual Stokes second-order theory, may be written as

$$\begin{aligned} f^{ii}(r,\theta,t) \;=\; & \frac{-ig^2k^2H^2}{8\sigma}\Bigg[(3\tanh^2 kd - 1)\sum_{n=0}\sum_{m=0}\beta_n\beta_m J_n(kr)J_m(kr)\cos n\theta\cos m\theta \\ & + 2\sum_{n=0}\sum_{m=0}\beta_n\beta_m J_n'(kr)J_m'(kr)\cos n\theta\cos m\theta \\ & + \frac{2}{(kr)^2}\sum_{n=0}\sum_{m=0}\beta_n\beta_m J_n(kr)J_m(kr)n\sin n\theta m\sin m\theta\Bigg]e^{-i2\sigma t} \end{aligned} \tag{A.36}$$

For numerical computation, the quadratic forcing terms may be written in a Fourier series form as a single summation with harmonics of $\cos n\theta$. This is accomplished by first writing Equation A.32 as

$$f(r,\theta,t) = \frac{-ig^2k^2H^2}{8\sigma} \sum_{n=0}\sum_{m=0} \left[h_{n,m}\cos(n-m)\theta + g_{n,m}\cos(n+m)\theta\right] e^{-i2\sigma t} \qquad \text{(A.37)}$$

where

$$h_{n,m} = \frac{\beta_n\beta_m}{2}\left[(3\tanh^2 kd - 1 + \frac{2nm}{(kr)^2})A_n(kr)A_m(kr) + 2A_n'(kr)A_m'(kr)\right] \qquad \text{(A.38)}$$

$$g_{n,m} = \frac{\beta_n\beta_m}{2}\left[(3\tanh^2 kd - 1 - \frac{2nm}{(kr)^2})A_n(kr)A_m(kr) + 2A_n'(kr)A_m'(kr)\right] \qquad \text{(A.39)}$$

Then, by grouping harmonics of $\cos n\theta$ as shown in Appendix A.3, the forcing is expressed with separable components of r, θ, and t, in the form

$$f(r,\theta,t) = \frac{-ig^2k^2H^2}{8\sigma} \sum_{p=0}^{\infty} \tilde{f}_p(r)\cos n\theta e^{-i2\sigma t} \qquad \text{(A.40)}$$

where $\tilde{f}$ is a nondimensional representation of the quadratic forcing.

A.3 Representation of Quadratic Terms by Fourier Series

The Fourier series form of the nondimensional quadratic forcing terms, given in Equations A.37 and A.40, is

$$\sum_{p=0}^{\infty} \tilde{f}_p(r)\cos n\theta = \sum_{n=0}^{\infty}\sum_{m=0}^{\infty} \left[h_{n,m}\cos(n-m)\theta + g_{n,m}\cos(n+m)\theta\right] \qquad \text{(A.41)}$$

Multiplying both sides by $\cos j\theta$ and integrating over $-\pi \le \theta \le \pi$ gives

$$\int_{-\pi}^{\pi} \sum_{p=0}^{\infty} \tilde{f}_p(r)\cos p\theta \cos j\theta d\theta = \qquad \text{(A.42)}$$

$$\int_{-\pi}^{\pi} \sum_{n=0}^{\infty}\sum_{m=0}^{\infty} \left[h_{n,m}\cos(n-m)\theta + g_{n,m}\cos(n+m)\theta\right]\cos j\theta d\theta \qquad \text{(A.43)}$$

Due to orthogonality, the left hand side requires that j=p while the right hand side contributes only when

$$n+m = p \qquad \text{or} \qquad \pm(n-m) = p \qquad \text{(A.44)}$$

When $p = 0$, the right hand side has non-zero terms for $n = m$; thus

$$\tilde{f}_0(r) = h_{0,0} + g_{0,0} + \sum_{n=1}^{\infty} h_{n,n} \qquad \text{(A.45)}$$

or since $g_{0,0} = h_{0,0}$

$$\tilde{f}_0(r) = 2h_{0,0} + \sum_{m=1}^{\infty} h_{m,m} \tag{A.46}$$

For $p > 0$, three conditions must be considered

$$n + m = p \tag{A.47}$$

$$\sum_{n=0}^{\infty}\sum_{m=0}^{\infty} g_{n,m}\cos(n+m)\theta = \sum_{p=1}^{\infty}\sum_{m=0}^{p} g_{m,p-m}\cos p\theta \tag{A.48}$$

$$n - m = p \tag{A.49}$$

$$\sum_{n=0}^{\infty}\sum_{m=0}^{\infty} h_{n,m}\cos(n-m)\theta = \sum_{p=1}^{\infty}\sum_{m=p}^{\infty} h_{m,m-p}\cos p\theta \tag{A.50}$$

$$m - n = p \tag{A.51}$$

$$\sum_{n=0}^{\infty}\sum_{m=0}^{\infty} h_{n,m}\cos(n-m)\theta = \sum_{p=1}^{\infty}\sum_{m=p}^{\infty} h_{m-p,m}\cos p\theta \tag{A.52}$$

Therefore for $p > 0$

$$\tilde{f}_p(r) = \sum_{m=p}^{\infty}(h_{m,m-p} + h_{m-p,m}) + \sum_{m=0}^{p} g_{m,p-m} \tag{A.53}$$

The final form of Equation A.41 is

$$\sum_{p=0}^{\infty}\tilde{f}_p(r)\cos p\theta =$$

$$2h_{0,0} + \sum_{m=1}^{\infty} h_{m,m} + \sum_{p=1}^{\infty}\left\{\sum_{m=p}^{\infty}(h_{m,m-p} + f_{m-p,m}) + \sum_{m=0}^{p} g_{m,p-m}\right\}\cos p\theta \tag{A.54}$$

A.4 Exact Form of f^{ii} Quadratic Forcing Terms

Based on the Bessel function identity

$$\sum_{n=0}^{\infty}\beta_n J_n(kr)\cos n\theta = e^{ikr\cos\theta} = e^{ikx} \tag{A.55}$$

the following relationships are found

$$\sum_{n=0}^{\infty}\beta_n J_n'(kr)\cos n\theta = i\cos\theta e^{ikr\cos\theta} \tag{A.56}$$

and

$$\sum_{n=0}^{\infty}\beta_n J_n(kr) n\sin n\theta = ikr\sin\theta e^{ikr\cos\theta} \tag{A.57}$$

Therefore, the terms in the f^{ii} forcing, given in Equation A.36, become

$$f^{ii}(r,\theta,t) = \frac{-ig^2k^2H^2}{8\sigma}\left[(3\tanh^2 kd - 1) - 2\cos^2\theta - 2\sin^2\theta\right]e^{i(2kr\cos\theta - 2\sigma t)} \quad \text{(A.58)}$$

Equivalent forms are then

$$f^{ii}(r,\theta,t) = \frac{-ig^2k^2H^2}{8\sigma}[3(\tanh^2 kd - 1)]e^{i(2kx-2\sigma t)} \quad \text{(A.59)}$$

or

$$f^{ii}(r,\theta,t) = \frac{-i3g^2k^2H^2}{8\sigma}(\tanh^2 kd - 1)\sum_{n=0}\beta_n J_n(2kr)\cos n\theta e^{-i2\sigma t} \quad \text{(A.60)}$$

A.5 Asymptotic Form of the Free Surface Forcing Terms

The asymptotic form of the free surface forcing terms may be obtained by first rewriting the function, $P(r,\theta,t)$ as

$$P = -i\left[e^{ikr\cos\theta} - \sum_{n=0}^{\infty}\beta_n\alpha_n H_n(kr)\cos n\theta\right]e^{-i\sigma t} \quad \text{(A.61)}$$

Since the Hankel function has asymptotic form

$$H_n(kr) \sim (\frac{2}{\pi kr})^{\frac{1}{2}}e^{ikr - in\pi/2 - i\pi/4} \quad \text{(A.62)}$$

the asymptotic form of P may be represented as

$$P \sim \left[e^{ikr\cos\theta} - \frac{1}{r^{1/2}}e^{ikr}g(\theta)\right]e^{-i\sigma t} \quad \text{(A.63)}$$

where $g(\theta)$ will be used to denote a general complex function of θ. Similarly, the terms R and T in Equations A.8 and A.10 may be represented as

$$R \sim \left[i\cos\theta e^{ikr\cos\theta} - \frac{1}{r^{1/2}}(i - \frac{1}{2kr})e^{ikr}g(\theta)\right]e^{-i\sigma t} \quad \text{(A.64)}$$

$$T \sim \left[-ikr\sin\theta e^{ikr\cos\theta} - \frac{1}{r^{1/2}}e^{ikr}g(\theta)\right]e^{-i\sigma t} \quad \text{(A.65)}$$

Therefore, the product terms P^2, R^2, and T^2, behave like

$$P^2 \sim \left[e^{i2kr\cos\theta} - \frac{1}{r^{1/2}}e^{ikr(1+\cos\theta)}g(\theta) + \frac{1}{r}e^{i2kr}g(\theta)\right]e^{-i2\sigma t} \quad \text{(A.66)}$$

$$R^2 \sim \left[-i\cos^2\theta e^{i2kr\cos\theta} - \frac{1}{r^{1/2}}(i - \frac{1}{2kr})e^{ikr(1+\cos\theta)}g(\theta)\right. \quad \text{(A.67)}$$

$$\left. + \frac{1}{r}(-1 - \frac{i}{kr} + \frac{1}{4(kr)^2})e^{i2kr}g(\theta)\right]e^{-i2\sigma t} \quad \text{(A.68)}$$

$$T^2 \sim \left[-(kr)^2\cos\theta e^{i2kr\cos\theta} - \frac{1}{r^{1/2}}kre^{ikr(1+\cos\theta)}g(\theta) + \frac{1}{r}e^{i2kr}g(\theta)\right]e^{-i2\sigma t} \quad \text{(A.69)}$$

The free surface forcing is defined by

$$f \sim (3\tanh^2 kd - 1)P^2 + 2R^2 + \frac{2}{(kr)^2}T^2 \tag{A.70}$$

Substitution of the asymptotic product terms into the expression for f leads to the following three asymptotic forms for the three types of forcing terms

$$f^{ii} \sim 3(\tanh^2 kd - 1)e^{i(2kr\cos\theta - 2\sigma t)} \tag{A.71}$$

$$f^{is} \sim \left[\frac{g(\theta)}{r^{1/2}} + \frac{g(\theta)}{r^{3/2}}\right] e^{i(kr(1+\cos\theta) - 2\sigma t)} \tag{A.72}$$

$$f^{ss} \sim \left[\frac{g(\theta)}{r} + \frac{g(\theta)}{r^2} + \frac{g(\theta)}{r^3}\right] e^{i(2kr - 2\sigma t)} \tag{A.73}$$

A.6 Quadratic Terms For Evaluation of Second-Order Free Surface

The quadratic terms in Equation 4.10 for the second-order water surface elevation are

$$\eta_{21} = \frac{1}{g^2}\Phi_{1t}\Phi_{1tz} - \frac{1}{2g}\left[\Phi_{1r}^2 + \frac{1}{r^2}\Phi_{1\theta}\Phi_{1\theta t}^2 + \Phi_{1z}^2\right] \tag{A.74}$$

From Appendix A.1, the various derivatives may be defined in terms of the functions P, R, and T, defined in Equations A.13 through A.22. Substitution of these expressions into Equation A.74 gives the following result

$$\begin{aligned}\eta_{21} &= \frac{kH^2}{16\tanh kd}\left[\tanh^2 kdP\hat{P} - R\hat{R} - \frac{1}{(kr)^2}T\hat{T}\right] \\ &+ \frac{kH^2}{32\tanh kd}\left[3\tanh^2 kdP^2 + R^2 + \frac{1}{(kr)^2}T^2\right] + c.c\end{aligned} \tag{A.75}$$

where the first term is not a function of time and represents a spatially varying mean water level, while the second term and its complex conjugate represent the second-order oscillatory water level components.

Verification of the derivation may be achieved by considering the case where the first order potential is given by only a plane wave with no cylinder present, and hence no scattered wave contributions. From Equations A.6 through A.11, the definitions of P, R, and T are

$$P = \sum_{n=0} \beta_n J_n(kr)\cos n\theta e^{-i\sigma t} = e^{i(kr\cos\theta - \sigma t)} \tag{A.76}$$

$$R = \sum_{n=0} \beta_n J_n'(kr)\cos n\theta e^{-i\sigma t} = i\cos\theta e^{i(kr\cos\theta - \sigma t)} \tag{A.77}$$

$$T = \sum_{n=0} \beta_n J_n(kr) n\sin n\theta e^{-i\sigma t} = ikr\sin\theta e^{i(kr\cos\theta - \sigma t)} \tag{A.78}$$

such that

$$P\hat{P} = 1 \tag{A.79}$$

$$R\hat{R} = \cos^2\theta \tag{A.80}$$

$$T\hat{T} = (kr)^2\sin^2\theta \tag{A.81}$$

$$P^2 = e^{i(2kx-2\sigma t)} \tag{A.82}$$

$$R^2 = -\cos^2\theta e^{i(2kx-2\sigma t)} \tag{A.83}$$

$$T^2 = -(kr)^2\sin^2\theta e^{i(2kx-2\sigma t)} \tag{A.84}$$

The quadratic terms then become

$$\eta_{21}^{ii} = \frac{kH^2}{16\tanh kd}(\tanh^2 - 1) + \frac{kH^2}{16\tanh kd}(3\tanh^2 kd - 1)\frac{e^{i2(kx-\sigma t)}}{2} + c.c \tag{A.85}$$

The leading term may be verified to be equal to the usual uniform setdown associated with plane waves at second-order, e.g Dean and Dalrymple (1984). The oscillatory portion is also correct; however, this will be more readily apparent after the second-order velocity potential is added.

In nondimensional form, with η_{21} normalized as

$$\tilde{\eta}_{21} = \frac{2\eta_{21}}{H} \tag{A.86}$$

the quadratic free surface components in Equation A.75 become

$$\tilde{\eta}_{21} = \frac{kH}{8\tanh kd}\left[\tanh^2 kdP\hat{P} - R\hat{R} - \frac{1}{(kr)^2}T\hat{T}\right] + \frac{kH}{16\tanh kd}\left[3\tanh^2 kdP^2 + R^2 + \frac{1}{(kr)^2}T^2\right] + c.c \tag{A.87}$$

Following the method presented in Appendix A.3, previously applied to the quadratic forcing in the combined free surface boundary condition, the nondimensional quadratic water surface components may be represented in the form of a Fourier series as

$$\eta_{21} = \frac{kH}{8\tanh kd}\sum_{n=0}^{\infty} G_n^s(r)\cos n\theta + \frac{kH}{8\tanh kd}\sum_{n=0}^{\infty} G_n^o(r)\cos n\theta\frac{e^{-i2\sigma t}}{2} + c.c. \tag{A.88}$$

where the radial functions for the steady and oscillatory terms are found to be

$$G_n^s(r) = 2h_{0,0}^s + \sum_{m=1}^{\infty} h_{m,m}^s + \sum_{m=p}^{\infty}(h_{m,m-p}^s + h_{m-p,m}^s) + \sum_{m=0}^{p} g_{m,p-m}^s \tag{A.89}$$

and

$$G_n^o(r) = 2h_{0,0}^o + \sum_{m=1}^{\infty} h_{m,m}^o + \sum_{m=p}^{\infty}(h_{m,m-p}^o + h_{m-p,m}^o) + \sum_{m=0}^{p} g_{m,p-m}^o \tag{A.90}$$

and where

$$h_{n,m}^s = \frac{\beta_n\hat{\beta}_m}{2}\left[(\tanh^2 kd - \frac{nm}{(kr)^2})A_n(kr)\hat{A}_m(kr) - A_n'(kr)\hat{A}_m'(kr)\right] \tag{A.91}$$

$$g_{n,m}^s = \frac{\beta_n\hat{\beta}_m}{2}\left[(\tanh^2 kd + \frac{nm}{(kr)^2})A_n(kr)\hat{A}_m(kr) - A_n'(kr)\hat{A}_m'(kr)\right] \tag{A.92}$$

$$h_{n,m}^o = \frac{\beta_n\beta_m}{2}\left[(3\tanh^2 kd + \frac{nm}{(kr)^2})A_n(kr)A_m(kr) + A_n'(kr)A_m'(kr)\right] \tag{A.93}$$

$$g_{n,m}^o = \frac{\beta_n\beta_m}{2}\left[(3\tanh^2 kd - \frac{nm}{(kr)^2})A_n(kr)A_m(kr) + A_n'(kr)A_m'(kr)\right] \tag{A.94}$$

A.7 Quadratic Terms For Evaluation of Second-Order Wave Forces

The free surface component of the quadratic force is defined in Equation 5.17 as

$$F_{21f} = -\frac{1}{2}\rho g a\int_{-\pi}^{+\pi}\eta_1^2\cos\theta d\theta \tag{A.95}$$

From Equation 4.9, let η_1 evaluated at $r = a$ be given by

$$\begin{aligned}\eta_1 &= \frac{1}{2}\left\{\frac{H}{2}\sum_{n=0}^{\infty}\beta_n\frac{2i}{\pi ka H_n'(ka)}\cos n\theta e^{-i\sigma t} + c.c.\right\} \\ &= \frac{H}{4}\left\{E + \hat{E}\right\}\end{aligned} \tag{A.96}$$

where

$$\begin{aligned}E &= \sum_{n=0}^{\infty}\frac{2i\beta_n}{\pi ka H_n'(ka)}\cos n\theta e^{-i\sigma t} \\ &= \sum_{n=0}^{\infty}\frac{2i\beta_n}{\pi ka}A_n e^{-i(\psi_n+\sigma t)}\end{aligned} \tag{A.97}$$

and where

$$A_n = \frac{1}{|H_n'(ka)|} \tag{A.98}$$

$$\psi_n = \tan^{-1}\left(Y_n'(ka)/J_n'(ka)\right) \tag{A.99}$$

The product term η_1^2 is then

$$\begin{aligned}\eta_1^2 &= \frac{H^2}{16}\left\{E^2 + 2E\hat{E} + \hat{E}^2\right\} \\ &= \frac{H^2}{8}E\hat{E} + \Re\left\{\frac{H^2}{8}E^2\right\}\end{aligned} \tag{A.100}$$

such that the quadratic free surface component of the second-order force becomes

$$\begin{aligned}F_{21f} &= -\frac{1}{2}\rho g a \frac{H^2}{8}\int_{-\pi}^{\pi} E\hat{E}\cos\theta d\theta \\ &\quad -\frac{1}{2}\rho g a \frac{H^2}{8}\Re\int_{-\pi}^{\pi} E^2\cos\theta d\theta\end{aligned} \tag{A.101}$$

From Equation A.97 the product term $E\hat{E}$ is

$$\begin{aligned}E\hat{E} &= \sum_{n=0}^{\infty}\sum_{m=0}^{\infty}\left(\frac{2}{\pi ka}\right)^2 \beta_n\hat{\beta}_m A_n A_m \cos n\theta \cos m\theta e^{-i(\psi_n-\psi_m)} \\ &= \frac{1}{2}\left(\frac{2}{\pi ka}\right)^2 \sum_{n=0}^{\infty}\sum_{m=0}^{\infty}\beta_n\hat{\beta}_m A_n A_m e^{-i(\psi_n-\psi_m)} \\ &\quad \cdot[\cos(n-m)\theta + \cos(n+m)\theta]\end{aligned} \tag{A.102}$$

Taking the integral of $E\hat{E}\cos\theta$ and employing the orthogonality properties of cosines as described in Appendix A.3, it is found that

$$\begin{aligned}\int_{-\pi}^{\pi} E\hat{E}\cos\theta d\theta &= \frac{\pi}{2}\left(\frac{2}{\pi ka}\right)^2 \sum_{n=1}^{\infty}\Big[\beta_n\hat{\beta}_{n-1}A_n A_{n-1}e^{-i(\psi_n-\psi_{n-1})} \\ &\qquad +\beta_{n-1}\hat{\beta}_n A_{n-1}A_n e^{-i(\psi_{n-1}-\psi_n)}\Big] \\ &\quad + \frac{\pi}{2}\left(\frac{2}{\pi ka}\right)^2 \sum_{n=0}^{1}\beta_n\hat{\beta}_{1-n}A_n A_{1-n}e^{-i(\psi_n-\psi_{1-n})}\end{aligned} \tag{A.103}$$

Reductions are possible since

$$\beta_n\hat{\beta}_{n-1} = 2i \quad \text{if } n = 1 \tag{A.104}$$

$$= 4i \quad \text{if } n \geq 1 \tag{A.105}$$

$$\beta_{n-1}\hat{\beta}_n = -2i \quad \text{if } n = 1 \tag{A.106}$$

$$= -4i \quad \text{if } n \geq 1 \tag{A.107}$$

$$\beta_n\hat{\beta}_{1-n} = 2e^{i(2n-1)\frac{\pi}{2}} \quad \text{all } n \tag{A.108}$$

Writing out a few terms of the series for $n = 0$ and $n = 1$ indicates that several terms solution for the integral may be combined to give

$$\int_{-\pi}^{\pi} E\hat{E}\cos\theta d\theta = 4\pi\left(\frac{2}{\pi ka}\right)^2 \sum_{n=1}^{\infty} A_n A_{n-1}\sin(\psi_n - \psi_{n-1}) \tag{A.109}$$

Inserting this result into the first term in the expression for the quadratic free surface force, in Equation A.101, gives the steady free surface force as

$$F_{21f}^{s} = -\rho g \frac{aH^2}{\pi(ka)^2} \sum_{n=1}^{\infty} A_n A_{n-1}\sin(\psi_n - \psi_{n-1}) \tag{A.110}$$

Considering the time-dependent terms in Equation A.101 gives the product terms

$$\begin{aligned} E^2 &= -\sum_{n=0}^{\infty}\sum_{m=0}^{\infty}\left(\frac{2}{\pi ka}\right)^2 \beta_n\beta_m A_n A_m e^{-i(\psi_n+\psi_m)}\cos n\theta\cos m\theta e^{-i2\sigma t} \\ &= -\frac{1}{2}\left(\frac{2}{\pi ka}\right)^2 \sum_{n=0}^{\infty}\sum_{m=0}^{\infty}\beta_n\beta_m A_n A_m e^{-i(\psi_n+\psi_m)} \\ &\quad \cdot\left[\cos(n-m)\theta + \cos(n+m)\theta\right] e^{-i2\sigma t} \end{aligned} \tag{A.111}$$

Taking the integral of $E^2\cos\theta$ and employing the orthogonality properties of cosines as described in Appendix A.3, it is found that

$$\begin{aligned} \int_{-\pi}^{\pi} E^2\cos\theta d\theta &= -\frac{\pi}{2}\left(\frac{2}{\pi ka}\right)^2 \sum_{n=1}^{\infty}\Big[\beta_n\beta_{n-1}A_n A_{n-1}e^{-i(\psi_n+\psi_{n-1})} \\ &\qquad -\beta_{n-1}\beta_n A_{n-1}A_n e^{-i(\psi_{n-1}+\psi_n)}\Big] e^{-i2\sigma t} \\ &\quad + \frac{\pi}{2}\left(\frac{2}{\pi ka}\right)^2 \sum_{n=0}^{1}\beta_n\beta_{1-n}A_n A_{1-n}e^{-i(\psi_n+\psi_{1-n})}e^{-i2\sigma t} \end{aligned} \tag{A.112}$$

Reductions are again possible since

$$\beta_n\beta_{n-1} = 2e^{i(2n-1)\frac{\pi}{2}} \quad \text{if } n = 1 \tag{A.113}$$

$$= 4e^{i(2n-1)\frac{\pi}{2}} \quad \text{if } n \geq 1 \tag{A.114}$$

$$\beta_{n-1}\beta_n = \beta_n\beta_{n-1} \tag{A.115}$$

$$\beta_n\beta_{1-n} = 2i \quad \text{if } n = 1 \tag{A.116}$$

$$= 4i \quad \text{if } n \geq 1 \tag{A.117}$$

Writing out a few terms of the series for $n = 0$ and $n = 1$ indicates that several terms in the solution for the integral may be combined to give

$$\int_{-\pi}^{\pi} E^2\cos\theta d\theta = -4\pi\left(\frac{2}{\pi ka}\right)^2 \sum_{n=1}^{\infty} A_n A_{n-1}e^{i\left[(2n-1)\frac{\pi}{2}-\psi_n-\psi_{n-1}\right]}e^{-i2\sigma t} \tag{A.118}$$

Inserting this result into the second term in the expression for the quadratic free surface force, in Equation A.101, gives the oscillatory free surface force as

$$F_{21f}^{o} = +\rho g \frac{aH^2}{\pi(ka)^2} \sum_{n=1}^{\infty} A_n A_{n-1} e^{\left[(2n-1)\frac{\pi}{2} - \psi_n - \psi_{n-1}\right]} e^{-i2\sigma t} \tag{A.119}$$

Now consider the quadratic velocity-square force component given in Equation 5.17 as

$$\begin{aligned} F_{21v} &= \frac{1}{2}\rho a \int_{-d}^{0}\int_{-\pi}^{\pi} (\nabla\Phi_1)^2_{r=a} \cos\theta \, d\theta \, dz \\ &= \frac{1}{2}\rho a \int_{-d}^{0}\int_{-\pi}^{\pi} \left\{ \left(\frac{1}{r}\Phi_{1\theta}\right)^2 + \Phi_{1z}^2 \right\}_{r=a}^{2} \cos\theta \, d\theta \, dz \end{aligned} \tag{A.120}$$

Let Φ_1, evaluated at $r = a$ be given by

$$\Phi_1 = \frac{1}{2}\left\{ -i\frac{gH}{2\sigma} \frac{\cosh k(d+z)}{\cosh kd} \sum_{n=0}^{\infty} \beta_n \left(\frac{2i}{\pi ka}\right) A_n \cos n\theta \, e^{-i(\psi_n + \sigma t)} \right\} + c.c \tag{A.121}$$

Defining the quantities

$$P = \sum_{n=0}^{\infty} \beta_n \left(\frac{2i}{\pi ka}\right) A_n \cos n\theta \, e^{-i(\psi_n + \sigma t)} \tag{A.122}$$

$$T = \sum_{n=0}^{\infty} \beta_n \left(\frac{2i}{\pi ka}\right) A_n n \sin n\theta \, e^{-i(\psi_n + \sigma t)} \tag{A.123}$$

the terms in the quadratic velocity-square force are then

$$\frac{1}{a^2}\Phi_{1\theta}^2 = -\frac{gkH^2}{8(ka)^2 \tanh kd} \frac{\cosh^2 k(d+z)}{\cosh^2 kd} \left\{ \Re\left(T^2\right) - T\hat{T} \right\} \tag{A.124}$$

$$\Phi_{1z}^2 = -\frac{gkH^2}{8(ka)^2 \tanh kd} \frac{\sinh^2 k(d+z)}{\cosh^2 kd} \left\{ \Re\left(P^2\right) - P\hat{P} \right\} \tag{A.125}$$

Evaluating the integrals over depth leads to the following form for the velocity square force components

$$\begin{aligned} F_{21v} = -\frac{\rho g a H^2}{32} \Bigg[& \frac{1}{(ka)^2}\left(1 + \frac{2kd}{\sinh 2kd}\right) \int_{-\pi}^{\pi} \left(\Re\left(T^2\right) - T\hat{T} \right) \cos\theta \, d\theta \\ & + \left(1 - \frac{2kd}{\sinh 2kd}\right) \int_{-\pi}^{\pi} \left(\Re\left(P^2\right) - P\hat{P} \right) \cos\theta \, d\theta \Bigg] \end{aligned} \tag{A.126}$$

From the previous definition of E in Equation A.97, it is noted that $P = E$ such that

$$\int_{-\pi}^{\pi} P\hat{P} \cos\theta \, d\theta = \frac{16}{\pi(ka)^2} \sum_{n=1}^{\infty} A_n A_{n-1} \sin\left(\psi_n - \psi_{n-1}\right) \tag{A.127}$$

and

$$\int_{-\pi}^{\pi} P^2 \cos\theta d\theta = -\frac{16}{\pi(ka)^2} \sum_{n=1}^{\infty} A_n A_{n-1} e^{\left[(2n-1)\frac{\pi}{2} - \psi_n - \psi_{n-1}\right]} e^{-i2\sigma t} \tag{A.128}$$

The remaining terms $T\hat{T}$ and T^2 may be expressed as

$$\begin{aligned} T\hat{T} &= \frac{1}{2}\left(\frac{2}{\pi ka}\right)^2 \sum_{n=0}^{\infty}\sum_{m=0}^{\infty} \beta_n \hat{\beta}_m A_n A_m e^{-i(\psi_n - \psi_m)} nm \left[\cos(n-m)\theta - \cos(n+m)\theta\right] \\ T^2 &= -\frac{1}{2}\left(\frac{2}{\pi ka}\right)^2 \sum_{n=0}^{\infty}\sum_{m=0}^{\infty} \beta_n \beta_m A_n A_m e^{-i(\psi_n - \psi_m)} \\ &\quad \cdot \left[\cos(n-m)\theta - \cos(n+m)\theta\right] e^{-i2\sigma t} \end{aligned} \tag{A.129}$$

Following the method presented in Appendix A.3, the integrals over θ required for the velocity-square forces may be found as

$$\begin{aligned} \int_{-\pi}^{\pi} T\hat{T} \cos\theta d\theta &= \frac{\pi}{2}\left(\frac{2}{\pi ka}\right)^2 \left[\sum_{n=1}^{\infty}\left(g_{n,n-1} + g_{n-1,n}\right) - \sum_{n=0}^{1} g_{n,1,n}\right] \\ &= \frac{\pi}{2}\left(\frac{2}{\pi ka}\right)^2 \left[\sum_{n=2}^{\infty}\left(g_{n,n-1} + g_{n-1,n}\right)\right] \end{aligned} \tag{A.130}$$

where

$$g_{n,m} = \beta_n \hat{\beta}_m A_n A_m nm e^{-i(\psi_n - \psi_m)} \tag{A.131}$$

It is found that

$$g_{n,n-1} = +4in(n-1) A_n A_{n-1} e^{-i(\psi_n - \psi_{n-1})} \tag{A.132}$$

$$g_{n-1,n} = -4in(n-1) A_n A_{n-1} e^{+i(\psi_n - \psi_{n-1})} \tag{A.133}$$

$$g_{n,n-1} + g_{n-1,n} = 8n(n-1) A_n A_{n-1} \sin(\psi_n - \psi_{n-1}) \tag{A.134}$$

and

$$\int_{-\pi}^{\pi} T\hat{T} \cos\theta d\theta = 4\pi \left(\frac{2}{\pi ka}\right)^2 \sum_{n=1}^{\infty} n(n-1) A_n A_{n-1} \sin(\psi_n - \psi_{n-1}) \tag{A.135}$$

Similarly

$$\begin{aligned} \int_{-\pi}^{\pi} T^2 \cos\theta d\theta &= -\frac{\pi}{2}\left(\frac{2}{\pi ka}\right)^2 \left[\sum_{n=1}^{\infty}\left(h_{n,n-1} + h_{n-1,n}\right) - \sum_{n=0}^{1} h_{n,1,n}\right] \\ &= -\frac{\pi}{2}\left(\frac{2}{\pi ka}\right)^2 \left[\sum_{n=2}^{\infty}\left(h_{n,n-1} + h_{n-1,n}\right)\right] \end{aligned} \tag{A.136}$$

where

$$h_{n,m} = \beta_n \beta_m A_n A_m nm e^{-i(\psi_n + \psi_m)} e^{-i2\sigma t} \tag{A.137}$$

It is found that

$$h_{n,n-1} = +4n(n-1) A_n A_{n-1} e^{i\left[(2n-1)\frac{\pi}{2} - \psi_n - \psi_{n-1}\right]} e^{-i2\sigma t} \tag{A.138}$$

$$h_{n-1,n} = h_{n,n-1} \tag{A.139}$$

$$h_{n,n-1} + h_{n-1,n} = 8n(n-1) A_n A_{n-1} e^{i\left[(2n-1)\frac{\pi}{2} - \psi_n - \psi_{n-1}\right]} e^{-i2\sigma t} \tag{A.140}$$

and

$$\int_{-\pi}^{\pi} T^2 \cos\theta \, d\theta = 4\pi \left(\frac{2}{\pi ka}\right)^2 \sum_{n=1}^{\infty} n(n-1) A_n A_{n-1} e^{i\left[(2n-1)\frac{\pi}{2} - \psi_n - \psi_{n-1}\right]} e^{-i2\sigma t} \tag{A.141}$$

Inserting the results from Equations A.127 and A.135 into Equation A.126 gives the steady velocity-square force component

$$\begin{aligned} F_{21v}^{s} = & +\frac{\rho g a H^2}{2\pi (ka)^2} \\ & \cdot \left[\left(1 + \frac{2kd}{\sinh 2kd}\right) \sum_{n=2}^{\infty} \frac{n(n-1)}{(ka)^2} A_n A_{n-1} \sin(\psi_n - \psi_{n-1}) \right. \\ & \left. + \left(1 - \frac{2kd}{\sinh 2kd}\right) \sum_{n=2}^{\infty} A_n A_{n-1} \sin(\psi_n - \psi_{n-1}) \right] \end{aligned} \tag{A.142}$$

Inserting the results from Equations A.128 and A.141 into Equation A.126 gives the oscillatory velocity-square force component

$$\begin{aligned} F_{21v}^{o} = & +\frac{\rho g a H^2}{2\pi (ka)^2} \left[\left(1 + \frac{2kd}{\sinh 2kd}\right) \sum_{n=2}^{\infty} \frac{n(n-1)}{(ka)^2} A_n A_{n-1} e^{i[(2n-1) - \psi_n - \psi_{n-1}]} \right. \\ & \left. + \left(1 - \frac{2kd}{\sinh 2kd}\right) \sum_{n=2}^{\infty} A_n A_{n-1} e^{i\left[(2n-1)\frac{\pi}{2} - \psi_n - \psi_{n-1}\right]} \right] e^{-i2\sigma t} \end{aligned} \tag{A.143}$$

APPENDIX B
DERIVATION OF COEFFICIENTS FOR SCATTERED WAVE SOLUTION

The second-order kinematic structural boundary condition

$$\tilde{\Phi}_{2r}^{H} = -\tilde{\Phi}_{2r}^{P} \tag{B.1}$$

may be satisfied by inserting the nondimensional expressions for the homogeneous solutions, $\tilde{\Phi}_2^H$, from Equation 3.24, and the particular solutions, $\tilde{\Phi}_2^P$, from Equation 3.77. Since all time dependence at frequency 2σ and angular dependence like $\cos n\theta$ may be separated from both sides of Equation B.1, the unknown coefficients $\tilde{a}_{n0}$ and $\tilde{a}_{nj}$ in the homogeneous, i.e. scattered, wave solution may be found from the expression

$$\begin{aligned}
&\tilde{a}_{n0}\frac{k_2}{k}\cosh k_2(d+z)H_n'(k_2a) + \sum_{j=1}^{\infty}\tilde{a}_{nj}\frac{\kappa_{2j}}{k}\cos\kappa_{2j}(d+z)K_n'(\kappa_{2j}a) \\
&= i\frac{3kH}{4}\frac{(\tanh^2 kd-1)\cosh 2k(d+z)}{\cosh 2kd(\tanh 2kd - 2\tanh kd)}\beta_n J_n'(2ka) \\
&+ i\frac{kH}{4}PV\int_0^{\infty}\left(\frac{\kappa}{k}\right)^2\frac{\cosh\kappa(d+z)}{\cosh\kappa d(\kappa\tanh\kappa d - k_2\tanh k_2 d)}\tilde{D}_n(\kappa)J_n'(\kappa a)d\kappa \\
&- \pi\frac{kH}{2}\left(\frac{k_2}{k}\right)^2\frac{\cosh k_2 d\cosh k_2(d+z)}{\sinh 2k_2 d + 2k_2 d}\tilde{D}_n(k_2)J_n'(k_2a)
\end{aligned} \tag{B.2}$$

Multiplying both sides of Equation B.2 by $\cosh k_2(d+z)$ and integrating over depth, using the orthogonality conditions between $\cosh k_2(d+z)$ and $\cos\kappa_{2j}(d+z)$ yields the result for $\tilde{a}_{n0}$ as

$$\begin{aligned}
&\tilde{a}_{n0}\frac{k_2}{k}H_n'(k_2a)\int_{-d}^{0}\cosh^2 k_2(d+z)dz \\
&= i\frac{3kH}{4}\beta_n J_n'(2ka)\frac{(\tanh^2 kd-1)}{\cosh 2kd(\tanh 2kd - 2\tanh kd)} \\
&\quad\cdot\int_{-d}^{0}\cosh 2k(d+z)\cosh k_2(d+z)dz \\
&+ i\frac{kH}{4}PV\int_0^{\infty}\left(\frac{\kappa}{k}\right)^2\frac{\tilde{D}_n(\kappa)J_n'(\kappa a)}{\cosh\kappa d(\kappa\tanh\kappa d - k_2\tanh k_2 d)}
\end{aligned}$$

$$\cdot \int_{-d}^{0} \cosh \kappa(d+z) \cosh k_2(d+z) dz d\kappa$$

$$- \pi \frac{kH}{2} \left(\frac{k_2}{k}\right)^2 \frac{\cosh k_2 d}{\sinh 2k_2 d + 2k_2 d} \tilde{D}_n(k_2) J_n'(k_2 a) \int_{-d}^{0} \cosh^2 k_2(d+z) dz \qquad \text{(B.3)}$$

This may be reduced by evaluating the integrals over depth to give

$$\begin{aligned}
\tilde{a}_{n0} &= i6kH \frac{k^2(\tanh^2 kd - 1)}{(4k^2 - k_2^2)} \frac{\cosh k_2 d}{\sinh 2k_2 d + 2k_2 d} \beta_n \frac{J_n'(2ka)}{H_n'(k_2 a)} \\
&+ ikH \frac{\cosh k_2 d}{(\sinh 2k_2 d + 2k_2 d)} \frac{1}{kH_n'(k_2 a)} PV \int_0^{\infty} \frac{\kappa^2 \tilde{D}_n(\kappa) J_n'(\kappa a)}{(\kappa^2 - k_2^2)} d\kappa \\
&- \pi \frac{kH}{2} \frac{k_2}{k} \frac{\cosh k_2 d}{\sinh 2k_2 d + 2k_2 d} \tilde{D}_n(k_2) \frac{J_n'(k_2 a)}{H_n'(k_2 a)}
\end{aligned} \qquad \text{(B.4)}$$

In a similar fashion, multiplying both sides of Equation B.2 by $\cos \kappa_{2j}(d+z)$ and integrating over depth, making use of the orthogonality between $\cos \kappa_{2j}(d+z)$ and $\cosh k_2(d+z)$ yields the result for $\tilde{a}_{nj}$

$$\begin{aligned}
&\tilde{a}_{nj} \frac{\kappa_{2j}}{k} K_n'(\kappa_{2j} a) \int_{-d}^{0} \cos^2 \kappa_{2j}(d+z) dz \\
&= i\frac{3kH}{4} \beta_n J_n'(2ka) \frac{(\tanh^2 kd - 1)}{\cosh 2kd(\tanh 2kd - 2\tanh kd)} \\
&\quad \cdot \int_{-d}^{0} \cosh 2k(d+z) \cos \kappa_{2j}(d+z) dz \\
&+ i\frac{kH}{4} PV \int_0^{\infty} \left(\frac{\kappa}{k}\right)^2 \frac{\tilde{D}_n(\kappa) J_n'(\kappa a)}{\cosh \kappa d(\kappa \tanh \kappa d - k_2 \tanh k_2 d)} \\
&\quad \cdot \int_{-d}^{0} \cosh \kappa(d+z) \cos \kappa_{2j}(d+z) dz d\kappa
\end{aligned}$$

Completing the integration over depth yields

$$\begin{aligned}
\tilde{a}_{nj} &= i6kH \frac{k^2(\tanh^2 kd - 1)}{(4k^2 + \kappa_{2j}^2)} \frac{\cos \kappa_{2j} d}{\sin 2\kappa_{2j} d + 2\kappa_{2j} d} \beta_n \frac{J_n'(2ka)}{K_n'(\kappa_{2j} a)} \\
&+ ikH \frac{\cos \kappa_{2j} d}{(\sin 2\kappa 2jd + 2\kappa_{2j} d)} \frac{1}{kK_n'(\kappa_{2j} a)} \int_0^{\infty} \kappa^2 \frac{\tilde{D}_n(\kappa) J_n'(\kappa a)}{\kappa^2 + \kappa_{2j}^2}
\end{aligned} \qquad \text{(B.5)}$$

APPENDIX C
USEFUL INTEGRALS

Based on the following dispersion relationships for first and second-order

$$\begin{aligned} \sigma^2 &= gk \tanh kd \\ \sigma^2 &= -g\kappa_j \tan \kappa_j d \\ 4\sigma^2 &= gk_2 \tanh k_2 d \\ 4\sigma^2 &= -g\kappa_{2j} \tan \kappa_{2j} d \end{aligned} \tag{C.1}$$

the following required integrals over depth are obtained

$$\int_{-d}^{0} \cosh^2 k(d+z)dz = \frac{\sinh 2kd + 2kd}{4k} \tag{C.2}$$

$$\int_{-d}^{0} \cosh k(d+z) \cos \kappa_j (d+z)dz = 0 \tag{C.3}$$

$$\int_{-d}^{0} \cosh^2 k_2(d+z)dz = \frac{\sinh 2k_2 d + 2k_2 d}{4k_2} \tag{C.4}$$

$$\int_{-d}^{0} \cosh k_2(d+z) \cos \kappa_{2j}(d+z)dz = 0 \tag{C.5}$$

$$\int_{-d}^{0} \cosh k_2(d+z) \cosh 2k(d+z)dz = \frac{\cosh k_2 d \cosh 2kd}{(4k^2 - k_2^2)} [2k \tanh 2kd - k_2 \tanh k_2 d] \tag{C.6}$$

$$\int_{-d}^{0} \cosh k_2(d+z) \cosh \kappa(d+z)dz = \frac{\cosh k_2 d \cosh \kappa d}{(\kappa^2 - k_2^2)} [\kappa \tanh \kappa d - k_2 \tanh k_2 d] \tag{C.7}$$

$$\int_{-d}^{0} \cos^2 \kappa_{2j}(d+z)dz = \frac{\sin 2\kappa_{2j} d + 2\kappa_{2j} d}{4\kappa_{2j}} \tag{C.8}$$

$$\int_{-d}^{0} \cos \kappa_{2j}(d+z) \cos \kappa_{2i}(d+z)dz = 0 \tag{C.9}$$

$$\int_{-d}^{0} \cos \kappa_{2j}(d+z) \cosh 2k(d+z) dz =$$
$$\frac{\cos \kappa_{2j} d \cosh 2kd}{(4k^2 + \kappa_{2j}^2)} [2k \tanh 2kd - k_2 \tanh k_2] \tag{C.10}$$

$$\int_{-d}^{0} \cos \kappa_{2j}(d+z) \cosh \kappa(d+z) dz =$$
$$\frac{\cos \kappa_{2j} d \cosh \kappa}{(\kappa^2 + \kappa_{2j}^2)} [\kappa \tanh \kappa d - k_2 \tanh k_2 d] \tag{C.11}$$

It is noted that while integrals that involve products of functions of the second order free wavenumbers, k_2 and κ_{2j}, vanish identically, integrals that involve cross-products of these functions with functions that depend on the second-order forced wave motions with wavenumber $2k$ and the continuum of wavenumbers, κ, do not vanish. Therefore, the scattering of the second-order forced waves produce scattered waves that both radiate away from the cylinder, with wavenumber k_2 as well as local evanescent motions with wavenumbers κ_{2j}.

APPENDIX D
RESULTS OF WAVE RUNUP EXPERIMENTS

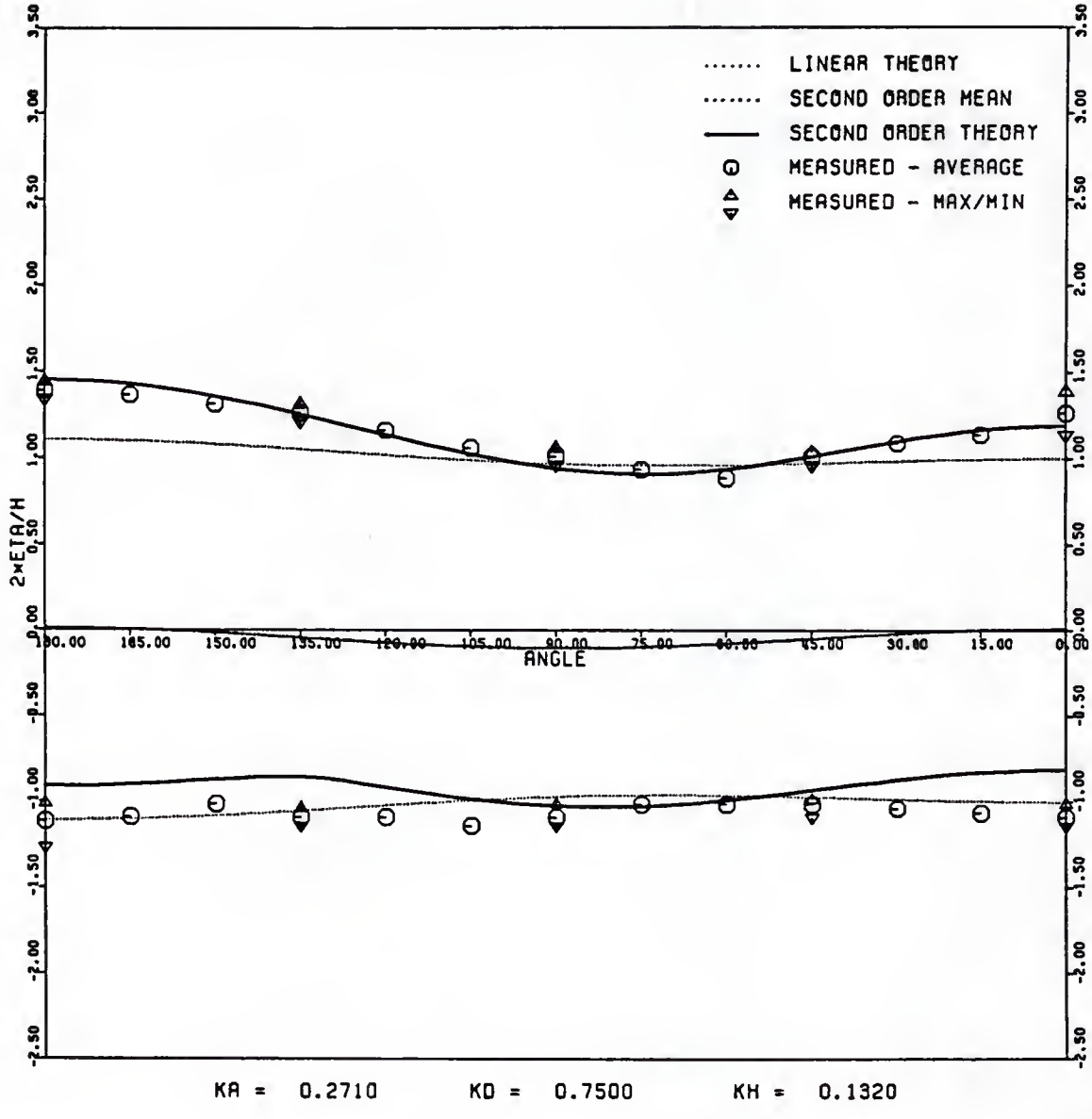

Figure D.1: Runup/rundown envelope for $ka = 0.271$, $kd = 0.750$, and $kH = 0.132$

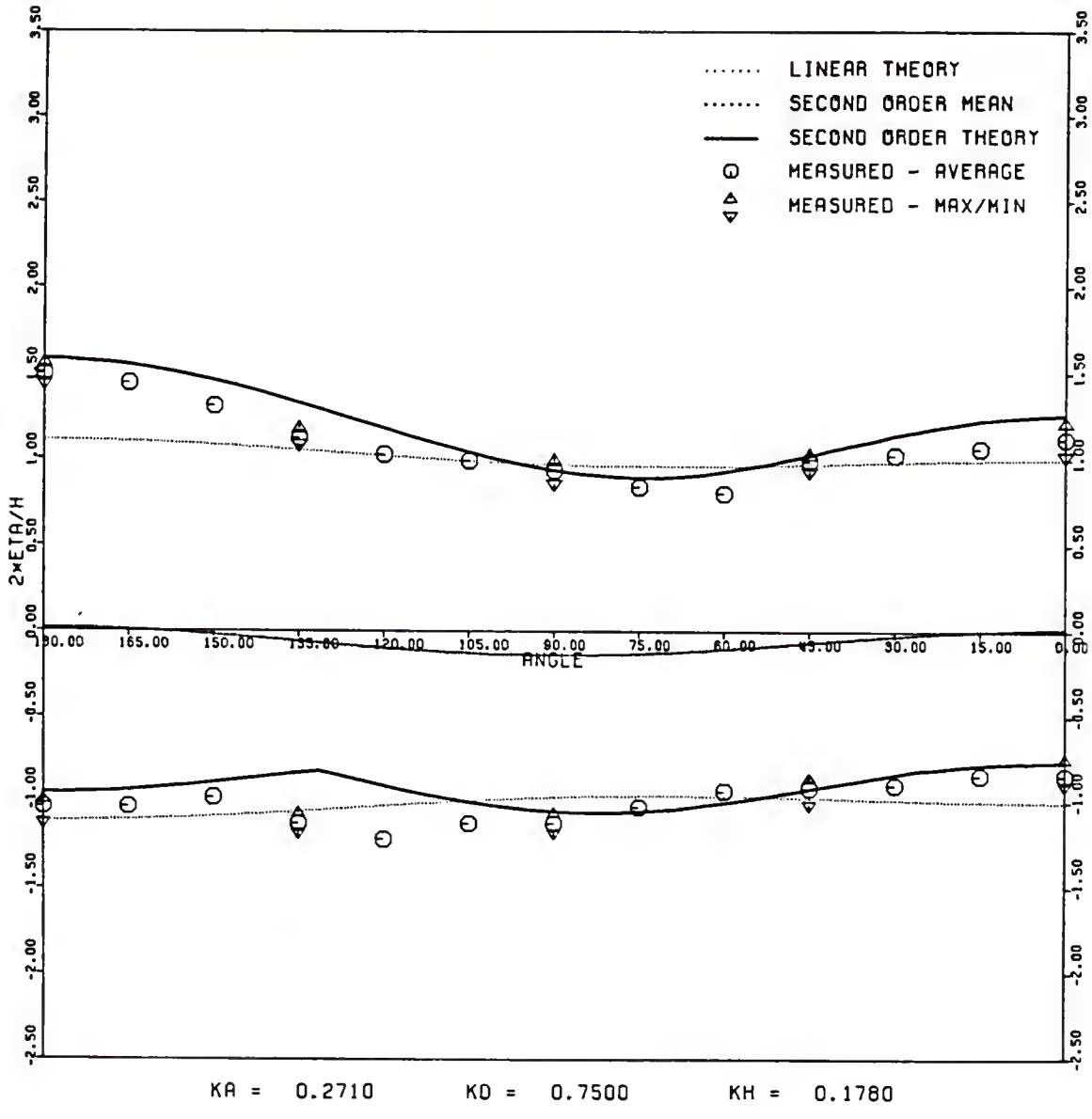

Figure D.2: Runup/rundown envelope for $ka = 0.271$, $kd = 0.750$, and $kH = 0.178$

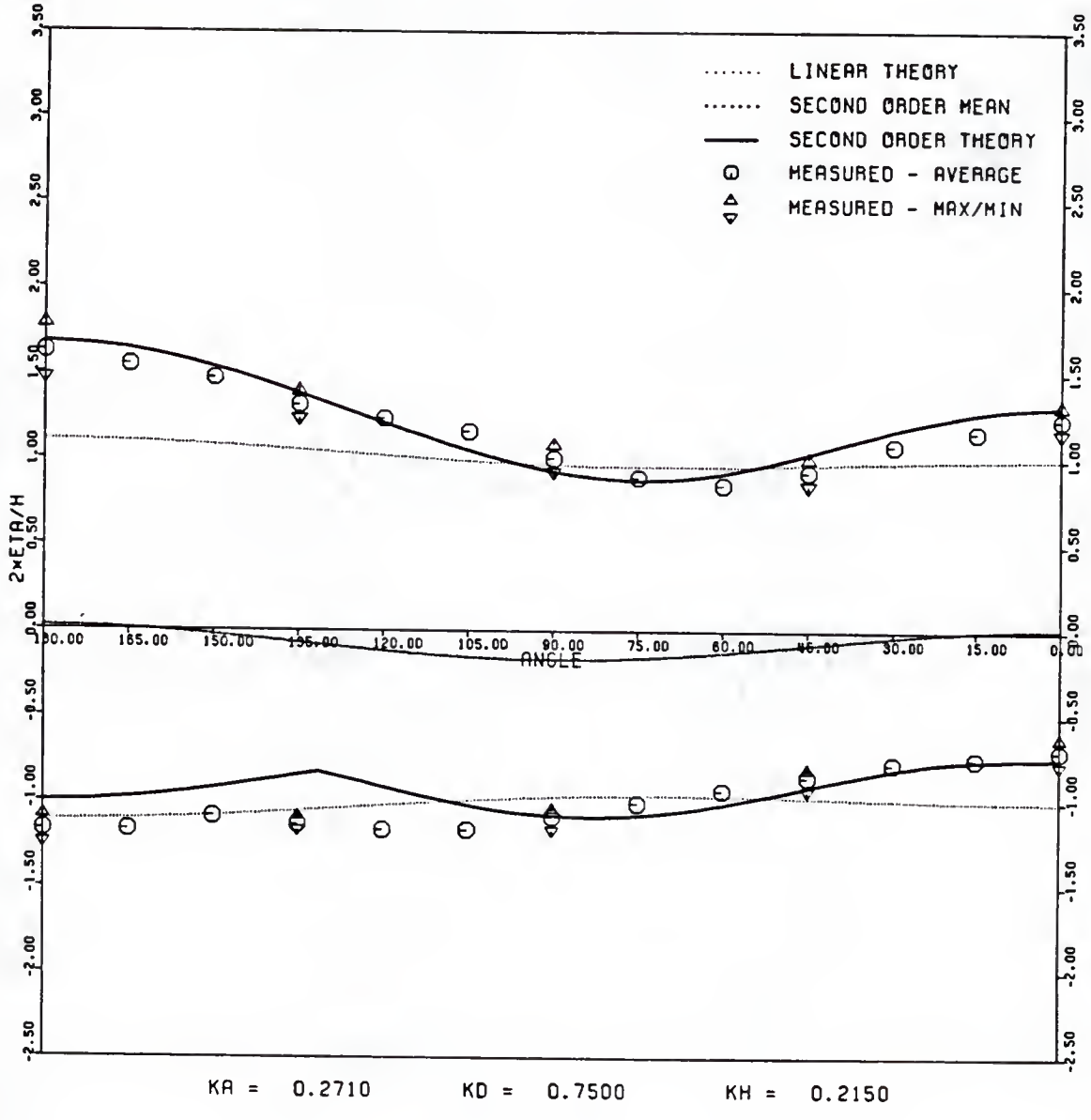

Figure D.3: Runup/rundown envelope for $ka = 0.271$, $kd = 0.750$, and $kH = 0.215$

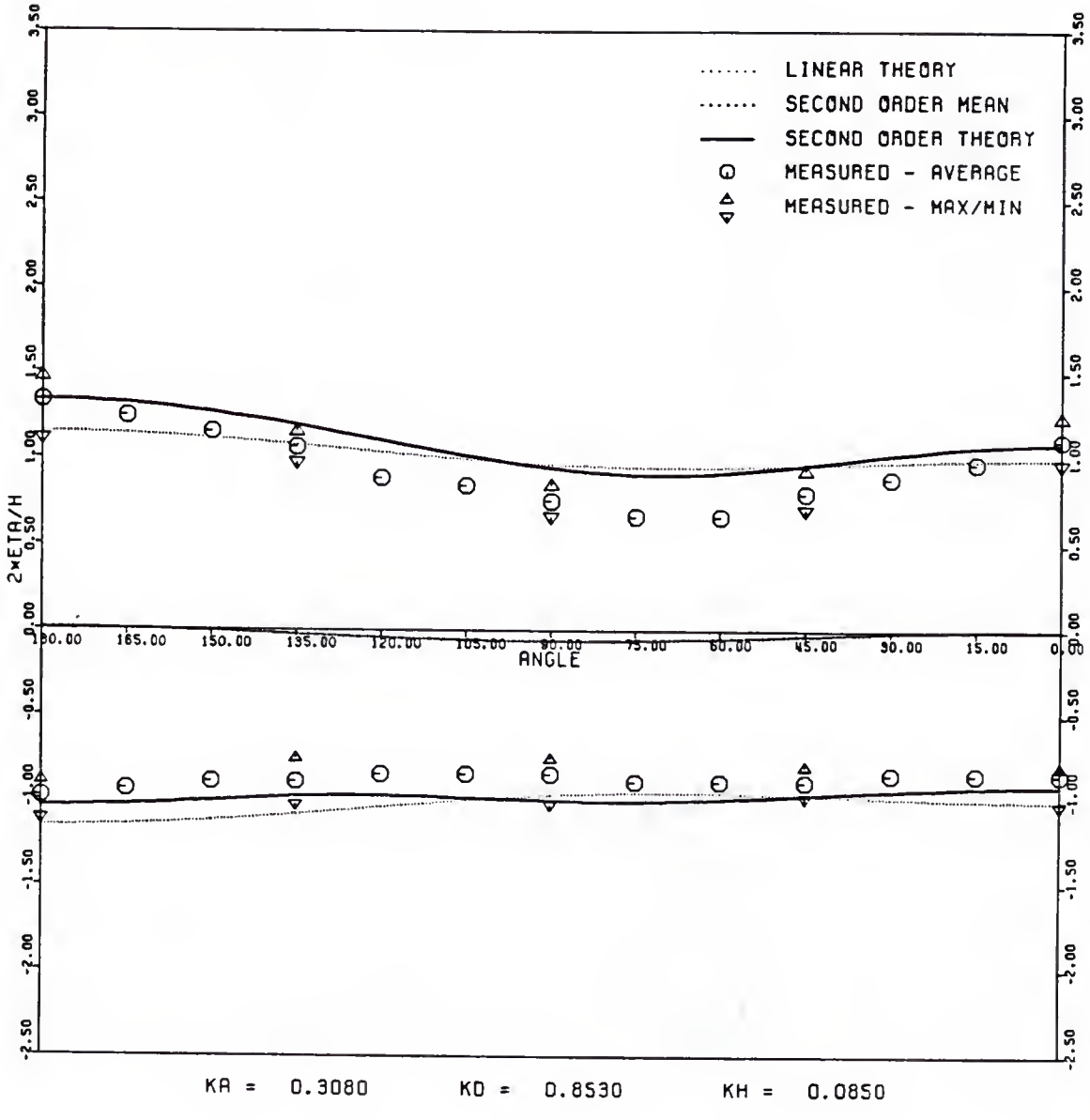

Figure D.4: Runup/rundown envelope for $ka = 0.308$, $kd = 0.853$, and $kH = 0.085$

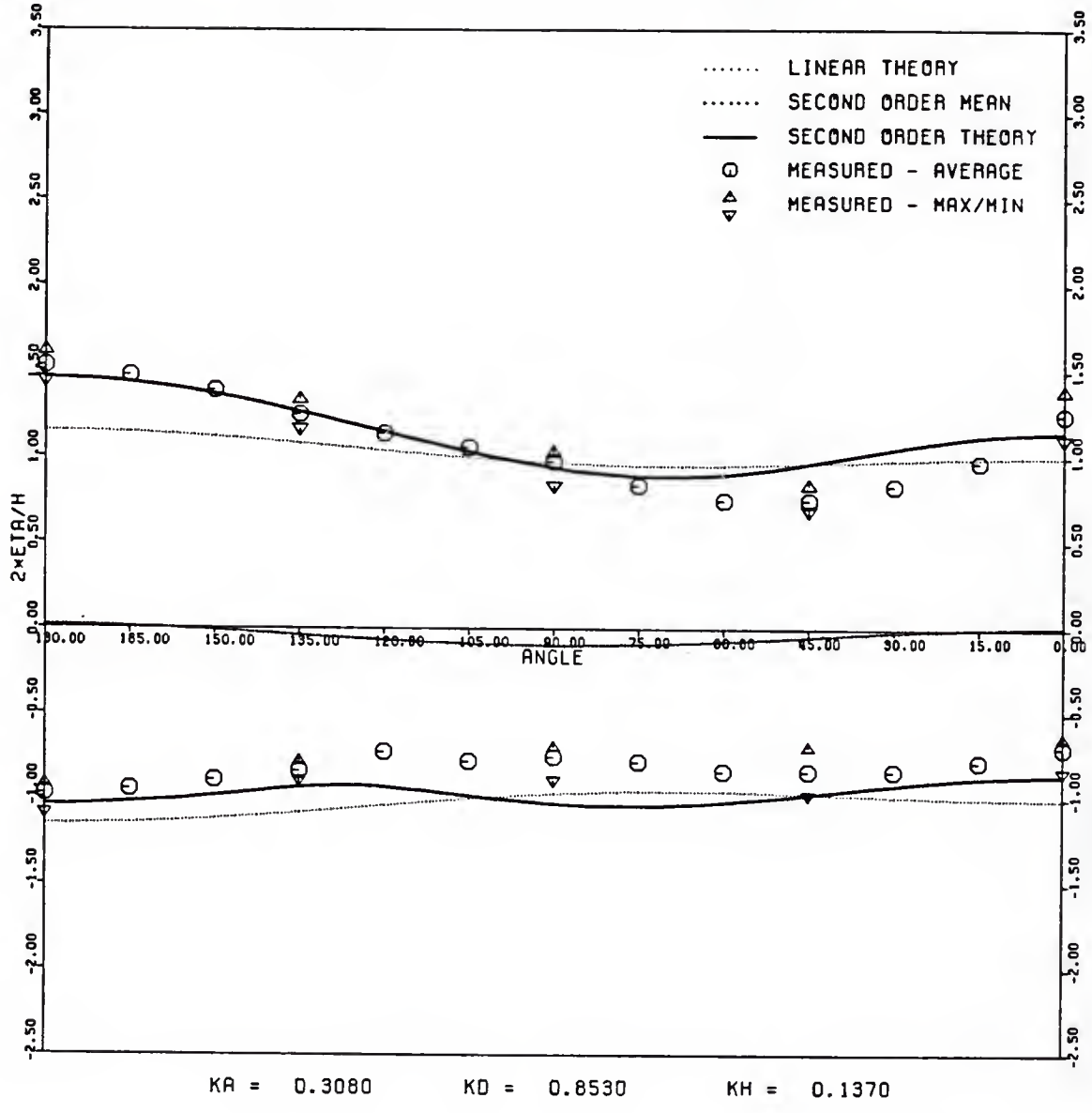

Figure D.5: Runup/rundown envelope for $ka = 0.308$, $kd = 0.853$, and $kH = 0.137$

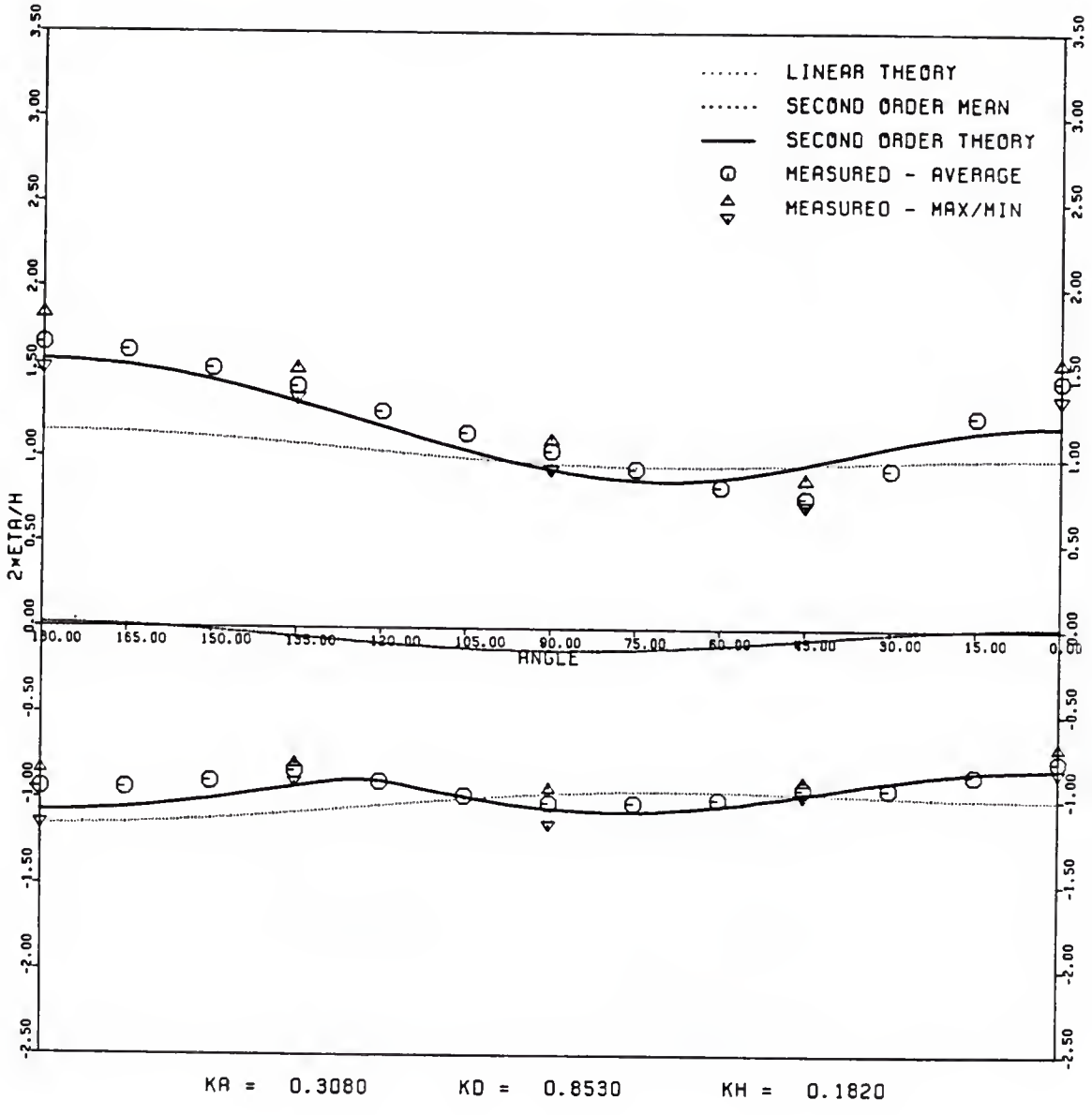

Figure D.6: Runup/rundown envelope for $ka = 0.308$, $kd = 0.853$, and $kH = 0.182$

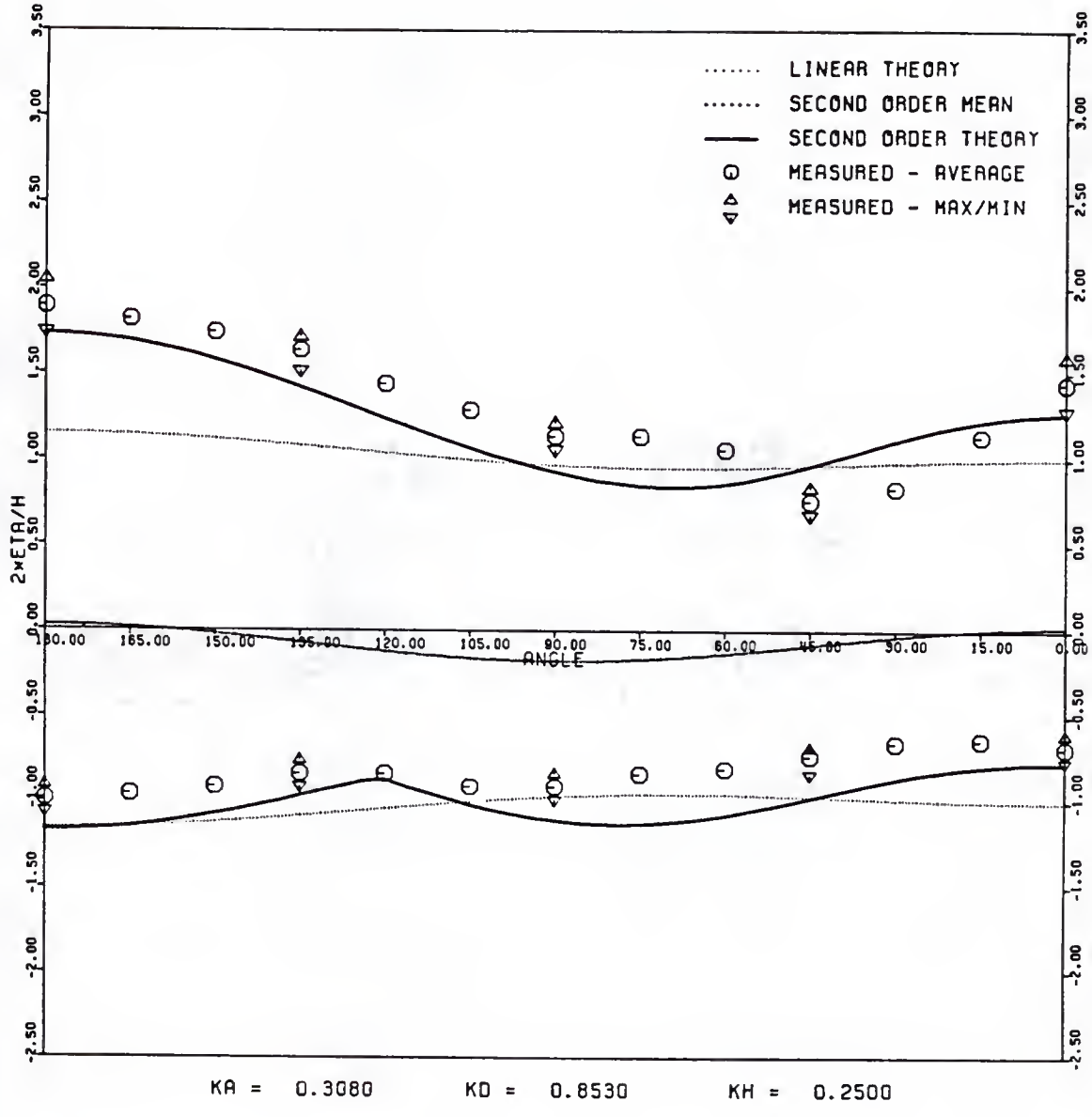

Figure D.7: Runup/rundown envelope for $ka = 0.308$, $kd = 0.853$, and $kH = 0.250$

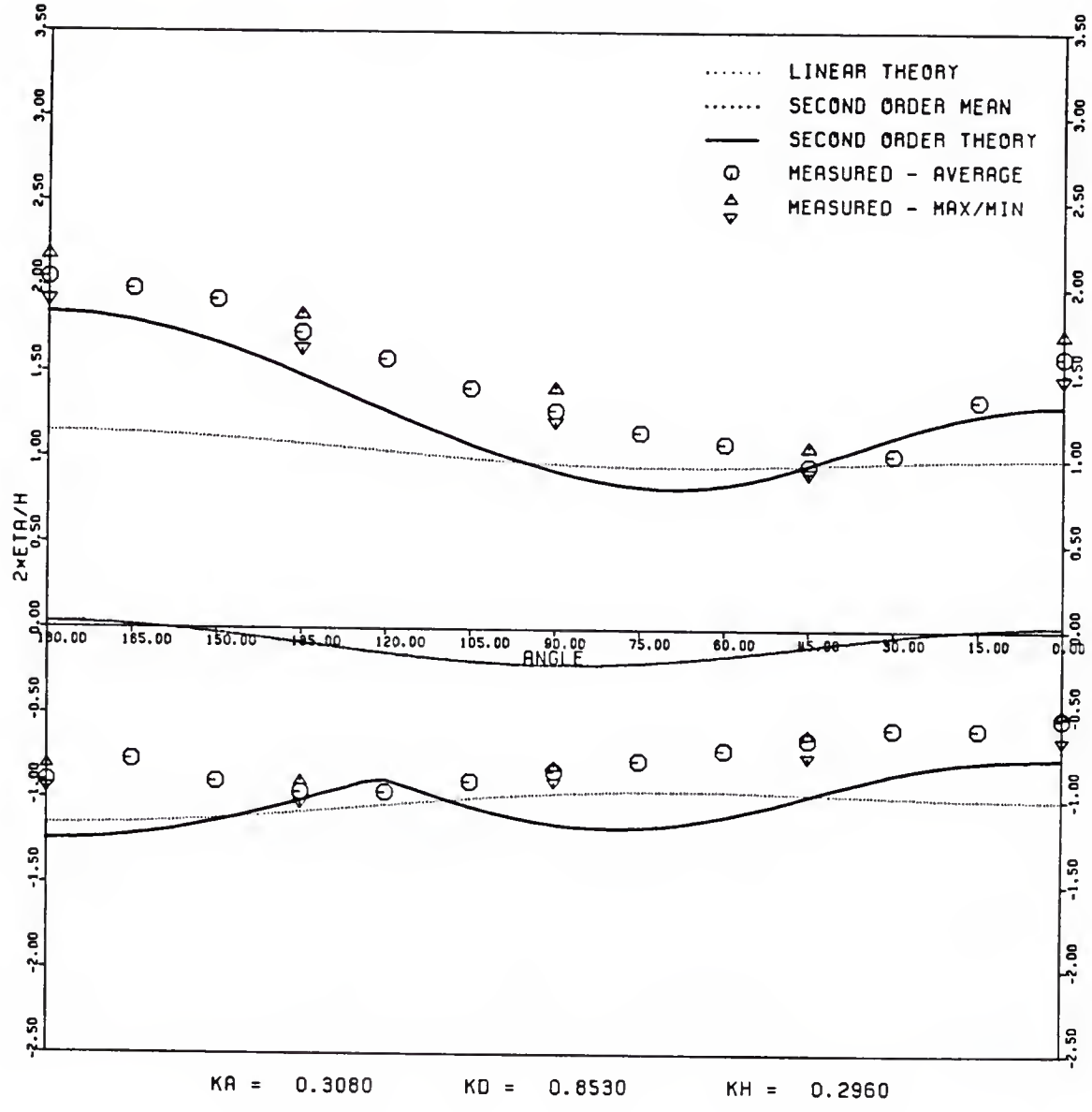

Figure D.8: Runup/rundown envelope for $ka = 0.308$, $kd = 0.853$, and $kH = 0.296$

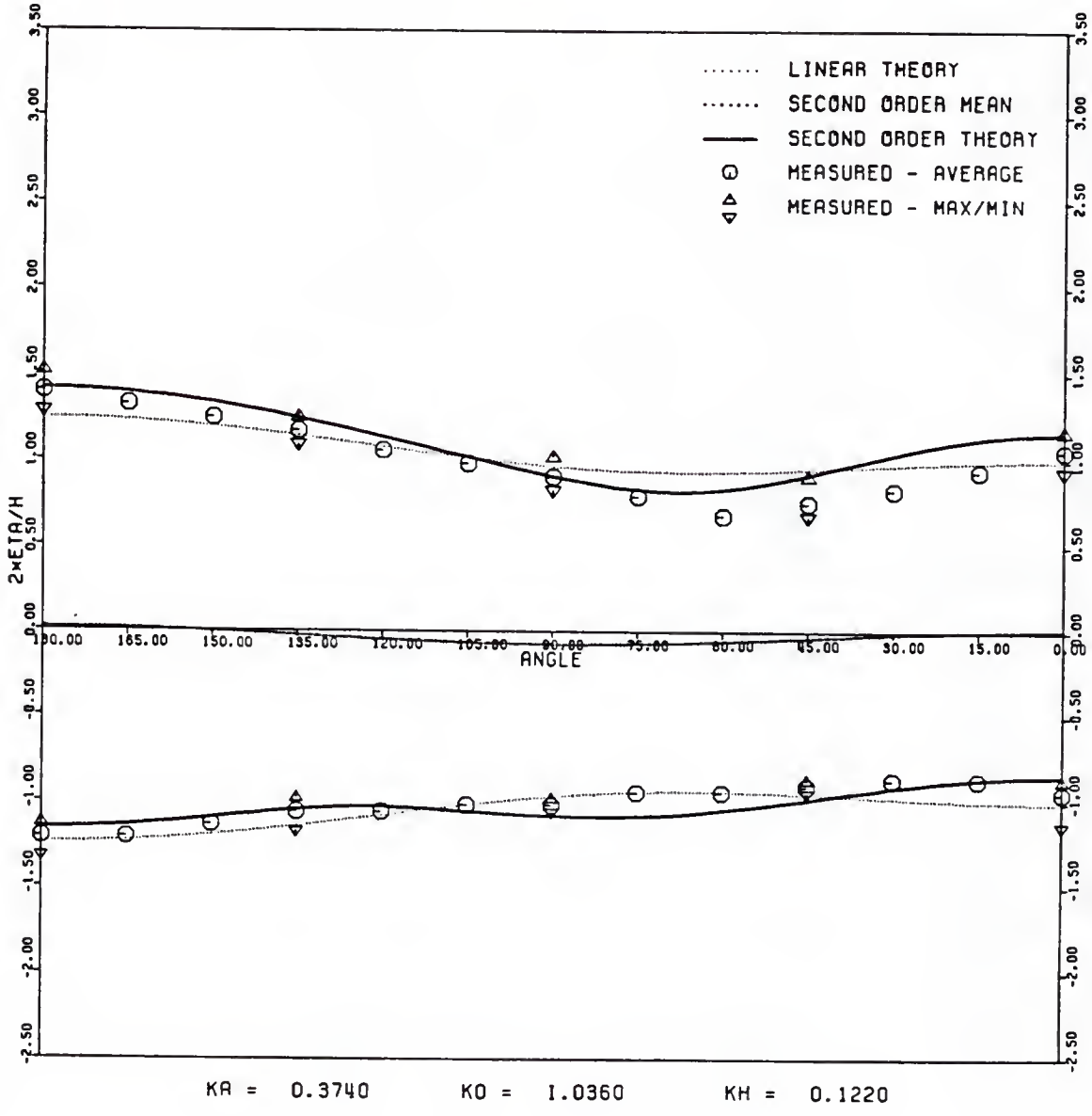

Figure D.9: Runup/rundown envelope for $ka = 0.374$, $kd = 1.036$, and $kH = 0.122$

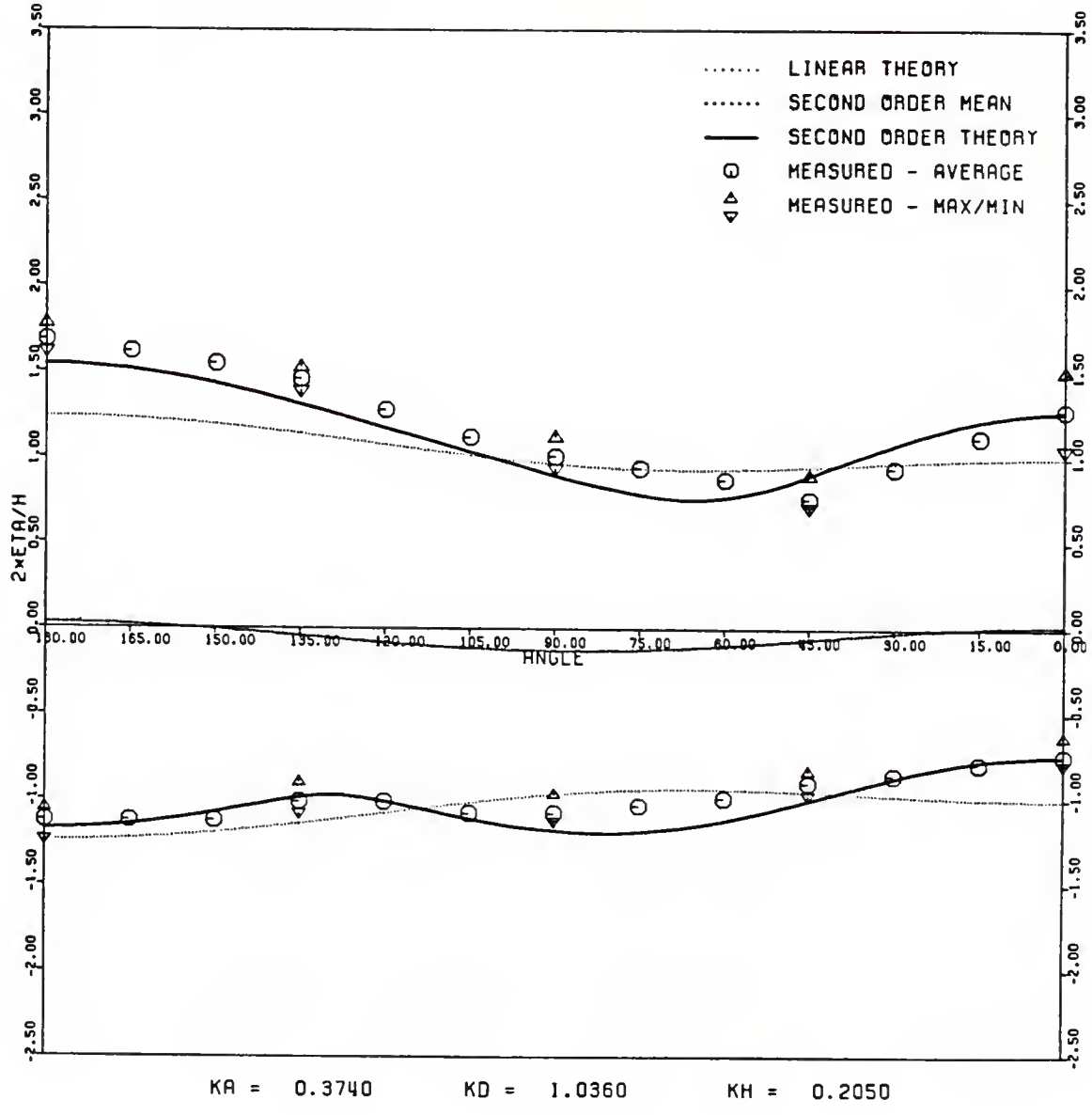

Figure D.10: Runup/rundown envelope for $ka = 0.374$, $kd = 1.036$, and $kH = 0.205$

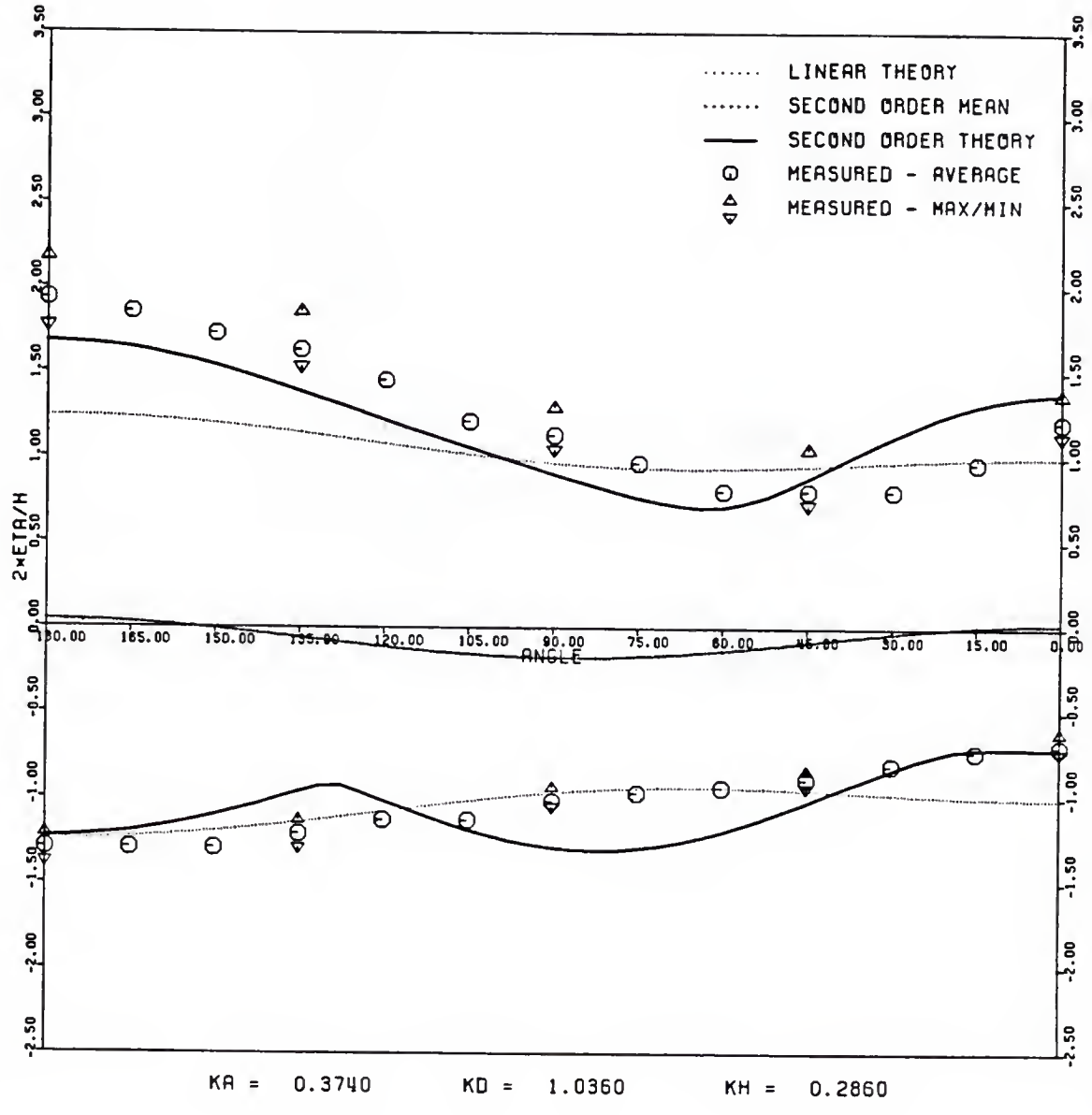

Figure D.11: Runup/rundown envelope for $ka = 0.374$, $kd = 1.036$, and $kH = 0.286$

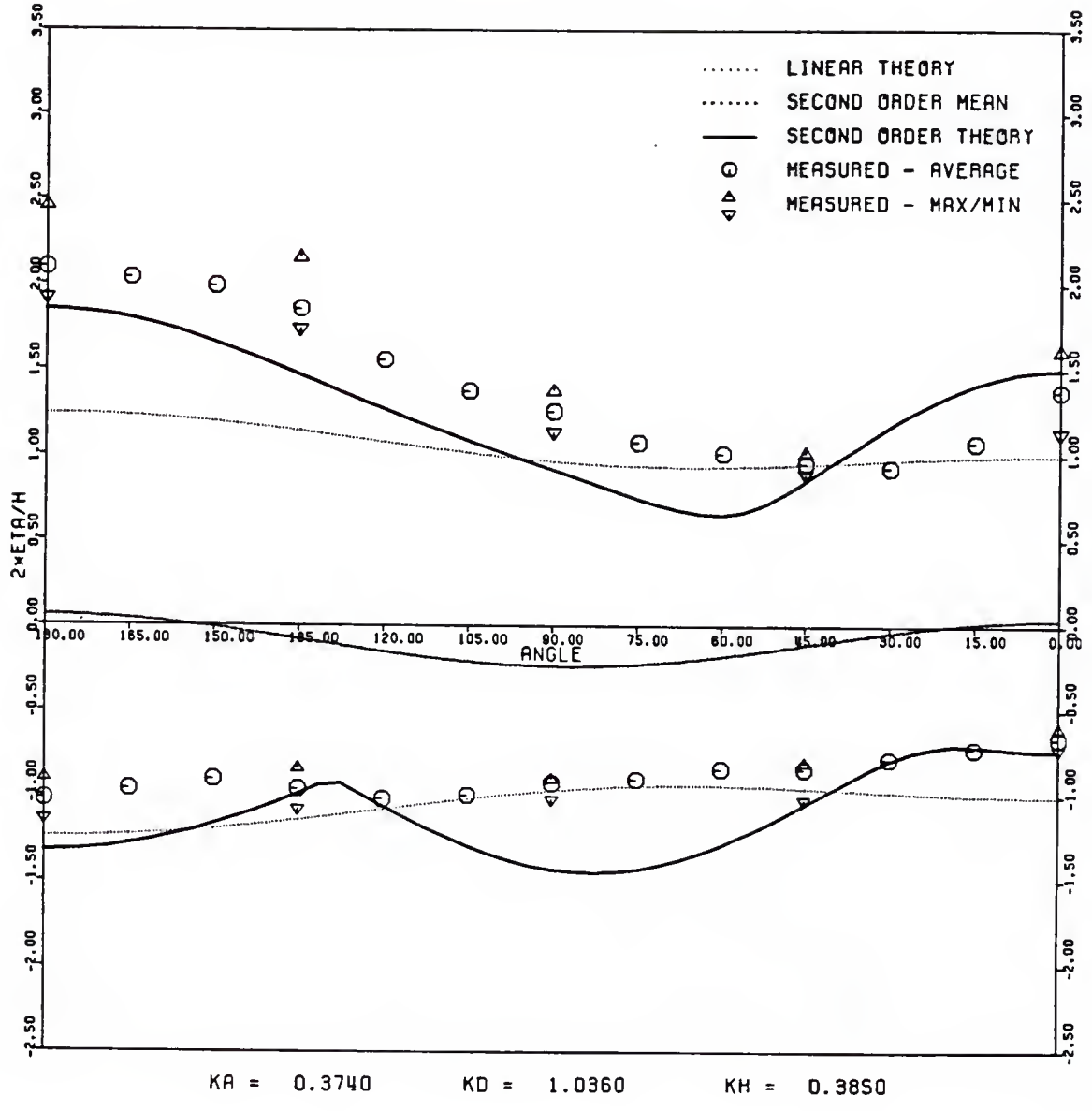

Figure D.12: Runup/rundown envelope for $ka = 0.374$, $kd = 1.036$, and $kH = 0.385$

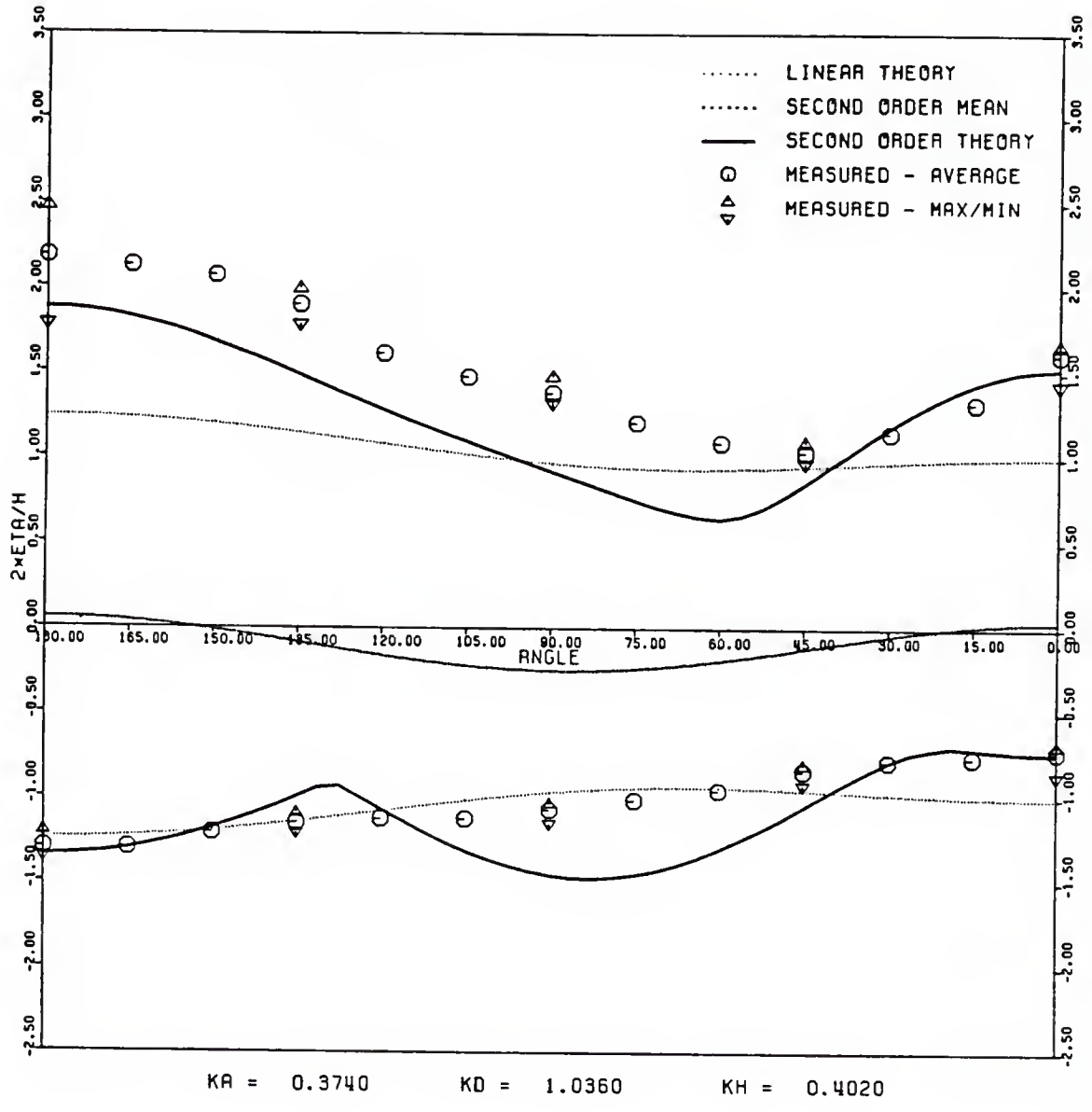

Figure D.13: Runup/rundown envelope for $ka = 0.374$, $kd = 1.036$, and $kH = 0.402$

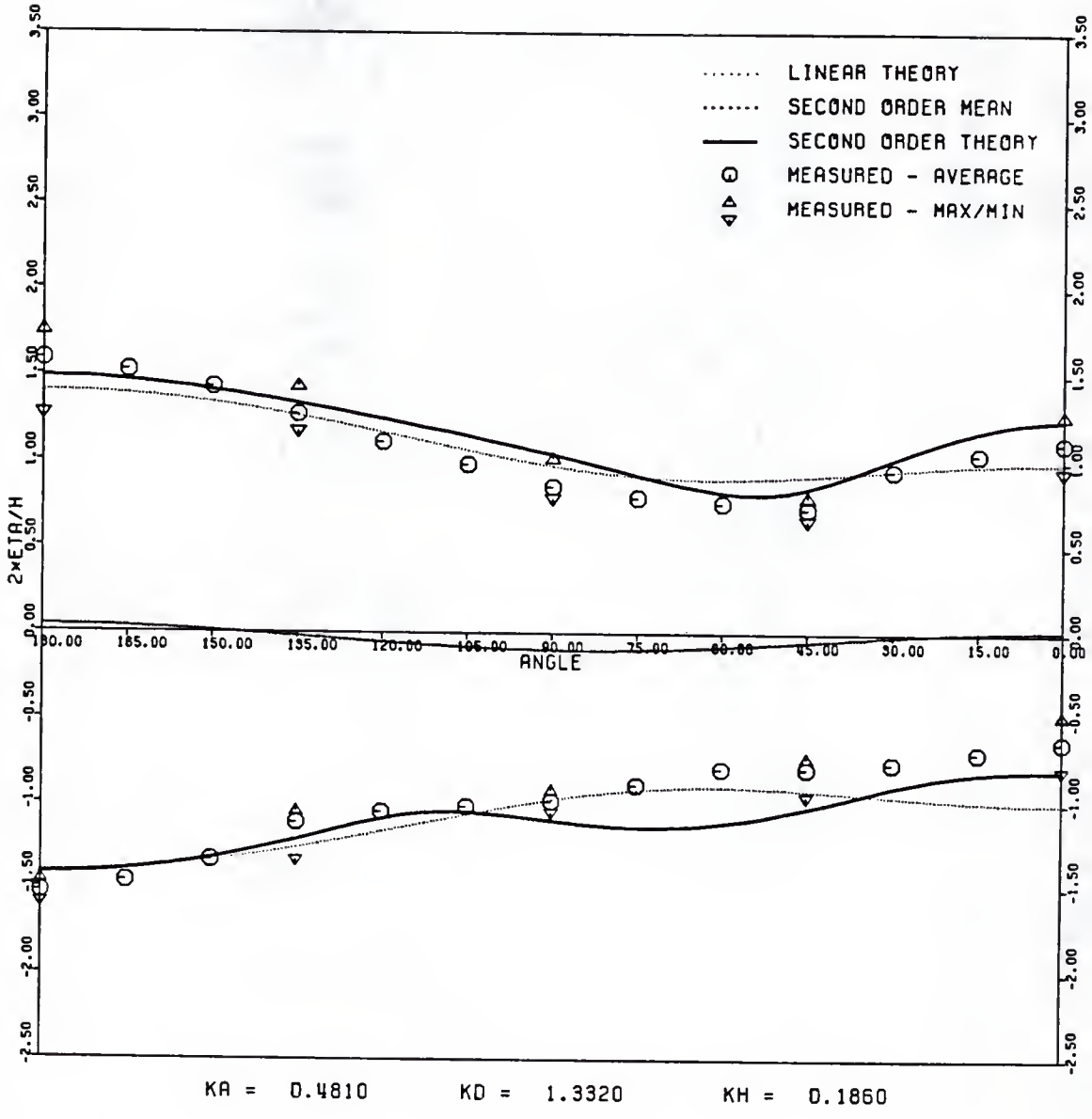

Figure D.14: Runup/rundown envelope for $ka = 0.481$, $kd = 1.332$, and $kH = 0.186$

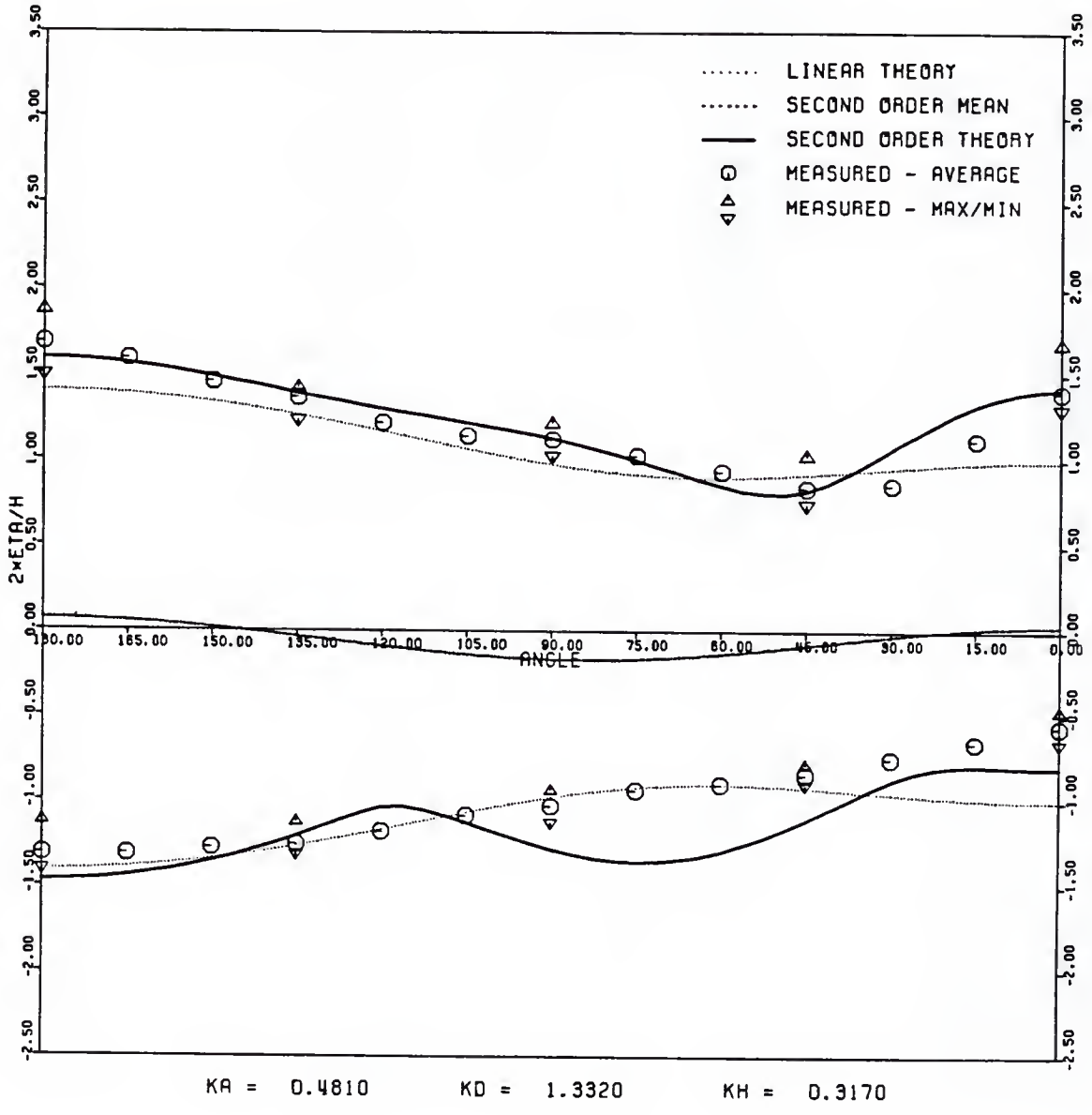

Figure D.15: Runup/rundown envelope for $ka = 0.481$, $kd = 1.332$, and $kH = 0.317$

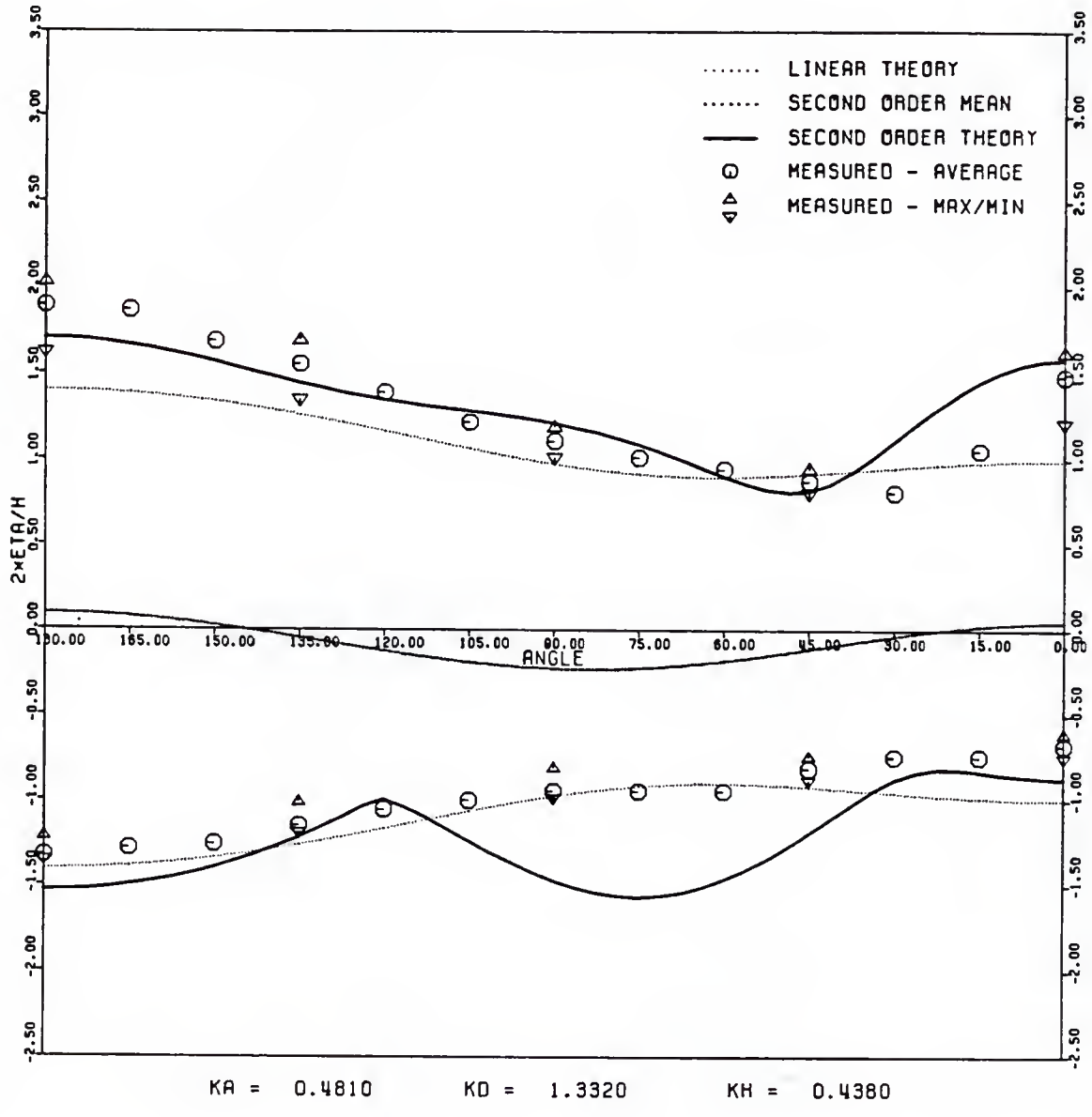

Figure D.16: Runup/rundown envelope for $ka = 0.481$, $kd = 1.332$, and $kH = 0.438$

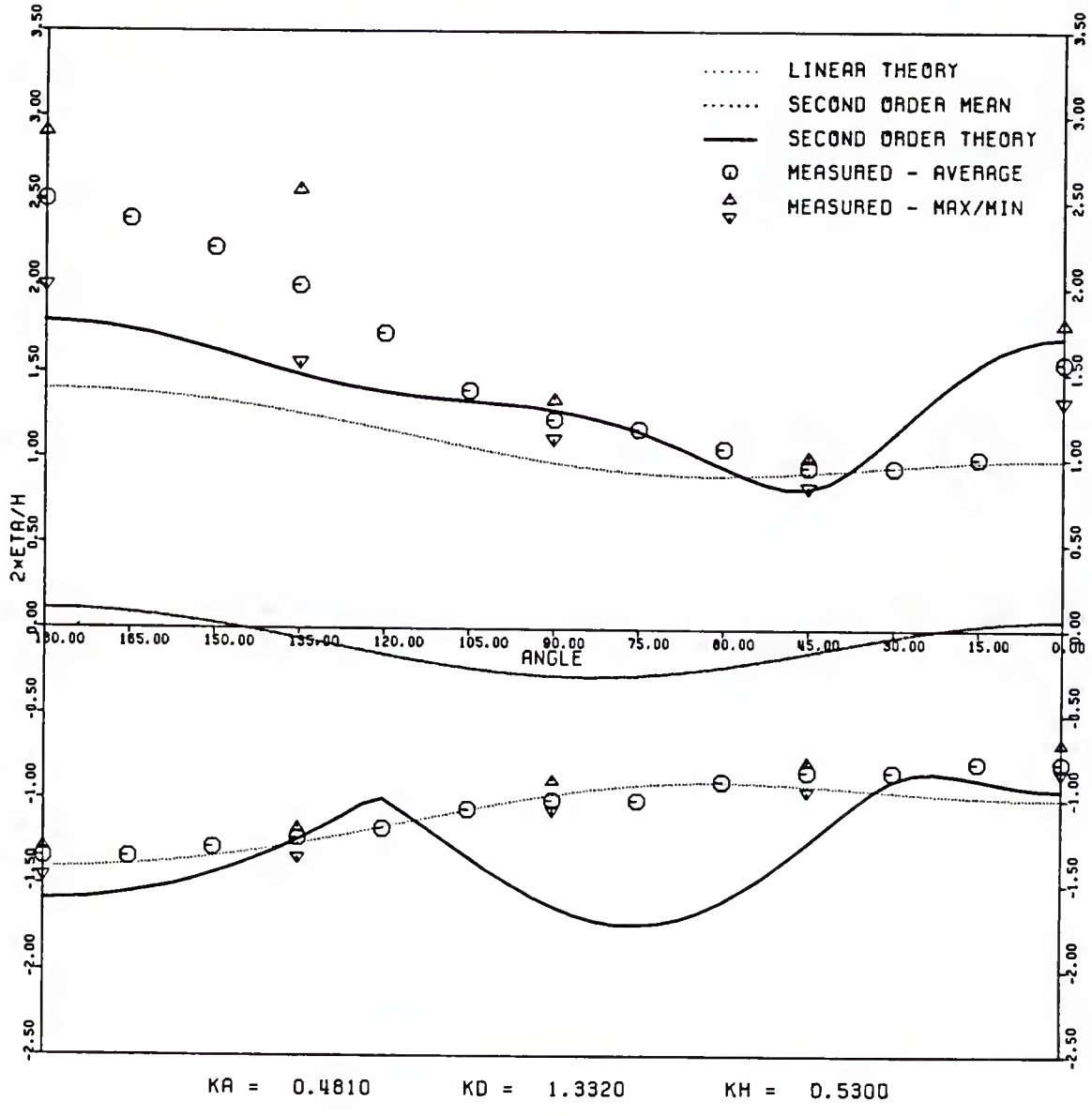

Figure D.17: Runup/rundown envelope for $ka = 0.481$, $kd = 1.332$, and $kH = 0.530$

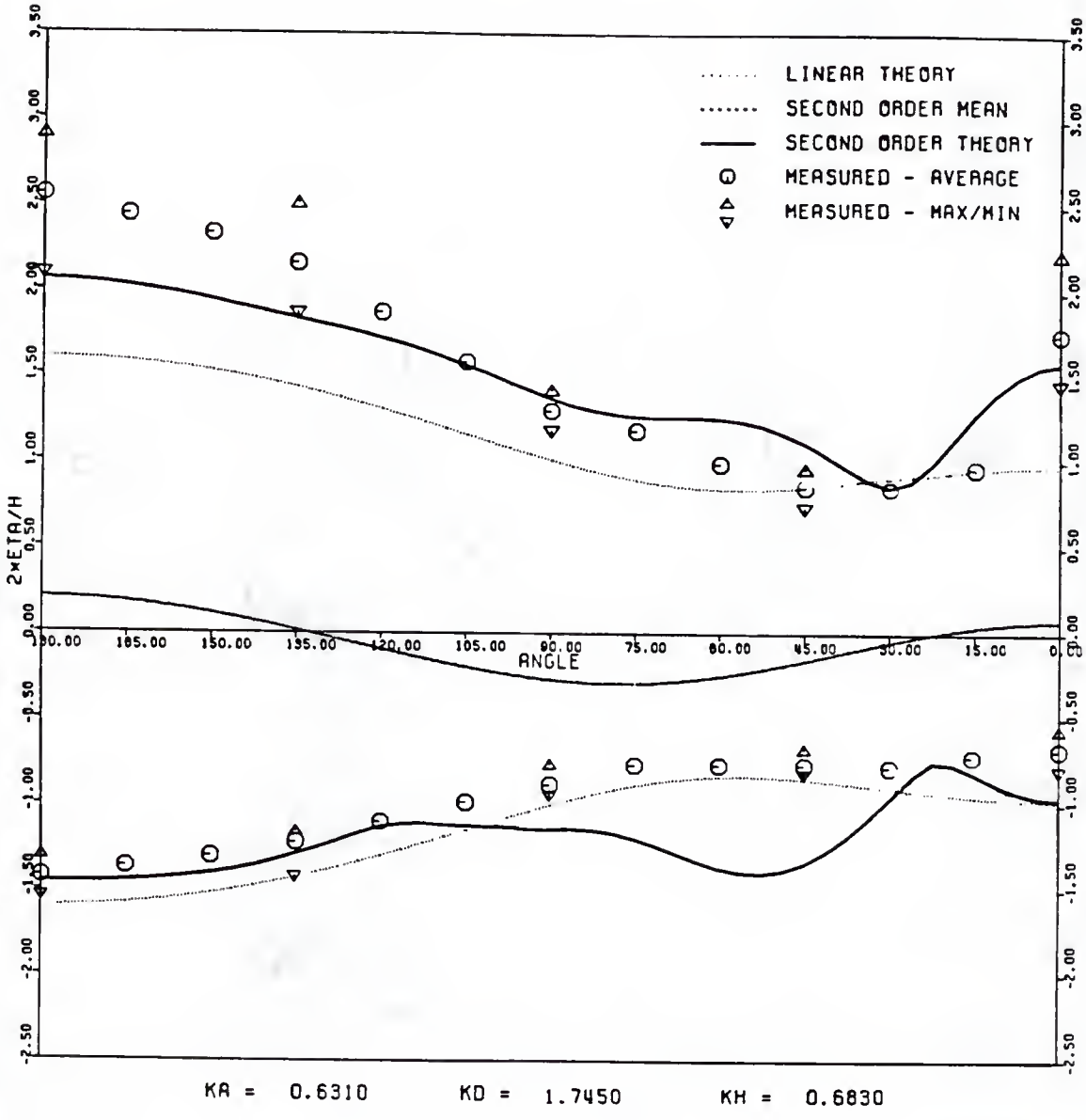

Figure D.18: Runup/rundown envelope for $ka = 0.631$, $kd = 1.745$, and $kH = 0.683$

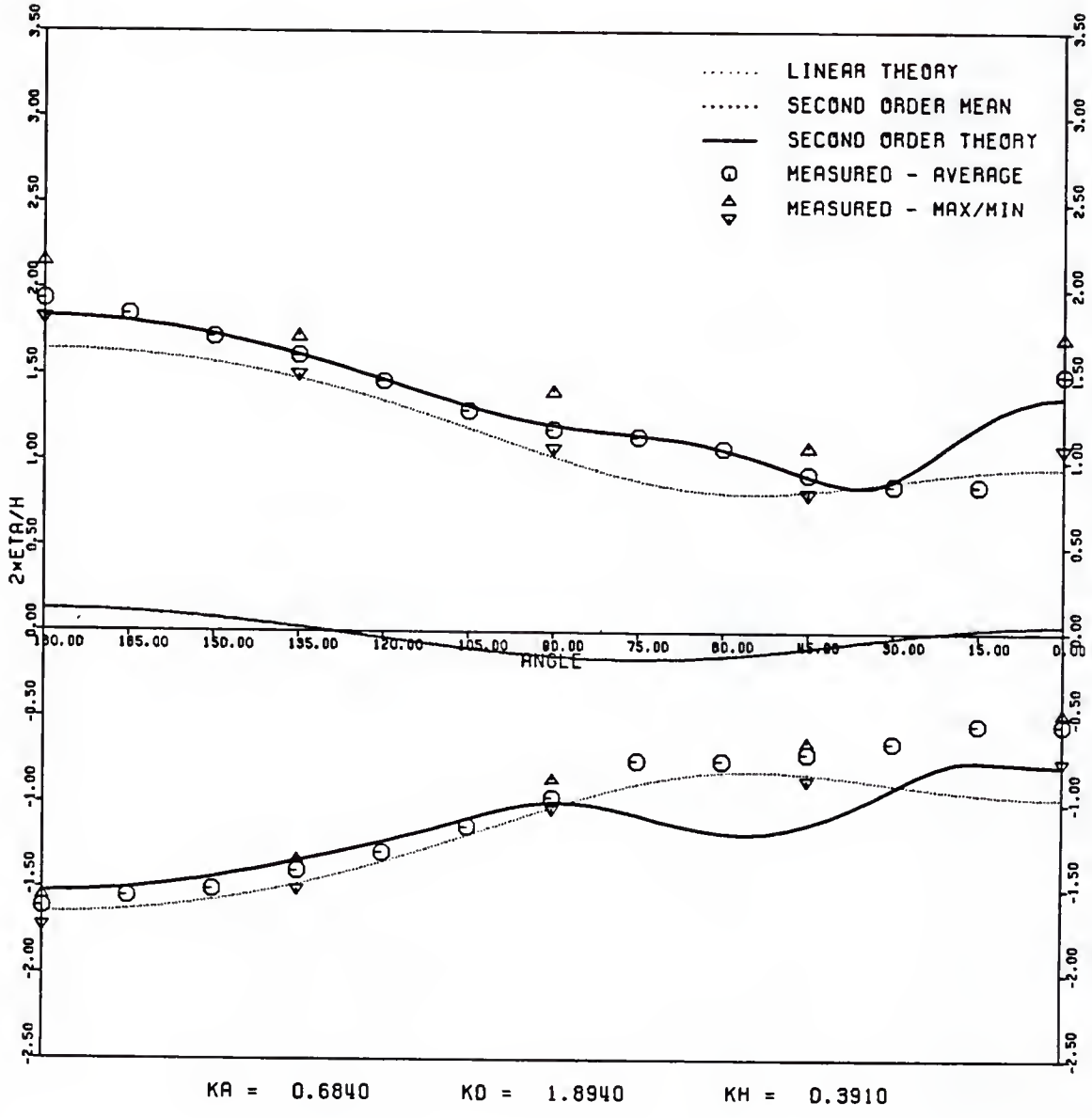

Figure D.19: Runup/rundown envelope for $ka = 0.684$, $kd = 1.894$, and $kH = 0.391$

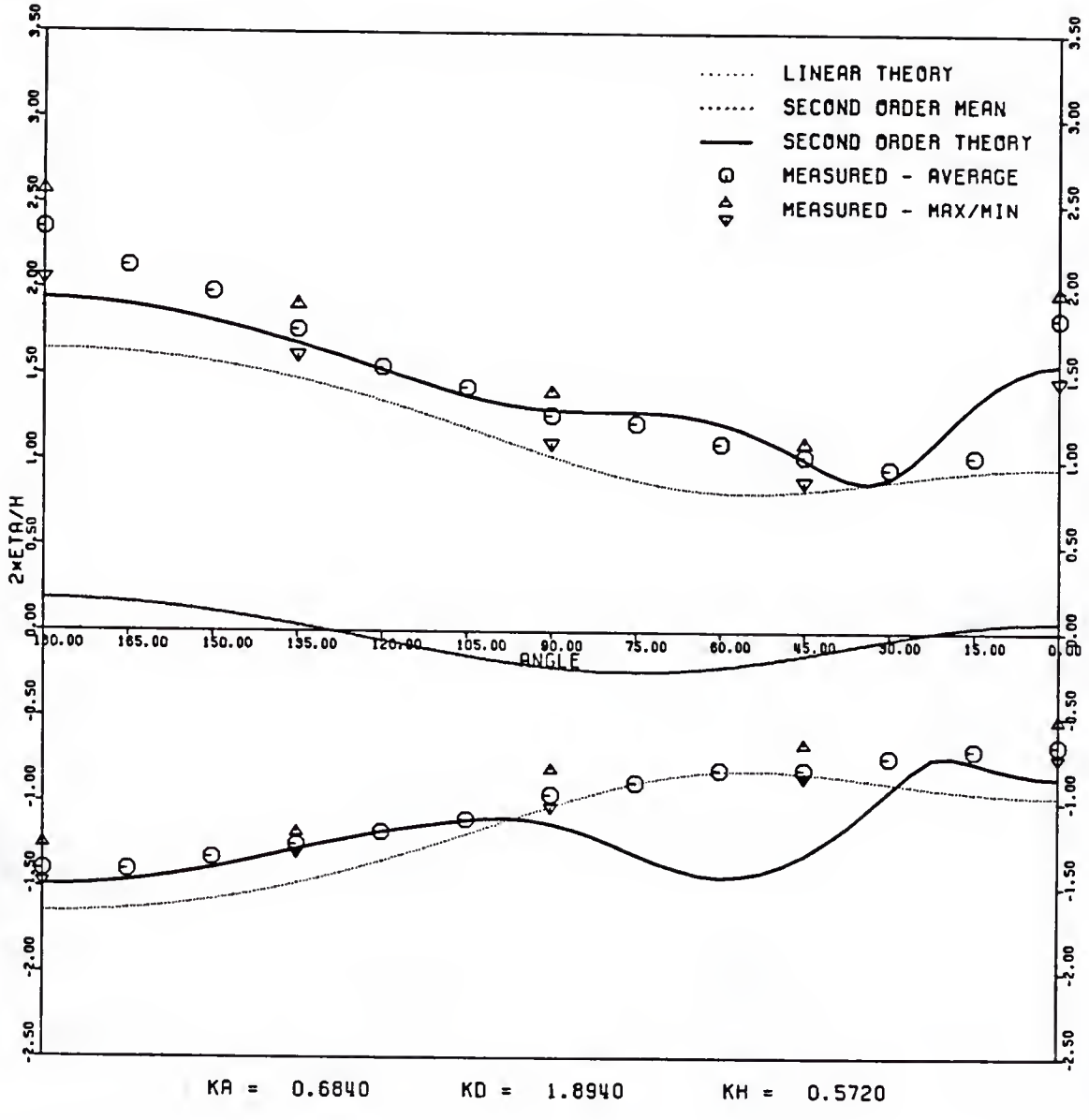

Figure D.20: Runup/rundown envelope for $ka = 0.684$, $kd = 1.894$, and $kH = 0.572$

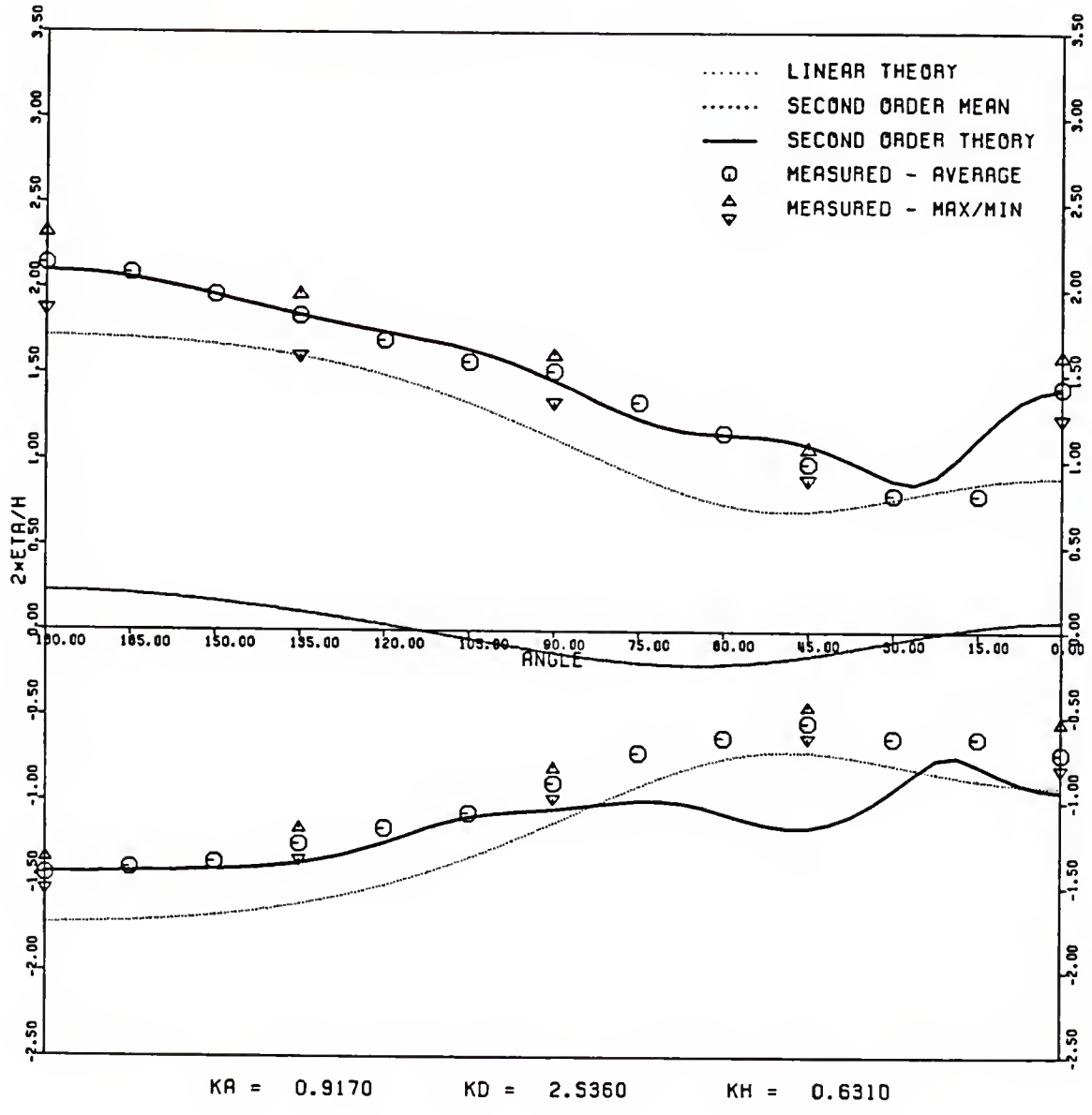

Figure D.21: Runup/rundown envelope for $ka = 0.917$, $kd = 2.536$, and $kH = 0.631$

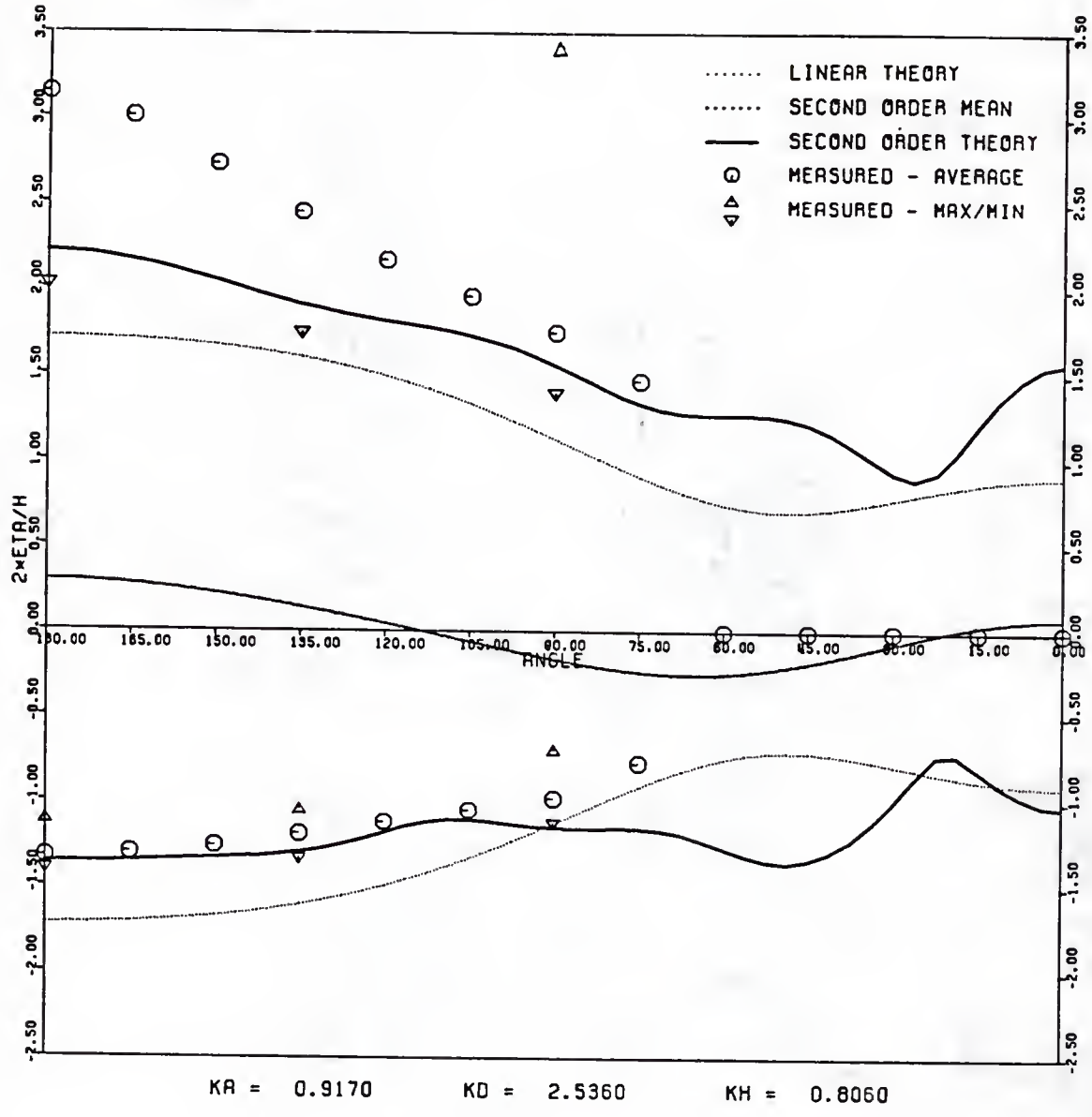

Figure D.22: Runup/rundown envelope for $ka = 0.917$, $kd = 2.536$, and $kH = 0.806$

APPENDIX E
RESULTS OF PHOTOPOLE EXPERIMENTS

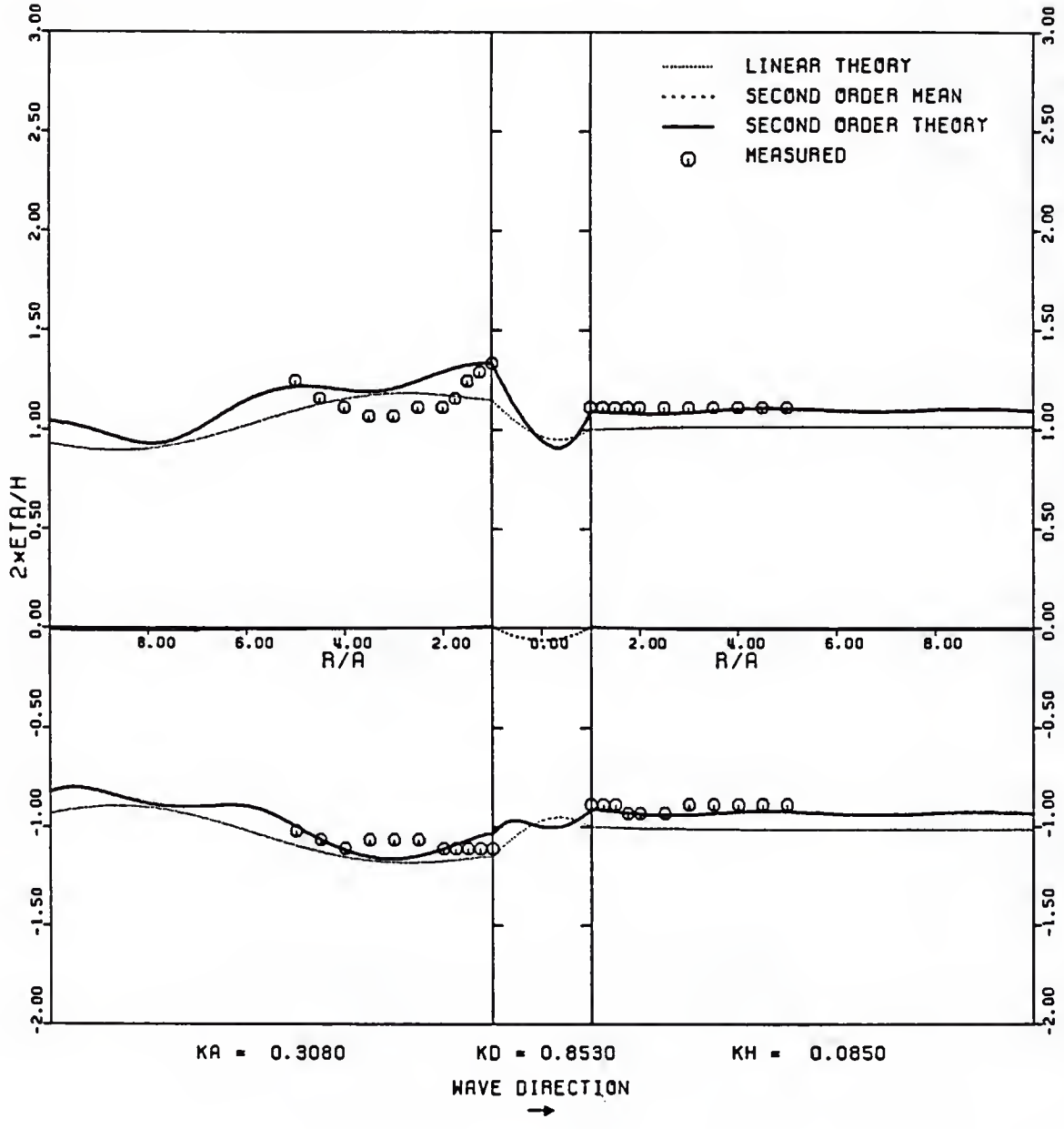

Figure E.1: Photopole data compared to theoretical wave envelope along x-axis for $ka = 0.308$, $kd = 0.853$, and $kH = 0.085$

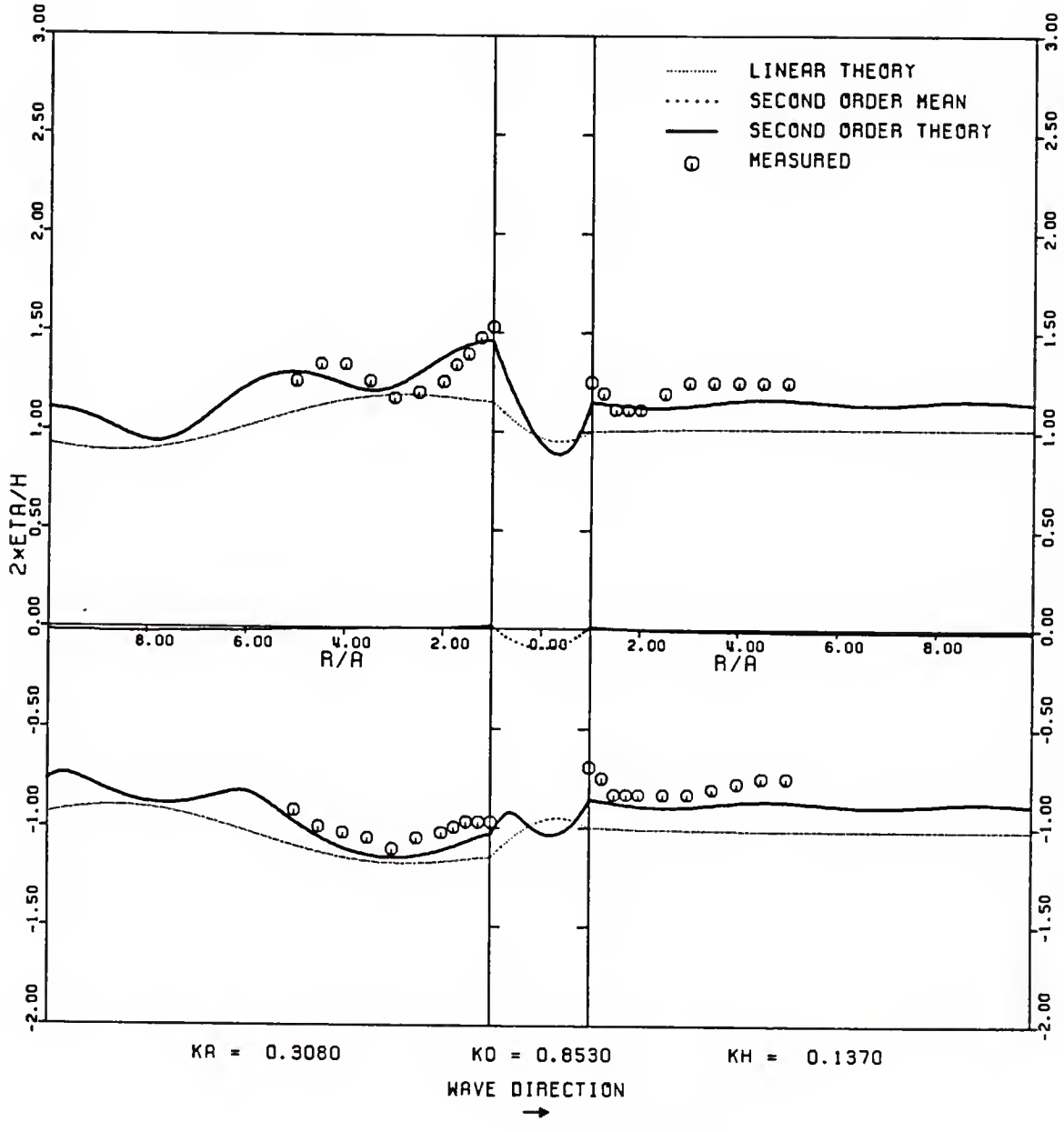

Figure E.2: Photopole data compared to theoretical wave envelope along x-axis for $ka = 0.308$, $kd = 0.853$, and $kH = 0.137$

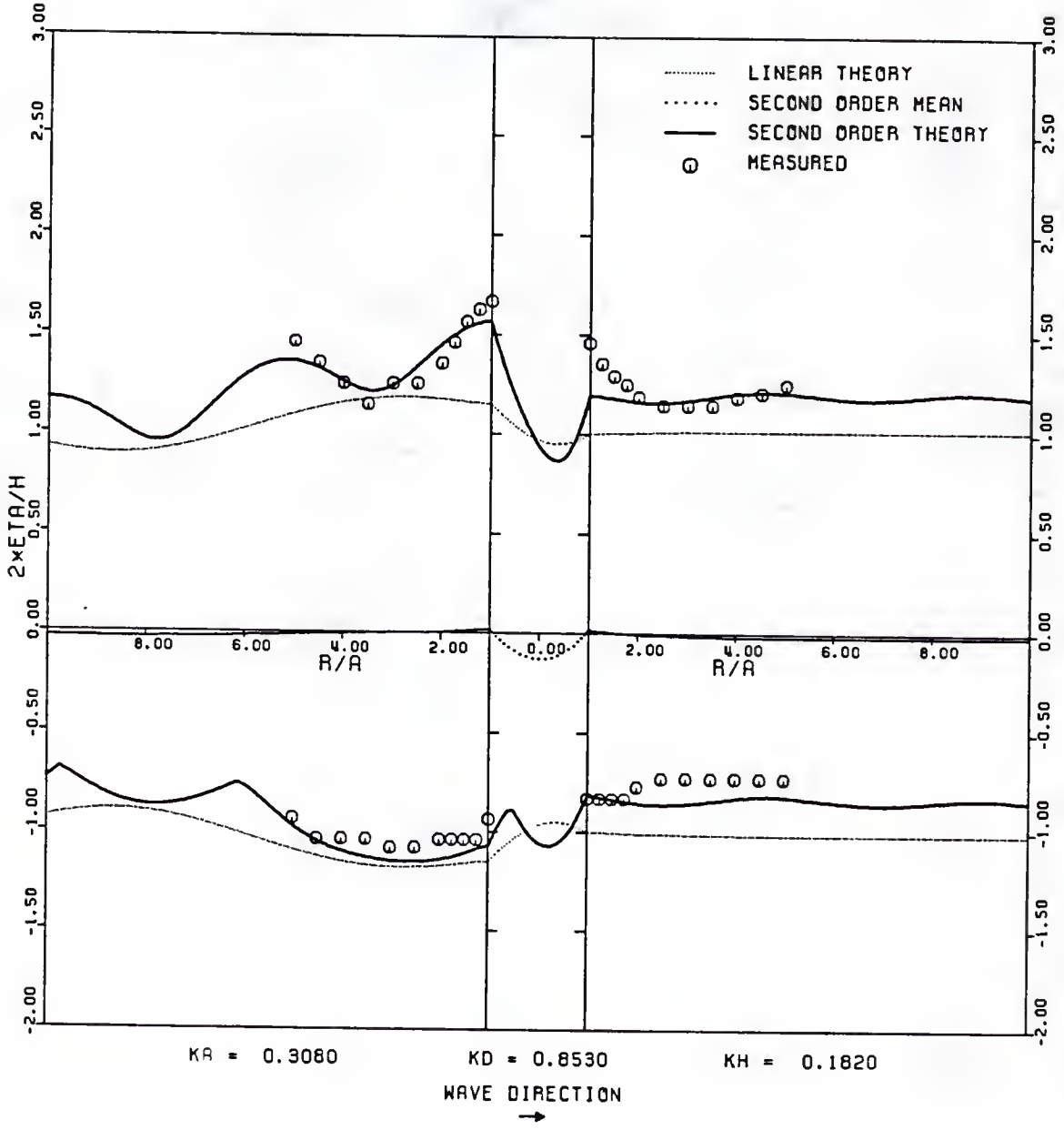

Figure E.3: Photopole data compared to theoretical wave envelope along x-axis for $ka = 0.308$, $kd = 0.853$, and $kH = 0.182$

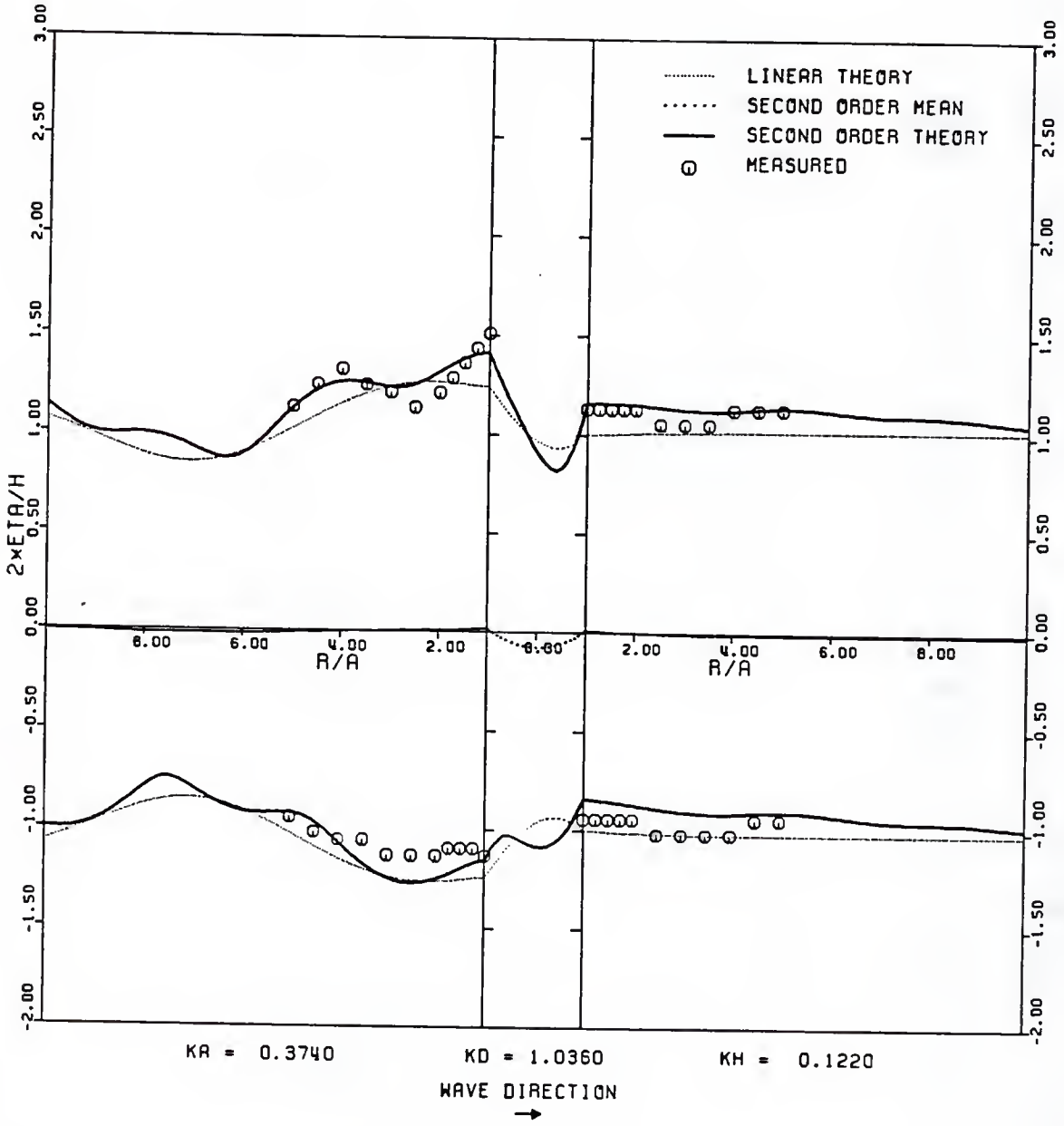

Figure E.4: Photopole data compared to theoretical wave envelope along x-axis for $ka = 0.374$, $kd = 1.036$, and $kH = 0.122$

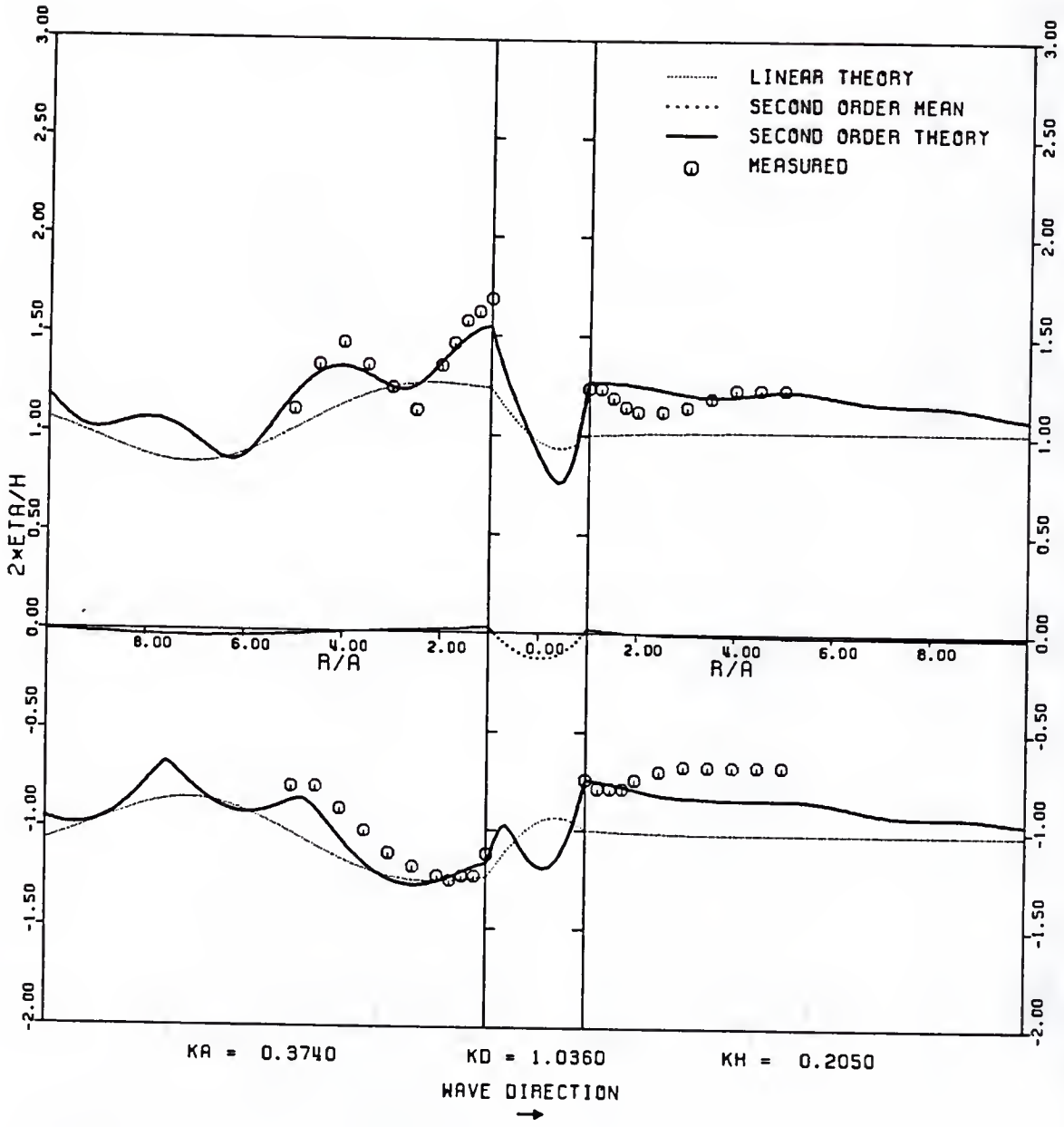

Figure E.5: Photopole data compared to theoretical wave envelope along x-axis for $ka = 0.374$, $kd = 1.036$, and $kH = 0.205$

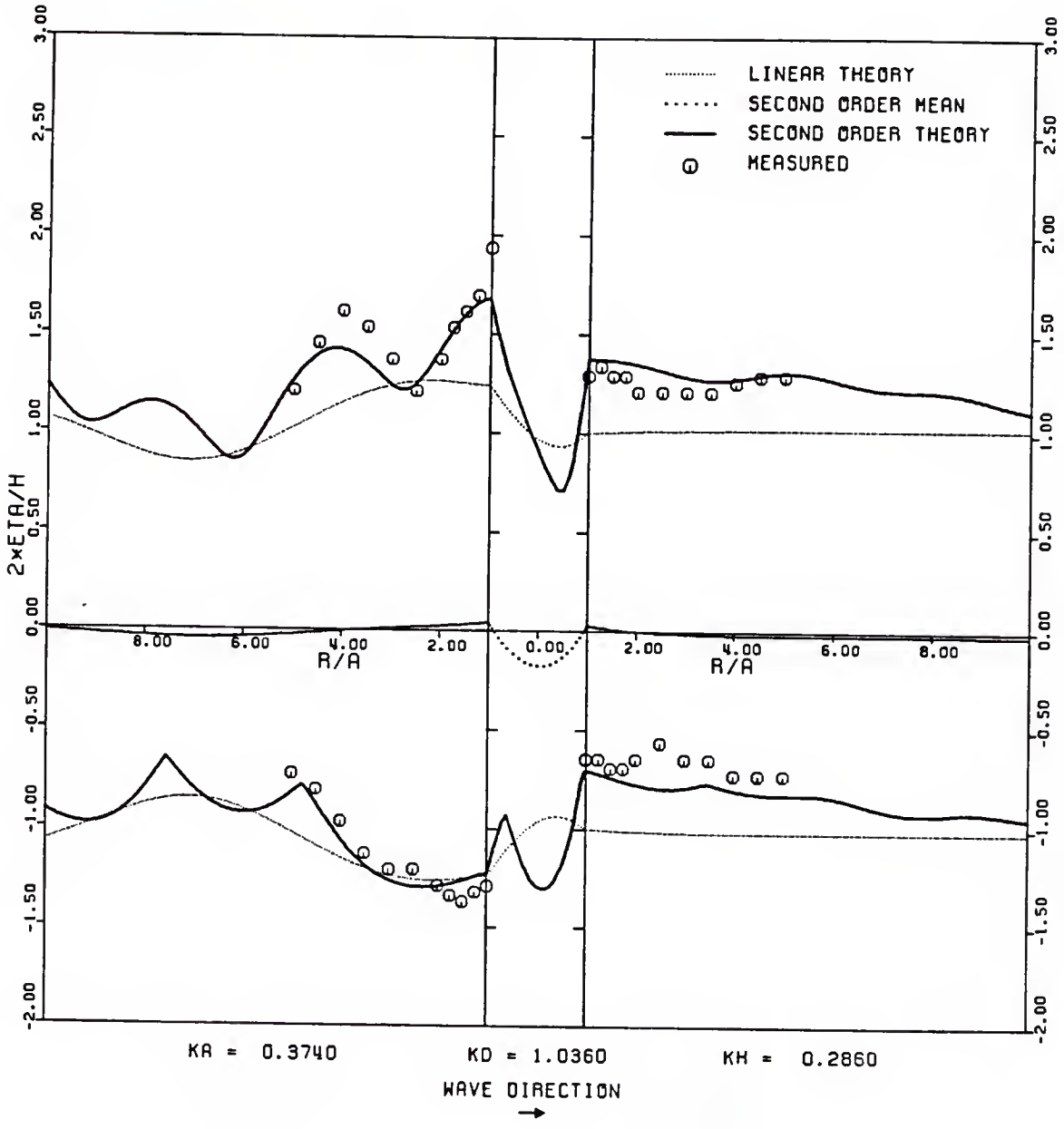

Figure E.6: Photopole data compared to theoretical wave envelope along x-axis for $ka = 0.374$, $kd = 1.036$, and $kH = 0.286$

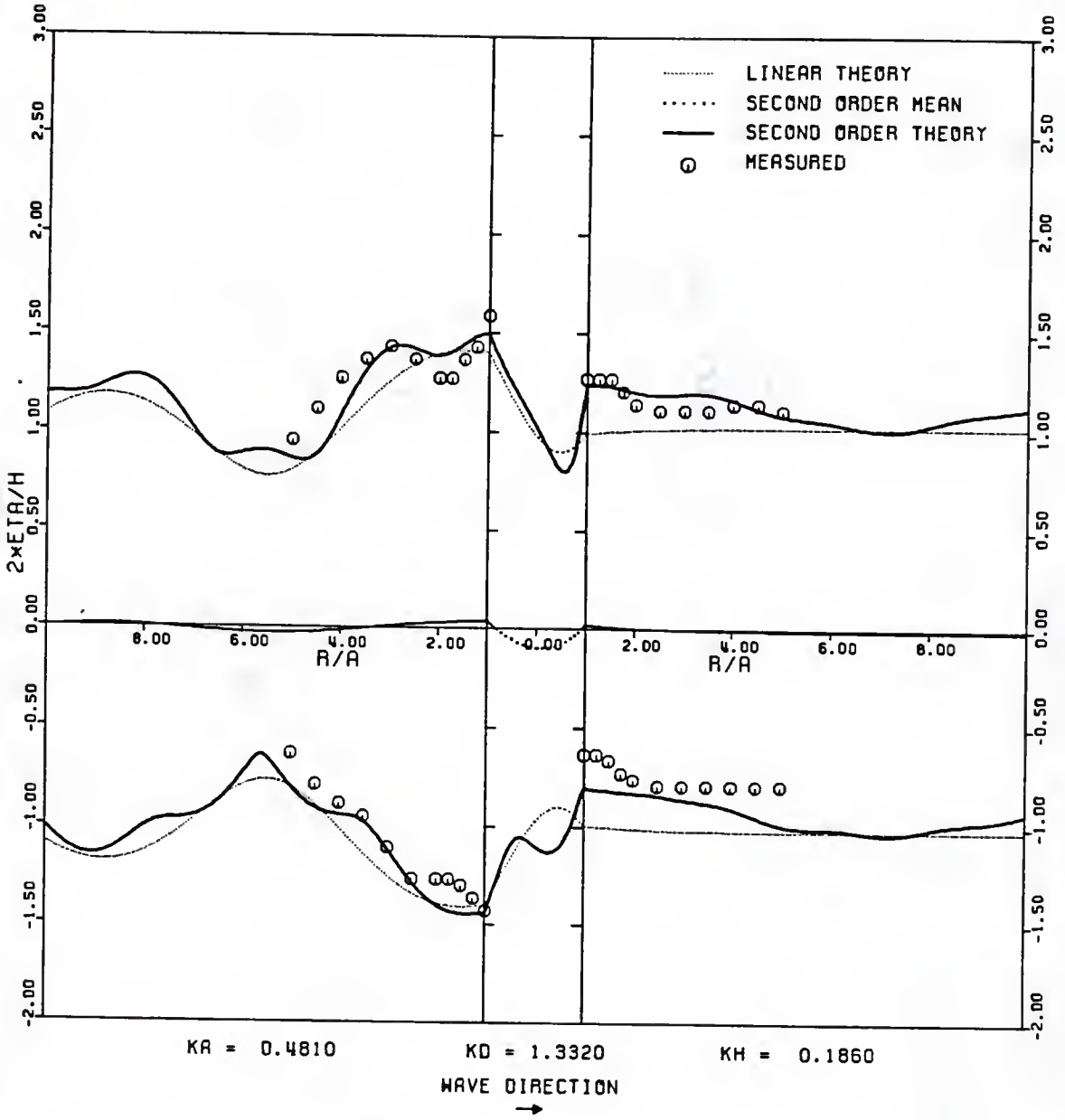

Figure E.7: Photopole data compared to theoretical wave envelope along x-axis for $ka = 0.481$, $kd = 1.332$, and $kH = 0.186$

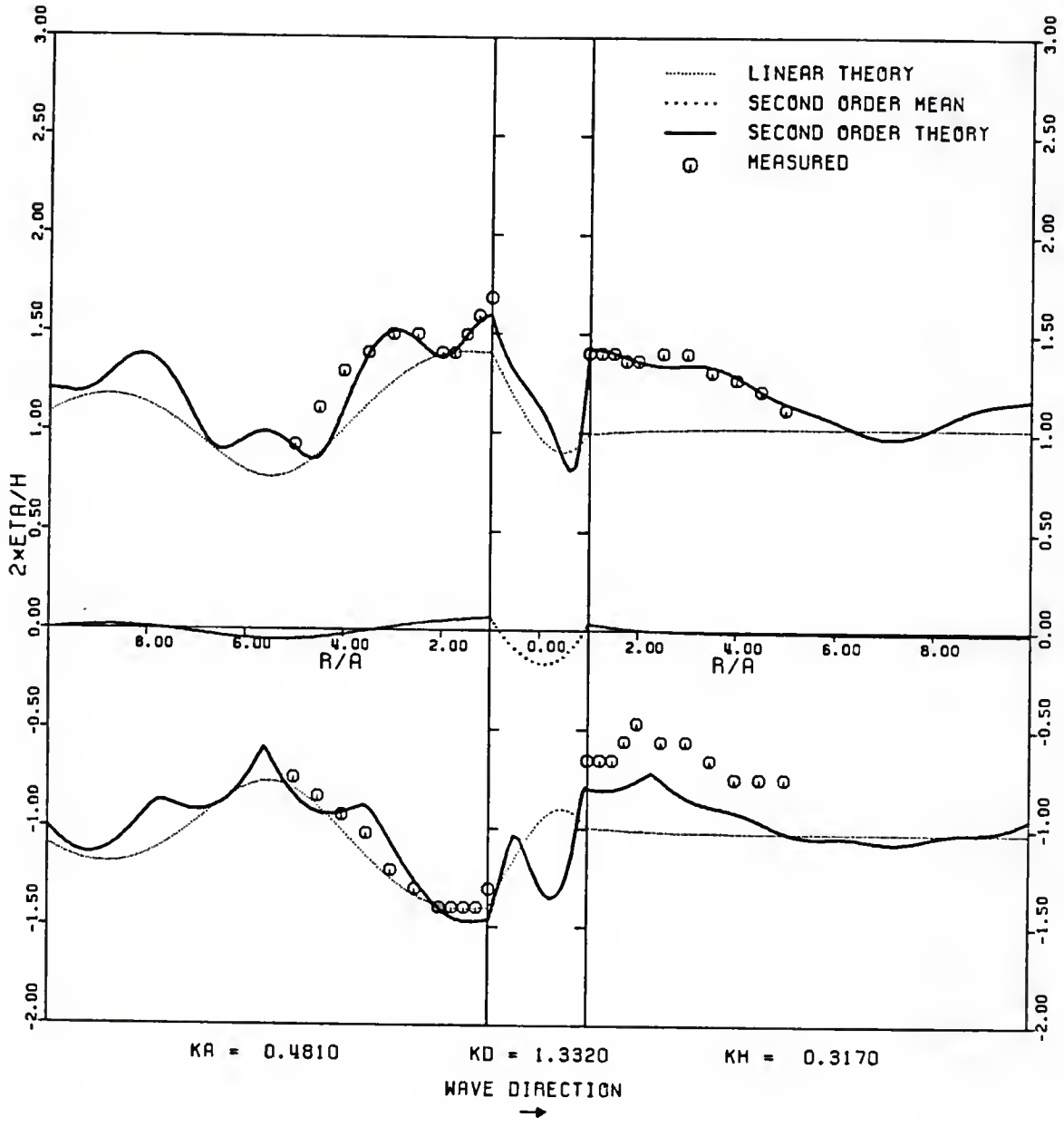

Figure E.8: Photopole data compared to theoretical wave envelope along x-axis for $ka = 0.481$, $kd = 1.332$, and $kH = 0.317$

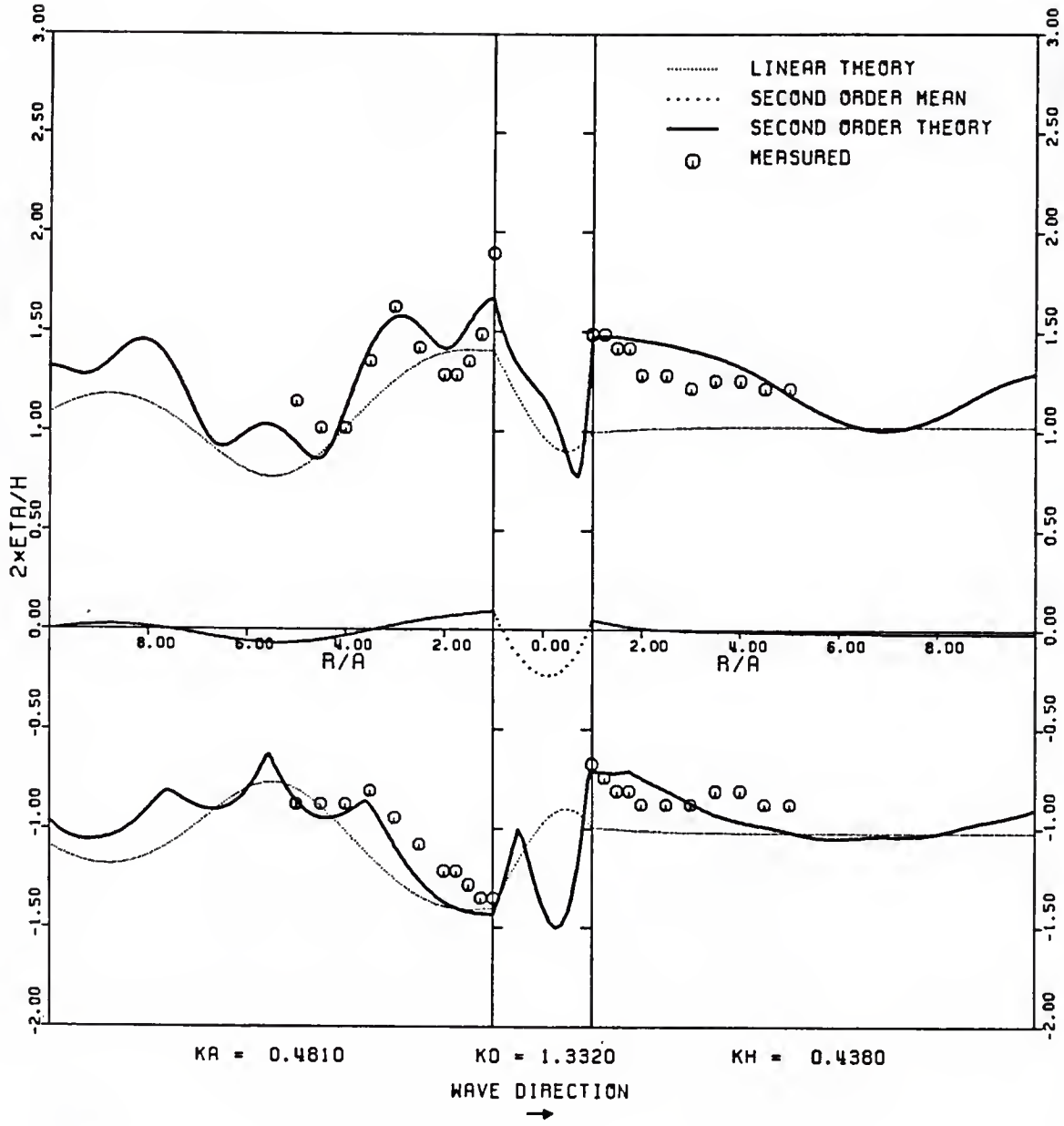

Figure E.9: Photopole data compared to theoretical wave envelope along x-axis for $ka = 0.481$, $kd = 1.332$, and $kH = 0.438$

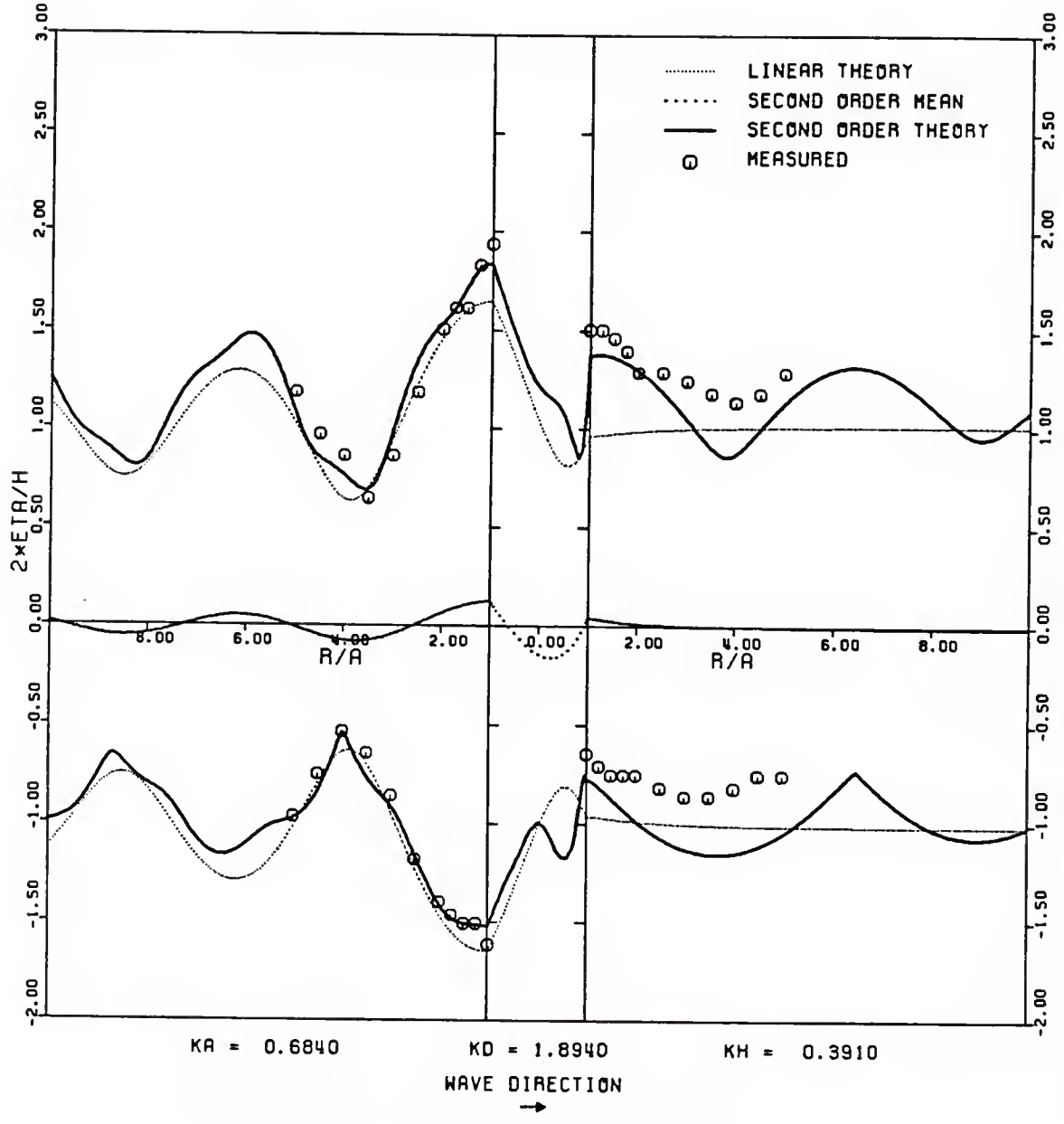

Figure E.10: Photopole data compared to theoretical wave envelope along x-axis for $ka = 0.684$, $kd = 1.894$, and $kH = 0.391$

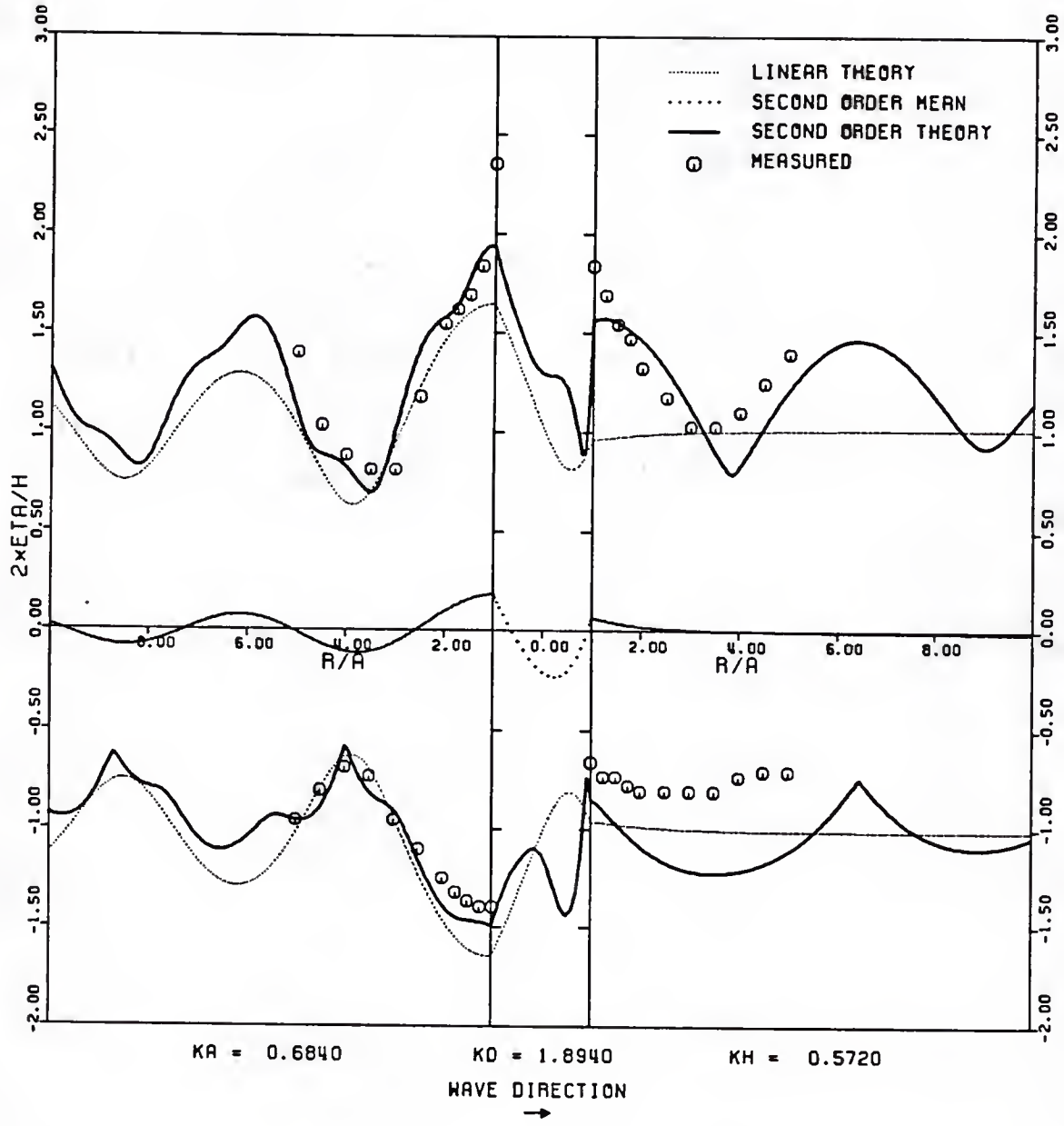

Figure E.11: Photopole data compared to theoretical wave envelope along x-axis for $ka = 0.684$, $kd = 1.894$, and $kH = 0.572$

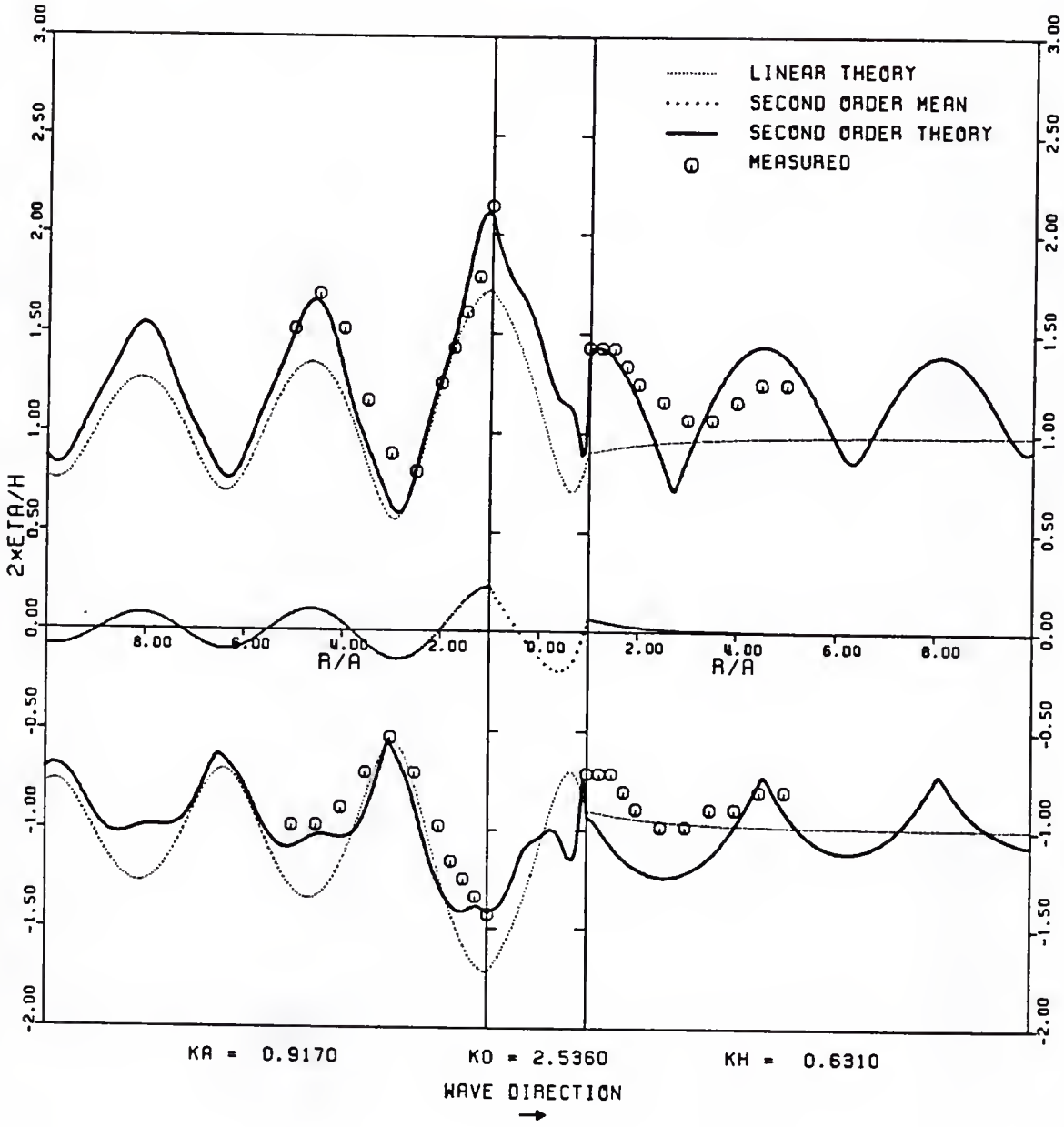

Figure E.12: Photopole data compared to theoretical wave envelope along x-axis for $ka = 0.917$, $kd = 2.536$, and $kH = 0.631$

APPENDIX F
RESULTS FOR WAVE FORCE EXPERIMENTS

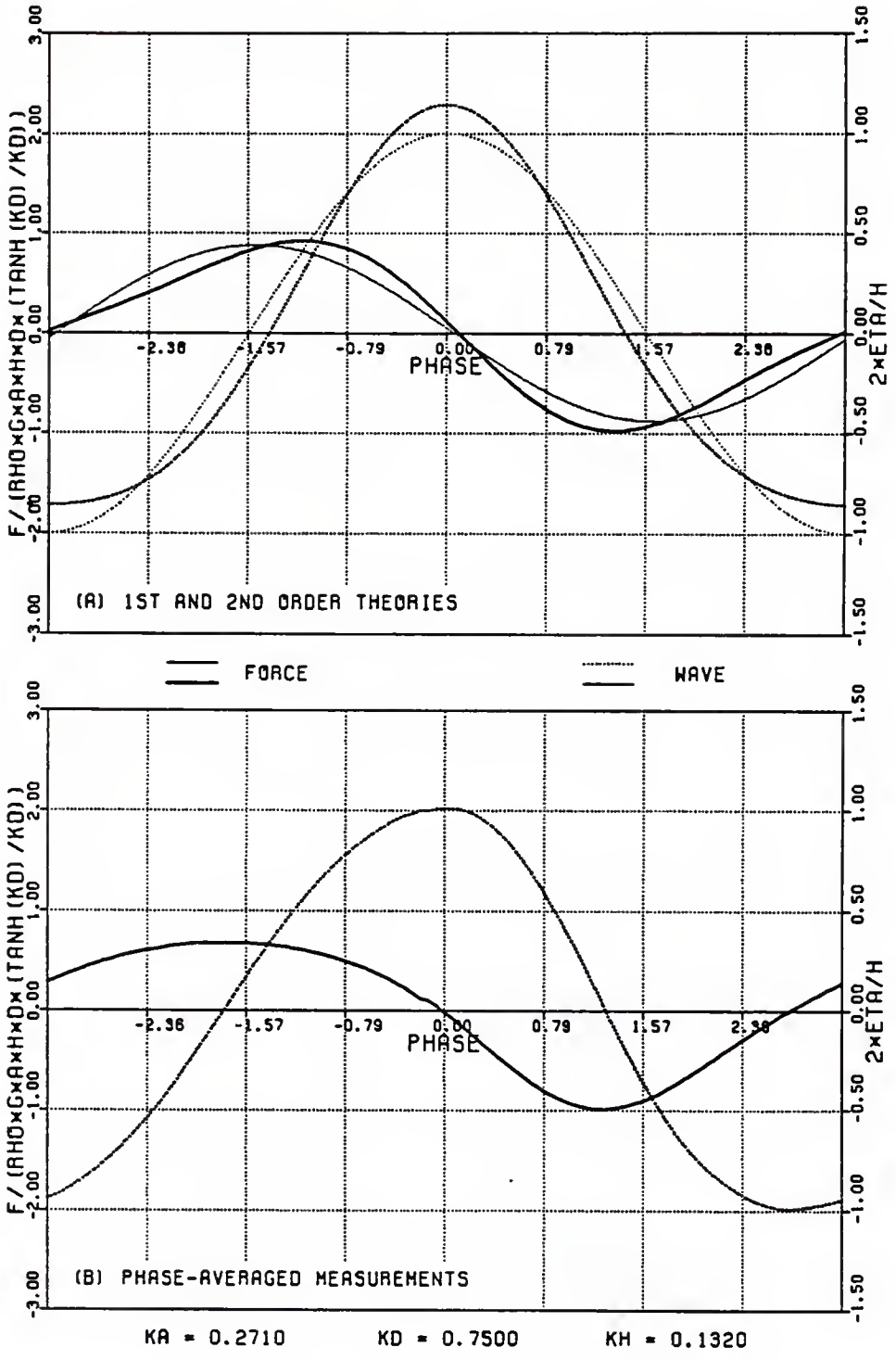

Figure F.1: Theoretical and experimental results for (1) wave profile at $r = 10a$ and $\theta = \pi/2$ and (2) depth-integrated force, for $ka = 0.271$, $kd = 0.750$, and $kH = 0.132$

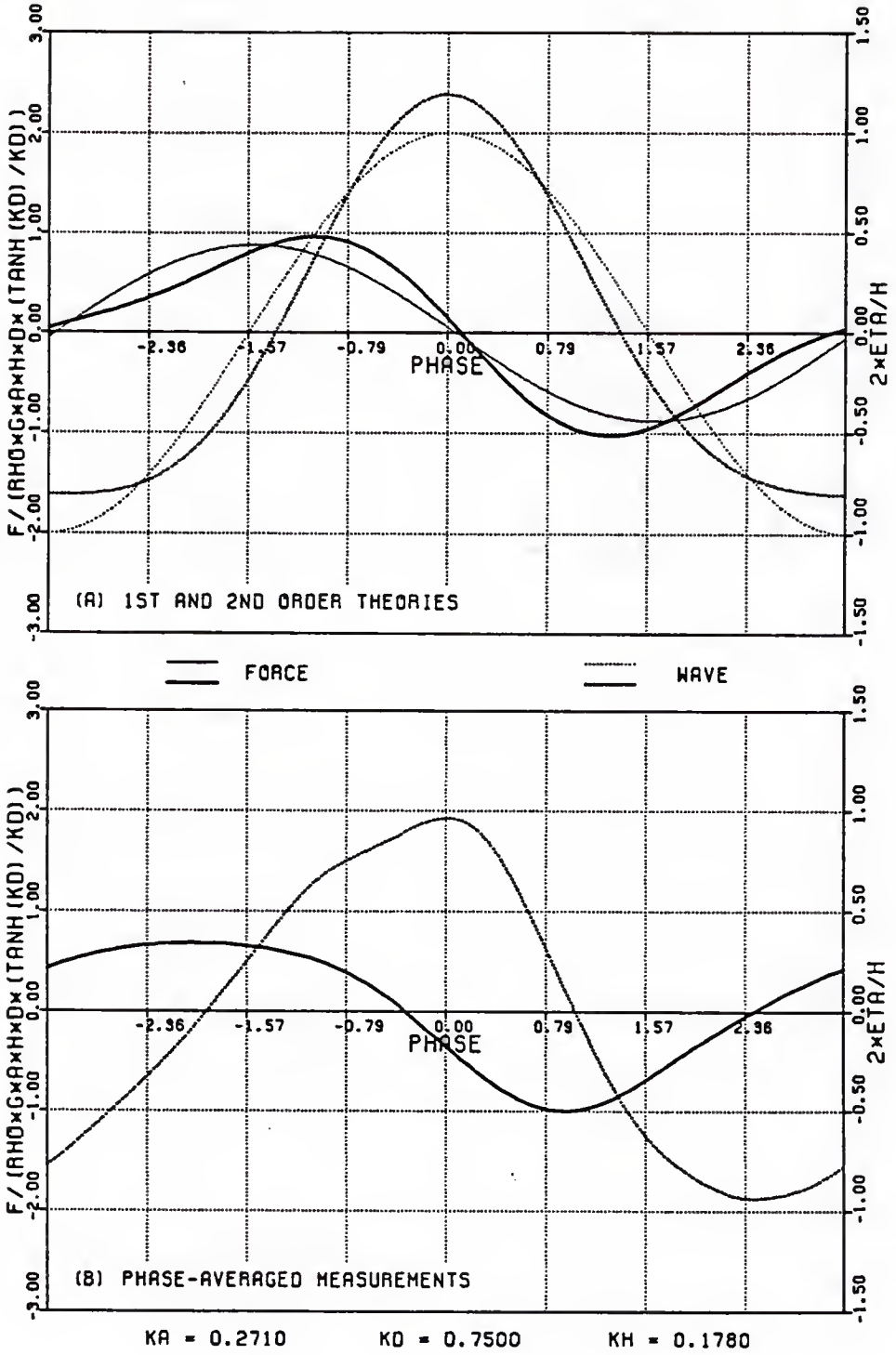

Figure F.2: Theoretical and experimental results for (1) wave profile at $r = 10a$ and $\theta = \pi/2$ and (2) depth-integrated force, for $ka = 0.271$, $kd = 0.750$, and $kH = 0.178$

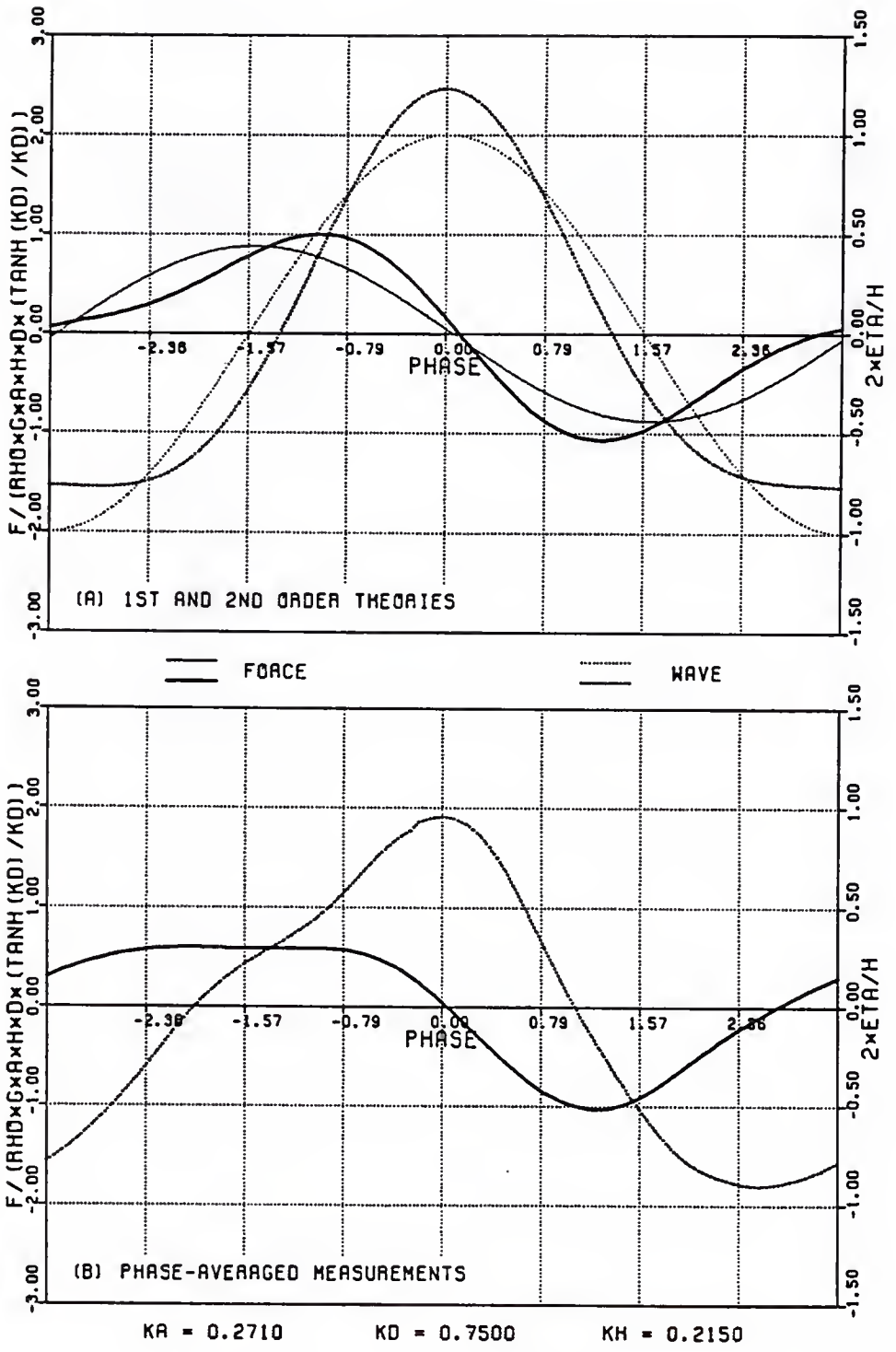

Figure F.3: Theoretical and experimental results for (1) wave profile at $r = 10a$ and $\theta = \pi/2$ and (2) depth-integrated force, for $ka = 0.271$, $kd = 0.750$, and $kH = 0.215$

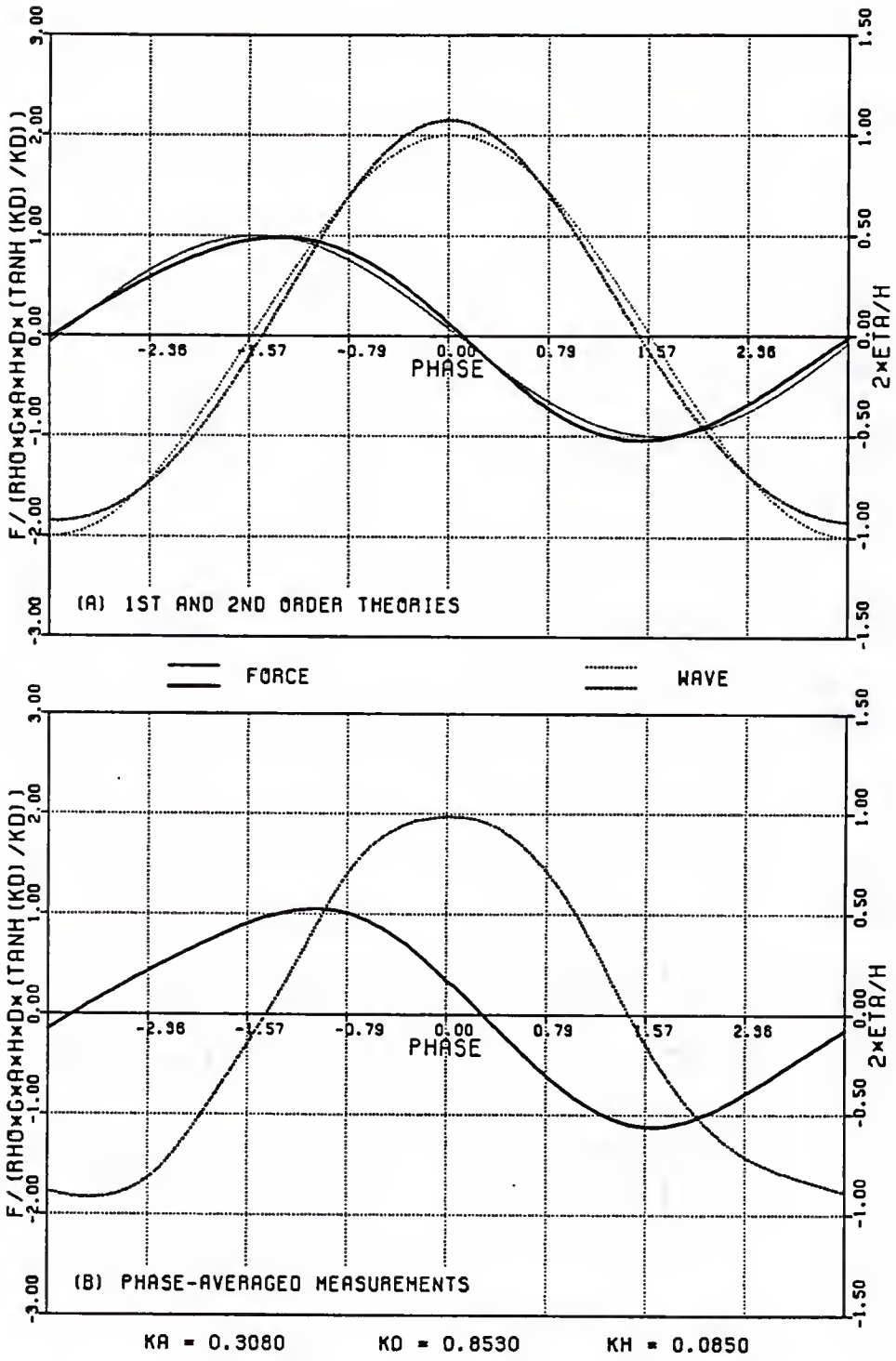

Figure F.4: Theoretical and experimental results for (1) wave profile at $r = 10a$ and $\theta = \pi/2$ and (2) depth-integrated force, for $ka = 0.308$, $kd = 0.853$, and $kH = 0.085$

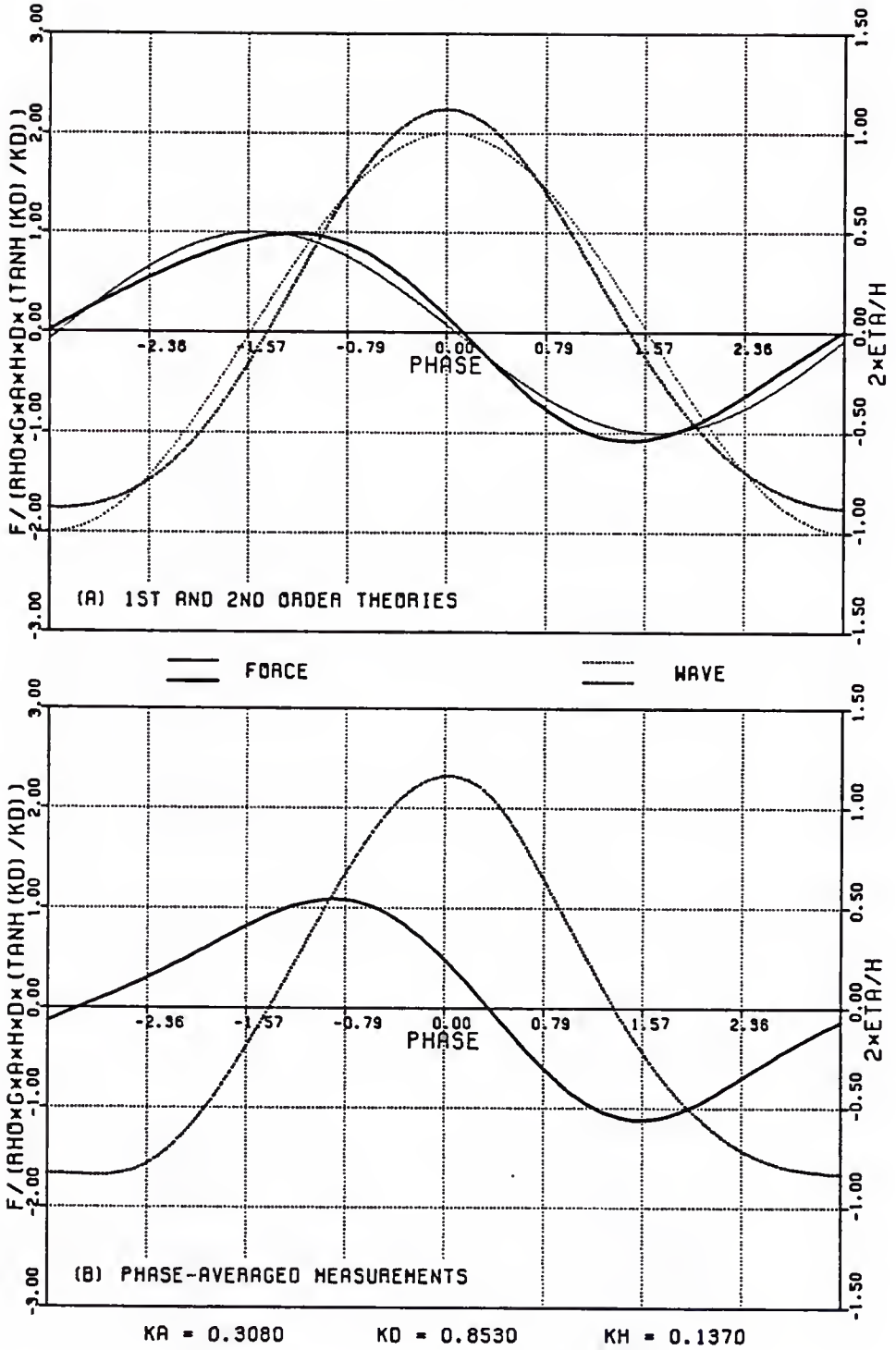

Figure F.5: Theoretical and experimental results for (1) wave profile at $r = 10a$ and $\theta = \pi/2$ and (2) depth-integrated force, for $ka = 0.308$, $kd = 0.853$, and $kH = 0.137$

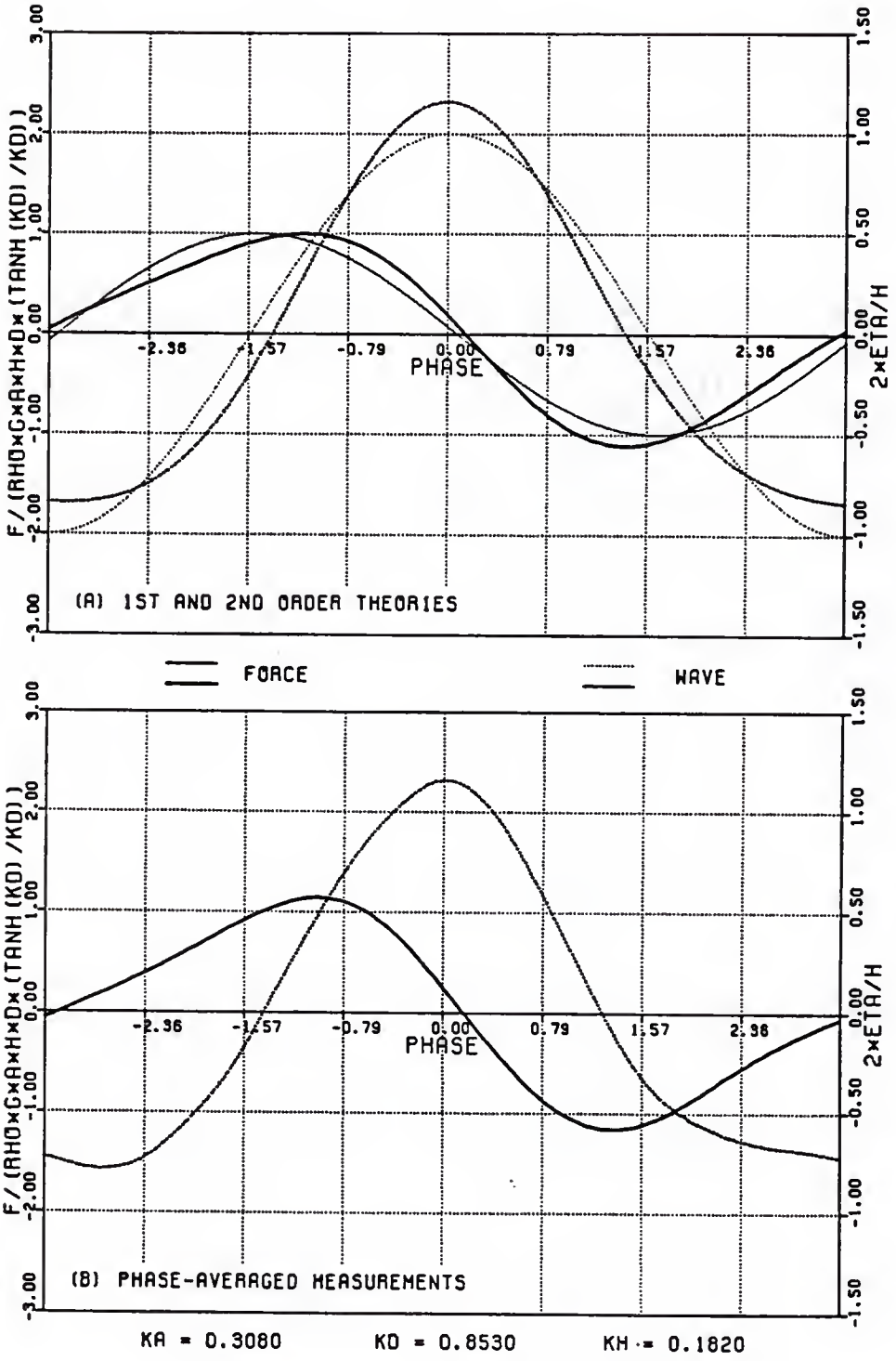

Figure F.6: Theoretical and experimental results for (1) wave profile at $r = 10a$ and $\theta = \pi/2$ and (2) depth-integrated force, for $ka = 0.308$, $kd = 0.853$, and $kH = 0.182$

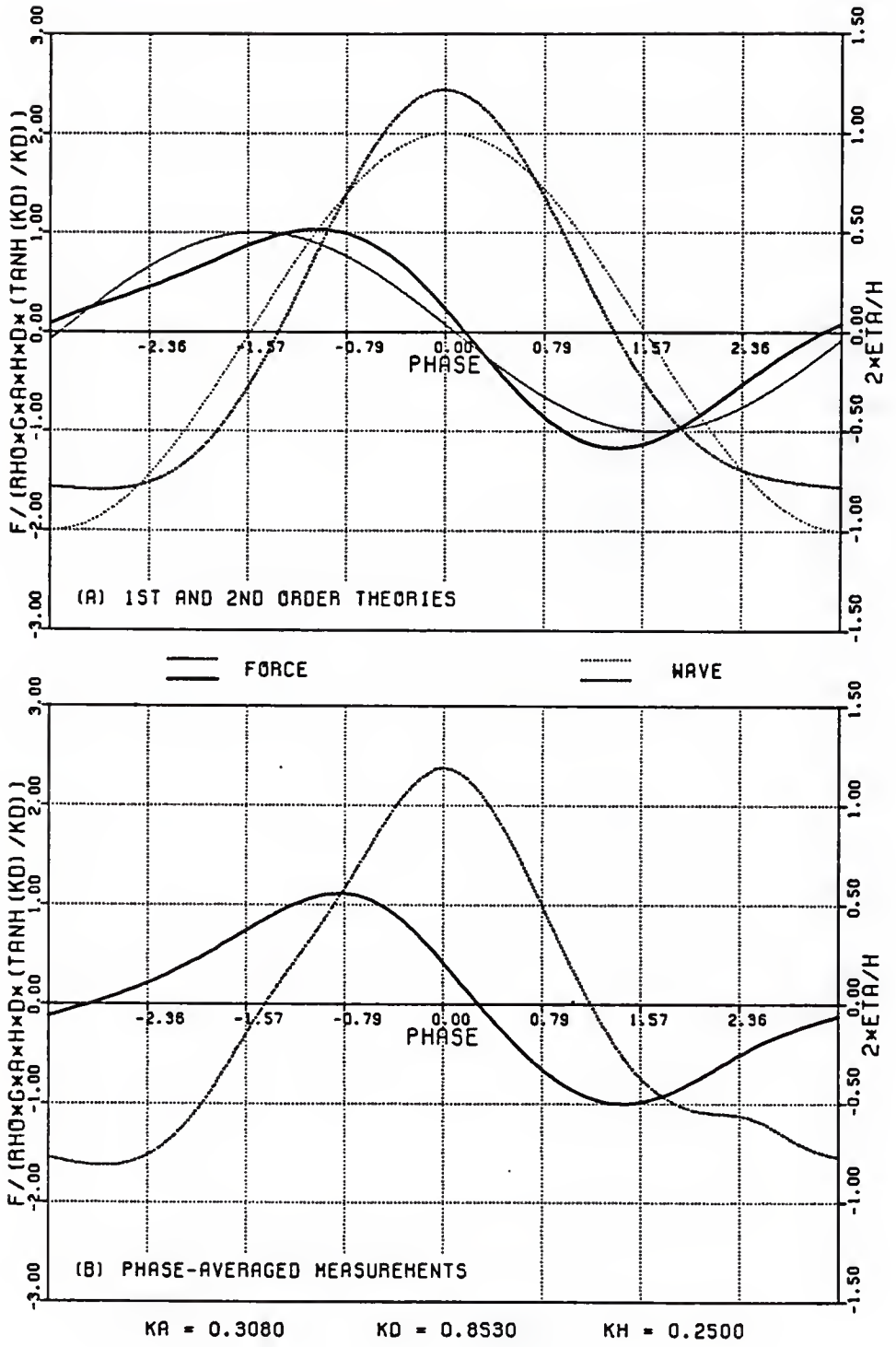

Figure F.7: Theoretical and experimental results for (1) wave profile at $r = 10a$ and $\theta = \pi/2$ and (2) depth-integrated force, for $ka = 0.308$, $kd = 0.853$, and $kH = 0.250$

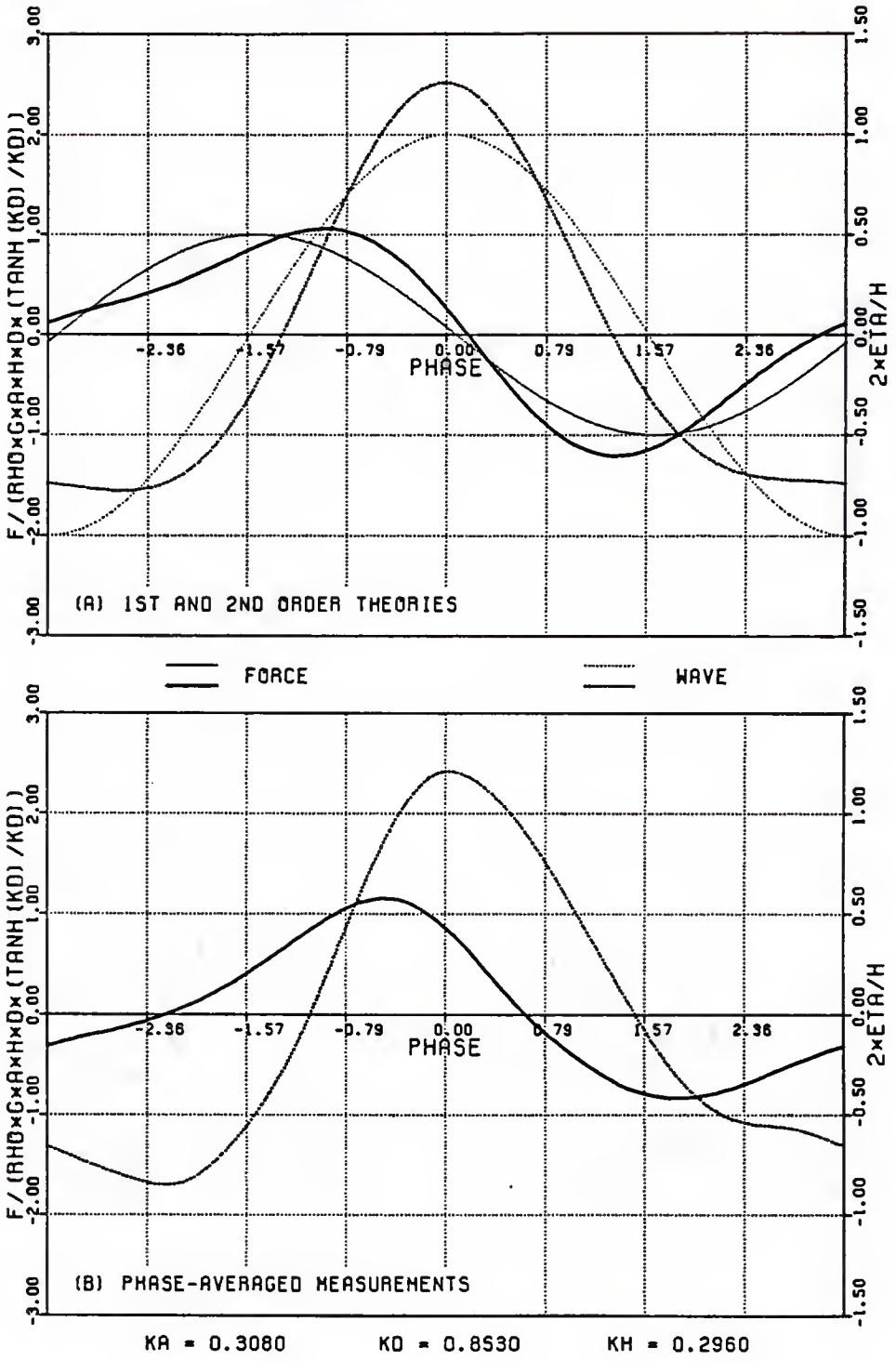

Figure F.8: Theoretical and experimental results for (1) wave profile at $r = 10a$ and $\theta = \pi/2$ and (2) depth-integrated force, for $ka = 0.308$, $kd = 0.853$, and $kH = 0.296$

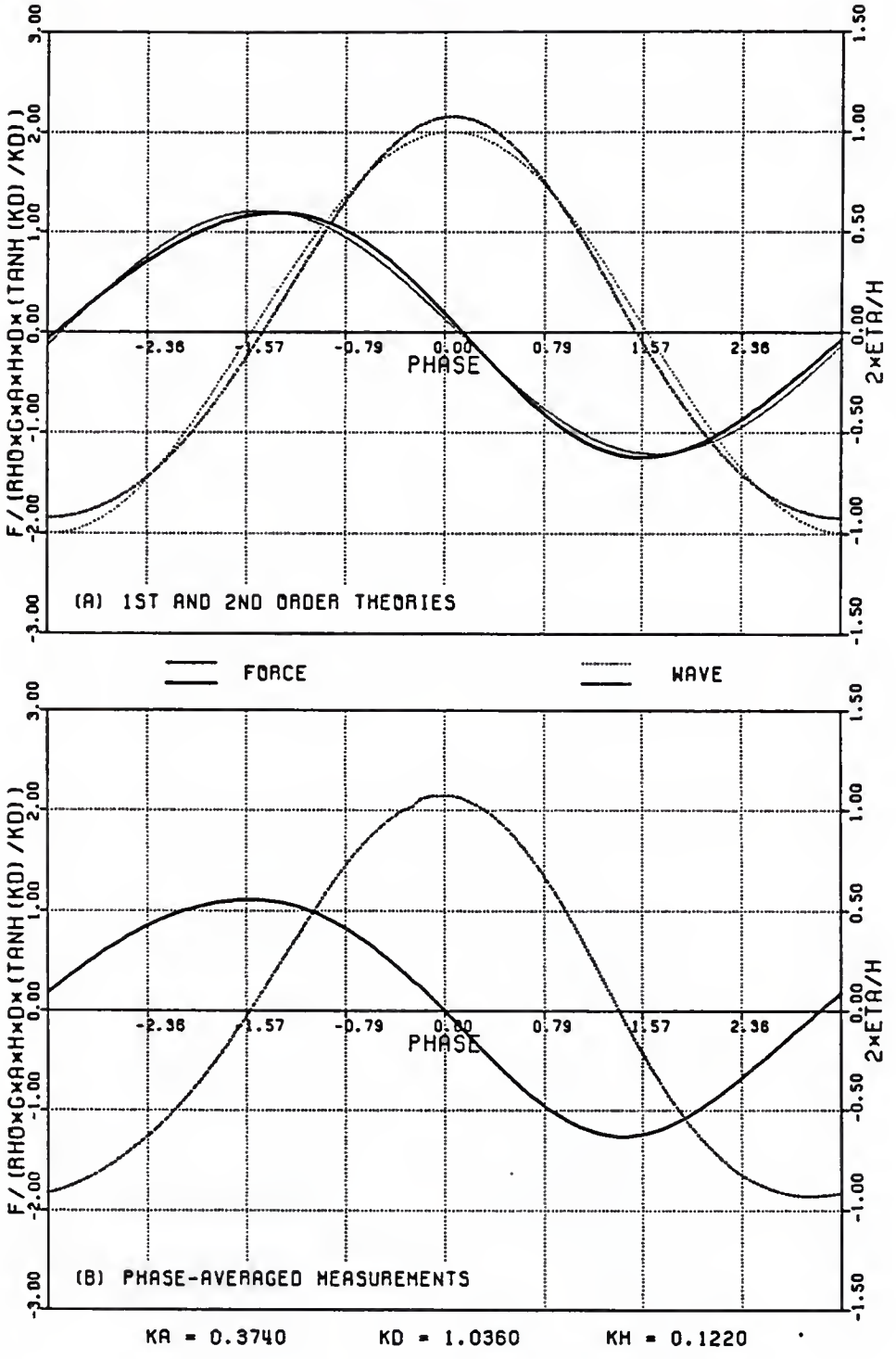

Figure F.9: Theoretical and experimental results for (1) wave profile at $r = 10a$ and $\theta = \pi/2$ and (2) depth-integrated force, for $ka = 0.374$, $kd = 1.036$, and $kH = 0.122$

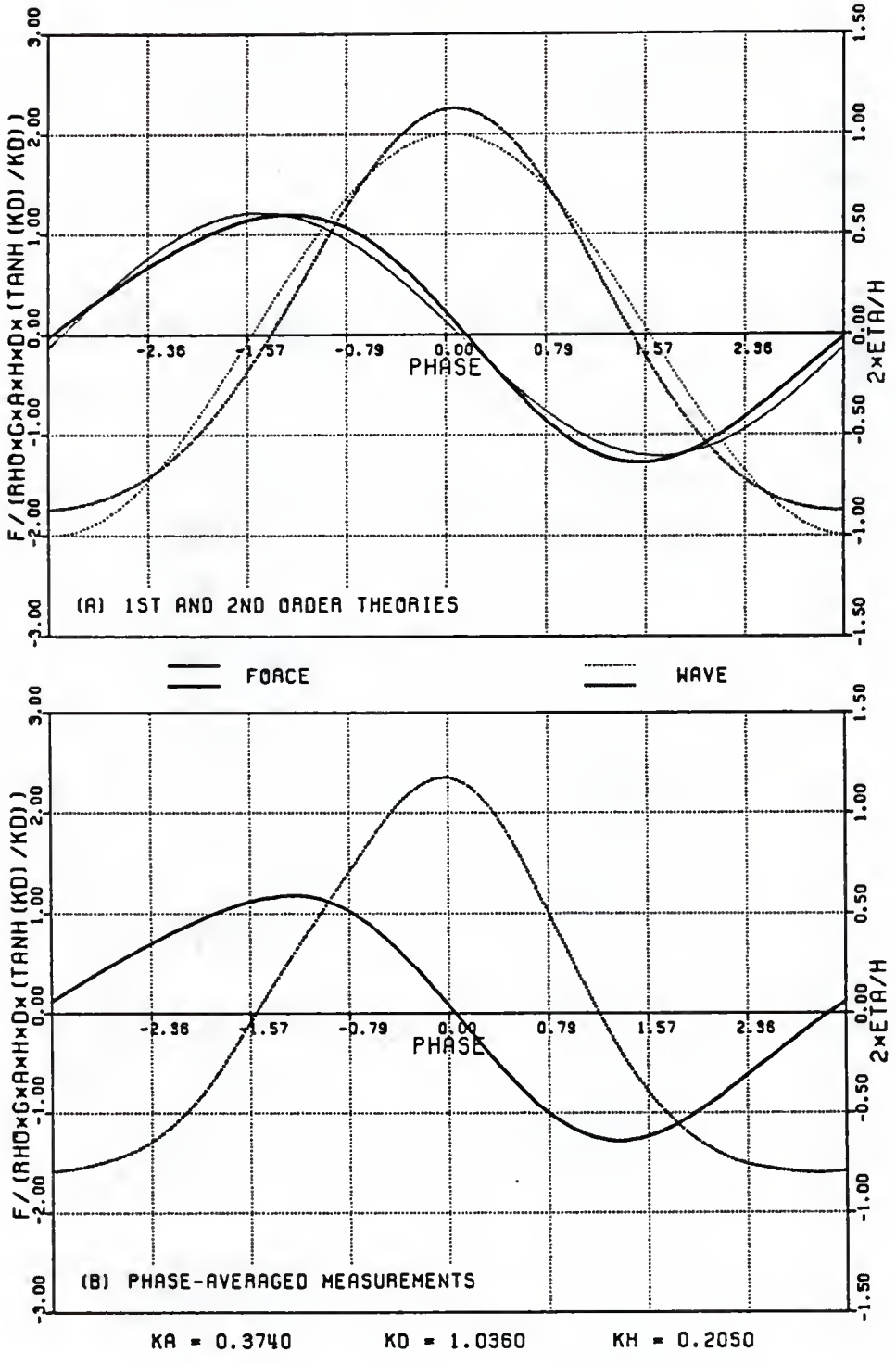

Figure F.10: Theoretical and experimental results for (1) wave profile at $r = 10a$ and $\theta = \pi/2$ and (2) depth-integrated force, for $ka = 0.374$, $kd = 1.036$, and $kH = 0.205$

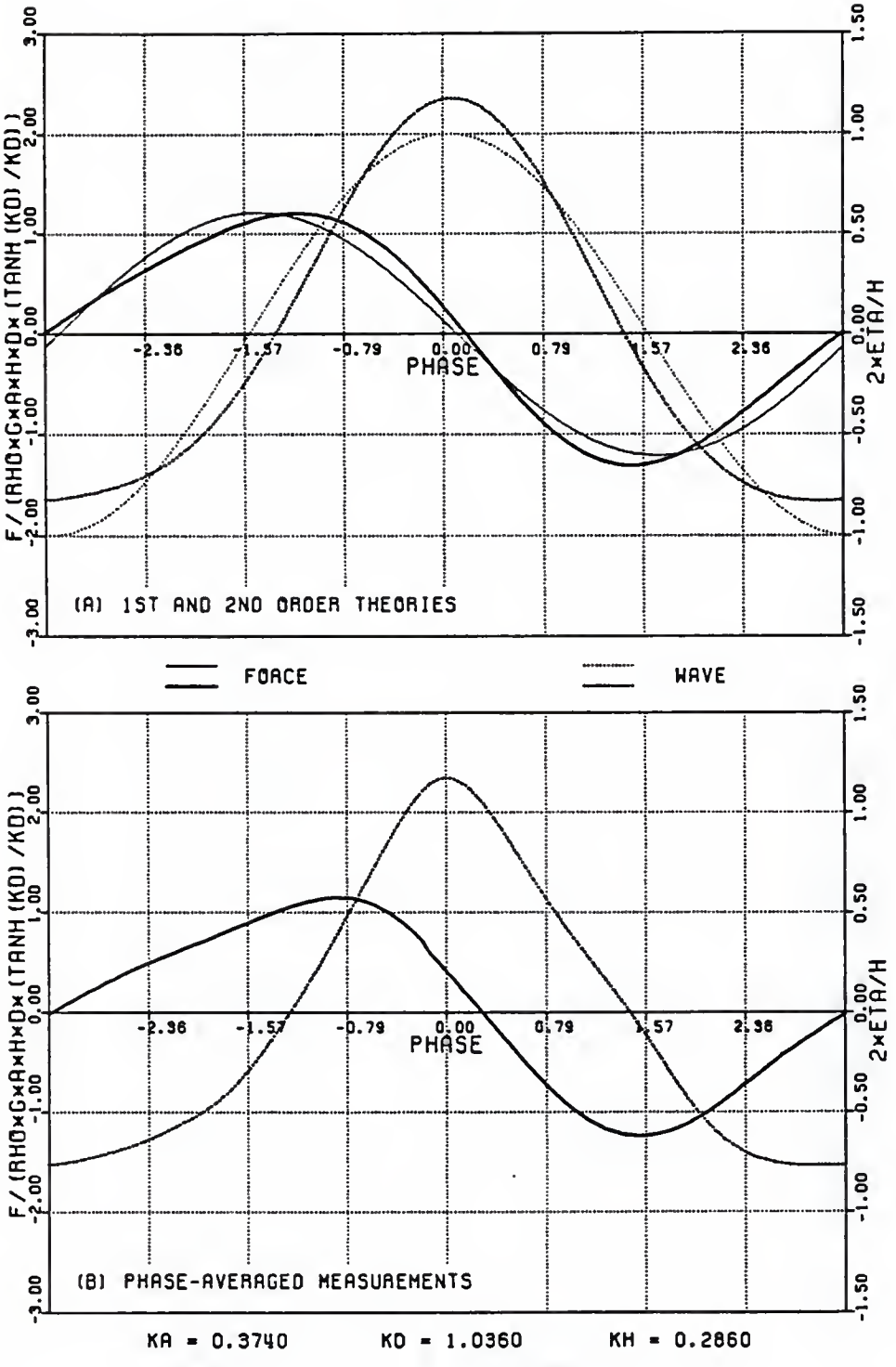

Figure F.11: Theoretical and experimental results for (1) wave profile at $r = 10a$ and $\theta = \pi/2$ and (2) depth-integrated force, for $ka = 0.374$, $kd = 1.036$, and $kH = 0.286$

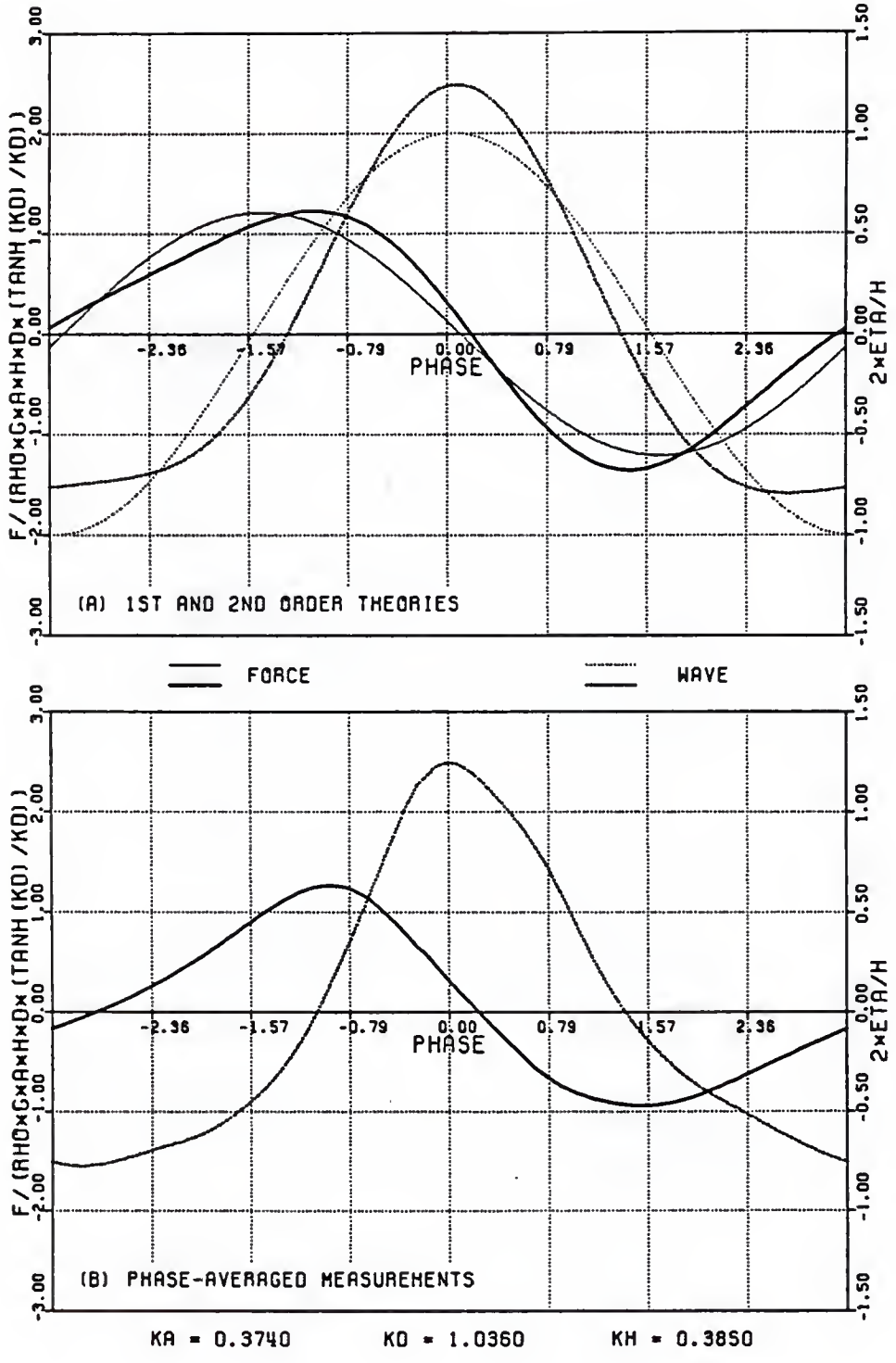

Figure F.12: Theoretical and experimental results for (1) wave profile at $r = 10a$ and $\theta = \pi/2$ and (2) depth-integrated force, for $ka = 0.374$, $kd = 1.036$, and $kH = 0.385$

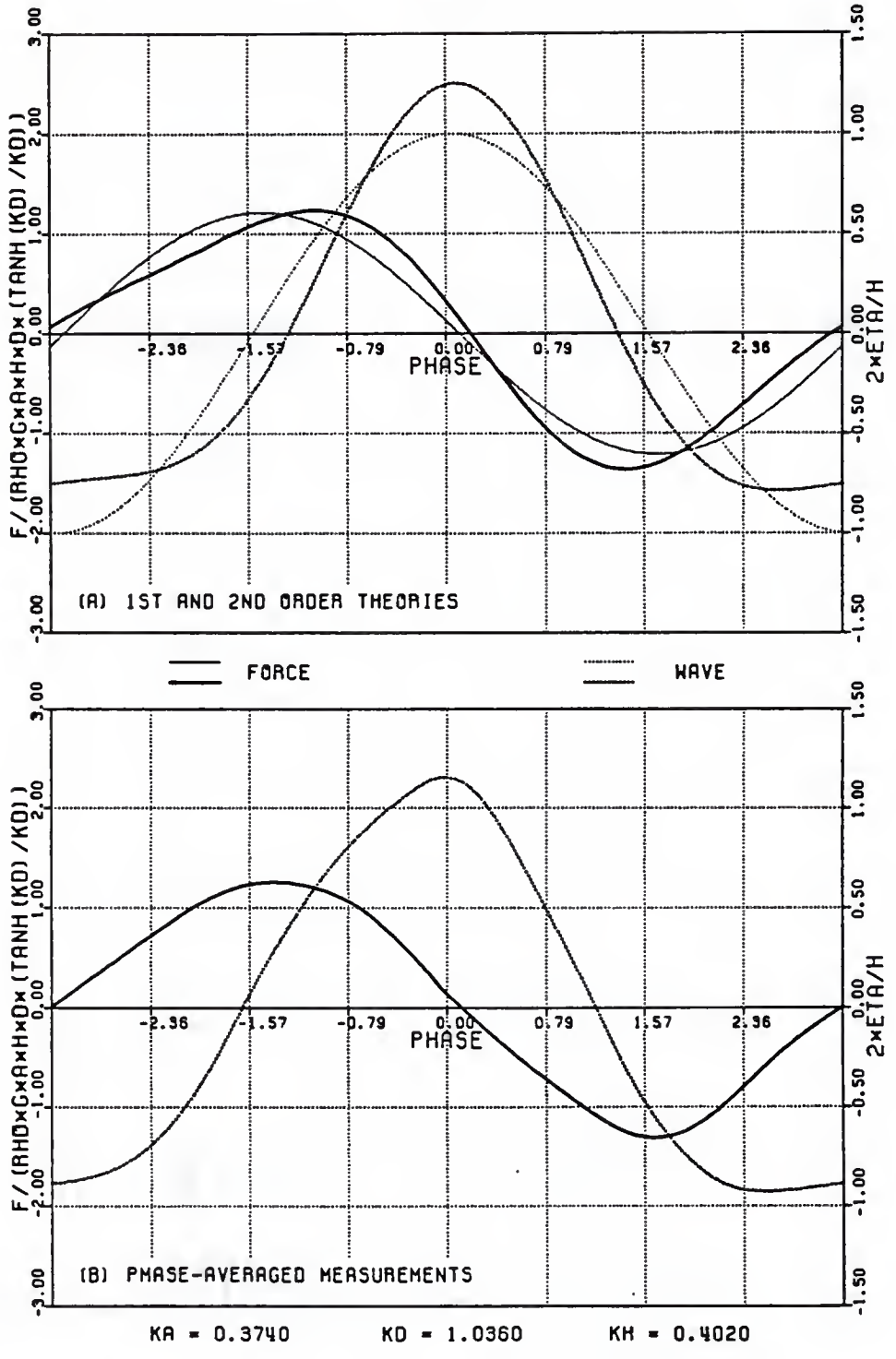

Figure F.13: Theoretical and experimental results for (1) wave profile at $r = 10a$ and $\theta = \pi/2$ and (2) depth-integrated force, for $ka = 0.374$, $kd = 1.036$, and $kH = 0.402$

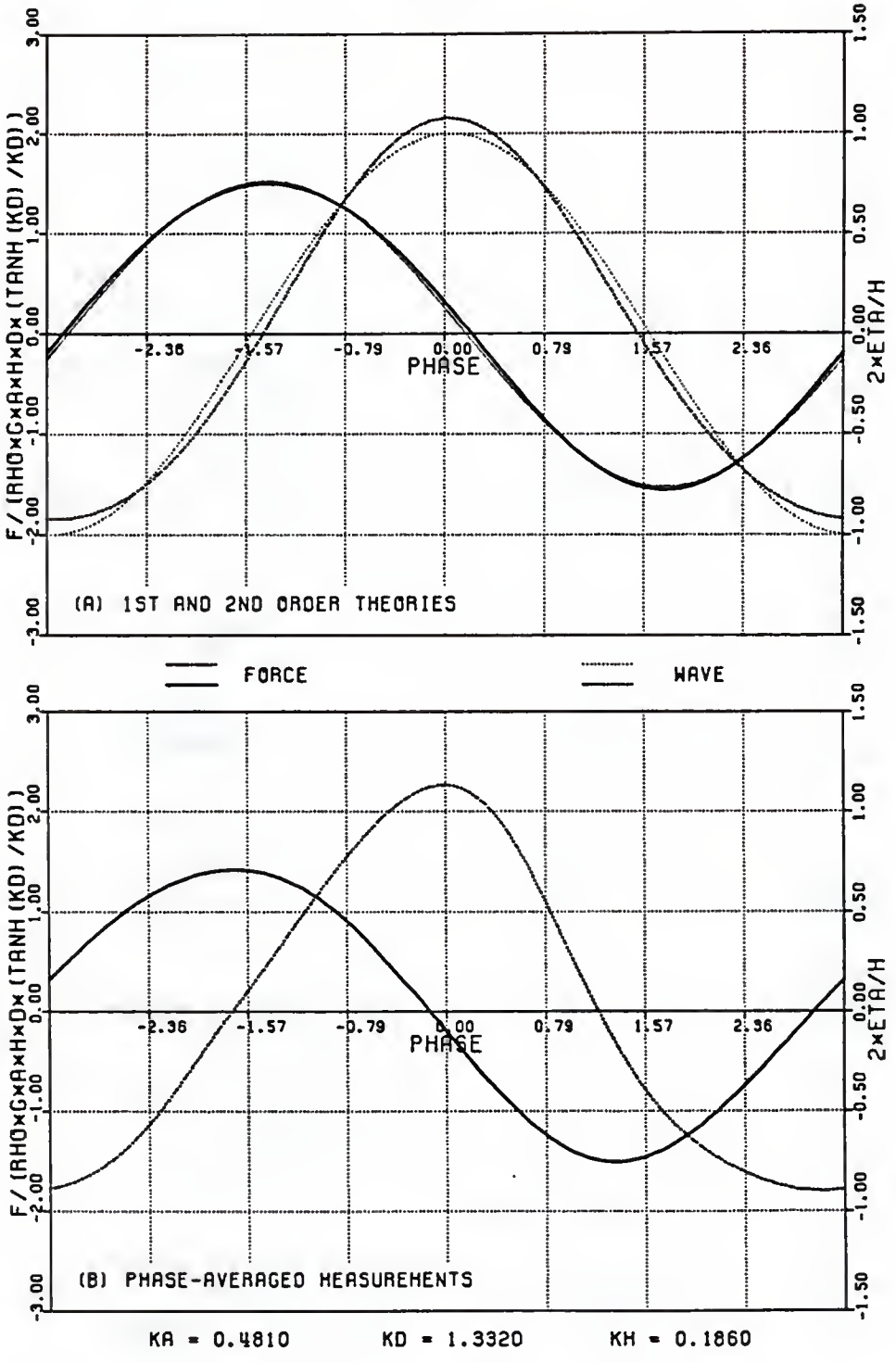

Figure F.14: Theoretical and experimental results for (1) wave profile at $r = 10a$ and $\theta = \pi/2$ and (2) depth-integrated force, for $ka = 0.481$, $kd = 1.332$, and $kH = 0.186$

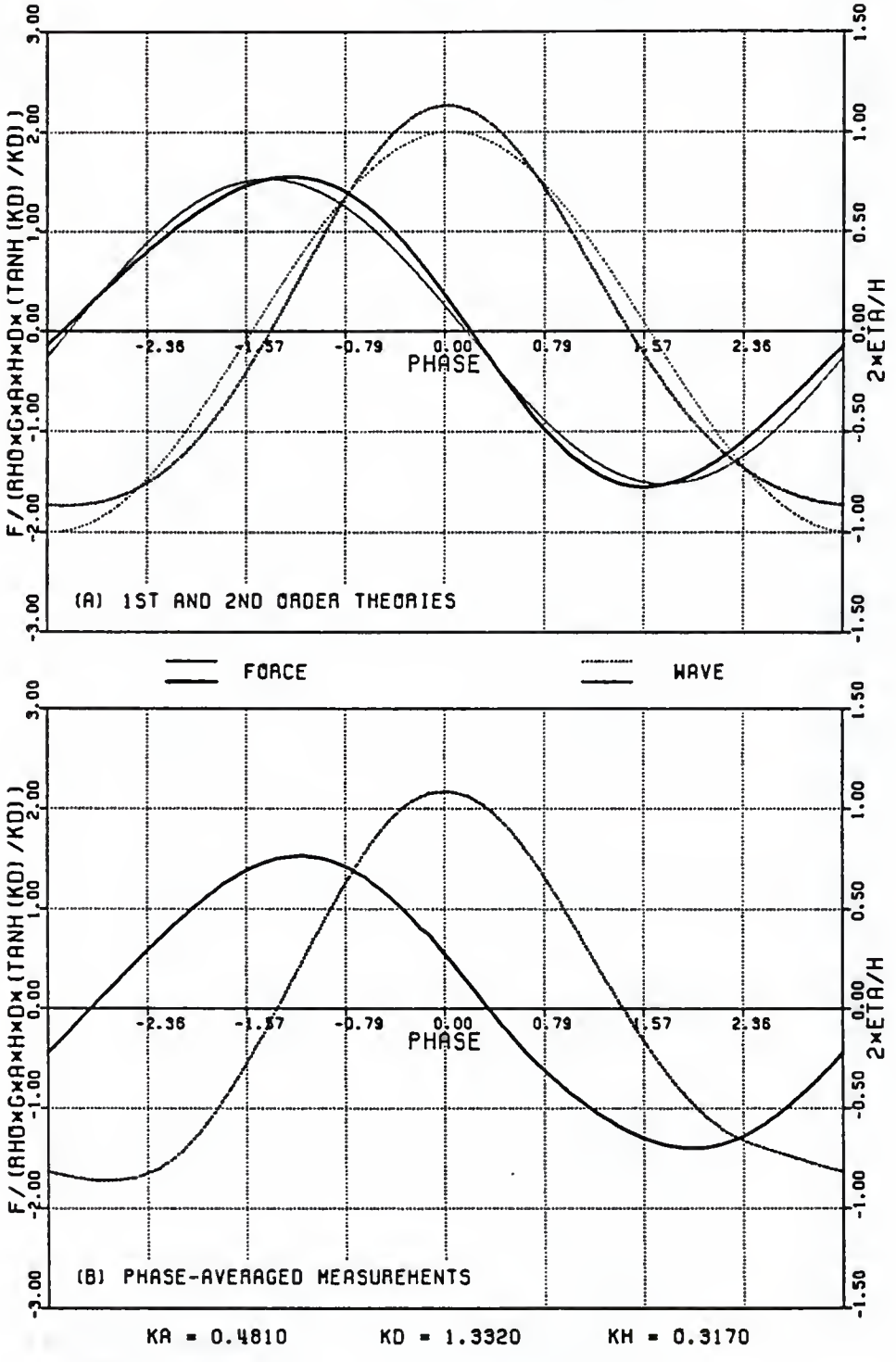

Figure F.15: Theoretical and experimental results for (1) wave profile at $r = 10a$ and $\theta = \pi/2$ and (2) depth-integrated force, for $ka = 0.481$, $kd = 1.332$, and $kH = 0.317$

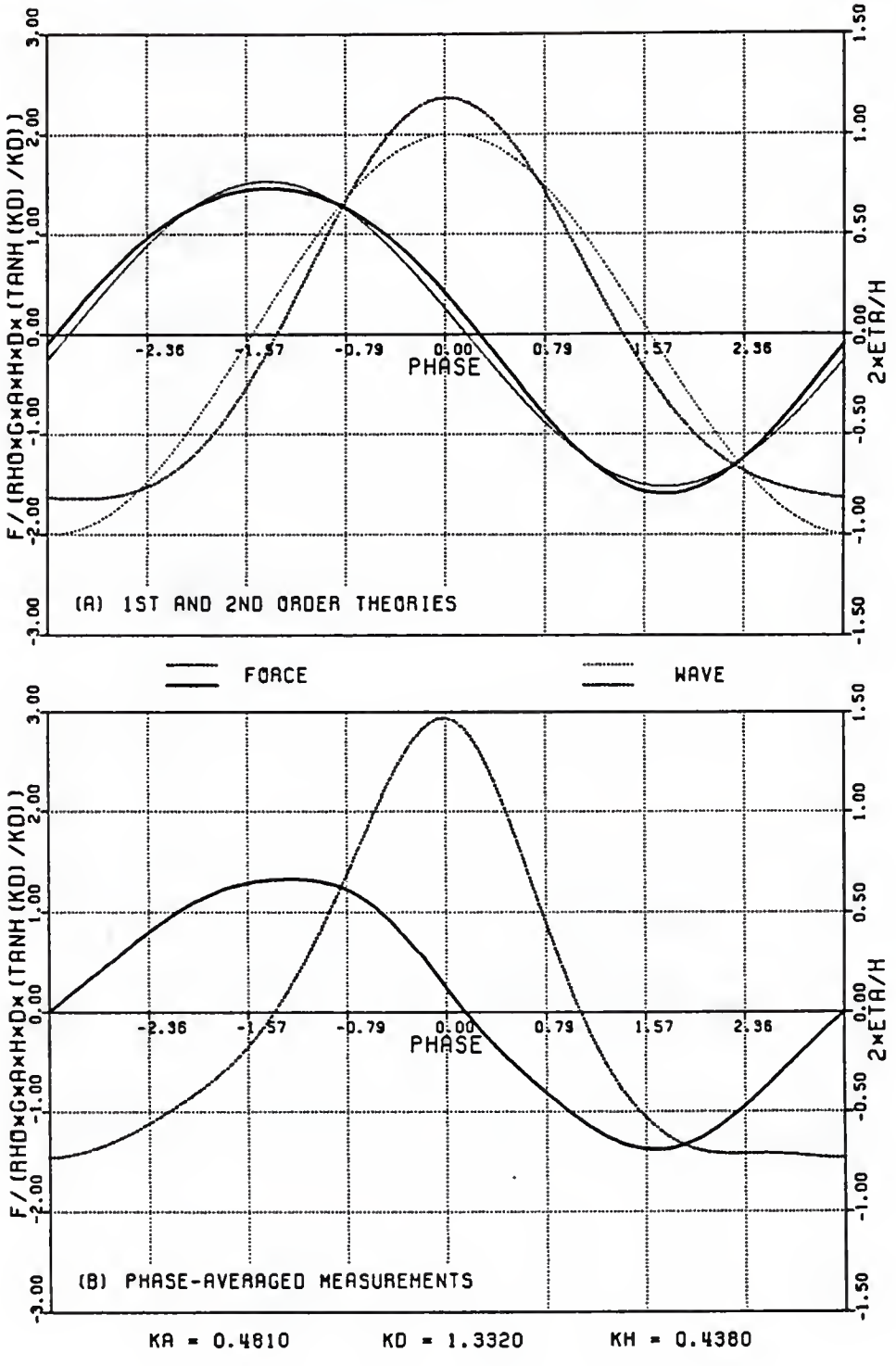

Figure F.16: Theoretical and experimental results for (1) wave profile at $r = 10a$ and $\theta = \pi/2$ and (2) depth-integrated force, for $ka = 0.481$, $kd = 1.332$, and $kH = 0.438$

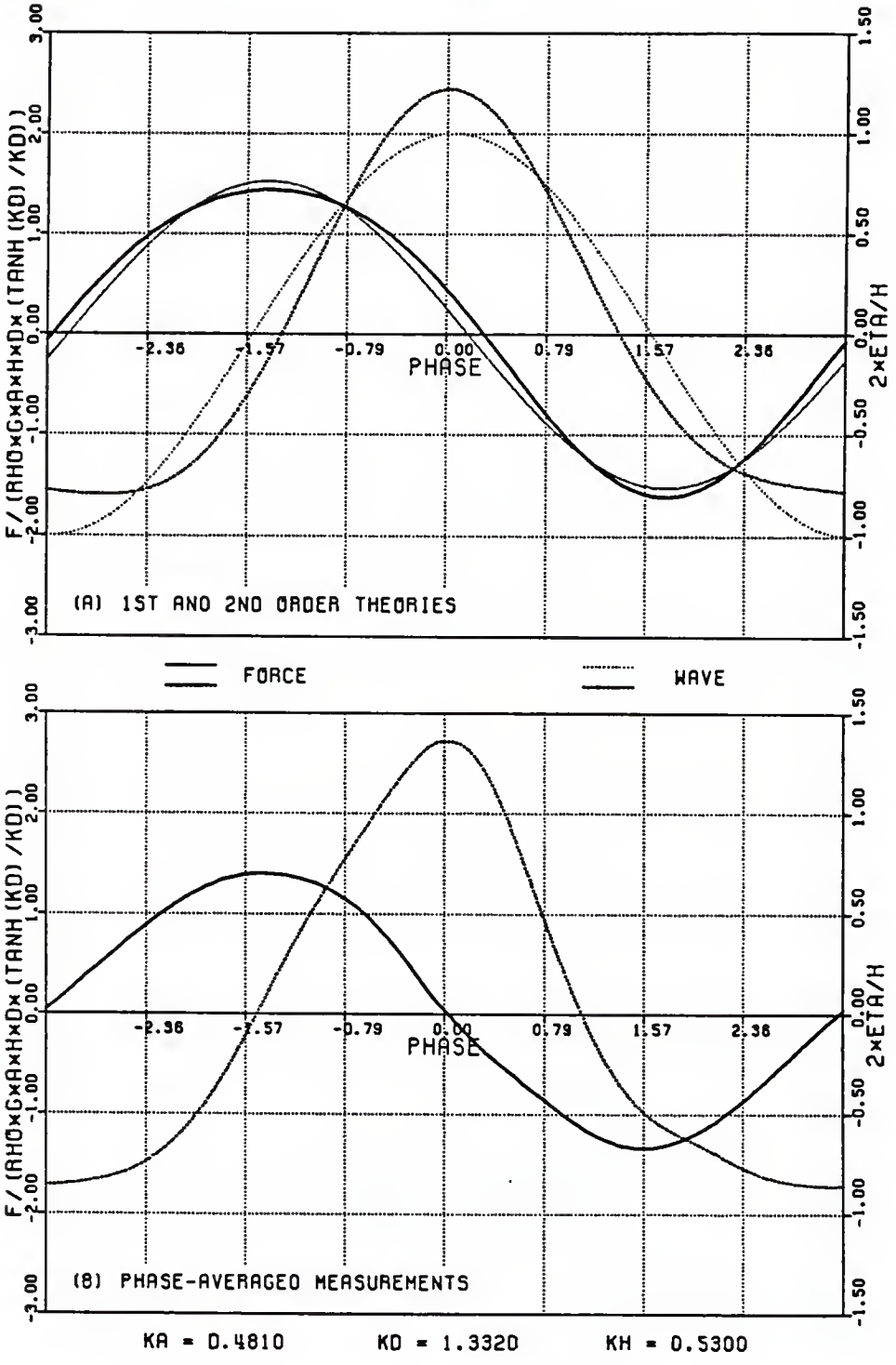

Figure F.17: Theoretical and experimental results for (1) wave profile at $r = 10a$ and $\theta = \pi/2$ and (2) depth-integrated force, for $ka = 0.481$, $kd = 1.332$, and $kH = 0.530$

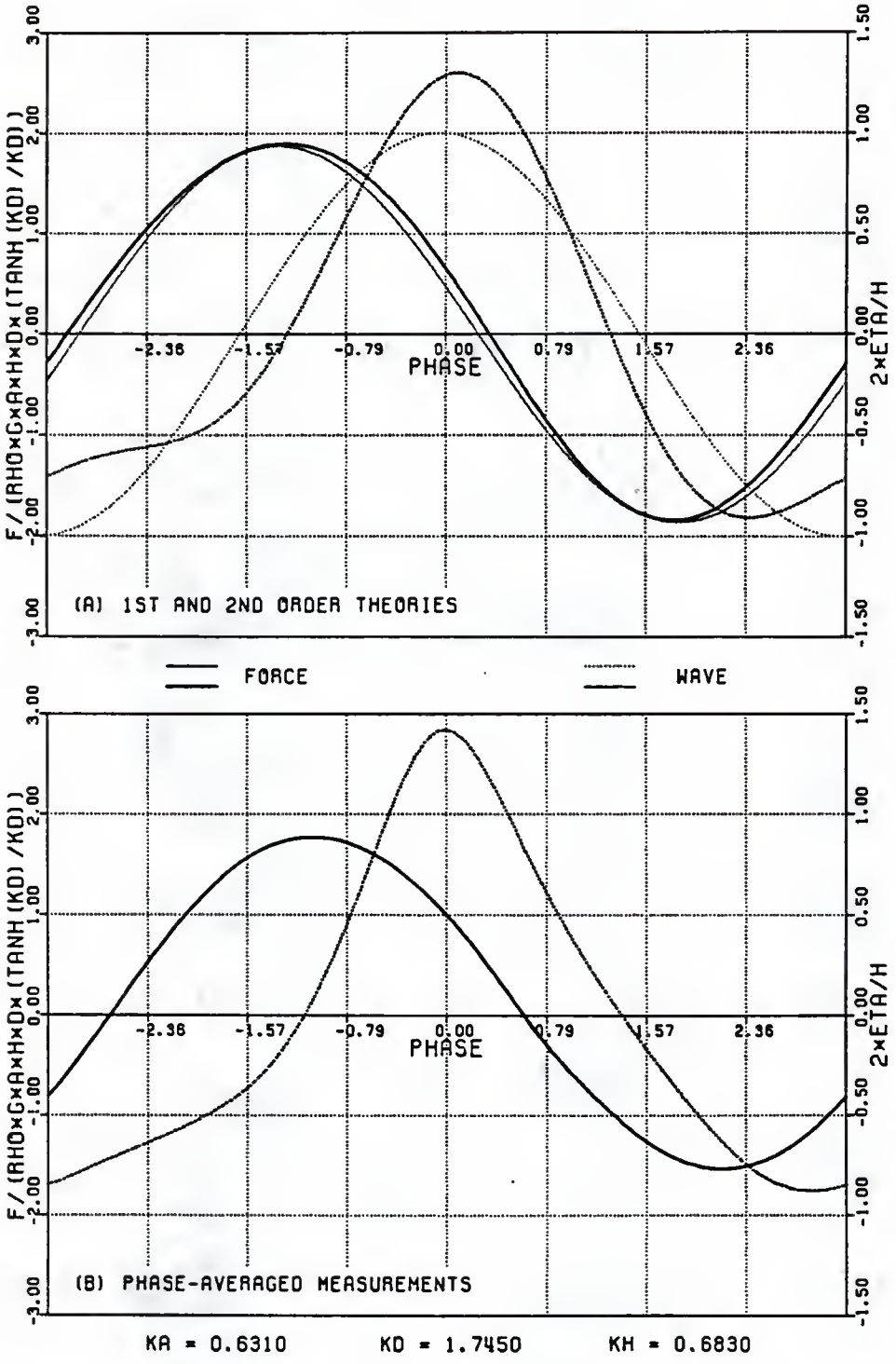

Figure F.18: Theoretical and experimental results for (1) wave profile at $r = 10a$ and $\theta = \pi/2$ and (2) depth-integrated force, for $ka = 0.631$, $kd = 1.745$, and $kH = 0.683$

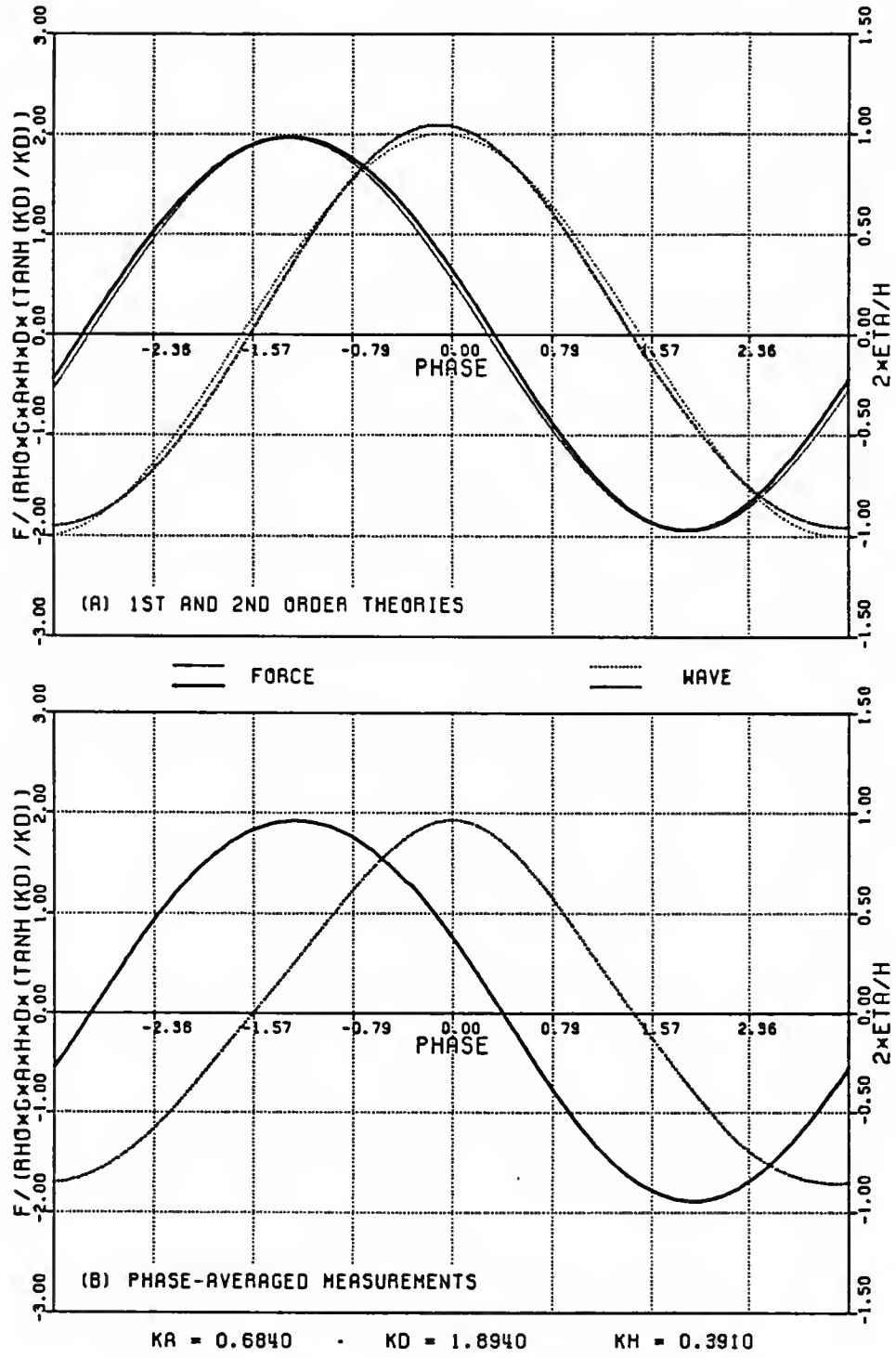

Figure F.19: Theoretical and experimental results for (1) wave profile at $r = 10a$ and $\theta = \pi/2$ and (2) depth-integrated force, for $ka = 0.684$, $kd = 1.894$, and $kH = 0.391$

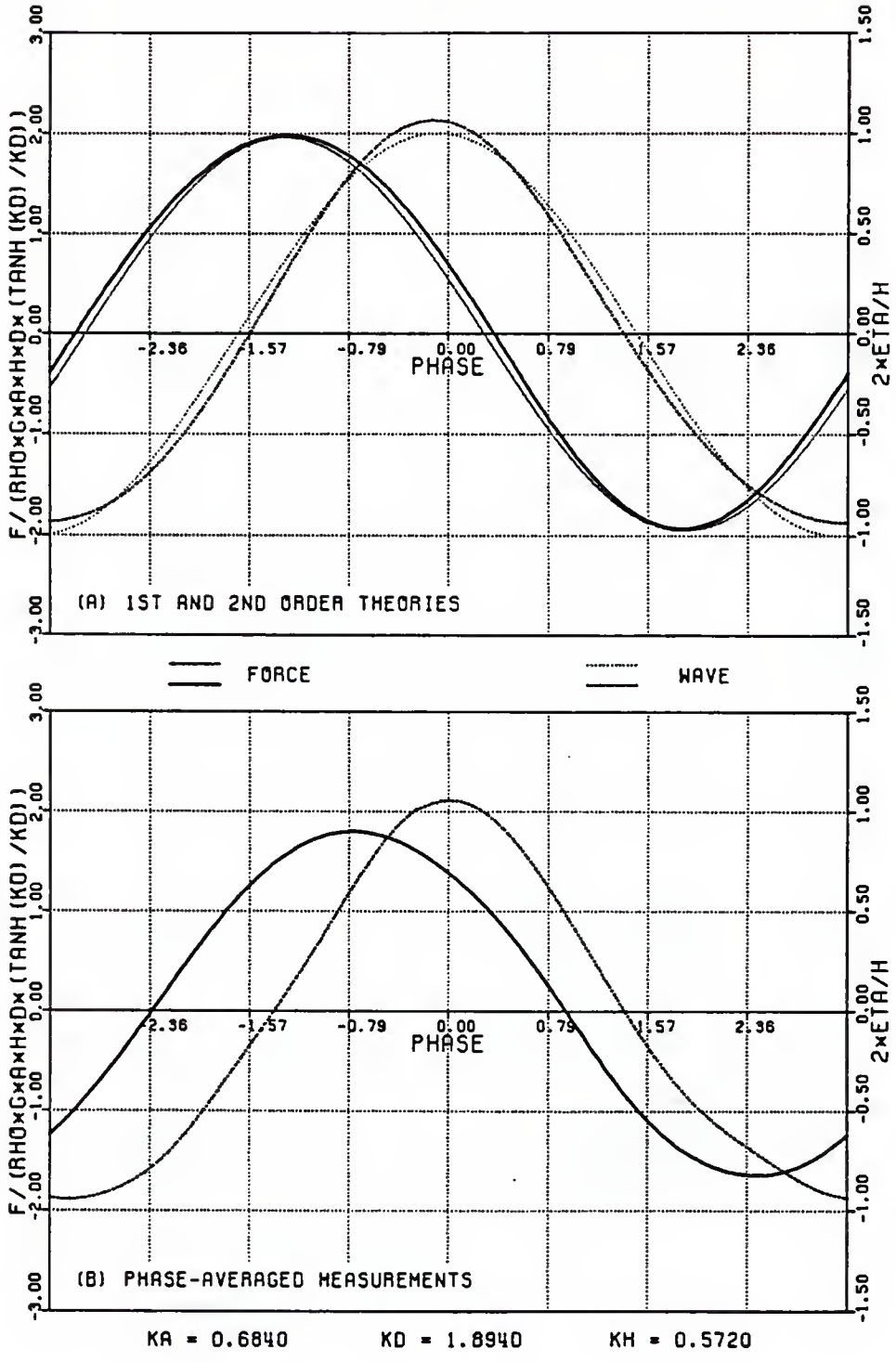

Figure F.20: Theoretical and experimental results for (1) wave profile at $r = 10a$ and $\theta = \pi/2$ and (2) depth-integrated force, for $ka = 0.684$, $kd = 1.894$, and $kH = 0.572$

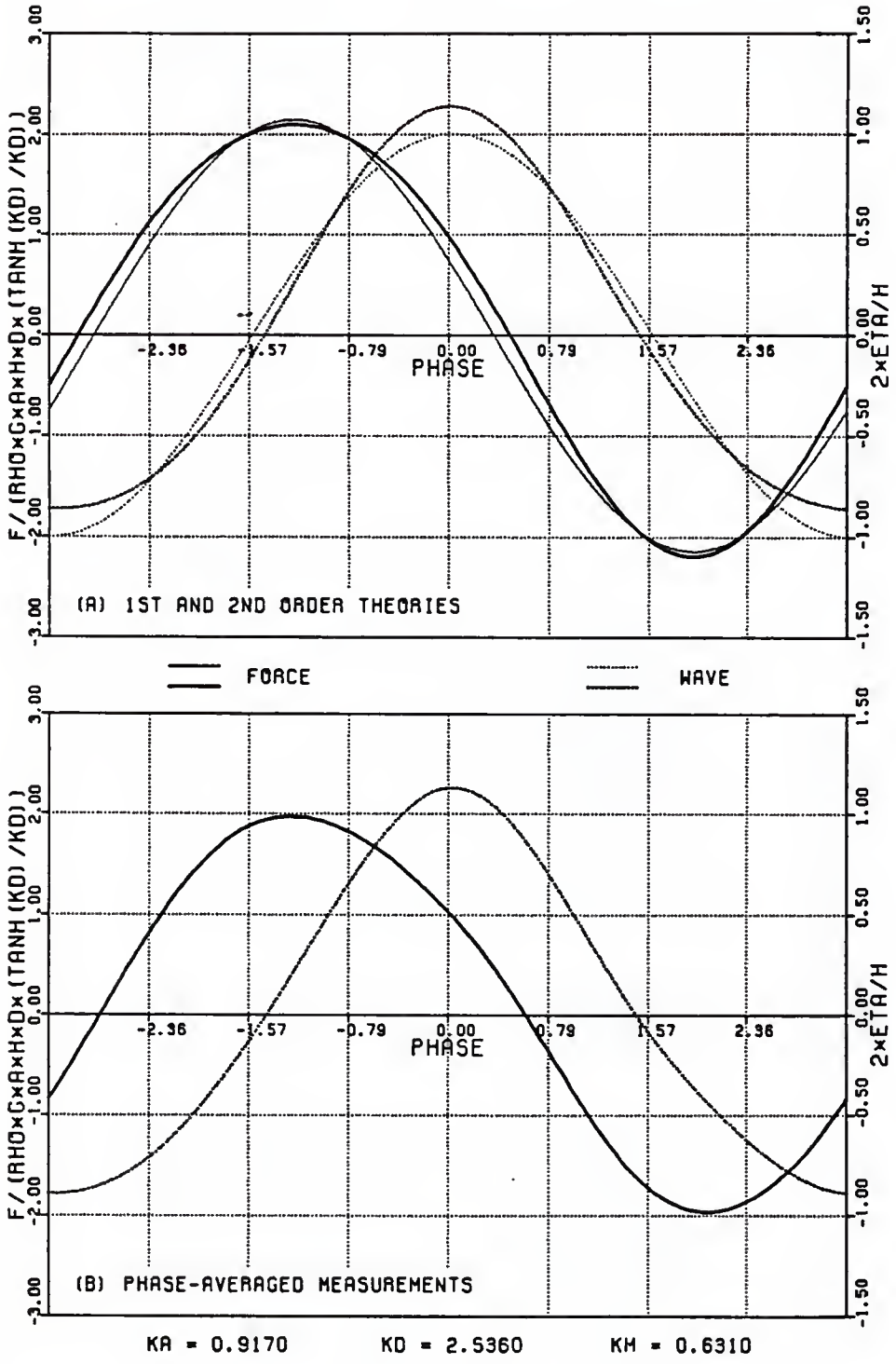

Figure F.21: Theoretical and experimental results for (1) wave profile at $r = 10a$ and $\theta = \pi/2$ and (2) depth-integrated force, for $ka = 0.917$, $kd = 2.536$, and $kH = 0.631$

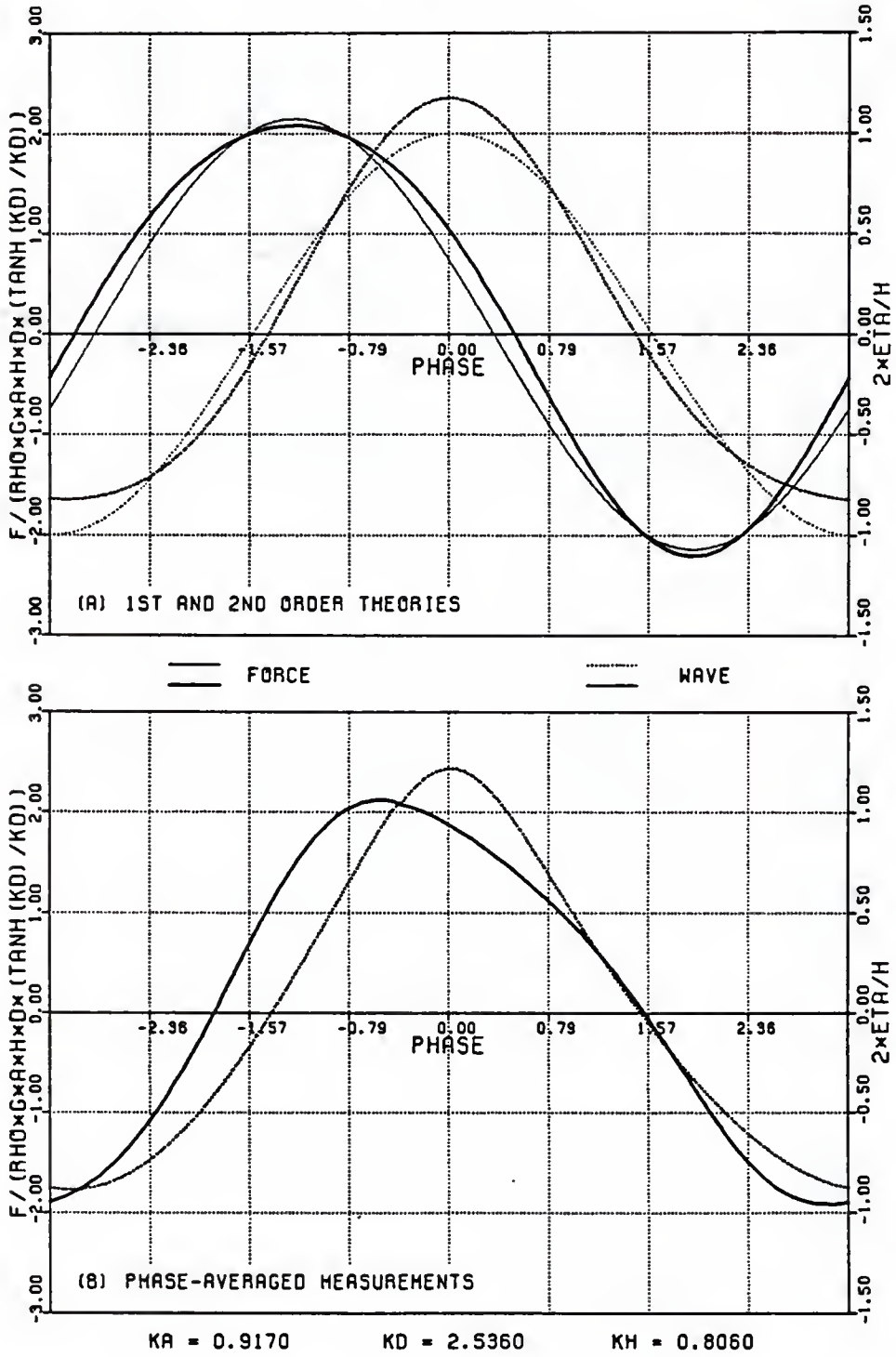

Figure F.22: Theoretical and experimental results for (1) wave profile at $r = 10a$ and $\theta = \pi/2$ and (2) depth-integrated force, for $ka = 0.917$, $kd = 2.536$, and $kH = 0.806$

BIBLIOGRAPHY

Abramowitz, M., and Stegun, I.A., 1972, Handbook of Mathematical Functions, Dover Publications, New York.

Biesel, F., 1963, "Radiating Second-Order Phenomena in Gravity Waves," Tenth Intl. Assoc. Hydr. Res., Vol. 1, Paper 1.27, pp. 198-203.

Buhr Hansen, J., and Svendsen, I.A., 1974, "Laboratory Generation of Waves of Constant Form," Proc. 14th Intl. Conf. Coastal Eng., Copenhagen, pp. 321-339.

Chakrabarti, S.K., 1972, "Nonlinear Wave Forces on Vertical Cylinder," J. Hydraulics Div., ASCE, Vol. 98, No. HY11, pp. 1895-1909.

Chakrabarti, S.K., 1975, "Second-Order Wave Force on Large Vertical Cylinder," J. Waterways, Harbors and Coastal Eng. Div., ASCE, Vol. 101, No. WW3, pp. 311-317.

Chakrabarti, S.K., 1977, Discussion of "Forces due to Nonlinear Waves on Vertical Cylinders," J. Waterways, Harbors and Coastal Eng. Div., ASCE, Vol. 103, No. WW3, pp. 404-407.

Chakrabarti, S.K., 1978, "Comments on Second-Order Wave Effects on Large Diameter Vertical Cylinder," J. Ship Res., Vol. 22, No.4, pp. 266-268.

Chakrabarti, S.K., 1983, "Nonlinear Wave Effects on Large Offshore Structures," Proc. Second Intl. Symp. Ocean Eng. and Ship Handling, Gothenburg, pp. 19-49.

Chakrabarti, S.K., 1984, "Steady Drift Force on Vertical Cylinder - Viscous vs. Potential," Appl. Ocean Res., Vol. 6, No. 2, pp. 73-82.

Chakrabarti, S.K., and Tam, W.A., 1973, "Gross and Local Wave Loads on a Large Vertical Cylinder - Theory and Experiment," Proc. Offshore Tech. Conf., Houston, Paper OTC 1818, Vol. 1, pp. 813-826.

Chakrabarti, S.K., and Tam, W.A., 1975, "Wave Height Distribution Around Vertical Cylinder," J. Waterways, Harbors, and Coastal Eng. Div., ASCE, Vol. 101, No. WW2, pp. 225-230.

Chen, M.C., 1979, "Nonlinear Diffraction Theory by an Eigenfunction Expansion of the Green's Function," Ph.D. Dissertation, Oregon State Univ., Corvalis.

Chen, M.C., and Hudspeth, R.T., 1982, "Nonlinear Diffraction by Eigenfunction Expansion," J. Waterway, Port, Coastal and Ocean Div., ASCE, Vol. 108, No. WW3, pp. 306-325.

Courant, R., and Hilbert, D., 1961, Methods of Mathematical Physics, Interscience Publishers, New York.

Dean, R.G., 1970, "Relative Validities of Water Wave Theories," J. Waterways, Harbors, and Coastal Eng. Div., ASCE, Vol. 96, No. WW1, pp. 105-119.

Dean, R.G., and Dalrymple, R.A., 1984, Water Wave Mechanics for Engineers and Scientists, Prentice-Hall, Englewood Cliffs, New Jersey.

Demirbilek, Z., and Gaston, J., 1985, "Nonlinear Wave Loads on a Vertical Cylinder," Ocean Eng., Vol. 12, No. 5, pp. 375-385.

Eatock Taylor, R., and Hung, S.M., 1987, "Second Order Diffraction Forces on a Vertical Cylinder in Regular Waves," Appl. Ocean Res., Vol. 9, No. 1, pp. 19-30.

Garrison, C.J., 1978, "Hydrodynamic Loading of Large Offshore Structures: Three-Dimensional Source Distribution Methods," In Numerical Methods in Offshore Engineering, eds. O. Zienkiewicz, R. Lewis, and K. Stagg, John Wiley and Sons, Chichester, pp. 97-140.

Garrison, C. J., 1979, "The Consistent Second-Order Theory of Wave/Structure Interaction," Naval Postgraduate School, Tech. Rpt. No. NPS-69-79-010, Monterey.

Hallermeier, R.J., 1976, "Nonlinear Flow of Wave Crests Past a Thin Pile," J. Waterways, Harbors, and Coastal Eng. Div., ASCE, Vol. 102, No. WW4, pp. 365-377.

Havelock, T.H., 1940, "The Pressure of Water Waves Upon a Fixed Obstacle," Proc. Royal Soc. London, Series A, Vol. 175, No. 963, pp. 409-421.

Herfjord, K., and Nielsen, F., 1986, "Nonlinear Wave Forces on Fixed Vertical Cylinder Due to Sum Frequency of Waves in Irregular Seas," Appl. Ocean Res., Vol. 8, No. 1.

Hobgen, N., and Standing, R.G., 1975, "Experience in Computing Wave Loads on Large Bodies," Proc. Offshore Tech. Conf., Houston, Paper No. OTC 2189, Vol. 11, pp. 413-431.

Hudimac, A.A., 1958, "The Motion of a Body in a Fluid with a Free Surface and Irregular Solid Boundaries," Inst. for Eng. Res., Univ. of Calif., Series No. 82, Issue No. 5.

Hunt, J.N., and Baddour, R.E., 1980a, "Second-Order Standing Waves Bounded by Circular Cylinders," J. Waterway, Port, Coastal and Ocean Div., ASCE, Vol. 106, No. WW1, pp. 122-127.

Hunt, J.N., and Baddour, R.E., 1980b, "Nonlinear Standing Waves Bounded by Cylinders," Q. J. Mech.Appl. Math., Vol. 33, Pt. 3, pp. 357-371.

Hunt, J.N., and Baddour, R.E., 1981, "The Diffraction of Nonlinear Progressive Waves by a Vertical Cylinder," Q. J. Mech. Appl. Math., Vol. 34, Pt. 1, pp. 69-89.

Hunt, J.N., and Williams, A.N., 1982, "Nonlinear Diffraction of Stokes Water Waves by a Circular Cylinder for Arbitrary Uniform Depth," J. de Mechanique Theorique et Appliquee, Vol. 1, No. 3, pp. 429-449.

Isaacson, M., 1977a, "Shallow Wave Diffraction Around Large Cylinder," J. Waterway, Port, Coastal and Ocean Div., ASCE, Vol. 103, No. WW1, pp. 69-82.

Isaacson, M., 1977b, "Nonlinear Wave Forces on Large Offshore structures," J. Waterway, Port, Coastal and Ocean Div., ASCE, Vol. 103, No. WW1, pp. 166-170.

Isaacson, M., 1977c, Discussion of "Forces due to Nonlinear Waves on Vertical Cylinders," J. Waterways, Harbors and Coastal Eng. Div., ASCE, Vol. 103, No. WW2, PP. 299-300.

Isaacson, M., 1978, "Wave Runup Around Large Circular Cylinder," J. Waterway, Port, Coastal, and Ocean Div., ASCE, Vol. 104, No.WW1, pp. 69-79.

Kurata, K., and Ijima, T., 1979, "Finite Element Analysis of Wave Forces on Structures," Proc. Civil Eng. in the Oceans, ASCE, San Francisco, Vol.1, pp. 172-186.

Laird, A.D.K., 1955, "A Model Study of Wave Action on a Cylindrical Island," Trans. Am. Geophys. Union, Vol. 36, No. 2, pp. 279-285.

Le Mehaute, B., 1969, "An Introduction to Hydrodynamics and Water Waves," Water Wave Theories,Vol. II, U.S. Dept of Commerce, TR ERL 118-POL-3-2.

Lighthill, J., 1979, "Waves and Hydrodynamic Loads," Proc. 2nd Intl. Conf. on Behaviour of Offshore structures, London, Vol. 1, pp. 1-40.

MacCamy, R.C., and Fuchs, R.A., 1954, "Wave Forces on Piles: A Diffraction Theory," U.S. Army Corps of Eng., Beach Erosion Board, Tech. Mem. No. 69.

Mei, C.C., 1983, The Applied Dynamics of Ocean Surface Waves, John Wiley and Sons, New York.

Miloh, T., 1980, "Irregularities in Solutions of Nonlinear Wave Diffraction Problem by Circular Cylinder," J. Waterway, Port, Coastal and Ocean Div., ASCE, Vol. 106, No. WW2, pp. 279-284.

Molin, B., 1979, "Second-Order Diffraction Loads Upon Three-Dimensional Bodies," Appl.Ocean Res., Vol. 1, No. 4, pp. 197-202.

Mogridge, G.R., and Jamieson, W.W., 1976, "Wave Loads on Large Circular Cylinders: A Design Method," Hydraulics Lab, Nat. Res. Council Canada, Rpt. No. MH-111.

Monacella, V.J., 1966, "The Disturbance Due to Slender Ship Oscillating in Waves in a Fluid of Finite Depth," J. Ship Res., Vol. 10, No. 4, pp. 242-252.

Morison, J.R., O'Brien, M.P., Johnson, J.W., and Schaaf, S.A., 1950, "The Force Exerted by Surface Waves on Piles," Petrol. Trans. AIME, Vol.189., pp. 149-154.

Nagai, S., 1973, "Wave Forces on Structures," In Advances in Hydroscience, ed. V.T. Chow, Vol. 9, Academic Press, New York, pp. 253-324.

Rahman, M., 1984, "Wave Diffraction by Large Offshore Structures: An exact Second-Order Theory," Appl.Ocean Res., Vol.6, No. 2, pp. 90-100.

Rahman, M., and Heaps, H.S., 1983, "Wave Forces on Offshore Structures: Nonlinear Wave Diffraction by Large Cylinders," J. Phys. Ocean., Vol. 13, pp. 2225-2235.

Raman, H., Jothishankar, N., and Venkatanarasaiah, P., 1977, "Nonlinear Wave Interaction with Vertical Cylinder of Large Diameter," J. Ship Res., Vol. 22, No. 2, pp. 120-124.

Raman, H., and Venkatanarasaiah, P., 1976a,"Forces due to Nonlinear Waves on Vertical Cylinders," J. Waterways, Harbors and Coastal Eng. Div., ASCE, Vol. 102, No. WW3, pp. 301-316.

Raman, H., and Venkatanarasaiah, P., 1976b, "Forces Due to Nonlinear waves on Vertical Cylinders of Large Diameter," Mitteilungen, Leichtweiss-Institut fur Wasserbau, Tech. Univ. Braunschweig, Vol.51, pp.101-136.

Sabuncu, T., and Goren, O., 1985, "Second-Order Vertical and Horizontal Wave Forces on a Circular Dock," Ocean Eng., Vol. 12, No. 4, pp. 341-361.

Sarpkaya, T., and Isaacson, M., 1981, Mechanics of Wave Forces on Offshore Structures, Van Nostrand Reinhold, New York.

Sneddon, I.N., 1951, Fourier Transforms, McGraw-Hill, New York.

Sommerfeld, A., 1949, Partial Differential Equations in Physics, Academic Press, New York.

Stoker, J.J., 1957, Water Waves, Interscience Publishers, New York.

U.S. Army Corps of Engineers, 1977, ShoreProtection Manual, U.S. Army Coastal Eng. Res. Center, Ft. Belvoir, Virginia.

Watson, G.N., 1962, Theory of Bessel Functions, Cambridge Univ. Press, Cambridge.

Wehausen, J.V., 1980, "Perturbation Methods in Diffraction," J. Waterway, Port, Coastal and Ocean Div., ASCE, Vol. 106, No. WW2, pp. 290-291.

Wehausen, J. V., and Laitone, E.V., 1960, "Surface Waves," In Encyclopedia of Physics, ed. S. Flugge, Springer-Verlag, Berlin, Vol. IX, pp. 446-778.

Yamaguchi, M., and Tsuchiya, Y., 1974, "Nonlinear Effect of Waves on Wave Pressure and Wave Force on a Large Cylindrical Pile,"Proc. Civil Eng. Soc. in Japan, No. 229, pp. 41-53.

BIOGRAPHICAL SKETCH

The author was born on October 18, 1958, in Gettysburg, Pennsylvania, but spent most of his life in State College, Pennsylvania, home of Penn State University. Despite growing up in the mountains, he developed an interest in marine science during annual summer vacations to the New Jersey shore. In 1975, he was selected as one of 42 high school juniors from around the United States to attend a National Science Foundation summer program on marine biology and oceanography at Wallops Island, Virginia. After graduating from State College Area High School in 1976, he enrolled in civil engineering at Penn State, emphasizing hydraulics and hydrology. At Penn State, he held leadership positions in several campus organizations and in Acacia Fraternity. He received his Bachelor of Science in Civil Engineering in 1980, with highest distinction. His professional career in ocean engineering began in 1980-1982 when he pursued his Master of Civil Engineering degree at the University of Delaware under Dr. Robert G. Dean. After graduating from Delaware in 1982, he worked as a coastal engineer for the U.S. Army Corps of Engineers in Anchorage, Alaska, where he was project manager for small boat harbor feasibility studies and a statewide wind and wave data collection program. In 1984, he started work toward his Ph.D. at the University of Florida, again under Dr. Dean, and he has worked on numerical modelling, laboratory experimentation, and field studies in the areas of coastal processes and offshore structures. Following graduation, he will be an Assistant Professor of Ocean Engineering at the U.S. Naval Academy in Annapolis, Maryland.

I certify that I have read this study and that in my opinion it conforms to acceptable standards of scholarly presentation and is fully adequate, in scope and quality, as a dissertation for the degree of Doctor of Philosophy.

Robert G. Dean, Chairman
Graduate Research Professor of Engineering Sciences

I certify that I have read this study and that in my opinion it conforms to acceptable standards of scholarly presentation and is fully adequate, in scope and quality, as a dissertation for the degree of Doctor of Philosophy.

Thomas T. Bowman
Associate Professor of Mathematics

I certify that I have read this study and that in my opinion it conforms to acceptable standards of scholarly presentation and is fully adequate, in scope and quality, as a dissertation for the degree of Doctor of Philosophy.

Joseph L. Hammack
Professor of Engineering Sciences

I certify that I have read this study and that in my opinion it conforms to acceptable standards of scholarly presentation and is fully adequate, in scope and quality, as a dissertation for the degree of Doctor of Philosophy.

Lawrence E. Malvern
Professor of Engineering Sciences

I certify that I have read this study and that in my opinion it conforms to acceptable standards of scholarly presentation and is fully adequate, in scope and quality, as a dissertation for the degree of Doctor of Philosophy.

Hsiang Wang
Professor of Coastal and Oceanographic Engineering

This dissertation was submitted to the Graduate Faculty of the College of Engineering and to the Graduate School and was accepted as partial fulfillment of the requirements for the degree of Doctor of Philosophy.

August 1987

Wayne H. Chen

Dean, College of Engineering

Dean, Graduate School

UNIVERSITY OF FLORIDA
3 1262 08553 9921